Pontifícia Universidade Católica
do Rio de Janeiro

Julio Alberto Rueda Cordero

Failure phenomena and fluid migration in naturally fractured rock formations

Tese de Doutorado

Thesis presented to the Programa de Pós-graduação em Engenharia Civil of PUC-Rio, in partial fulfillment of the requirements for the degree of Doutor em Engenharia Civil.

Advisor: Profª. Deane Roehl

Co-advisor: DSc. Eleazar Cristian Mejia Sanchez

Rio de Janeiro

July 2021

PONTIFÍCIA UNIVERSIDADE CATÓLICA
DO RIO DE JANEIRO

Julio Alberto Rueda Cordero

Failure phenomena and fluid migration in naturally fractured rock formations

Thesis presented to the Programa de Pós-graduação em Engenharia Civil of PUC-Rio, in partial fulfillment of the requirements for the degree of Doutor em Engenharia Civil. Approved by the undersigned Examination Committee.

Profª. Deane de Mesquita Roehl
Advisor
Departamento de Engenharia Civil e Ambiental – PUC-Rio

DSc. Eleazar Cristian Mejia Sanchez
Co-Advisor
Instituto Tecgraf – PUC-Rio

Prof. Celso Romanel
Departamento de Engenharia Civil e Ambiental – PUC-Rio

Prof. Luiz Fernando Martha
Departamento de Engenharia Civil e Ambiental – PUC-Rio

Prof. Marcelo Javier Sánchez Castilla
Texas A&M University

Dr. Leonardo Cabral Pereira
CENPES/Petrobras

Dr. Francisco Henriques Ferreira
CENPES/Petrobras

Rio de Janeiro, July 29th, 2021

Julio Alberto Rueda Cordero

Graduated in Civil Engineering from Industrial University of Santander, UIS – Colombia in 2009. Masters in Civil Engineering from Pontifical Catholic University of Rio de Janeiro – Brazil in 2013. Consultant for computational geomechanics projects at UIS-Ecopetrol (Colombia) and assistant professor at Industrial University of Santander in 2015 – 2017. Researcher at the Tecgraf Institute – PUC-Rio 2011-2014 and 2017-2021. In 2017 he started the doctoral program at PUC-Rio in the research line of computational geomechanics.

Bibliographic data

Rueda, Julio Alberto

Failure phenomena and fluid migration in naturally fractured rock formations / Julio Alberto Rueda Cordero; advisor: Deane de Mesquita Roehl; co-advisor: Cristian Mejia Sanchez. – 2021.
177 f. il. (color.) ; 30 cm

Tese (Doutorado) – Pontifícia Universidade Católica do Rio de Janeiro, Rio de Janeiro, Departamento de Engenharia Civil e Ambiental, 2021.
Inclui bibliografia.

1. Engenharia civil – Teses. 2. Geomecânica computacional. 3. Método dos elementos finitos. 4. Fragmentação de malha. 5. Propagação de fraturas. 6. Produção de formações fraturadas. I. Roehl, Deane. II. Mejia, Cristian. III. Pontifícia Universidade Católica do Rio de Janeiro. Departamento de Engenharia Civil. IV. Título.

CDD: 624

To my parents for their support and encouragement.

Acknowledgements

I would like to thank my parents for their support, love and affection, and for the teachings of life. Even from a distance they were always present. My sisters, for encouraging me to continue on the academic journey. Jéssika, my inspiring wife, for her love, company and affection, and unconditional support.

I would also like to thank in particular all those who contributed to the development of this thesis:

my advisors Professor Deane Roehl and Cristian Mejia, for following up. His guidance and encouragement were essential for carrying out this work. Thanks for all the knowledge transmitted

the professors who contributed to my academic education, and for the opportunity to improve and acquire new knowledge

the Tecgraf Institute for the opportunity to work with a topic of great relevance and challenges

all colleagues and friends of the group, especially Cristian, Roberto, Renato and Nilthson, for the help and friendship offered throughout the journey.

This study was financed in part by the Coordenação de Aperfeiçoamento de Pessoal de Nível Superior - Brasil (CAPES) - Finance Code 001;

This research was funded by the Conselho Nacional de Desenvolvimento Científico e Tecnológico – (CNPq) –140826/2018-1; the Fundação de Amparo à Pesquisa do Estado do Rio de Janeiro – (FAPERJ) – E-26/200.781/2019; the Petrobras - ANP n° 20234-1, "SONAR" (PUC-Rio/Petrobras/ANP), and the PUC-Rio. Their support is gratefully acknowledged

Abstract

Rueda Cordero, Julio Alberto; Roehl, Deane; Mejia, Cristian. **Failure phenomena and fluid migration in naturally fractured rock formations.** Rio de Janeiro, 2021. 177p. PhD Thesis - Departamento de Engenharia Civil e Ambiental, Pontifícia Universidade Católica do Rio de Janeiro.

The presented study proposes robust numerical models to simulate the phenomena present in fracture propagation and fluid migration problems in fractured media. An innovative mesh fragmentation technique with an intrinsic pore-cohesive zone approach is developed to simulate unrestricted hydraulic fracture propagation in fractured media. The proposed method allows studying the effect of some primary parameters on hydraulic and natural fracture interaction. A new 3D hydromechanical formulation for an enhanced dual-porosity/dual-permeability model is proposed to represent a fractured porous formation more realistically in reservoir simulations. The new model allows the study of the impacts of natural fractures with different orientations at multiple scales on the hydromechanical behavior of the reservoir. Finally, this research work proposes a new methodology that integrates a robust fracture propagation model and reservoir simulation, improving the evaluation of production performance. We simulate several hydraulic fracturing scenarios for the assessment of the cumulative production of the reservoir. Moreover, we combined discrete fracture and enhanced dual porosity-dual permeability models to study the effects of fractures of multiple lengths on the hydraulically stimulated reservoir. The developed models are compared against experimental tests, analytical and numerical solutions. The comparative results show excellent agreement and validate the fully coupled hydromechanical formulations. From the numerical results, it was possible to identify the dominant parameters that influence hydraulic fracturing and the production performance of the hydraulically stimulated deposits.

Keywords

Finite Element Method; mesh fragmentation; Hydraulic Fracturing; Intersection between hydraulic and natural fractures; Reservoir simulation.

Resumo

Rueda Cordero, Julio Alberto; Roehl, Deane; Mejia, Cristian. **Fenômenos de falha e migração de fluido em formações rochosas naturalmente fraturadas**. Rio de Janeiro, 2021. 177p. Tese de Doutorado - Departamento de Engenharia Civil e Ambiental, Pontifícia Universidade Católica do Rio de Janeiro.

O presente estudo propõe modelos numéricos robustos para simular os fenômenos presentes nos problemas de propagação de fraturas e migração de fluidos em formações fraturadas. Uma técnica de fragmentação de malha com uma abordagem de zona poro-coesiva é desenvolvida para simular a propagação não planar de fraturas em formações fraturadas. O modelo proposto permite estudar os efeitos dos parâmetros primários sobre a interação de fraturas hidráulicas e naturais. O trabalho desenvolve uma nova formulação hidromecânica 3D do dupla porosidade e dupla permeabilidade aprimorada para a representação mais realista do médio fraturado em simulações de reservatório. O modelo permite estudar o impacto de fraturas naturais de múltiplas escalas e orientações no desempenho do reservatório. Finalmente, o trabalho propõe uma nova metodologia que integra ~~os~~ modelos robustos de propagação de fratura e simulação de reservatório, ~~para~~ aprimorando a avaliação do desempenho da produção. Foram simulados múltiplos cenários de fraturamento hidráulico para avaliar a produção dos reservatórios. Também foram integrados modelos de fratura discreta e dupla porosidade-dupla permeabilidade para estudar os efeitos de fraturas de múltiplas escalas no reservatório estimulado hidraulicamente. Os modelos desenvolvidos foram comparados com testes experimentais, soluções analíticas e numéricas. Os resultados mostram excelente concordância e validam as formulações hidromecânicas. A partir dos resultados numéricos, se identificaram os parâmetros dominantes que influenciam o resultado do fraturamento hidráulico e a produção dos depósitos hidraulicamente estimulados.

Palavras Chave

Método dos Elementos Finitos; Fragmentação de malha; Fraturamento Hidráulico; Interseção entre fraturas; Simulação de reservatórios.

Contents

List of Figures

List of tables

1
Introduction

1.1.
Problem description and research motivation

Hydraulic fracturing (hydraulic stimulation) is a technique in which a mixture of hydraulic viscous fluids is pumped into the well in order to initiate and extend fractures in the rock formation. In many conventional reservoirs, short fractures are sufficient to increase permeability and obtain economical production (HOLDITCH, 2006). In contrast, in low permeability reservoirs, it is essential to create long hydraulic fractures that stimulate natural fracture networks to increase drainage paths and well-reservoir connectivity (MCCLURE; HORNE, 2014; RUTLEDGE; MAYERHOFER; PHILLIPS, 2004; WENG et al., 2011; WENG; VARAHANARESH; KRESSE, 2015).

The characteristics of natural fracture systems play a very important role in the development of oil and gas fields. Problems of lost circulation during drilling operations are directly related to induced fractures and the presence of natural fractures. It is believed that the resulting complexity of the stimulated fracture network geometry is due to the interaction between hydraulic and natural fractures. During the hydraulic fracturing treatment, environmental damages can be generated due to uncontrollable propagation of fractures, which can connect them to shallower aquifer layers (DAVIES et al., 2014) or geological faults with a potential risk of reactivation (RUTQVIST et al., 2013; SHEN; SHEN, 2014). Moreover, high fracture density between injector and producer wells can lead to Early Water Breakthrough (EWBT), affecting recovery methods in the regions of interest (BRATTON et al., 2006). On the other hand, cemented or mineralized fractures can form barriers that prevent fluid migration (DERSHOWITZ et al., 2000).

The success of hydraulic stimulation treatments to enhance the production of low permeability reservoirs depends on the interaction of induced and pre-existing fractures (RAHMAN; RAHMAN, 2013). Experimental observations have shown different events that can occur when hydraulic fractures interact with natural

fractures (JEFFREY; ZHANG; BUNGER, 2010). Cemented fractures are more likely to be crossed, while frictional fractures are more prone to slippage on the weakness plane (FATAHI; HOSSAIN; SARMADIVALEH, 2017; LI et al., 2017; WANG et al., 2018). Figure 1.1 illustrates the interaction modes between hydraulic and natural fractures. Hydraulic fractures can be arrested by sliding along the natural fracture, opening the natural fracture and integrating to the hydraulic fracture network, or crossing the natural fracture. In some cases, the natural fracture is dilated at a short distance and, subsequently, propagates through the rock in the most favorable direction depending mainly on the relative orientation of the natural fracture to the stress state (JEFFREY; ZHANG; THIERCELIN, 2009; WENG, 2015).

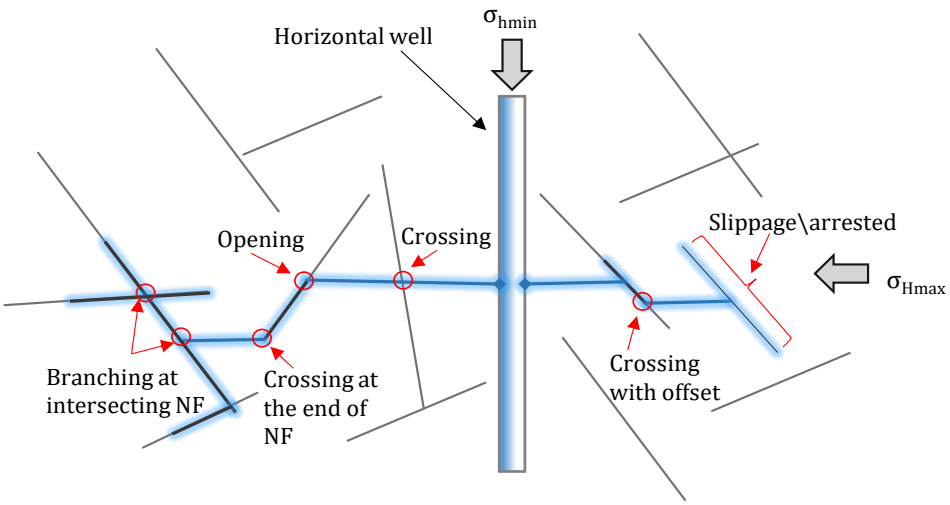

Figure 1.1. Schematic representation of the interaction process between hydraulic fracture and natural fractures

Laboratory tests and analytical solutions have focused on frictional interfaces to study and understand those events (BLANTON, 1982; CHUPRAKOV; MELCHAEVA; PRIOUL, 2014; GU et al., 2012; POTLURI; ZHU; HILL, 2005; RENSHAW; POLLARD, 1994; ZHOU; XUE, 2011). Recent researches have focused directly on the development of numerical algorithms to model hydraulic fracture propagation in rock formations, which is characterized by their different mechanical properties, in-situ stresses, and natural discontinuities. These models have been used to capture the final geometry of the stimulated fracture network. However, fluid-driven fracture propagation in naturally fractured reservoirs is a complex process, and its numerical modeling represents a great challenge even in 2D cases. The difficulty arises mainly from fracture mechanisms and the non-linear coupling process, which involves the interaction of different phenomena such as

(1) induced rock deformation by the fluid pressure on the fracture surface, (2) fluid flow inside and across the fracture, (3) fracture propagation in the rock formation, and (4) interaction with natural fractures. Also, fracture propagation models cannot evaluate and estimate the production performance of the stimulated reservoirs.

In the production stage, fractures control fractured rock's mechanical response (GUTIERREZ; YOUN, 2015), and they are dominant conduits for fluid transport (SHIN; SANTAMARINA, 2019). Traditionally, explicit (discrete fracture models) or implicit (continuum approaches) methods are used in heterogeneous reservoir simulation for production forecasting. Discrete fracture models (DFMs) represent fracture systems more realistically. This approach considers the effect of individual fractures on fluid flow explicitly and simulates the complex flow patterns in a fracture network more accurately (KARIMI-FARD; DURLOFSKY; AZIZ, 2004; KIM; DEO, 2000; MOINFAR et al., 2011). However, DFMs are computationally demanding for field-scale reservoir simulations. Although more simplified in the characterization of naturally fractured reservoirs than DFMs, implicit methods are more feasible. The implicit Dual porosity and dual permeability (DPDP) models are frequently preferred for field-scale modeling of the multiscale system owing to the low number of fitting parameters that allow efficient historical data calibration (ASHWORTH; DOSTER, 2019). However, in conventional studies, the simulation of a fractured reservoir focuses mainly on the hydraulic problem. Coupled geomechanics and fluid flow analyses are generally assumed to be 2D or limited to simplified orthogonal natural fractures. Moreover, traditional reservoir simulations do not incorporate the complex fracture network created by hydraulic fracturing in naturally fractured formations. In some cases, it is assumed that only natural fractures intercepted by planar hydraulic fractures placed at predefined locations were stimulated (SUPPACHOKNIRUN; TUTUNCU, 2017). Such assumptions can result inadequate for a realistic representation of reservoir conditions and lead to inaccurate production forecasting. Furthermore, the representation of the characteristics of the fracture system with varying intensity and persistence over a wide range of orientation, separation, aperture, and scales [1,2] needs to be included.

In this context, this work proposes the development of new hydromechanical numerical approaches for unrestricted fluid-driven fracture propagation and reservoir simulation in order to study the dominant factors that affect hydraulic fracturing treatment and the associated production performance.

1.2. Research objectives

This research work aims to provide robust 2D/3D numerical models to study the phenomena presented in fracture propagation and fluid migration problems in fractured media. For this purpose, a fully coupled hydromechanical approach is proposed to simulate unrestricted fluid-driven fracture propagation in a naturally fractured media. Another goal is to understand the role of natural fractures of multiple scales on the hydro-mechanical behavior of the reservoir. This is achieved by the implementation of a new 3D hydro-mechanical formulation for an enhanced dual-porosity/dual-permeability model (EDPDP) to represent a fractured porous formation more realistically. Finally, the thesis aims to combine fracture propagation models and reservoir simulations to study the dominant factors that affect hydraulic fracturing and the production performance of the hydraulically stimulated reservoirs.

Specific objectives of the individual chapter are following:

- Study the physics involved in the hydraulic fracturing and production process;
- Develop a novel mesh fragmentation technique to simulate unrestricted hydraulic fracture propagation in naturally fractured rock formations;
- Study the main parameters that affect the hydraulic and natural fracture interaction.
- Improve the dual-porosity and dual-permeability formulation for the simulation of deformable fractured reservoirs aiming at accuracy and computational efficiency;
- Study the critical factors that affect the hydromechanical behavior and the production performance of a reservoir with fractures of multiple scales.
- Develop techniques to integrate fracture propagation models and reservoir simulations.
- Study the dominant parameters that influence the hydraulic fracturing treatment and production performance of the naturally fractured and hydraulically stimulated reservoir.

1.3. Thesis organization

The outline of this thesis is as follows:

Chapter 2 presents the comprehensive literature review of the numerical models to simulate hydraulic fracturing and fluid flow of naturally fractured reservoirs.

Chapter 3 presents the development of the numerical models for simulation of unrestricted fracture propagation in naturally fractured formations using the Intrinsic Cohesive Zone Model. An algorithm for inserting the special interface elements into conventional 2D/3D finite element meshes is described. Finally, validation of the proposed numerical methodologies using literature data on experimental test results is also included.

Chapter 4 studies the effect of some primary parameters on the hydraulic and natural fracture interaction. The results of the new approach are compared against analytical and numerical solutions. Finally, some advantages and limitations of the proposed methodology are discussed.

Chapter 5 presents the development of new numerical models to represent a fractured porous formation more realistically. It describes the formulation of the enhanced dual porosity/dual permeability model to represent complex fracture sets. It also presents the comparison of the proposed numerical models against the discrete fracture model to assess its accuracy. Finally, it is presented some applications of reservoir simulation to study the effects of multiple sets of fractures of different scales and arbitrary orientation on fluid flow and pore pressure distribution.

Chapter 6 introduces a new methodology integrating the hydraulic fracture propagation model and reservoir simulation. Several scenarios considering complex fracture networks are investigated to understand the dominant factors influencing hydraulic fracturing and the associated reservoir production. Finally, it is presented the integration of implicit and explicit models to study the impact of primary and secondary fractures on the production performance of the hydraulically stimulated reservoir.

Chapter 7 summarizes the conclusions in this thesis. Future works are proposed.

2
Literature review

2.1. Hydraulic fracturing in naturally fractured formations

Hydraulic fracturing is one of the main stimulation techniques to improve oil and gas recovery from low permeability reservoirs. This technique consists of the fluid injection under high pressure into the rock formation to initiate and propagate induced fluid-driven fractures. The induced fractures form fluid paths of high permeability and enhance well-reservoir connectivity. Applications of hydraulic fracturing also include cave inducement in mines (JEFFREY; MILLS, 2000; VAN AS; JEFFREY, 2000), disposal of wastes in shale (DE LAGUNA, 1966; MALONEY; YOXTHEIMER, 2012), rockburst control in deep mining (BOARD et al., 1992), assessment of in situ stresses (DESROCHES, 1995), and energy production from geothermal reservoirs (BARBIER, 2002; O'SULLIVAN; PRUESS; LIPPMANN, 2001). Given its broad range of engineering applications, modeling hydraulic fracturing has attracted numerous research contributions since the 1950s (GREEN; SNEDDON, 1950; KHRISTIANOVIC; ZHELTOV, 1955; NORDGREN, 1972; PERKINS; KERN, 1961; SNEDDON, 1946).

Simplified 2D models based on PKN, KGD, or penny-shaped solutions, as shown in Figure 2.1, have been proposed to design the hydraulic fracturing treatment (ADACHI; DETOURNAY, 2002, 2008; BUNGER; DETOURNAY; GARAGASH, 2005; DETOURNAY, 2016; DONTSOV, 2016, 2017; GARAGASH; DETOURNAY; ADACHI, 2011; SAVITSKI; DETOURNAY, 2002). These models aim at predicting fluid pressure evolution, opening, size, and profile of the fracture, given the injection rate, fluid rheology, and rock properties. As pointed out by (ADACHI; DETOURNAY, 2008), these idealized models are important tools to study different propagation regimes. However, analytical solutions do not require a detailed description of rock properties, and they adopt simplifications in terms of opening, crack pressure field and consider infinite elastic homogeneous media (ADACHI; DETOURNAY, 2008).

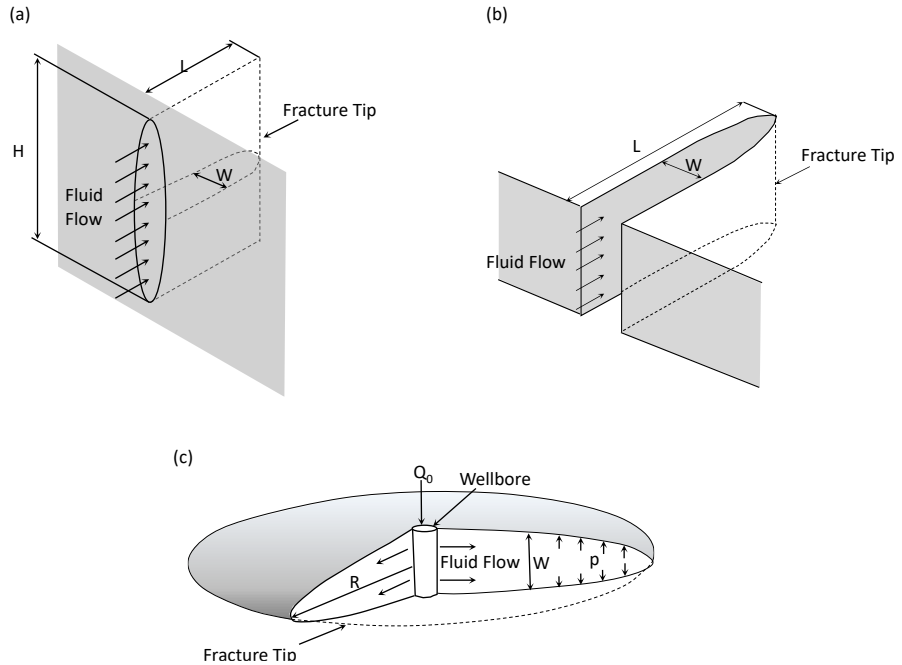

Figure 2.1. Schematic of fracture geometry of analytical solutions: a) PKN, b) KGD, and c) Penny shaped.

Due to geometry limitations of the analytical models, the P3D (pseudo-3-D) model has been developed to determine the fracture height from the local fluid pressure, in-situ stresses, and rock toughness (NASIRISAVADKOUHI, 2015). Nevertheless, those models cannot simulate fracturing with arbitrary paths and assume a strict stress field (LI et al., 2015). Furthermore, this model neglects the hydromechanical effects within the porous medium and in the interaction with natural fractures. Such assumptions can result in inadequate forecasting models for hydraulic fracture propagation in naturally fractured formations.

The success of the hydraulic fracturing treatment in an unconventional reservoir is limited to the interaction between induced and pre-existing fractures. On the one hand, the stimulated fractures enlarge the contact area with the reservoir, increasing drainage paths for fluid flow and improving productivity. On the other hand, activated natural fractures can divert fluid flow from the main hydraulic fracture or reduce its width, causing proppant bridging. Consequently, premature blockage of the proppant transport (screen out) can occur, causing the hydraulic treatment to fail (POTLURI; ZHU; HILL, 2005). Therefore, understanding hydraulic fracture behavior and its interaction with pre-existing fractures are essential to inhibit unfavorable fracture propagation reducing the associated environmental risks, and identify suitable fracturing geometries to optimize production performance.

2.1.1.
Interaction between natural and hydraulic fractures

The interaction between hydraulic fractures (HF) and pre-existent natural fractures (NF) is one of the main sources of complex fracture networks. Several types of interaction may occur during the hydraulic fracture propagation towards a pre-existent fracture (see Figure 2.2). Depending on the in-situ stresses, the fluid pressure, and the approach angle, the interaction can lead to slippage/arrest (Figure 2.2b) and crossing (Figure 2.2 c). The case of slippage or arrest occurs when the natural fracture shear stress reaches its shear strength. Opening occurs when the fracturing fluid pressure is larger than the normal compressive stress on the natural fracture. Consequently, the natural fracture slips and the fluid flows into its channels (Figure 2.2d). During the opening of the natural fracture, the fluid pressure can continue to increase and may exceed the rock tensile strength leading to further fracture propagation (Figure 2.2g).

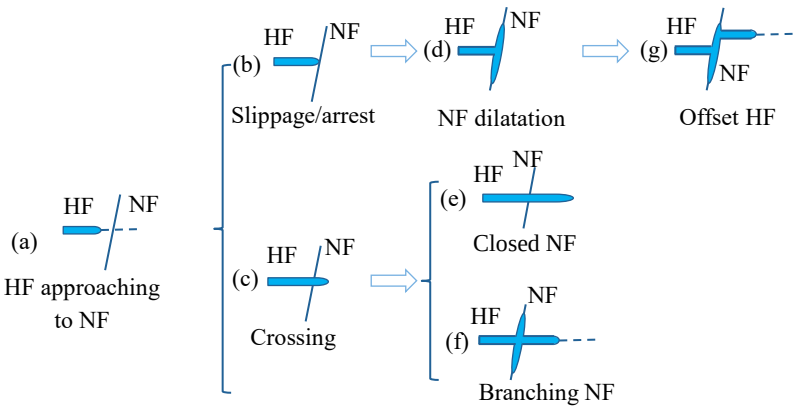

Figure 2.2 Schematic representation of the interaction process between hydraulic fracture and natural fractures.

Besides that, for high compressive stresses acting on the natural fracture, the hydraulic fracture propagates through it without a change in direction (Figure 2.2c). Consequently, the hydraulic fracture can propagate through the rock formation, and the natural fracture remains closed (Figure 2.2e). However, if the hydraulic fluid pressure exceeds the normal compressive stress or if the stress on the natural fracture plane reaches the shear strength, the natural fracture can open or slip, respectively, generating a branch (Figure 2.2f).

Several experimental works and analytical solutions have been conducted to investigate the interaction between hydraulic and natural fractures (BLANTON, 1982; CHUPRAKOV; MELCHAEVA; PRIOUL, 2014; GU et al., 2012; POTLURI;

ZHU; HILL, 2005; RENSHAW; POLLARD, 1994; ZHOU; XUE, 2011). The results show that the approach angle, friction coefficient, and the contrast of horizontal stresses have a great influence on the mode of hydraulic fracture propagation (CHENG; JIN; CHEN, 2015; WARPINSKI; TEUFEL, 1987). However, these methods have some limitations because experimental models are expensive and extremely time-consuming. Generally, they are performed on plugs and considering low pressures. Furthermore, analytical models perform over-simplifications in terms of the fracture pressure field and elastic homogeneous media hypothesis in stationary conditions.

2.1.2. Numerical modeling

Owing to the limitations of experimental models and analytical solutions, recent research works have focused on the development of numerical algorithms to model hydraulic fracture propagation in fractured reservoirs. Methods such as the Discrete Element Method (DEM), the Displacement Discontinuity Method (DDM), Lattice Element Method (LEM), and the Extended Finite Element Method (XFEM) or Generalized Finite Element Method (GFEM) have been presented as viable alternatives to simulate the interaction of hydraulic and natural fractures and predict the final geometry of the hydraulic fracture network. However, these methods are complex in the treatment of fracture interaction, even in 2D cases.

The Discrete Element Method (DEM) represents the domain of interest as an assembly of particles or blocks, which continuously interact through their contacts. Interaction of hydraulic and natural fractures studies have been performed using this numerical method (FATAHI; HOSSAIN; SARMADIVALEH, 2017; ZHOU et al., 2017). In these studies, natural fractures are simulated by replacing contact or parallel bonds with smooth joint bonds. The main drawback of this method is the trial-and-error calibration of micro-parameters (spring stiffness and strengths) to recover the macroscopic properties.

The Displacement Discontinuity Method (DDM) developed by (CROUCH, 1976) is a special case of the Boundary Element Method (BEM) formulation. The method is based on the analytical solution of the problem of a constant displacement discontinuity over a line segment of an infinite and elastic solid. The method only requires the discretization of the contours of the fracture surface and does not need remeshing for new fractures. In hydraulic fracturing modeling, DDM

is often used to simulate hydraulic and natural fracture interaction considering elastic and impermeable media (XIE et al., 2018; XIE; MIN; SHEN, 2016). However, in most DDM models, the simulation of hydraulic and natural fracture interaction is based on crossing analytical criteria under plane strain conditions and local Mohr-Coulomb law. Therefore, applying DDM to naturally fractured reservoirs in a fully coupled manner is still challenging (WANG, 2019).

Lattice Element Method (LEM) is generally defined as an assembly of discrete one-dimensional elements for the representation of a solid structure. This method is usually used to simulate the fracturing process of heterogeneous materials (NIKOLIĆ et al., 2018; WONG, 2017). The LEM approach has some limitations related to values of Poisson's ratio aiming to represent the macroscopic elastic behavior of the discretization (GRASSL et al., 2015). Furthermore, structured meshes can strongly bias the cracking patterns (WONG et al., 2015).

Extended Finite Element Method (XFEM) or Generalized Finite Element Method (GFEM) are modifications of the finite element method (FEM). The fracture is represented using enrichment functions on the adjacent nodes to the fracture. These methods have gained popularity to simulate hydraulic and natural fracture interactions once the fracture path can be modeled independently of the mesh (KESHAVARZI; JAHANBAKHSHI, 2013; KHOEI; VAHAB; HIRMAND, 2016; TALEGHANI, 2010; WANG et al., 2018). A recent work (CRUZ; ROEHL; VARGAS, 2018) presents an extension of the XFEM method for multiple fracture interaction. This technique is computationally efficient because re-meshing or insertion of new elements is not necessary. However, the method has limitations to model propagation of irregular fracture geometries in heterogeneous materials, and the treatment of fracture interaction is complex even in 2D cases. Additionally, the implementation in existing finite element codes is not straightforward.

2.1.3. Finite Element Method (FEM)

The Finite element method (FEM) is one of the most widely used approaches for the study of continuous media. This method can simulate the behavior of discontinuities through interface elements or through adaptive meshes. The interface element finds a broad range of engineering applications where the crack paths are known as delamination in composite materials (ORTIZ; PANDOLFI, 1999; TURON et al., 2005), fault activation (PEREIRA et al., 2014; RUEDA et al., 2014), and grain boundary cracks in brittle materials (ZAVATTIERI; ESPINOSA,

2001). Extrinsic or Intrinsic interface element fragmentation is necessary to simulate complex crack patterns during crack propagation. Crack branching (GEUBELLE; BAYLOR, 1998), mesoscale, and microscale arbitrary crack propagation in fiber-reinforced material (WU et al., 2013), or heterogeneous material characterized by inclusions (BENEDETTO; CAGGIANO; ETSE, 2018; DAI; NG, 2014; WANG et al., 2015) have been simulated with these approaches. In the extrinsic approach, based on the local criterion of stress or strain, an adaptive insertion of cohesive interface elements in the mesh (in space and time) is required. In the intrinsic approach, cohesive interface elements are inserted in the discretization of the structure before the simulation starts. Both approaches have their advantages and drawbacks. In the extrinsic fragmentation process, new elements are inserted at the edges of regular elements during the simulation. Therefore, this process requires an elaborated data structure to update the modified mesh once new nodes and interface elements are inserted. Also, computational parallelization becomes challenging due to the complexity associated with the topological propagation changes in the mesh. In general, the discrete discontinuity is investigated using the cohesive zone model (CZM) that defines the constitutive response directly in terms of traction versus separation. This model avoids the singularity of the stress field at the crack tip, which is present in classical linear elastic fracture mechanics. The extrinsic cohesive zone model considers that the separation only occurs when interfacial traction meets certain damage initiation criteria $T(\delta)$ in terms of stress or strain. Subsequently, the material stiffness progressively degrades, and finally is null at the critical separation δ_c. This behavior is shown in Figure 2.3a. On the other hand, the intrinsic cohesive model considers an initial interfacial traction-separation until it reaches the maximal interfacial strength $T(\delta)$. Thenceforth, the material stiffness is progressively degraded, and finally vanishes at the critical separation δ_c, as illustrates Figure 2.3b.

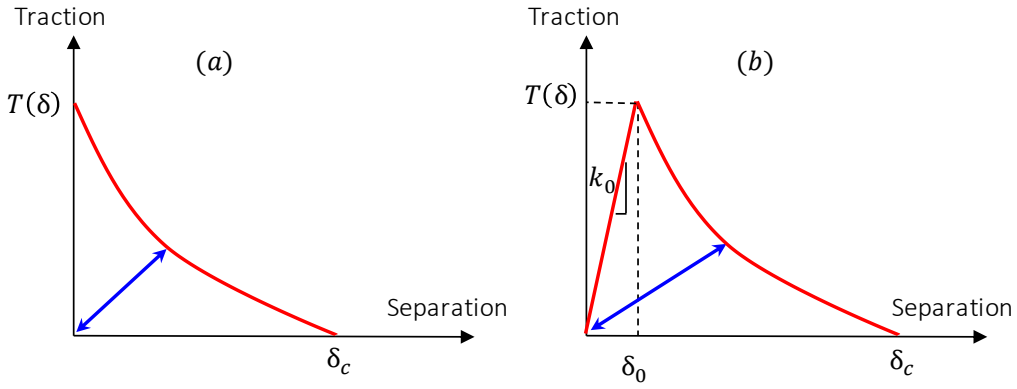

Figure 2.3. Comparison of two cohesive zone models (CZM): (a) extrinsic model; (b) intrinsic model.

In general, intrinsic models consider that all cohesive elements are embedded in the mesh since the beginning of the simulation. Therefore, the topological mesh connectivity remains constant during the simulation process. Intrinsic models are easier to implement in terms of mesh and computational parallelization (RADOVITZKY et al., 2011). However, they introduce artificial compliance that depends on element surface and cohesive parameters related to bulk properties. The “artificial compliance” phenomenon can be reduced by increasing the initial stiffness of the cohesive elements. Extrinsic models avoid this artificial effect (ZHANG; PAULINO; CELES, 2007). Nevertheless, this issue also arises in the extrinsic approach if the inserted fracture closes under compressive load.

The coupled hydromechanical double-noded interface element has been formulated to simulate fluid flow in pre-existing discontinuities (NG; SMALL, 1997; SEGURA; CAROL, 2008a, 2008b). However, these formulations do not consider normal flow. (BALDONI; MILLARD, 1998) and (GUIDUCCI et al., 2002) proposed the hydromechanical model using a special triple-noded zero thickness interface element to simulate transversal permeability. The classical nodes of the conventional double-noded interface element define the joint surfaces, with 2 degrees of freedom to represent the relative mechanical displacement and one to house the fluid pressure. Additionally, this element has an inner node to represent fluid flow inside the discontinuity. This special element has been combined with a cohesive zone model to simulate planar hydraulic fracture propagation (CARRIER; GRANET, 2012; CHEN et al., 2009; ZIELONKA et al., 2014). In these simulations, hydraulic fractures are modeled by non-intersecting predefined cohesive paths. Recently, triple-noded zero thickness interface elements have been used to simulate the interaction between hydraulic and natural fractures (DAHI

TALEGHANI et al., 2018; GONZALEZ; TALEGHANI; OLSEN, 2015; GUO et al., 2015; HADDAD; DU; VIDAL-GILBERT, 2017; NIKAM et al., 2016; RUEDA CORDERO; MEJIA; ROEHL, 2017). In these cases, the intersected elements needed a special treatment to ensure continuity in pressure along the hydraulic fracture and natural fractures. Gonzalez (GONZALEZ; TALEGHANI; OLSEN, 2015) defined four triangular elements in the intersection. Haddad (HADDAD; DU; VIDAL-GILBERT, 2017) and Taleghani (DAHI TALEGHANI et al., 2018) applied constraints through additional governing equations to couple the inside pore pressure degrees of freedom at all inner nodes at the intersection. Guo (GUO et al., 2015) and Rueda et al. (RUEDA CORDERO; MEJIA; ROEHL, 2017) merge the inner nodes in the intersection to ensure that the injected fluid flows longitudinally to the fracture paths. The implementation of this last configuration, merge the inner nodes, seems easier than those proposed by Gonzalez (GONZALEZ; TALEGHANI; OLSEN, 2015), Haddad (HADDAD; DU; VIDAL-GILBERT, 2017) and Taleghani (DAHI TALEGHANI et al., 2018). Regardless of the choice of those configurations, the hydromechanical CZM cannot predict the path and propagation direction of the hydraulic fracture. Then, an intrinsic cohesive approach may be a solution to overcome these limitations. Although the implementation of intrinsic cohesive elements is straightforward in the conventional finite element mesh, the pre-processing step to insert a cohesive interface element at every face of general finite elements is non-trivial.

Recently, (RUEDA CORDERO et al., 2019) developed an intrinsic cohesive methodology for a 2D fully coupled simulation of unrestricted hydraulic crack propagation in naturally fractured media. The numerical procedure provides good agreement with the laboratory tests and shows the robustness of the proposed computational algorithm. The presented mesh fragmentation is extensible to three dimensions. With this methodology, it is possible to simulate a re-initiated fracture from the crack tip, crossing with an offset, branching, and multiple cracks, without worrying about multiple crack interactions. Moreover, aspects as simplicity of mesh data structure and successful representation of localized failure and complex crack patterns are the most important reasons for implementing intrinsic CZM in this work.

2.2. Fluid flow in naturally fractured reservoir

Fractured reservoirs are composed of intact rock blocks separated by faults, fractures, bedding planes, and fissures. Those reservoirs are very heterogeneous in porosity and permeability due to the characteristics of the fracture system with varying intensity and persistence over a wide range of orientation, separation, aperture, and scales (GONG; ROSSEN, 2018; KUCHUK; BIRYUKOV, 2014). Those fractures play an essential role in many engineering applications such as nuclear waste disposal (KIM et al., 2019; SILVEIRA; ALVIM; RIVERO OLIVA, 2013; YANG, 2012), geological sequestration and storage of CO_2 (BIGI et al., 2013; MARCH; DOSTER; GEIGER, 2018), and oil/gas/geothermal reservoir production (GHASSEMI; ZHOU, 2011; O'SULLIVAN; PRUESS; LIPPMANN, 2001; RUEDA CORDERO et al., 2019, 2020b; XU; DOWD; TIAN, 2015). Natural discontinuities reduce the mechanical strength of the formation and alter its fluid flow characteristics (SHAHID; FOKKER; ROCCA, 2016). Natural fractures sealed by mineralization are poorly conductive and can act as impermeable barriers. Similarly, discontinuities generated under compactional shear stresses, called deformation bands, exhibit a region with reduced porosity and permeability, which may also act as a barrier (FOSSEN et al., 2007). On the other hand, infilled and/or stimulated fractures enhance the permeability of the formation and well-reservoir connectivity.

In this context, accurate models of naturally fractured reservoirs are required to understand the effect of fractures on reservoir behavior and their impact on hydrocarbon production to optimize oil recovery performance.

2.2.1. Naturally fractured reservoir simulation

In the last years, numerical models have sought to incorporate more realistic representations of the geological structure to obtain a more accurate interpretation of the fractured reservoir behavior (NORBECK et al., 2016). Discrete fracture models and dual porosity approaches are commonly used to represent the fluid flow through fractured porous media (LEE; CHOI; CHO, 1999; YAO; HUANG, 2017) (ZIDANE; FIROOZABADI, 2018).

Discrete fracture models (DFM) represent the characteristic of the fracture system more accurately and represent the effect of individual fractures on the

mechanical deformation and flow pattern explicitly (KARIMI-FARD; DURLOFSKY; AZIZ, 2004; KIM; DEO, 2000). Fractures are represented by lines and surfaces in two-dimensional and three-dimensional problems, respectively (FADAKAR ALGHALANDIS, 2017; NOORISHAD; MEHRAN, 1982). By adopting an appropriate mesh discretization, the DFM can describe heterogeneities, anisotropy, and fracture distribution of fractured media. Several numerical discretization methods are adopted, such as the finite difference (LEE; LOUGH; JENSEN, 2001; ZHOU; SHI; WANG, 2014), finite volume (GRANET et al., 2014; KARIMI-FARD; DURLOFSKY; AZIZ, 2004; MONTEAGUDO; FIROOZABADI, 2007), mimetic finite difference (YAN et al., 2016, 2019), finite element (FLEMISCH et al., 2018; FUMAGALLI; KEILEGAVLEN; SCIALÒ, 2019; KIM; DEO, 2000; THOMAS; PALUSZNY; ZIMMERMAN, 2020), etc. However, DFMs are computationally demanding for field-scale reservoir simulations. Besides, explicit approaches have limited application due to the lack of reliable data regarding fracture distribution and patterns (CLEMO, 1994).

Although more simplified in the characterization of naturally fractured reservoirs, dual porosity and dual permeability models (DPDP) models are widely used for their low computational cost. DPDP models may be useful to simulate sets of high-density fractures of small or medium length, where the representation of each fracture is complex and computationally expensive (CLEMO, 1994). The original dual-porosity (DP) concept proposed by Barenblatt (BARENBLATT; ZHELTOV; KOCHINA, 1960) consists of the superposition of two porous systems with different characteristics. The fractures act as intercommunicated drainage paths of high permeability while the rock matrix performs as fluid storage. The two systems are linked through transfer functions, which are evaluated through the analytical solution of the pressure diffusion between matrix and fractures for a simple fracture set, or through numerical and laboratory experiments for several fracture sets (BARENBLATT; ZHELTOV; KOCHINA, 1960; KAZEMI et al., 1976; LIM; AZIZ, 1995; MAIER et al., 2013; WARREN; ROOT, 1963). (WARREN; ROOT, 1963) improved the dual-porosity model, which assumes orthogonal fractures parallel to the principal axes. (KAZEMI et al., 1976) extended that approach to multiphase flow. Fractures isolate block matrix, and flow occurs through fracture channels and between matrix and fractures. Figure 2.4 depicts the idealization of naturally fractured systems through a dual-porosity model.

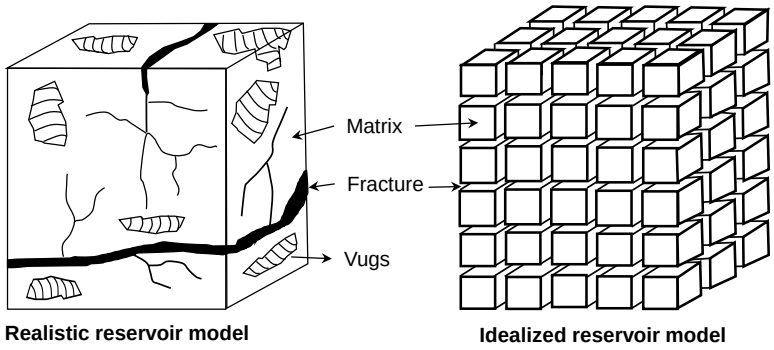

Figure 2.4. The idealization of a naturally fractured system with a dual-porosity model.

(BLASKOVICH et al., 1983) and (HILL; THOMAS, 1985) introduced the dual-porosity/dual permeability (DPDP) model that allows physical communication between blocks and incorporates the occurrence of fluid flow between them. The dual porosity/dual permeability approach has been generalized to include subgrid-scale heterogeneities into the large-scale flow and transport (ZYVOLOSKI; ROBINSON; VISWANATHAN, 2008). The matrix-fracture transfer shape factor is generalized for irregular block matrices (HEINEMANN; MITTERMEIR, 2012). Recently, this model has also been extended to the triple-porosity/triple permeability model to study fractured vuggy carbonate reservoirs (YAO; HUANG, 2017).

To combine the advantages of implicit and explicit fracture representations, the embedded discrete fracture model (EDFM) emerged as a promising alternative to model complex fracture systems (LEE; LOUGH; JENSEN, 2001; LI; LEE, 2006; YAN et al., 2016). The EDFM directly includes the fracture contribution into the flow matrix without any spatial partitioning, avoiding complex discretization. Considering the advantage of the EDFM in terms of accuracy and computational efficiency, several applications have been performed: fracture propagation in a fractured reservoir (NORBECK et al., 2016) and optimization of multistage hydraulic fracture in a horizontal well (XU et al., 2018). Recently, several works have focused on the extension of the EDFM to overcome some limitations. (XU et al., 2019) extended the EDFM to corner-point grids with a full-permeability-tensor. (ŢENE et al., 2017) proposed the pEDFM adjusting matrix-matrix and fracture-matrix transmissibility to deal with problems where the fracture permeability lies below that of the matrix. (RAO et al., 2020) modified pEDFM to handle more general cases selecting projected faces of fracture cells. (CAO et al., 2019) proposed a new EDFM for the matrix-fracture flux using the boundary element method to incorporate reservoir anisotropy effects. (CHEN et al., 2020) proposed

a streamlined tracing framework applied in several applications using the DPDP system via EDFM. Although the EDFM has been applied successfully to a highly fractured reservoir with complex fracture configurations, most of the existing EDFMs are based on the finite difference method and required further improvements or combinations with other methods to handle more general applications. More recently, (MEJIA et al., 2021) propose a new embedded discrete fracture approach based on the finite element method to model fluid flow through highly fractured porous media. The proposed approach includes natural fractures through a multi-freedom constraint method followed by a static condensation procedure of the element's degrees of freedom. Thus, this proposal avoids complex meshes, improves computational efficiency, and keeps the solution accuracy. An additional advantage is that this approach guarantees the compatibility between fracture and porous matrix within a standard finite element mesh. Therefore, the pore pressure field obtained with the proposed embedded approach is very close to the field provided by the explicit approach with zero-thickness interface elements.

Aiming at accuracy and computational efficiency, the integration between DFM and DPDP models has been encouraged recently for flow analysis with fractures of various lengths. Gong (GONG, 2007) presented a hybrid method that allows some regions of the model to be treated using the DFM and others with the multiple sub-region (MSR) method using a DPDP representation. The hybrid method may be appropriate to simulate connected and disconnected fractures or enhanced accuracy in some reservoir regions. Maier et al. (MAIER et al., 2013) presented a multi-rate dual-porosity model to simulate small-length fractures and integrate it with DFM to simulate large-length heterogeneities such as fractures. Dong et al. (DONG et al., 2017) proposed a method that integrates the embedded discrete fracture model EDFM and dual-porosity, dual-permeability (DPDP) concepts to model the production process in shale oil reservoirs.

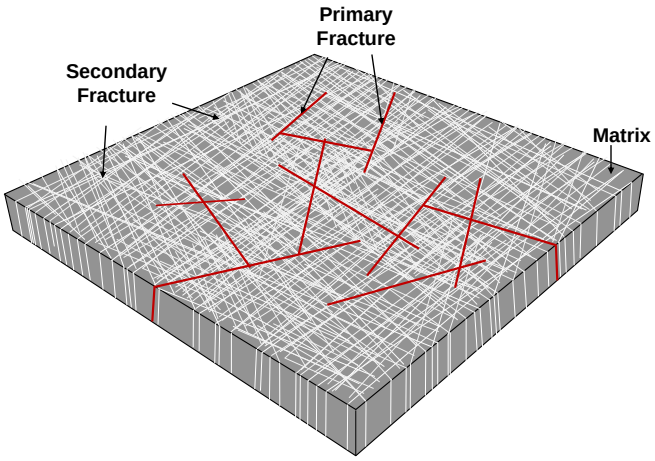

Figure 2.5. Schematic representation of fractured rock media

The mentioned works do not consider the rock and fracture deformability and focus on reservoir flow issues. Nevertheless, there are currently some reservoir formation that show significant alteration in their petrophysical characteristics due to the changes in the stress state (CHEN; TEUFEL, 2000). For that reason, the role of geomechanics is even more important in fractured media owing to the presence of fractures that are more sensitive to stress changes than the rock matrix is. Stress/strain changes due to production and/or injection result in opening, and closing (HERMANSEN et al., 2000). This variation of the geomechanical parameters affects the permeability (magnitude and direction), one of the factors that control the management of naturally fractured reservoirs (BAGHERI; SETTARI, 2008).

(RUEDA; MEJIA; ROEHL, 2019) proposed a method that integrates DPDP and DFM models in a deformable fractured media to study the geomechanical effects of fractures of multiple lengths in the reservoir. The results show that fractures of small and medium length enhance the permeability of naturally fractured reservoirs and support the application of the proposed model for production simulation of the stimulated reservoir with fractures of multiple length scales.

2.3. Related research in the Multiphysics Modeling and Simulation group at Institute Tecgraf PUC-Rio

In the last decade, the Multiphysics Modeling and Simulation group at Tecgraf PUC-Rio has been conducting research work applied to fracture problems. (RUEDA, 2013) implemented a 2D finite element methodology to study fault reactivation in oil reservoirs during the production process. (SILVA, 2015)

presented an Extended Finite Element Method (XFEM) implementation for two-dimensional analysis of fracture propagation following the Linear Elastic Fracture Mechanics theory. (BARBOZA, 2015) investigated the fracture process in structures with quasi-brittle materials using the finite element method (FEM) based on the cohesive zone model. (RAMIREZ, 2016) extended the methodology presented by (RUEDA, 2013) to assess 3D geological fault reactivation.(GUTIÉRREZ, 2016) analyzed the hydraulic fracturing technique to better understand the interaction between rock and injected fluid. Planar fracture propagation was simulated using FEM and the pore cohesive zone model. (CASTANEDA, 2017) presented a numerical analysis of non-planar hydraulic fracture propagation using the extended finite element method (XFEM) and cohesive zone model (CZM). (BENDEZU, 2017) applied XFEM to investigate rock blasting based on the phantom node method where discontinuities in the displacement fields are introduced through new degrees of freedom in overlapping elements. (PEREIRA, 2018) discussed the criteria for nucleation and propagation of fractures and their implementation in the XFEM context. The implementations of crack growth criteria were made in an in-house framework GeMA (Geo Modelling Analysis)(MENDES; GATTASS; ROEHL, 2016). (CRUZ, 2018) extended the XFEM to simulate multiple fracture interactions during the hydraulic fracture propagation in a naturally fractured formation. New contributions are being conducted to the development of new numerical methods for robust 3D simulations of unrestricted fracture propagation and fluid flow migration in naturally fractured media.

3
Intrinsic cohesive zone model for unrestricted fluid-driven fracture propagation

The content of this chapter comprises the papers of (RUEDA CORDERO; MEJIA SANCHEZ; ROEHL, 2019b). This chapter provides the theoretical formulation of hydraulic fracturing physics. It defines the physical equations that govern the hydromechanical behavior of the porous media and the constitutive relations of the fractures. Moreover, it presents a novel mesh fragmentation technique to simulate unrestricted hydraulic fracture propagation in fractured media. This method is based on the hydromechanical zero thickness interface element combined with the cohesive zone model (CZM). An algorithm for inserting the special triple-noded interface elements into conventional 2D/3D finite element meshes is described. A simple but effective topological data structure that considers each finite element independently of others is introduced. The proposed topological structure ensures the generation of new nodes and faces necessary for the insertion of interface elements. The implementation is validated through literature data on experimental test results.

3.1.
Governing equations

In order to simulate the hydraulic fracturing process and the interaction with natural fractures, several components are coupled: (1) mechanical deformation of the rock induced by fluid pressure on the fracture surface, (2) fluid flow inside the fracture, (3) fracture propagation in the rock formation, (4) fluid transfer between the fracture and the porous medium, and (5) interaction with natural fractures.

3.1.1.
Mechanical behavior of saturated porous media

A rock mass is a non-uniform material composed of intact rock and discontinuities. The formulation presented in this work considers a homogeneous, isotropic, linear elastic rock material undergoing small strains. Biot's theory (BIOT,

1941) is adopted to model the saturated porous media. The conservation of the linear momentum balance in the saturated porous media takes the form:

$$\nabla \cdot \boldsymbol{\sigma} + \rho\, \boldsymbol{g} = \mathbf{0} \tag{3.1}$$

where $\boldsymbol{\sigma}$ is the stress tensor, ρ is the density of the saturated porous medium, and $\mathbf{g}$ is the gravity vector. The relationship between total stresses and effective stresses in porous media is given by (TERZAGHI, 1943):

$$\boldsymbol{\sigma} = \boldsymbol{\sigma}' - \alpha\, \boldsymbol{p} \tag{3.2}$$

Here, $\boldsymbol{\sigma}'$ is the effective stress tensor (compression are negative hereafter), $\boldsymbol{p}$ is the pore pressure, and α is the Biot coefficient that is defined as

$$\alpha = 1 - \frac{K}{K_s} \tag{3.3}$$

where K and K_s are the volumetric deformation moduli of the porous medium and solid grain, respectively. For incompressible solid grains, observe that $K_s \to \infty$ and $\alpha = 1$. The constitutive relation in the bulk material is given by:

$$\boldsymbol{\sigma}' = \boldsymbol{D_e} : \boldsymbol{\varepsilon} \tag{3.4}$$

where $\boldsymbol{\varepsilon}$ is the strain vector and $\boldsymbol{D_e}$ is the elasticity matrix.

3.1.2. Pore pressure diffusion in a permeable rock formation

The continuity equation of the fluid flow through a permeable porous medium is:

$$\alpha \nabla \cdot \dot{\boldsymbol{u}} + \nabla \cdot \boldsymbol{q} + \frac{\mathbf{1}}{M}\dot{\boldsymbol{p}} = 0 \tag{3.5}$$

where $\dot{\boldsymbol{u}}$ is the deformation velocity vector, $\boldsymbol{q}$ is Darcy's velocity vector of the pore fluid, and M is Biot's modulus defined as:

$$\frac{1}{M} = \frac{n_m}{K_w} + \frac{1 - n_m}{K_s} \tag{3.6}$$

where K_w is the bulk modulus of the fluid, and n_m is the porosity of the porous medium.

Considering laminar and uniform fluid flow by Darcy's law, the specific fluid flow is given by:

$$\boldsymbol{q} = \frac{\boldsymbol{k_m} A}{\mu} \nabla \boldsymbol{p} \tag{3.7}$$

where $\boldsymbol{k_m}$ is the permeability of the porous medium, A is the cross-section area, μ is fluid viscosity and $\boldsymbol{p}$ is the fluid pressure.

3.2. Fracture constitutive relations

Discontinuities can be defined as planes of physical weakness. They have a relevant effect on stress transmission, reduces the mechanical strength of the formation, and alter the behavior of the fluid flow. Based on the poroelasticity theory for a fracture under the influence of internal fluid pressure and disregarding the body forces, the equilibrium equation is established:

$$\boldsymbol{\sigma'} - \boldsymbol{m}.\boldsymbol{p} = 0 \tag{3.8}$$

where $\boldsymbol{m} = \{1 \quad 0\}$ is the vector form of the Kronecker delta, $\boldsymbol{\sigma'}$ and $\boldsymbol{p}$ are the effective stress and fluid pressure vectors, respectively. The fracture behavior is represented by a traction-separation relationship to describe the initial elastic response until it reaches a specific interfacial strength. The hydromechanical relations of induced and natural fractures are described below.

3.2.1. Elastic behavior

The mechanical behavior at the discontinuity is expressed directly in terms of a traction-separation law. A relationship to describe the elastic response of discontinuity can be represented as:

$$\begin{Bmatrix} \tau_s \\ \tau_t \\ \sigma'_n \end{Bmatrix} = \boldsymbol{D}_e \begin{Bmatrix} \delta_s \\ \delta_t \\ \delta_n \end{Bmatrix} \tag{3.9}$$

where $\boldsymbol{D}_e$ is the elastic matrix which adopts the following simple form:

$$\boldsymbol{D}_e = \begin{Bmatrix} k_s & 0 & 0 \\ 0 & k_t & 0 \\ 0 & 0 & k_n \end{Bmatrix} \tag{3.10}$$

with k_n the normal stiffness, k_s and k_t the shear stiffness in two orthogonal in plane directions; σ'_n is the normal effective stress on the fracture surface and τ_s, τ_t are the shear stresses; δ_n, δ_s and δ_t are their corresponding normal and shear separations on the fracture surface.

3.2.2. Hydraulic fracture propagation

In general, four stages can be considered during the fracturing process. The first stage represents the intact and continuum material. In the second stage, fracture propagation begins. The third stage describes the fracturing evolution. Finally, in the fourth stage, the hydraulic fracture is established. This behavior can be modeled using the pore pressure cohesive zone model (CZM). This model avoids stress singularity in linear elastic fracture mechanics (LEFM) and represents the damage zone ahead of a hydraulic crack tip. Then, rock behavior during hydraulic fracturing is represented by two laws: a strain-stress relationship to describe the elastic response of the rock material and the cohesive law that controls fracture initiation and propagation. The process of degradation begins when a function in terms of stress meets its critical values (CAMACHO; ORTIZ, 1996). After that, damage evolution characterizes the progressive degradation of the material stiffness (CAMANHO; DÁVILA, 2002) according to linear or exponential softening (Figure 3.1).

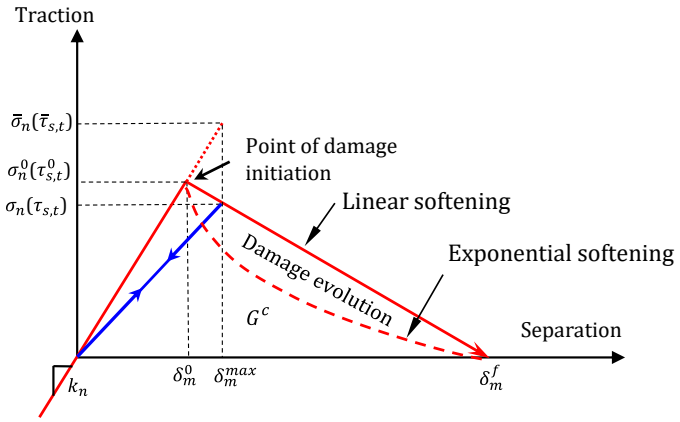

Figure 3.1. A typical response of the damage model with linear or exponential softening

In naturally fractured media, normal traction is mainly induced by hydraulic pressure, while shear traction may be generated by geo-stress contrast or shear stress around natural fractures (KHOEI et al., 2015; KHOEI; VAHAB; HIRMAND, 2016). For that reason, the quadratic nominal stress criterion is adopted to predict the element damage initiation. This criterion combines normal and shear failure and assumes damage initiation when the quadratic interaction function involving the nominal stress ratios reaches the value 1 (CAMACHO; ORTIZ, 1996):

$$\left\{\frac{\langle \sigma'_n \rangle}{\sigma'^0_n}\right\}^2 + \left\{\frac{\tau_s}{\tau_s^0}\right\}^2 + \left\{\frac{\tau_t}{\tau_t^0}\right\}^2 = 1 \tag{3.11}$$

where σ'^0_n is the effective tensile strength, and τ_s^0, τ_t^0 are the shear strengths; σ'_n and τ_s, τ_t represent the normal effective and shear tractions on the interface, respectively; <> is the Macaulay bracket which returns zero for negative stresses (compression) and the effective tensile stress value for positive stresses. Once damage initiation occurs, the stresses are affected by the damage variable according to:

$$\sigma_n = \begin{cases} (1-D)\bar{\sigma}'_n, & tensile\ state \\ \bar{\sigma}'_n, & compresive\ state \end{cases} \tag{3.12}$$

$$\tau_{s,t} = (1-D)\bar{\tau}_{s,t} \tag{3.13}$$

where $\bar{\sigma}'_n$ and $\bar{\tau}_s$, $\bar{\tau}_t$ are the normal effective and shear stresses predicted by the elastic traction separation law for the current relative displacements. D is a scalar damage variable, which has zero value at the point of damage initiation and one when the element is totally damaged. For linear softening behavior, the evolution of the damage variable D is expressed as (CAMANHO; DÁVILA, 2002):

$$D = \frac{\delta_m^f.(\delta_m^{max} - \delta_m^{\mathbf{0}})}{\delta_m^{max}.(\delta_m^f - \delta_m^{\mathbf{0}})} \tag{3.14}$$

where δ_m^{max} is the maximum value of the effective displacement attained during the loading history; $\delta_m^{\mathbf{0}}$ and δ_m^f are the effective displacements at damage initiation and at complete failure, respectively. The effective displacement δ_m is defined as:

$$\delta_m = \sqrt{\langle \delta_n \rangle^2 + {\delta_s}^2 + {\delta_t}^2} \tag{3.15}$$

For exponential softening, the evolution of the damage variable D is expressed as:

$$D = 1 - \left\{\frac{\delta_m^0}{\delta_m^{max}}\right\}\left\{1 - \frac{1 - e^{-\vartheta\frac{(\delta_m^{max} - \delta_m^0)}{(\delta_m^f - \delta_m^0)}}}{1 - e^{-\vartheta}}\right\} \tag{3.16}$$

where ϑ is a non-dimensional material parameter that defines the rate of damage evolution and e^x is the exponential function. The effective displacements at failure δ_m^f can be calculated based on the tensile and shear strengths and the fracture energy, as follows:

$$\delta_m^f = \frac{2\,G^c}{T_{eff}^0} \tag{3.17}$$

where T_{eff}^0 is the effective traction at damage initiation defined as:

$$T_{eff}^0 = \sqrt{(\sigma_n'^0)^2 + (\tau_s^0)^2 + (\tau_t^0)^2} \tag{3.18}$$

and G^c is the fracture energy which is equal to the area under the traction-separation curve, as shown in Figure 3.1. The Benzeggagh-Kenane model (BENZEGGAGH; KENANE, 1996) is adopted to simulate damage evolution during the fracture propagation process. This criterion is useful when the critical fracture energies of rock material along the first and the second shear directions are similar. The critical energy considers mixed damage mechanisms according to:

$$G^c = G_n^c + (G_s^c - G_n^c)\left\{\frac{G_S}{G_T}\right\}^\eta \tag{3.19}$$

where G_n^c and G_s^c are mode-I and mode-II critical fracture energies, respectively; $G_S = G_s + G_t$, $G_T = G_n + G_S$; G_n, G_s and G_t are the work done by the tractions and their conjugate relative displacements in the normal, first, and second shear directions, respectively, and η is a material parameter. This work adopts $\eta = 2.28$.

3.2.3. Natural fracture: closure, friction, opening, and shear dilation

A nonlinear elastic closure model is used to prevent overlapping of fracture surfaces under effective compressive stresses. Figure 3.2 illustrates the empirical

model proposed by (BANDIS; LUMSDEN; BARTON, 1983), in which fracture closure is stress-dependent and defined by:

$$\sigma'_n = \frac{k_{n0}\,\delta_n}{1-\frac{\delta_n}{\delta_{max}}} \tag{3.20}$$

$$k_n = \frac{\partial \sigma'_n}{\partial \delta_n} = \frac{k_{n0}\delta_{max}^2}{(\delta_{max}+\delta_n)^2} \tag{3.21}$$

where σ'_n is the normal effective stress (negative in compression), k_{n0} is the initial normal stiffness, δ_n is the fracture closure, and δ_{max} is the maximum closure.

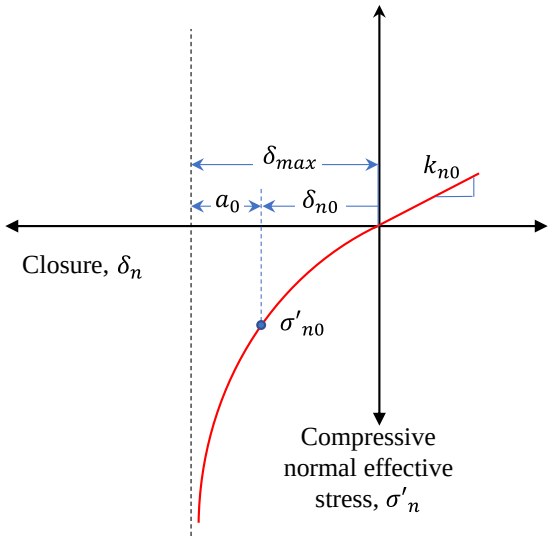

Figure 3.2. Nonlinear behavior of fractures under effective compressive normal stress

This nonlinear closure model avoids excessive fracture penetration when natural fractures are submitted to high compressive stresses. As compressive stresses increase, the curve becomes asymptotic to the vertical line, which defines the limit of maximum closure δ_{max}. This value is experimentally obtained, as described in (BANDIS; LUMSDEN; BARTON, 1983). For practical purposes, considering an initial effective stress state σ'_{n0} that induces an initial closure δ_{n0}, δ_{max} can be estimated from equation (3.20) by the expression:

$$\delta_{max} = \frac{a_0 + \sqrt{{a_0}^2 + {}^{4a_0\sigma'_{n0}}/_{k_{n0}}}}{2} \tag{3.22}$$

where a_0 is the initial fracture aperture.

The phenomenon of activation of natural discontinuities was the first possible cause of fluid flow in areas with pre-existing fractures (SIBSON, 1981). This behavior can be simulated by the Coulomb friction model with zero tension cut-off, which was implemented in this work (see Figure 3.3). This criterion assumes that reactivation occurs when the resultant shear stress τ_R acting on the fracture surface reaches the limit value τ_{slip} expressed in terms of the effective normal stress σ_n' (negative compression):

$$\tau_{slip} = c - \sigma_n' tan\phi \tag{3.23}$$

where c is the fracture cohesion, and ϕ is the friction angle.

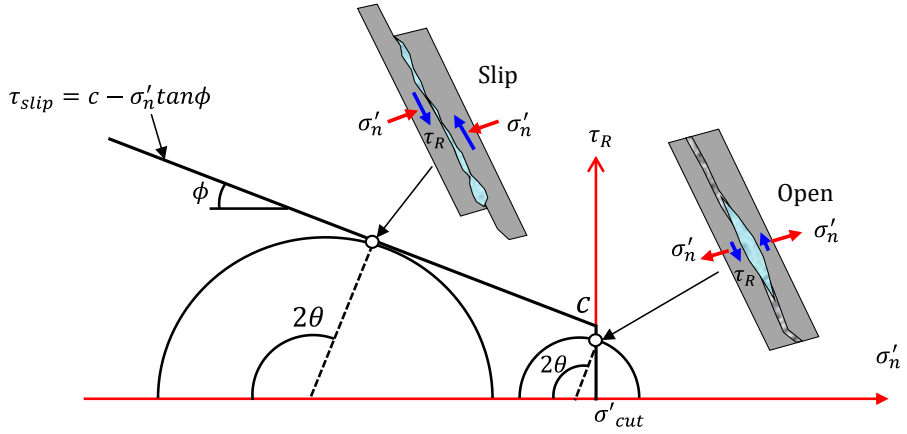

Figure 3.3. Coulomb friction failure criterion.

Alternatively, the natural fracture opens when the effective normal stress on the surface reaches the tension cutoff, σ_{cut}'. The yield functions for slip and opening are formulated according to:

$$f_s = |\tau_R| - \tau_{slip} \tag{3.24}$$

$$f_n = \sigma_n' - \sigma_{cut}' \tag{3.25}$$

where $\tau_R = \sqrt{\tau_s^2 + \tau_t^2}$ is the effective shear stress on the failure plane.

In addition to the changes in the aperture by normal stress variation, we include the contribution of shear dilation to represent the effect of asperities of natural rough-walled fractures (see Figure 3.4). Then, a non-associated flow rule considering a potential plastic function is adopted, as follows:

$$P = |\tau_R| - c + \sigma_n' tan\psi \tag{3.26}$$

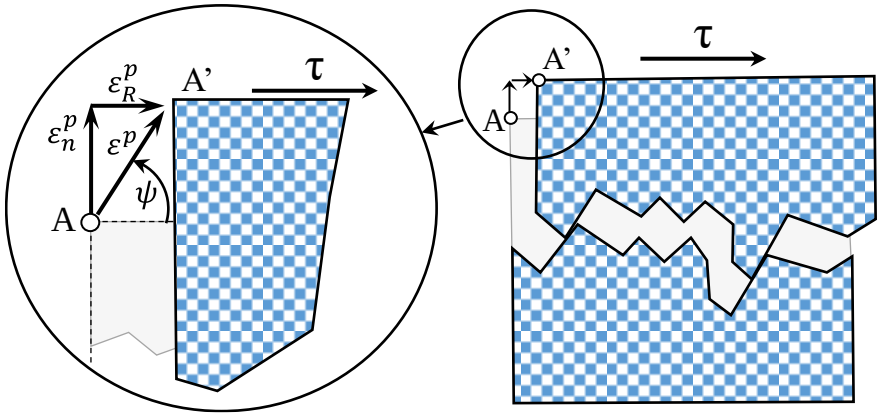

Figure 3.4. Shear dilation due to the effect of fracture asperities

In this expression, ψ is the dilatancy angle that controls the volume change or dilation during plastic shear strains. For concrete and rock, the dilatancy angle is significantly smaller than the friction angle. In this work, the relation $\psi = \phi/4$ is adopted (VERMEER, P.A., DE BORST, 1984).

Considering an implicit stress integration, the normal effective σ'_n and shear τ_s , τ_t stress components can be obtained by,

$$\begin{Bmatrix} \tau_s \\ \tau_t \\ \sigma'_n \end{Bmatrix} = \begin{Bmatrix} \bar{\tau}_s \\ \bar{\tau}_t \\ \bar{\sigma}'_n \end{Bmatrix} - \boldsymbol{D}_e \begin{Bmatrix} \Delta\varepsilon_s^p \\ \Delta\varepsilon_t^p \\ \Delta\varepsilon_n^p \end{Bmatrix} \tag{3.27}$$

where $\Delta\varepsilon_n^p$ represents the normal plastic strain; $\Delta\varepsilon_s^P$ and $\Delta\varepsilon_t^p$ are the tangential plastic strains; $\bar{\tau}_s$, $\bar{\tau}_t$ and $\bar{\sigma}'_n$ are the effective stresses predicted by the linear elastic model and $\boldsymbol{D}_e$ is the elastic constitutive matrix defined in eq (3.10). The non-associative flow rule relates the incremental plastic strain $\Delta\varepsilon^p$ to the plastic potential function $P(\boldsymbol{\sigma})$ by,

$$\Delta\boldsymbol{\varepsilon}^p = \lambda \left\{\frac{\partial P}{\partial \boldsymbol{\sigma}}\right\} \tag{3.28}$$

where λ is the plastic multiplier that can be obtained by imposing the plastic condition $f_{s,n}\left(\bar{\boldsymbol{\sigma}} - \boldsymbol{D}_e \lambda \left\{\frac{\partial P}{\partial \boldsymbol{\sigma}}\right\}\right) = 0$ solution. Finally, the elastoplastic matrix is defined as:

$$\boldsymbol{D}_{ep} = \boldsymbol{D}_e - \frac{\boldsymbol{D}_e \cdot \left\{\frac{\partial P}{\partial \boldsymbol{\sigma}}\right\} \cdot \left\{\frac{\partial f_{s,n}}{\partial \boldsymbol{\sigma}}\right\}^T \cdot \boldsymbol{D}_e}{\left\{\frac{\partial f_{s,n}}{\partial \boldsymbol{\sigma}}\right\}^T \cdot \boldsymbol{D}_e \cdot \left\{\frac{\partial P}{\partial \boldsymbol{\sigma}}\right\}} \tag{3.29}$$

3.2.4. Fluid flow inside the fractures

The continuity equation of mass conservation combines fluid flow along and across the discontinuity according to

$$\frac{\partial \delta_n}{\partial t} + \frac{\partial q_s}{\partial s} + v_t + v_b = 0 \tag{3.30}$$

where q_s [m²/s] is the tangential flow inside the fracture; δ_n is the crack aperture; v_t and v_b [m/s] are the fluid flow velocities leaking through the top and bottom fracture surfaces to the surrounding porous medium. Figure 3.5 shows a schematic representation of the fluid flow inside the fractures.

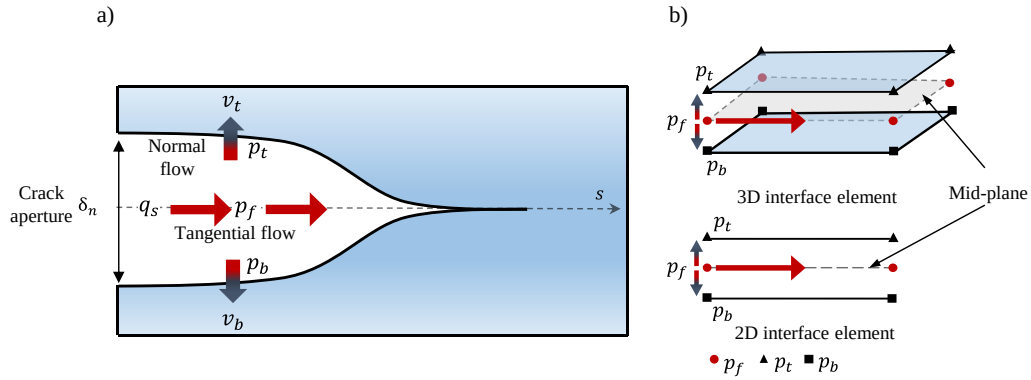

Figure 3.5. Fluid flow pattern inside the fracture (a) and 2D/3D interface element (b).

Generally, the Navier–Stokes (N-S) equation describes the behavior of slow flow of viscous and Newtonian fluid along rough-walled fractures with variable aperture (BRUSH; THOMSON, 2003; SARKAR; TOKSOZ; BURNS, 2004). However, the implementation of N-S equation is not trivial due to its highly nonlinear nature, complex parameters, and irregular rock fracture geometry (CHEN; ZHAO; SUN, 2013). In this work, assuming small fracture apertures, description of fluid flow inside the crack is governed by Reynold's lubrication theory and follows the simplified solution for flow between smooth parallel plates (i.e., Poiseuille flow).

$$q_s = -\frac{\delta_n^3}{12.\mu}.\frac{\partial p_f}{\partial s} \tag{3.31}$$

here μ [Pa s] is the fluid viscosity, p_f [Pa] is the internal fluid pressure along the fracture parameterized with the curvilinear coordinate, s. In this case, the fluid is considered incompressible with Newtonian rheology. The assumption zero-lag is valid for high confining stresses (ADACHI; DETOURNAY, 2008), which is the case here. The assumption of fluid flow in narrow surfaces applies in cases where the fracture aperture is several orders of magnitude than the fracture planes. Hence, the lubrication theory is widely used in hydraulic fracturing.

The normal flow reflects the fluid leak-off from fractures into the surrounding porous formation. This flow can be defined by the pressure-dependent leak-off model (SETTARI; PRICE H.S., 1984).

$$\begin{aligned} v_t &= c_t.(p_f - p_t) \\ v_b &= c_b.(p_f - p_b) \end{aligned} \tag{3.32}$$

where p_t and p_b [Pa] are the pore pressures in the adjacent porous material on the top and bottom fracture surfaces, and c_t and c_b[m/(Pa×s)] are pressure-dependent leak-off coefficients. These coefficients can be interpreted as the permeability of a finite layer of material on the fracture surfaces. (REMIJ et al., 2015) derived an expression for c_t and c_b using the 1D analytical solution for a semi-infinite formation:

$$c_{t,b} = \frac{\kappa}{2\sqrt{\frac{c_v\, t}{\pi}}} \tag{3.33}$$

with $\kappa = k/\mu$ [m^2/(Pa s)], where k[m^2] is the absolute permeability of the porous medium; t [s] is the expired time after the discontinuity was inserted; c_v [m^2/s] is the fluid diffusivity coefficient given by (COUSSY, 2004; RICE; CLEARY, 1976):

$$c_v = \kappa\, M \frac{K + \frac{4}{3}G}{K_u + \frac{4}{3}G} \tag{3.34}$$

where G [Pa] is the shear modulus and K_u [Pa] is the undrained bulk modulus defined as:

$$K_u = K + \alpha^2 M \tag{3.35}$$

The parameters $K, \alpha,$ and M were defined in sections 3.1.1 and 3.1.2.

3.2.5. Interaction between hydraulic and natural fractures

Generally, natural fractures are partially or completely sealed. They act as planes of weakness and can be activated in hydraulic fracture treatments. Therefore, two scenarios can be considered to study the effect of sealed and open fractures in the final geometry of a hydraulic fracture. In the former case, during the interaction, the fluid along the hydraulic fracture is transferred into natural fractures when activation criteria are met (see section 3.2.3). In this case, the elements are activated following the Coulomb friction criterion inducing slippage and propagation along the natural fracture (Figure 3.6a). On the other hand, when the normal stress of the natural fracture reaches the tension cutoff limit, it induces the opening of the natural fracture (Figure 3.6b). In the latter case, the fluid is directly transferred along the open natural fracture following the cubic law.

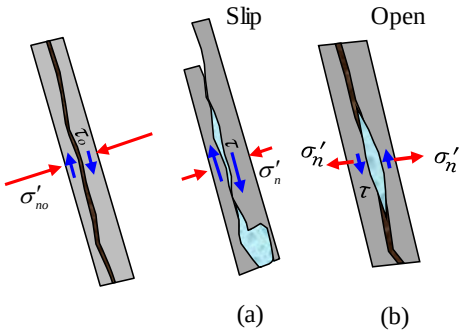

Figure 3.6. Natural fracture behavior when activated: (a) shear slip, (b) open by traction.

3.2.6. Fracture propagation regimes

Several works have focused on the search of analytical solutions for the problem of hydraulic fractures. Some simplified models are defined in the form of regular asymptotic expansions that can be used to study the influence of physical processes involved in fracture propagation (ADACHI; DETOURNAY, 2008, 2008; BUNGER; DETOURNAY; GARAGASH, 2005; DETOURNAY, 2004; GARAGASH;

DETOURNAY; ADACHI, 2011). Two of these processes correspond to the asymptotic dissipative mechanisms (energy dissipated by the fluid viscosity and the fracture propagation). Two others consist of fluid balance mechanisms (fluid storage inside the fracture and fluid leak-off from the fracture into the surrounding porous material). These mechanisms can be classified according to four limiting fracture propagation regimes: storage-viscosity dominated (M), storage-toughness dominated (K), leak-off-viscosity dominated ($\tilde{M}$), and leak-off- toughness dominated ($\tilde{K}$). These fracture propagation regimes can be represented in a parametric space where each limiting regime corresponds to one of the rectangle vertices with one of the mechanisms represented and the others neglected. Figure 3.7 illustrates the parametric space ($\mathcal{K}$, $\mathcal{C}$), where each side of the space represents asymptotic regimes.

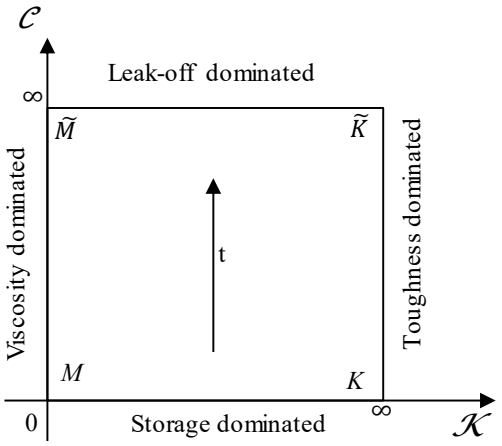

Figure 3.7. Hydraulic fracture parametric space in the permeable medium (BUNGER; DETOURNAY; GARAGASH, 2005; CARRIER; GRANET, 2012)

The analytical solution is based on linear elastic fracture mechanics (LEFM) (DONTSOV, 2017). The assessment of the fluid leak-off velocity follows from (HOWARD; FAST, 1957):

$$v(x,t) = \frac{2C_l}{\sqrt{t - t_0(x)}} \tag{3.36}$$

where $t_0(x)$ is the time at which the fracture arrives at x, and C_l is Carter's leak-off coefficient. (CARRIER; GRANET, 2012) presented an expression that relates Carter's leak-off coefficient and parameters of the surrounding medium.

$$C_l \approx \frac{k}{\mu}\frac{\sigma_0}{\sqrt{\pi c_v}} \tag{3.37}$$

where σ_0 denotes the confining stress. The dimensionless toughness $\mathcal{K}$, viscosity $\mathcal{M}$ and leak-off $\mathcal{C}$ parameters can be defined as (ADACHI; DETOURNAY, 2008):

$$\mathcal{K} = \frac{8K_{Ic}}{\sqrt{2\pi}}\left(\frac{1}{Q_0 E'^3 \mu'}\right)^{1/4}, \quad \mathcal{M} = \mathcal{K}^{-4}, \quad \mathcal{C} = 2C_l\left(\frac{E't}{Q_0^3\mu'}\right)^{1/6} \tag{3.38}$$

with

$$E' = \frac{E}{1-\nu^2}, \qquad \mu' = 12\mu, \qquad K_{Ic} = \sqrt{E'G_c} \tag{3.39}$$

where Q_0 is the fluid injection rate, E is the Young's Modulus, ν is Poisson's coefficient, μ is the fluid viscosity, and G_c is the critical fracture energy.

Several studies (CARRIER; GRANET, 2012; CHEN, 2012; CHEN et al., 2009; GARAGASH, 2019) have shown the ability of cohesive zone models to simulate hydraulic fracture propagation in storage-viscosity ($\mathcal{M}$), storage-toughness ($\mathcal{K}$), leak-off-viscosity ($\tilde{\mathcal{M}}$) and leak-off-toughness ($\tilde{\mathcal{K}}$) dominated regimes. For those regimes, we extend the use of the cohesive zone model to study the impact of the presence of a natural fracture on the hydraulic fracture propagation in a porous rock formation.

3.3. Coupled finite element formulation

The finite element formulation for a triple-noded interface element follows a similar procedure to the one adopted by (NG; SMALL, 1997) and (SEGURA; CAROL, 2004). That formulation assumes small-strain theory, isothermal conditions, incompressible Newtonian fluid, and neglects inertial forces. According to the principle of effective stresses for discontinuities, the fluid pressure inside the fracture influences the normal stress component inducing fracture closure, opening, or propagation. Figure 3.8 shows the triple-noded interface element for 2D (left) and 3D (right) cases.

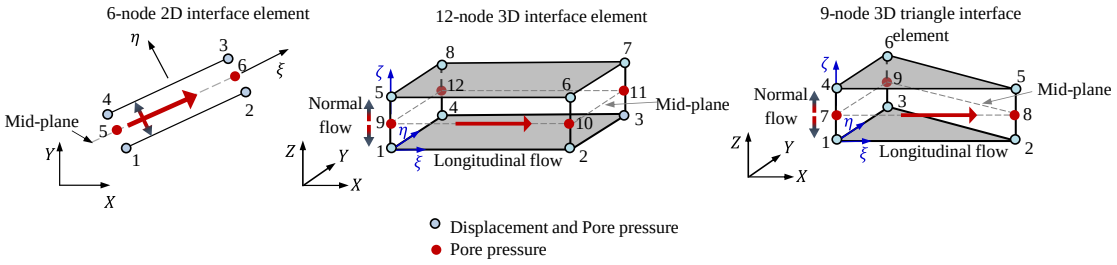

Figure 3.8. Schematic representation of the triple-noded 2D/3D interface element

The fully coupled hydromechanical finite element formulation is presented for the 3D quadrilateral interface element with 12 nodes (see Figure 3.8): 4 nodes at the top, 4 nodes at the base, and 4 at the mid-plane. The formulation considers pore pressure p degrees-of-freedom for nodes located at the mid-plane (nodes 9,10,11,12) and displacement u and pore pressure p degrees-of-freedom for nodes at the top and base (nodes 1 to 8). As proposed by (SEGURA; CAROL, 2004) and (NG; SMALL, 1997), the displacement in the global system (X, Y, Z) are transformed to the displacement $\boldsymbol{u}$ in the local system (x, y, z) using a rotation matrix $\boldsymbol{R}$.

$$\boldsymbol{u} \approx \boldsymbol{R}.\boldsymbol{U} \tag{3.40}$$

The separation $\boldsymbol{\delta}$ at the fracture surface along the normal and tangential direction is approximated from the local nodal displacements using a local displacement-separation matrix $\boldsymbol{L}$ and shape functions $\boldsymbol{N_u}$.

$$\boldsymbol{\delta} \approx \boldsymbol{N_u}.\boldsymbol{L}.\boldsymbol{u} \tag{3.41}$$

The pore pressure drop at the top and base ($\Delta\boldsymbol{p_T}$, $\Delta\boldsymbol{p_B}$) is interpolated from the nodal pore pressure jump $\Delta\boldsymbol{p}$ in the local coordinate system using shape functions $\boldsymbol{N}_p$.

$$\begin{aligned} \Delta\boldsymbol{p_T} &\approx \boldsymbol{N}_p.\Delta\tilde{\boldsymbol{p}}_{\boldsymbol{t}} \\ \Delta\boldsymbol{p_B} &\approx \boldsymbol{N}_p.\Delta\tilde{\boldsymbol{p}}_{\boldsymbol{b}} \end{aligned} \tag{3.42}$$

where $\Delta\tilde{\boldsymbol{p}}_{\boldsymbol{t}} = \boldsymbol{p}_m - \boldsymbol{p}_t$ and $\Delta\tilde{\boldsymbol{p}}_{\boldsymbol{b}} = \boldsymbol{p}_m - \boldsymbol{p}_b$ represent the nodal pore pressure jump from the mid-plane nodes $\boldsymbol{p}_m = \{p_9 \quad p_{10} \quad p_{11} \quad p_{12}\}^T$, to the top $\boldsymbol{p}_t = \{p_5 \quad p_6 \quad p_7 \quad p_8\}^T$, and bottom $\boldsymbol{p}_b = \{p_1 \quad p_2 \quad p_3 \quad p_4\}^T$ nodes, respectively.

The governing equations (3.8) and (3.30) can be discretized using the standard Galerkin Method resulting in the following set of coupled equations:

$$\boldsymbol{K_e}.\boldsymbol{U} - \boldsymbol{L_e}.\boldsymbol{P} = \boldsymbol{f_u} \tag{3.43}$$

$$\boldsymbol{L_e^T}.\dot{\boldsymbol{U}} - \boldsymbol{H_e}.\boldsymbol{P} = \boldsymbol{Q_p} \tag{3.44}$$

$\boldsymbol{K_e}$ represents the stiffness matrix, $\boldsymbol{L_e}$ is the coupling matrix, $\boldsymbol{H_e}$ is the permeability matrix, and $\boldsymbol{f_u}$ and $\boldsymbol{Q_p}$ stand for the external force and external flow vector, respectively.

$$\left.\begin{aligned} \boldsymbol{K_e} &= \int_{\Gamma} \boldsymbol{B_u^T}.\boldsymbol{D_t}.\boldsymbol{B_u}.\boldsymbol{dS} \\ \boldsymbol{L_e} &= \int_{\Gamma} \boldsymbol{B_u^T}.\boldsymbol{m}.\boldsymbol{N_p}.\boldsymbol{dS} \\ \boldsymbol{H_e} &= \boldsymbol{\psi}(\boldsymbol{Q_{Le}}, \boldsymbol{Q_{Te}}, \boldsymbol{Q_{Be}}) \end{aligned}\right\} \tag{3.45}$$

with $\boldsymbol{B_u}$ is the strain-displacement matrix, $\boldsymbol{D_t}$ is the tangential constitutive matrix that depends on the interface material response, $\boldsymbol{Q_{Le}} = \int_{\Gamma} \boldsymbol{B_p^T}.k_l.\boldsymbol{B_p}.ds$ is the longitudinal fluid flow matrix at the mid-plane, $\boldsymbol{B_p}$ is the matrix of derivatives of the shape functions, $\boldsymbol{Q_{Te}} = \int_{\Gamma} {\boldsymbol{N_p}}^T.c_t.\boldsymbol{N_p}.ds$, and $\boldsymbol{Q_{Be}} = \int_{\Gamma} {\boldsymbol{N_p}}^T.c_b.\boldsymbol{N_p}.ds$ are the normal conductivity matrix at the top and bottom fracture surfaces, respectively.

3.4. Model implementation

Cohesive zone models (CZM) have been used effectively to simulate hydraulic fracture propagation and, more recently, for the interaction with natural fractures (DAHI TALEGHANI et al., 2018; GONZALEZ; TALEGHANI; OLSEN, 2015; GUO; LIU, 2014; HADDAD; DU; VIDAL-GILBERT, 2017; MEJIA SANCHEZ; RUEDA CORDERO; ROEHL, 2020; NIKAM et al., 2016; RUEDA CORDERO; MEJIA; ROEHL, 2017). However, the major disadvantage of the CZM is the inability to predict the path and propagation direction of the hydraulic fracture (DAHI TALEGHANI; GONZALEZ; SHOJAEI, 2016). To overcome this disadvantage, a mesh fragmentation algorithm (MeshFrag) is developed. The mesh fragmentation consists of the insertion of zero-thickness interface elements between every edge of continuum elements. We adopt an unstructured Delaunay triangulation algorithm to introduce some generality to describe a heterogeneous structure, crack propagation, and fracture paths.

3.4.1.
Mesh Fragmentation: algorithm MeshFrag

There is a total lack of discussion on implementation aspects of the insertion of the special hydromechanical triple-noded interface elements into an existing finite element mesh. Also, to our knowledge, no commercial or open-source codes have this capability. Hence, an intrinsic mesh fragmentation algorithm, MeshFrag, is presented in order to simulate unrestricted hydraulic crack propagation. The algorithm developed in Matlab supports triangle, quadrilateral, tetrahedral, hexahedral, and wedge elements for 2D/3D analyses. The workflow follows the conventional procedure with the three main phases: model generation, solution, and result interpretation. The insertion of the triple-noded interface elements is based on the fragmentation of conforming meshes and happens in the pre-processing phase, as shown in Figure 3.9. For this purpose, node duplication, updating of the topological connectivity, and generation of extra fracture faces are required. Subsequently, the conventional doubled-noded interface element is inserted at every edge of the continuum finite elements. Finally, we add the middle-edge nodes of the triple-noded interface elements, which require special treatment to ensure continuity of the fluid field. Figure 3.10 outlines the fragmentation steps of a conventional 2D finite element mesh.

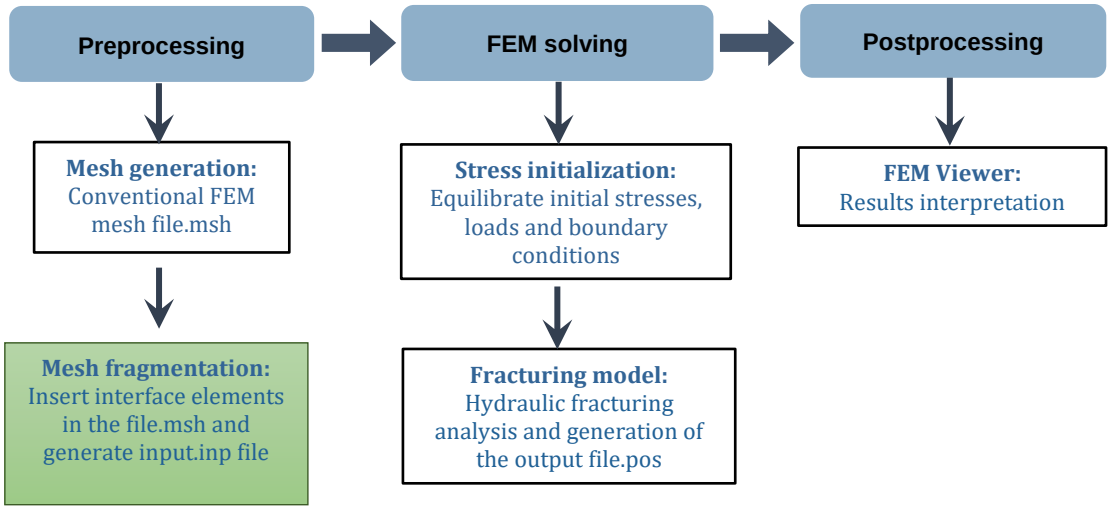

Figure 3.9. Workflow to simulate unrestricted fracture propagation in fractured media.

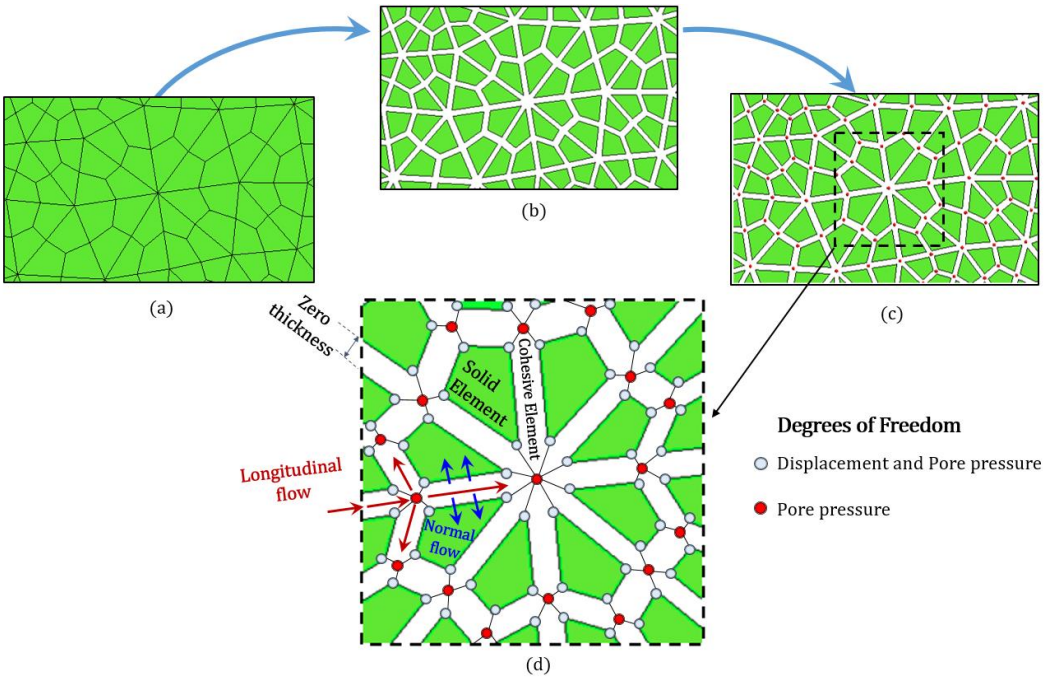

Figure 3.10. Mesh fragmentation scheme: (a) conventional mesh; (b) duplicate nodes and insert interface elements at the edges of the continuum elements; (c) insertion of intermediate pore pressure nodes; (d) detail of the intersection of several hydromechanical cohesive interface elements.

This methodology is independent of the mesh generation software. Here Gmsh preprocessor (GEUZAINE; REMACLE, 2009) is used for practical examples. This preprocessor combines geometrical entities into more meaningful groups to define domains, boundary conditions, and material properties. By default, in the MSH file format, if physical groups are defined, the output mesh only contains those elements that belong to at least one physical group. Thus, some rules are defined to regularize the process.

The topological entities created by Gmsh are identified by italic typeset. Each physical group (attached to elements) is considered to have a different material. Therefore, a physical group is composed of a prefix that defines some procedures and is followed by the material name. For example, it is usually convenient to keep the original nodes in some specific regions denoted by the prefix *gce_*. On the other hand, we define the prefix *intraface_* to fragment a region of continuum elements. Interfaces, joints, or predefined fractures are attached to the line and surface elements for 2D and 3D cases, respectively. These entities are referenced by the prefix *coh_*. Finally, we use the prefix *bc_* to reference boundary conditions on the nodes. Figure 3.11 shows a scheme of a total and a partial fragmentation according to the adopted prefixes.

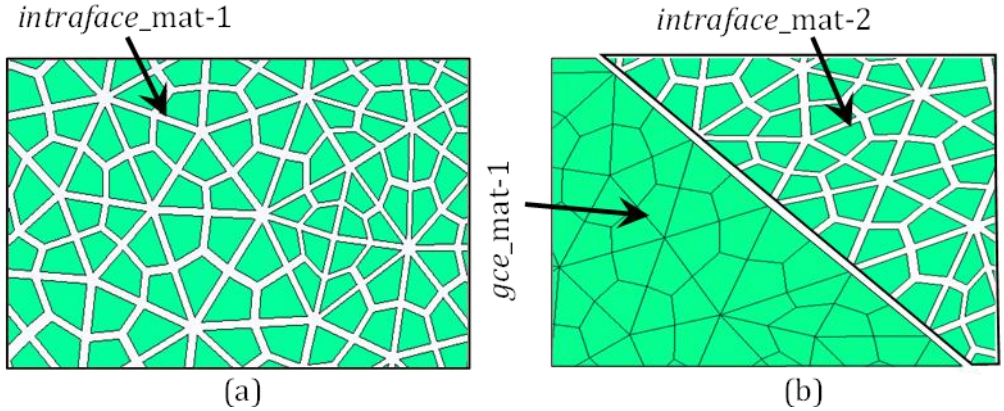

Figure 3.11. Defining element groups - (a) total fragmentation (b) partial fragmentation.

As described above, the first stage is to read the MSH file created by the preprocessor program and recognize the physical groups. The second stage consists of the fragmentation process, which is followed by creating the input file for the FEM solver.

3.4.1.1. Mesh fragmentation for modeling of hydraulic crack propagation

The insertion of triple-noded interface elements in a conforming finite element mesh requires topological changes. In this work, we propose the following procedure.

1. **Duplicate nodes:** element groups denoted as *intraface_* are fragmented. In this case, an original node shared by n elements is duplicated by n nodes. Node duplication is the outcome of mesh fragmentation.

2. **Update topological connectivity:** a simple topological data structure is employed in the mesh fragmentation process. The proposed data structure is used for triangle and quadrilateral elements with 3 and 4 nodes, respectively. We create new tables when fragmentation occurs. A new table of nodes stores the new node indices (Id), the original indices (OId) of the sequential element connectivity, and their corresponding x and y coordinates. A second new element table saves the material id and the new nodal connectivity. Figure 3.12 shows an example of the data structure used in the mesh fragmentation.

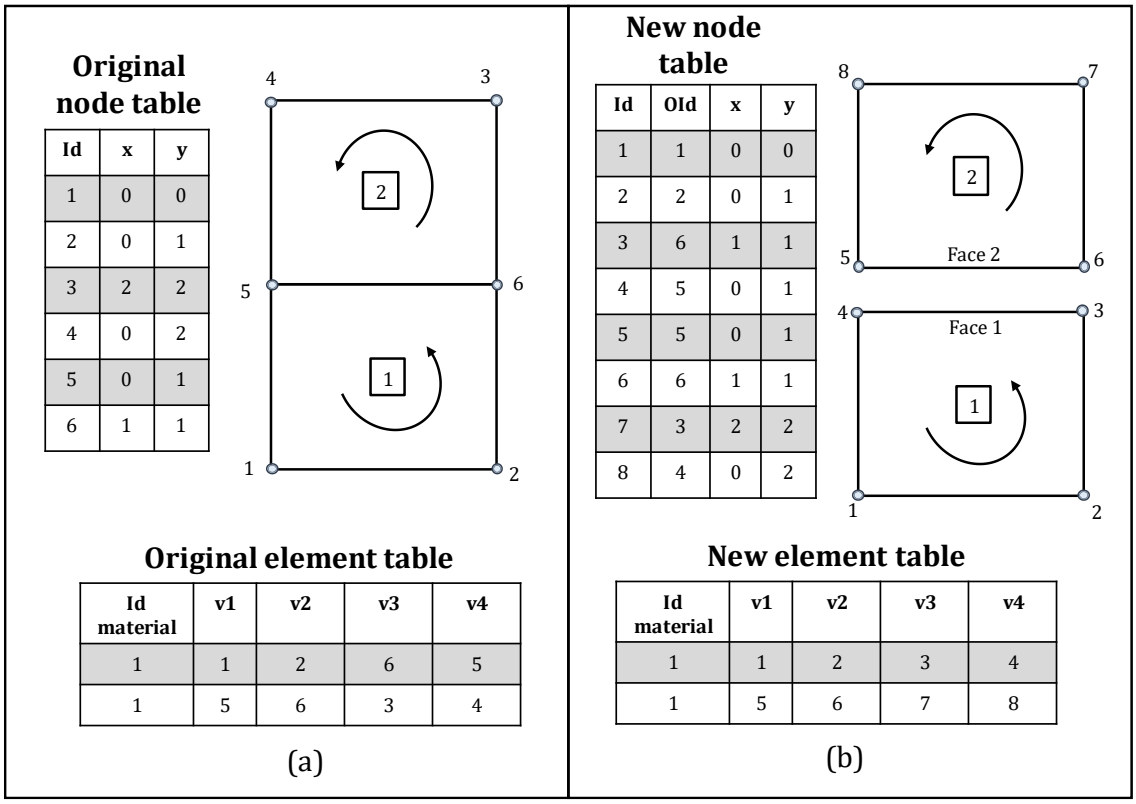

Figure 3.12. Updating topological connectivity – (a) original; (b) new

In this data structure, each element is assumed to be independent of the others. Therefore, nodes and elements can be updated based on their own information. This procedure ensures the generation of new nodes and faces necessary for the insertion of interface elements. The original node indices (OId) are essential to identify faces shared by two elements (Step 4). For example, face 1 formed by Id nodes 4 and 3 and face 2 formed by Id nodes 5 and 6 share the same OId nodes 5 and 6 (Figure 3.12b).

3. **Generate extra fracture faces:** in order to create the interface elements, a face table saves the material id of its corresponding element and the updated nodal incidence of every face.

4. **Create the double-noded interface element:** the conventional double-noded interface element is created when two faces share the original nodal incidence.

5. **Check predefined interface material:** interfaces, joints, or predefined fractures are attached to the line and surface elements for 2D and 3D cases and saved in the table of *intMat*. This table stores the material id and the original nodal incidence of the interface element. The material id of the created

interface element is updated if it shares the same original nodal incidence with some predefined *intMat* element.

6. **Create and insert the middle nodes:** the middle nodes of the interface elements need special treatment to ensure the continuity of the fluid field. The insertion of the middle nodes of each interface element is based on the verification of the coordinates and nodal incidence of the created middle nodes. Therefore, a new middle node is created, provided that its coordinates and nodal incidence are different from those of the previously created middle nodes. Finally, the middle nodes are inserted into the interface elements. Figure 3.13 shows the nodal incidence changes to insert the triple-noded interface element in a conventional 2D mesh (Steps 1, 2, 4, and 6).

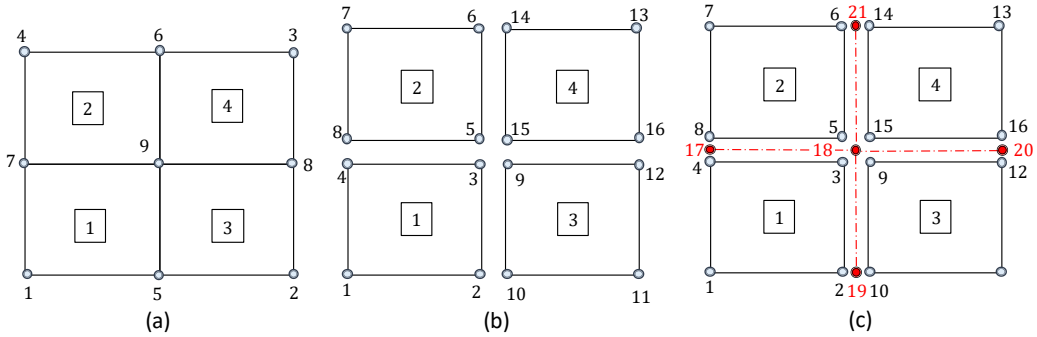

Figure 3.13. Updating nodal incidence to insert the 2D triple-noded interface element: (a) original FEM mesh; (b) mesh fragmentation and insertion of double–noded interface element; (c) insertion of middle nodes.

7. **Create the input file for the FEM solver:** the final step is to write an input file for the processing in a finite element solver. Thus, user functions can be implemented for this purpose. For such, the triple-noded interface element must be available in the software library. In this work, we have used the commercial software Abaqus®/Standard (2017) for practical examples. In this software, the triple-noded displacement and pore pressure cohesive interface element is used to simulate the fractures, while continuum displacement and pore pressure elements are used to model the surrounding medium. More details of cohesive-element size, meshing scheme, and far-field boundary conditions can be found in (CHEN, 2012).

3.4.2.
Stress initialization

In naturally fractured media, the in-situ stresses play an important role in hydraulic fracture propagation. Abaqus/Standard provides a geostatic procedure as the first step of geotechnical problems. In this work, stress initialization corresponding to the geostatic step occurs in two stages. The first stage calculates the loads to equilibrate the in-situ stress field. Therefore, the displacements of all nodes are restricted in the model. Subsequently, the initial stresses $\boldsymbol{S}_{coh} = \{\tau_s = \boldsymbol{S}_L(1,3) \quad \tau_t = \boldsymbol{S}_L(2,3) \quad \sigma_n = \boldsymbol{S}_L(3,3)\}^T$ acting on all cohesive interface elements are obtained from the in-situ stresses via tensor transformation. Here $\boldsymbol{S}_L$ is the initial stress tensor in the local system that is defined in the Abaqus user subroutine sigini (SMITH, 2016) according to the following expression:

$$\boldsymbol{S}_L = \boldsymbol{R}^T . \begin{bmatrix} \sigma'_x & 0 & 0 \\ 0 & \sigma'_y & 0 \\ 0 & 0 & \sigma'_z \end{bmatrix} . \boldsymbol{R} \tag{3.46}$$

where σ'_x, σ'_y and σ'_z are the effective stresses in x, y, z directions attributed to continuum elements, and $\boldsymbol{R}$ is the stress transformation matrix that can be expressed in terms of the interface dip angle φ and strike angle θ (Figure 3.14) as:

$$\boldsymbol{R} = \begin{bmatrix} sin(\theta) & cos(\theta) & 0 \\ cos(\varphi)\, cos(\theta) & -cos(\varphi)\, sin(\theta) & -sin(\varphi) \\ -sin(\varphi)\, cos(\theta) & sin(\varphi) sin(\theta) & -cos(\varphi) \end{bmatrix} \tag{3.47}$$

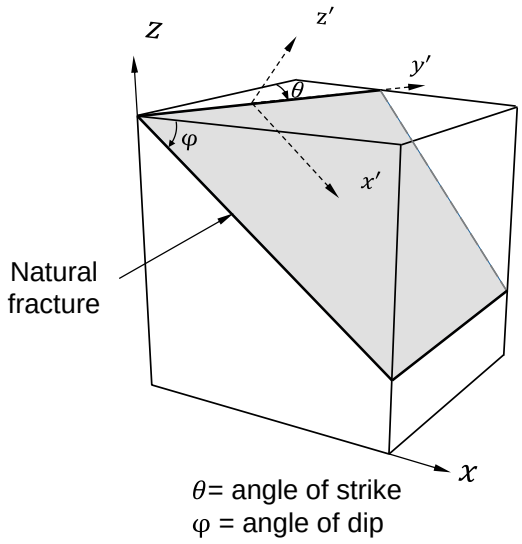

Figure 3.14. Schematic representation of an oriented fracture.

Finally, the nodal reactions in the system can be obtained. The second stage allows verifying that an initial geostatic stress field (assigned to the interface and continuum elements) is in equilibrium with the applied boundary conditions and loads (nodal reactions obtained in the first stage). The hydromechanical analysis starts when the in-situ stress field is equilibrated and produces zero deformation. More details about this procedure can be found in (SMITH, 2016).

3.5. Effect of the interface element stiffness on the elastic response of the material

The intrinsic cohesive model introduces artificial compliance that alters the elastic response of the material prior to the onset of a hydraulic fracture. This phenomenon is called "artificial compliance" and can be reduced by increasing the initial stiffness of the cohesive elements. The normal stiffness (k_n) and shear stiffness (k_s) can be defined in terms of the elastic properties of the surrounding rock material as:

$$\text{Elastic stiffness} \begin{cases} k_n = \dfrac{\acute{\alpha}}{t_m} E \\ k_{s,t} = \dfrac{\acute{\alpha}}{t_m} G \end{cases} \tag{3.48}$$

where E and G are the Young's and the shear modulus of the adjacent material, t_m is the mechanical thickness, and $\acute{\alpha}$ is a hardening factor much larger than 1 ($\acute{\alpha} \gg 1$). This factor should be high enough to provide a reasonable stiffness but small enough to avoid numerical problems such as spurious oscillations of the interface element (JIN; ARSON; BUSETTI, 2016; JIN et al., 2017; TURON et al., 2005). Values of $\acute{\alpha}/t_m$ = 0.1, 1, 10 and 100 mm^{-1} were considered in a compression test in order to study the influence of the stiffness parameter on the elastic response of the material. A rectangle of 0.4 x 1 m is compressed by applying a distributed pressure of 1 MPa at the model top surface. The base is constrained in the y-direction, while the left and right sides are constrained in the x-direction. Figure 3.15 shows these conditions and the finite element mesh with 22756 elements and 30528 nodes. The numerical model assumes a Young's Modulus equal to 1e+04 MPa and Poisson's ratio equal to 0.20.

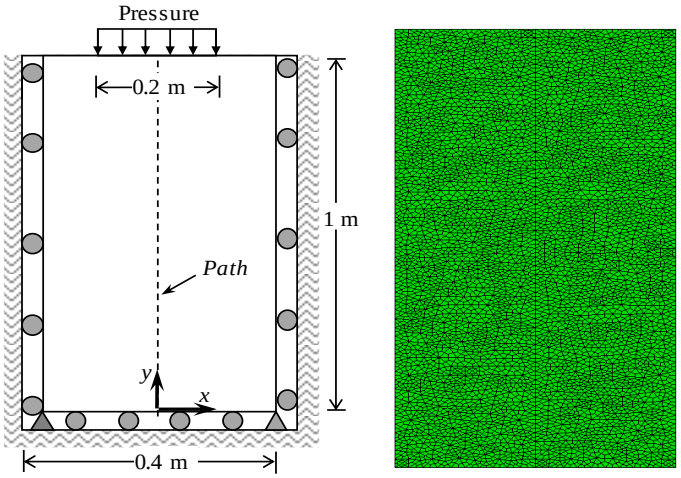

Figure 3.15. Compression test and finite element mesh of the numerical model

Figure 3.16 shows the numerical results associated with the effect of $\acute{\alpha}/t_m$ on the elastic response of the model and their comparisons against a numerical solution considering only continuum elements. Figure 3.17 shows the vertical stress distribution for (a) $\acute{\alpha}/t_m = 0.1$ mm^{-1}, (b) $\acute{\alpha}/t_m = 10$ mm^{-1} and (c) continuum model. As one would expect, the general response of the model is sensitive to the relation $\acute{\alpha}/t_m < 1$ mm^{-1}, but tends to describe the continuum response as $\acute{\alpha}/t_m > 1$ mm^{-1}. In this test, $\acute{\alpha}/t_m \geq 10$ mm^{-1} ensures the appropriate representation of the elastic response of the material prior to the onset of hydraulic fracture (Figure 3.16 and Figure 3.17).

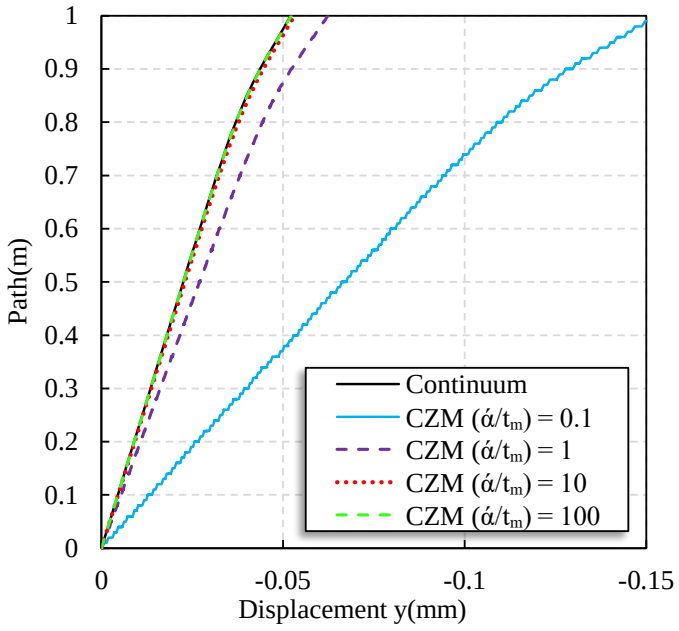

Figure 3.16. Effect of $\acute{\alpha}/t_m$ (mm^{-1}) of the interface element on the elastic response of the model.

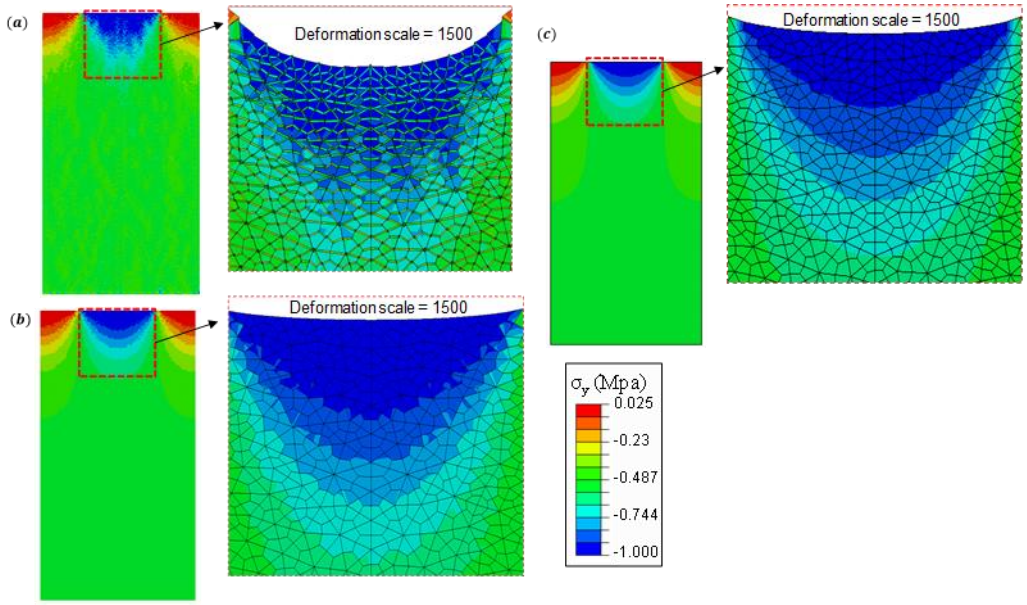

Figure 3.17. Vertical stress distribution for (a) $\dot{\alpha}/t_m = 0.1$ mm^{-1}, (b) $\dot{\alpha}/t_m = 10$ mm^{-1} and (c) continuum model.

3.6. Intrinsic CZM against laboratory tests

In this section, several experimental examples have been simulated to demonstrate the capabilities of the proposed numerical methodology. The first example studies the hydraulic fracture propagation in a pre-fractured rock. Mesh dependency and computational time of the proposed methodology are also evaluated. The second example demonstrates the unrestricted fracture propagation under a normal stress regime. In this case, hydraulic fracture propagation is initiated from an unfavorable perforation angle.

3.6.1. Hydraulic fracture propagation in a fractured rock sample

This example is presented to give a better understanding of the behavior of the hydraulic fracture in a naturally fractured formation. (KHOEI et al., 2015) performed a hydraulic fracturing experimental test in two naturally fractured rocks under plane strain conditions. Moreover, the authors (KHOEI et al., 2015) compared the measured experimental data with those of the numerical results obtained from the XFEM method. Here, we compare our numerical results with CZM elements and those obtained by (KHOEI et al., 2015) from two laboratory tests and numerical results using XFEM. Figure 3.18 illustrates a schematic representation of the geometry, boundary conditions, and the triangle mesh of the

simulated test. Table 3.1 presents the dimensions of the models as well as the coordinates of the initial notch and the natural fracture and material properties of the rock specimens. As referred by (KHOEI et al., 2015), the rock is considered impermeable. The fluid is injected at a constant pressure P_{inj} = 39.3 MPa through the hydro-fracture mouth. The fracturing fluid is assumed to be water with viscosity μ = 1e-03 Pa s.

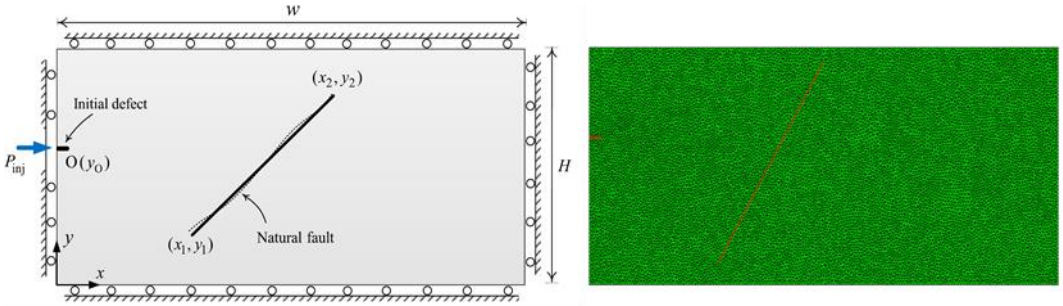

Figure 3.18. Schematic view of the geometry and boundary conditions of hydraulic fracturing experimental tests by (KHOEI et al., 2015) and finite element mesh.

Table 3.1. Geometry and mechanical properties of the rock sample

	Width w (mm)	Height H (mm)	(x1,y1) (mm)	(x2,y2) (mm)	yo (mm)
Specimen 1	111	45	(30.5;4)	(55.4;42.16)	27.9
Specimen 2	110	54	(12.13;8.82)	(98.12;46.07)	26.9
	Young´s Modulus E (GPa)	Poisson ratio v	Tensile strength σ_n^0 (MPa)	Fracture energy G_c (J/m²)	
Specimen 1	36.5	0.25	29.2	330	
Specimen 2	32.5	0.25	22.3	330	

The natural fracture stiffness and strength are considered equivalent to 10% of the corresponding rock properties; hence natural fractures are more sensitive to stress changes than the rock matrix. As referred by (KHOEI et al., 2015), the rock is considered impermeable in the first test. Four different triangular meshes are evaluated to study the mesh dependency and the computational time of the proposed approach. We use unstructured meshes based on Delaunay algorithm to reduce certain bias on crack propagation. Only the left region, where the crack will appear, was refined and fragmented with constant element size l_i (red elements in Figure 3.19). Interface element length l_i = 2 mm, 1.2 mm, 0.9 mm and 0.7 mm were considered. Table 3.2 shows the total number of elements, the nodes and the processing time on a desktop computer equipped with an Intel® Xeon® CPU X5650 @ 2.67 GHz (2 processors) for the adopted meshes. In this work, no attempt was made to optimize the CPU time in the different analyzes.

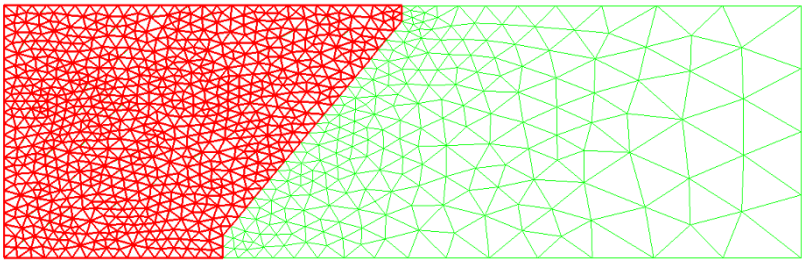

Figure 3.19. Finite element triangular mesh. Interface element length l_i =2 mm

Table 3.2. Mesh specifications and processing time

Model	l_i (mm)	Nodes	Elements	Time (s)
Mesh 1	2	5277	3963	390
Mesh 2	1.2	14405	10877	751
Mesh 3	0.9	25227	19098	1572
Mesh 4	0.7	43535	32918	3673

Figure 3.20 shows the influence of mesh size on the evolution of the hydraulic fracture propagation pattern. It is clear that the fracture patterns are influenced by mesh refinement. Figure 3.21 compares the hydraulic fracture trajectories between laboratory test 1 (KHOEI et al., 2015) and the numerical solutions. For Mesh 1 ($l_i = 2$ mm), the fracture is deviated from its correct path. This effect is reduced for more refined meshes. However, higher refinement results in higher computational cost (Table 3.2). We notice that for Mesh 3 ($l_i = 0.9$ mm) and Mesh 4 ($l_i = 0.7$ mm), the hydraulic fracture paths differ very little from the experimental test 1 (KHOEI et al., 2015). On the other hand, the processing time for the model with Mesh 4 is 2.34 times higher than for Mesh 3 (Table 3.2). Therefore, the initial mesh should be well balanced in terms of refinement to obtain a reliable solution and optimize the computational cost.

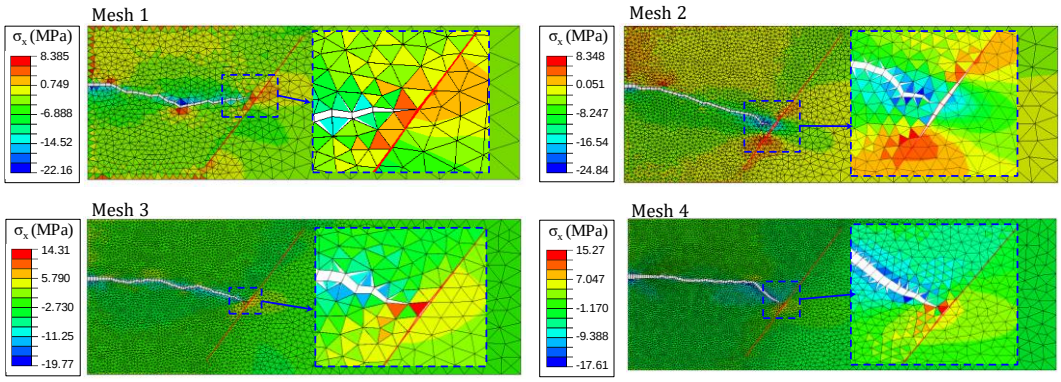

Figure 3.20. Stress distribution in the x direction for meshes 1, 2, 3 and 4 when the HF meets the NF. Displacements are magnified 20 times for demonstration purposes.

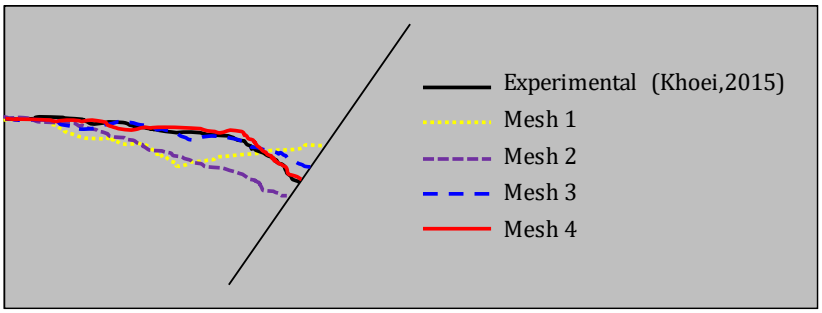

Figure 3.21. Comparison of hydraulic fracture trajectory between laboratory test 1 (KHOEI et al., 2015) and intrinsic CZM fragmentation.

In the second test, we have considered rock permeability k = 0.1 mD and porosity n = 20% in order to demonstrate the capability of the presented approach to simulate hydraulic fracture propagation in a porous media. Bilinear 4-node quadrilateral displacement and pore pressure plane strain elements (CPE4P) are used to model the porous rock. Figure 3.22 shows the pore pressure distribution and the minimum principal stress for this test. Figure 3.22a displays that the fluid flow inside the hydraulic fracture is transferred to the natural fracture. Figure 3.23 illustrates the hydraulic fracture trajectory between laboratory test 2 and numerical simulations with XFEM (KHOEI et al., 2015) against intrinsic CZM fragmentation.

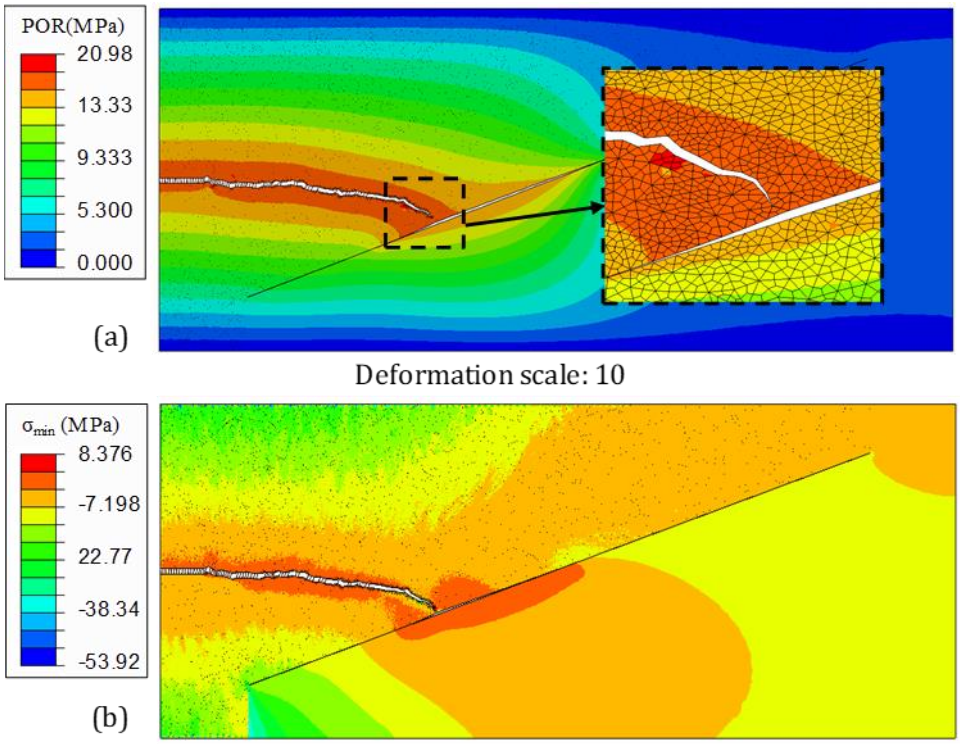

Figure 3.22. Hydraulic fracture and natural fracture interaction: pore pressure distribution (a); minimum principal stress (b).

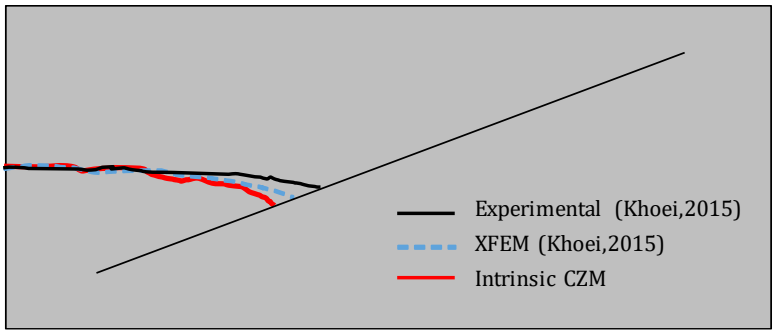

Figure 3.23. Comparison of hydraulic fracture trajectory between experimental test 2, numerical simulations with XFEM (KHOEI et al., 2015), and intrinsic CZM fragmentation.

Figure 3.23 also shows that the numerical simulations predict the hydraulic fracture trajectory accurately. Experimental conditions, rock specimen heterogeneity, permeability, fracture propagation criteria, among others, may explain the slight discrepancies. It is evident that the natural fracture affects the hydraulic fracture trajectory, which tends to curve when approaching the NF. Therefore, unrestricted fracture propagation is essential to predict complex fracture patterns in the hydraulic fracturing simulation in fractured formations.

3.6.2. Hydraulic fracture propagation from oriented perforation

(LIU et al., 2020) studied the effect of the perforation orientation on hydraulic fracturing. A series of laboratory fracturing experiments were performed using rectangular blocks of purple sandstone with dimensions of 0.3 m x 0.3 m x 0.3 m. The wellbore was drilled in the center of the block aligned with the vertical stress. Several perforation orientations were considered: $\theta = 0$, 15, 30, 45, 60, 75, and 90 degrees from the maximum horizontal stress. All samples were confined in a triaxial loading vessel subject to the principal stresses of 7 MPa in the vertical direction, 6 MPa, and 4 MPa, maximum and minimum horizontal stresses, respectively. Figure 3.24 shows a schematic representation of the core sample and the tetrahedral mesh with 44069 nodes and 29975 elements. The fracturing fluid is a high-viscosity oil with μ = 70 mPa s. Table 3.3 presents the physical and mechanical properties. The numerical simulation is performed considering $\theta = 0$, 30, 60, and 90 degrees. Homogenous and isotropic rock material was assumed, and the casing or cement was not considered in the numerical models.

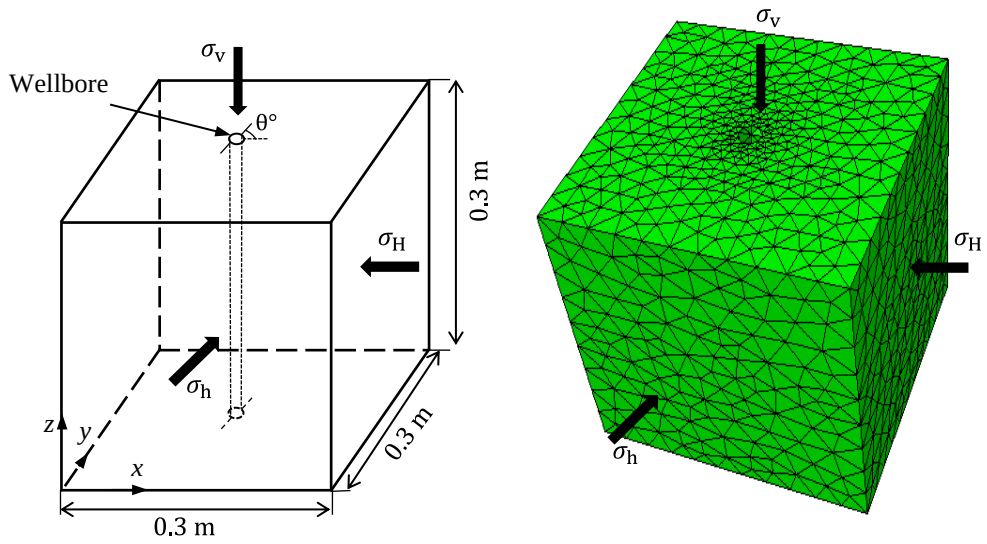

Figure 3.24. Schematic view of the geometry and finite element mesh of the numerical model.

Table 3.3. Geometry and mechanical properties of the rock sample

Rock sample properties	values
Dimension	0.3 x 0. 3 x 0.3 m
well diameter	0.025 m
Perforation length	0.010 m
Young's Modulus	2.86e07 kPa
Poisson ratio	0.23
Min Horizontal Stress	4000 kPa
Max Horizontal Stress	6000 kPa
vertical Stress	7000 kPa
Fracture toughness	1.067 MPa $m^{1/2}$
Porosity	7.1%
Uniaxial tensile strength	3200 kPa
Fluid viscosity	70e-06 kpa s
Injection rate	6.67e-07 m^3/s

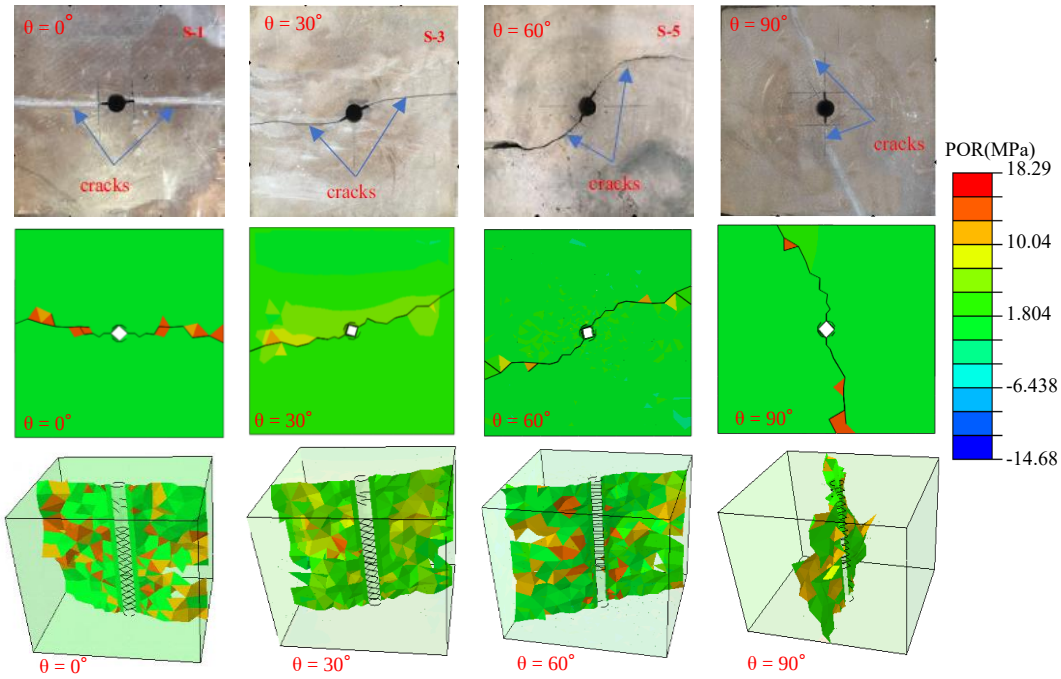

Figure 3.25. Comparison of the hydraulic fracture trajectory between laboratory tests (LIU et al., 2020) and intrinsic CZM fragmentation approach for the perforation orientations at $\theta = 0°, 30°, 60°$ and $90°$.

Figure 3.25 shows the comparison results of the numerical simulation against some photographs from available experimental tests (LIU et al., 2020). There is a good agreement between the numerical and the experimental results in terms of hydraulic fracture path. Notice that the fracture initially propagates along with the orientation of the perforations and gradually turns towards the direction of the maximum horizontal stress.

4
Study of hydraulic and natural fracture interaction

The content of this chapter comprises the papers of (MEJIA SANCHEZ; RUEDA CORDERO; ROEHL, 2020; RUEDA CORDERO et al., 2019). This chapter studies the effect of some primary parameters on the hydraulic and natural fracture interaction. The results of the new approach are compared against analytical and numerical solutions. Moreover, the influence of parameters such as rock permeability, fluid viscosity, in-situ stresses, fracture orientation, friction angle, injection flow rate, and distance from the borehole to natural fracture are also investigated. The proposed computational framework addresses important challenges in the simulation of induced fracture propagation in fractured media: formation of multiple fractures, including complex patterns, branching, propagation from the natural crack tip, crossing with an offset, and multiple cracks interaction. The study can provide guidance for a better understanding of the complex process of hydraulic fracturing and its interaction with natural fractures. Finally, some advantages and limitations of the proposed methodology are discussed.

4.1.
Influence of natural fractures on fluid-driven fractures in all asymptotic propagation regimes

The hydraulic fracture problem under limiting propagation regimes has been extensively studied using analytical solutions (ADACHI; DETOURNAY, 2002, 2008; DETOURNAY, 2004; DONTSOV, 2016) and numerical approaches (CARRIER; GRANET, 2012; CHEN, 2012; CHEN et al., 2009; GARAGASH, 2019; MANZOLI et al., 2019). However, investigation of the impact of natural fractures on the fluid-driven fracture in all asymptotic propagation regimes is relatively limited. Furthermore, aspects such as rock permeability, fluid viscosity, initial stress state, leak-off, injection time, and intercepting angle still need further studies. Those aspects are particularly important for evaluating induced and natural fracture interaction and the final configuration of the stimulated fracture network. This section aims at investigating the impacts of natural fractures on hydraulic fracturing in four limiting propagation regimes: toughness-storage, leak-off-

toughness, storage-viscosity, and leak-off-viscosity dominated. We analyze fracture propagation through an intact rock and compare our model with analytical solutions (considering KGD conditions) and numerical results obtained by (CARRIER; GRANET, 2012). Subsequently, we include natural fractures with different orientations to evaluate their influence in the final configuration of the hydraulic fracture in all asymptotic propagation regimes.

4.1.1. Model description

Fracture propagation through intact rock is analyzed under plane strain conditions. Problem symmetry allows modeling half of the plane strain domain. Subsequently, a natural fracture with a length of 2.5 m located at 2.5 m of the injection point is included to study its impact on hydraulic fracture propagation. The surface is assumed frictional and non-cohesive, with a friction coefficient of 0.60 and a dilation angle of 7.75°. Different intercepting angles (30°, 60°, 90°) of the hydraulic fracture with the natural fracture are studied. Figure 4.1 shows the adopted geometry, boundary conditions, and finite element mesh. The initial mesh is well balanced in terms of mesh size. Furthermore, we use unstructured meshes based on Voronoi and Delaunay triangulation discretization to reduce bias on fracture propagation. Hydraulic fracture propagation is triggered by the injection of a Newtonian incompressible fluid at the fracture mouth at a constant rate Q_o = 5E-4 m^2/s. The 60×45 m^2 domain is under an isotropic compressive stress state σ'_o. Table 4.1 lists the rock parameters used in the numerical models.

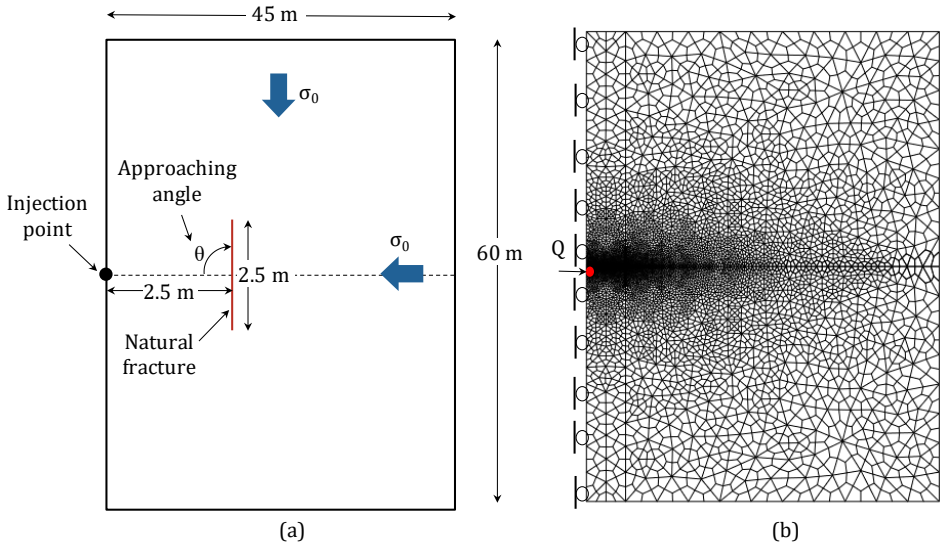

Figure 4.1. Schematic model representation: (a) geometry and dimensions; (b) boundary conditions and finite element mesh.

Table 4.1. Intact rock, fracture, and pumping parameters for the numerical tests

Categories	Variables	Units	Values
Rock	Young's modulus, E	GPa	17
	Poisson's coefficient, υ	-	0.2
	Biot coefficient, α	-	0.75
	Biot modulus, M	MPa	68.7
	Porosity, n_m	%	20
	Tensile strength, σ_n^0	MPa	1.25
Hydraulic fracture	Fracture energy, G^c	kN/m	0.12
	Stiffness $k_n = k_s$	GPa/mm	170
Natural fracture	Friction angle, ϕ	º	31
	Stiffness $k_n = k_s$	GPa/mm	1.7
Pumping parameters	Injection rate, Q_0	m²/s	5.00E-04

4.1.2. Storage-toughness-dominated regime

A first simulation is performed considering an initial compressive stress $\sigma'_o = -3.7$ MPa, fluid viscosity $\mu = 0.0001$ Pa.s, rock permeability $k = 10^{-16}$ m², and injection time t = 7 s. With these parameters, the dimensionless toughness, $\mathcal{K}$ = 2.89, viscosity $\mathcal{M} = 1.42 \times 10^{-2}$, and leak-off $\mathcal{C} = 0.19$ (see section 3.2.6), ensure that fracture propagation stays in the storage-toughness regime. Figure 4.2 displays (a) net fluid injection pressure $(p_f + \sigma'_o)$, (b) aperture at the fracture mouth, and (c) predicted fracture length along the time. In general, it is observed a good agreement between numerical and analytical solutions. For the net fluid injection pressure, Figure 4.2a, a small deviation from the analytical solution is observed in both numerical approaches. These differences can be related to hydromechanical coupling within the porous media that is taken into account in the numerical models and not in the analytical solution. This hydromechanical effect can alter the response of the system, generating the so-called back stress effect. This phenomenon is attributed to fluid leakage through the fracture faces, which increases the fluid pressure in the formation and generates additional compressional effective stresses (KOVALYSHEN, 2010; VANDAMME; ROEGIERS, 1990).

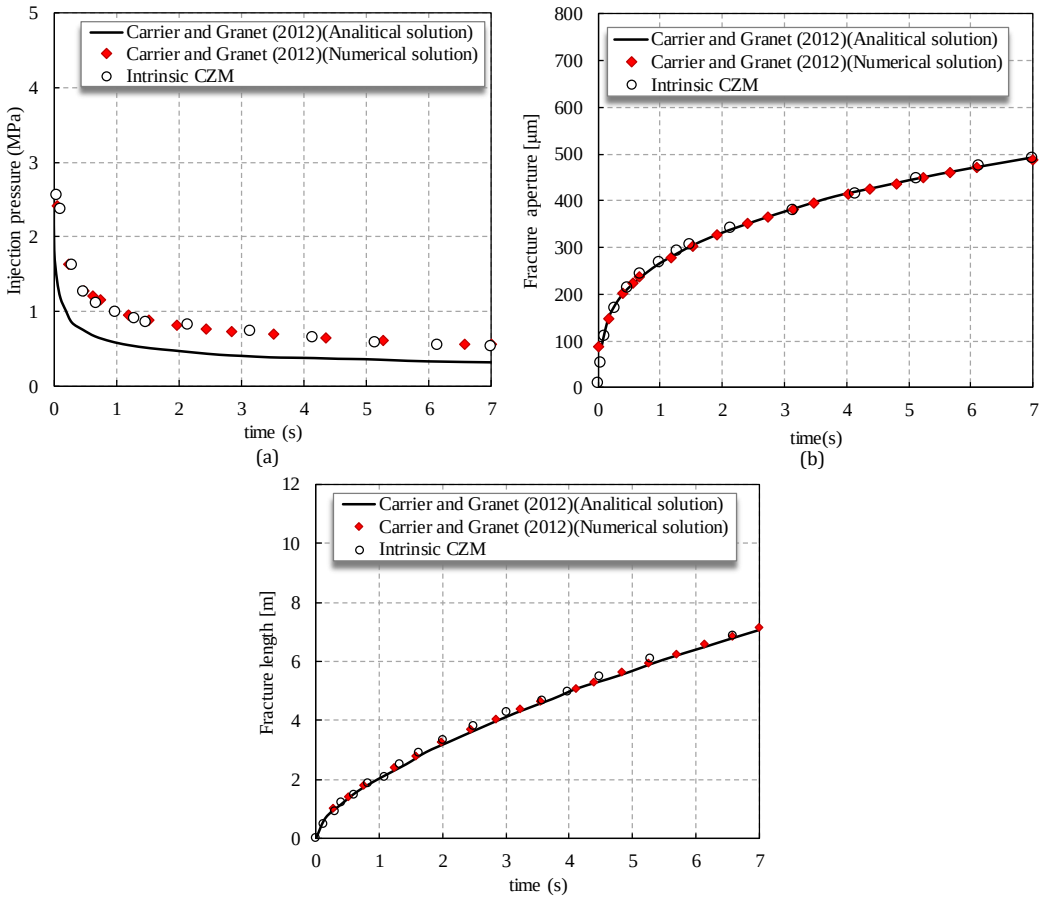

Figure 4.2. Comparison between the intrinsic CZM against the analytical (Near-K) and numerical results reported by (CARRIER; GRANET, 2012): (a) injection net pressure, (b) fracture mouth aperture, and (c) fracture length.

Next, we study the impact of a natural fracture (NF) with different interception angles (30°, 60°, 90°). Figure 4.3 shows that the hydraulic fracture (HF) dilates the NF in all cases. For the storage-toughness-dominated regime, the interaction between induced and natural fractures (NFs) is demonstrated by the pore pressure distribution for different times (1.5, 2.5, and 7 s). It shows that (i) the hydraulic fracture intercepts the natural fracture at 1.5 s, (ii) the injected fluid reaches the tip of the natural fracture at 2.0 s, and finally (iii) the hydraulic fracture propagates from the tip of the natural fracture following the most favorable direction. For approach angles 30° and 60°, the HF partially dilates the natural fracture. In these cases, the upper segment of the natural fracture is compressed due to changes in the stress field induced by the hydraulic fracture. On the other hand, for the intercepting angle of 90°, the hydraulic fracture branches into the natural fracture.

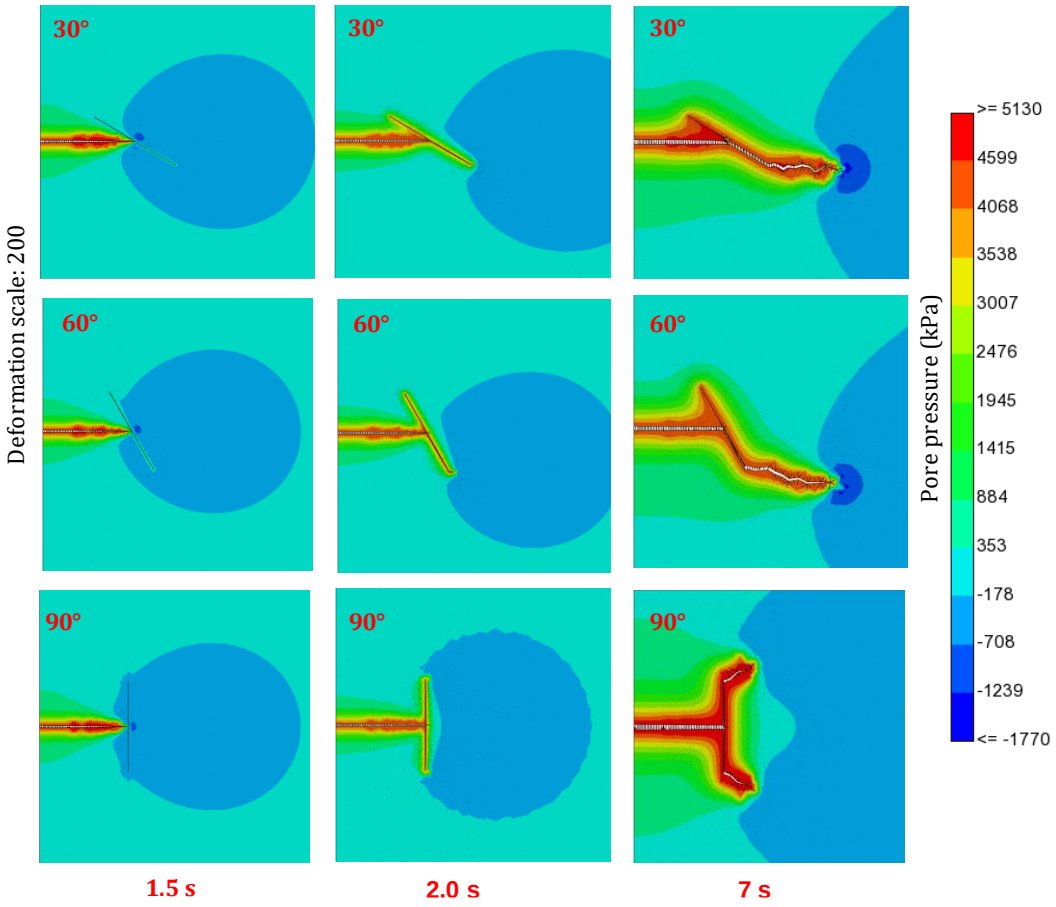

Figure 4.3. Fracture propagation processes in the storage-toughness-dominated regime for different angles of approach (30°, 60°, 90°).

Figure 4.4 shows fluid pressure and the normal stress along the path formed by points A-B-C when the HF meets the NF. It can be noticed that the pore pressure is uniform along the fracture. This effect is directly related to the low viscosity of the injected fluid. In this case, the fluid pressure is higher than the normal stress of the natural fracture inducing its opening. Figure 4.5 shows the fracture profile at 1.5, 2.0, 7.0 s in the storage-toughness-dominated regime for different approach angles (30°, 60°, 90°).

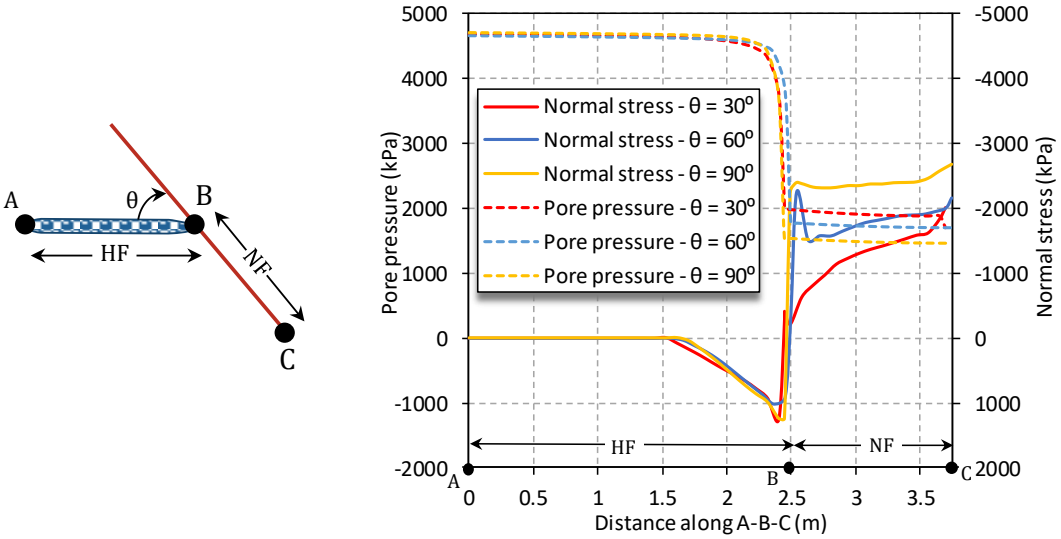

Figure 4.4. Pore pressure and normal stress along the path A-B-C when the hydraulic fracture intercepts the natural fracture (t = 1.5 s)

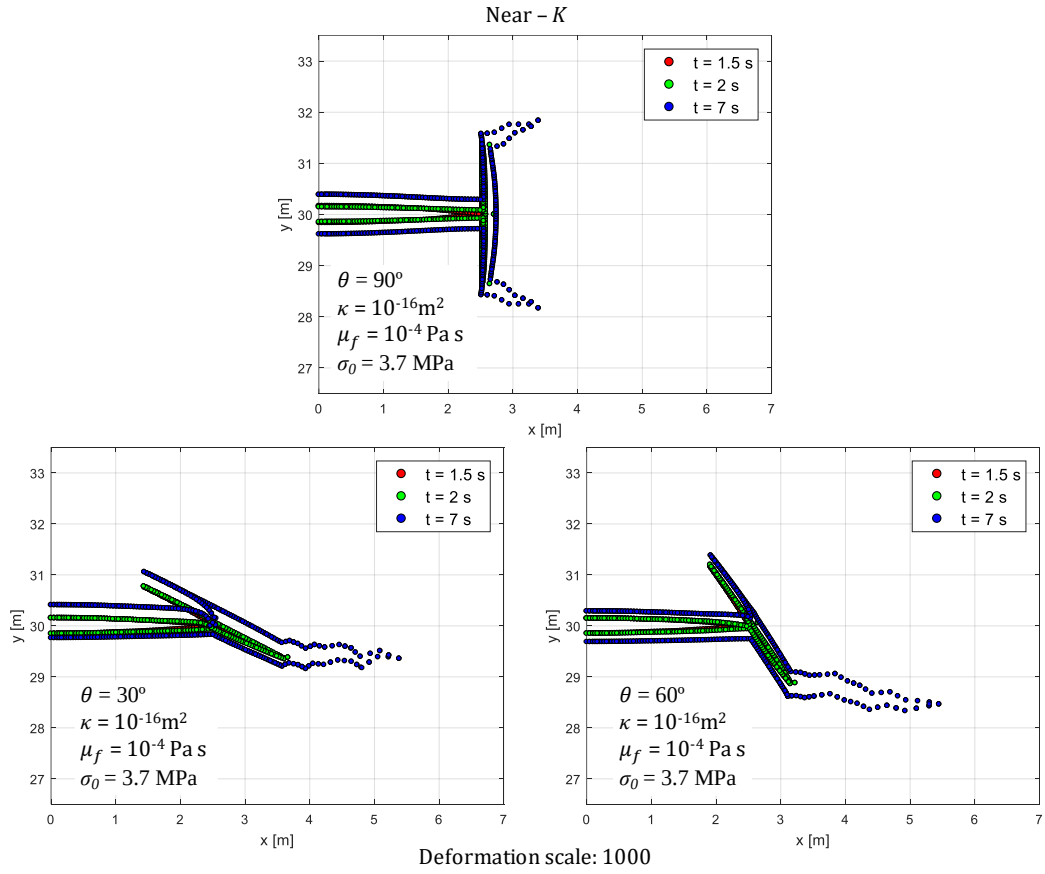

Figure 4.5. Fracture profile at 1.5, 2.0, 7.0 s in storage-toughness dominated regime for different angles of approach (30°, 60°, 90°).

Figure 4.6 shows (a) fluid injection pressure and (b) fracture aperture along the time. It indicates a slight difference in the results until the injected fluid reaches the tip of the natural fracture at 2.0 s. Subsequently, the net pressure increases

until it reaches the required pressure to propagate from the tip of the natural fracture into the rock formation (Figure 4.6a). For the intercepting angle of 90°, the pressure increment is higher because the HF branches into the NF. This pressure increment is directly reflected in the aperture of the crack mouth (Figure 4.6b).

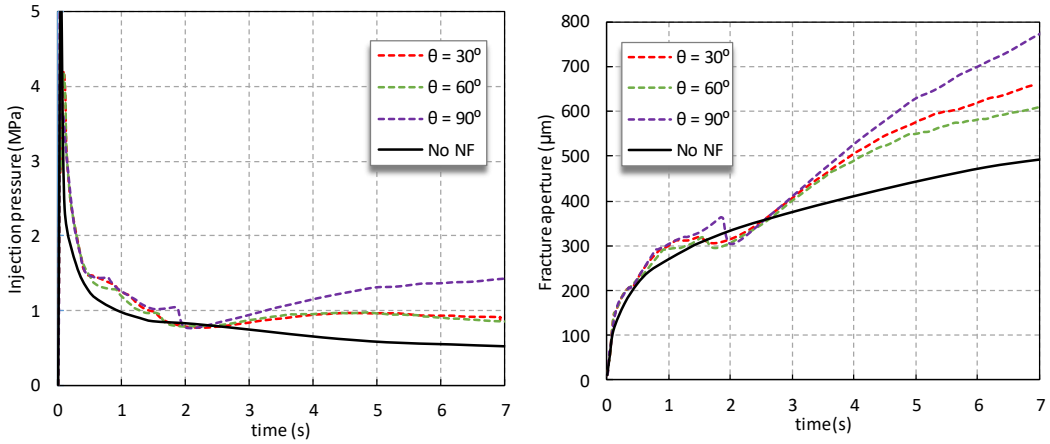

Figure 4.6. Injection net pressure (a) and fracture aperture (b).

4.1.3. Storage-viscosity-dominated regime

In this case, the simulation is performed considering an initial compressive stress $\sigma'_o = -3.7$ MPa, viscosity $\mu = 0.1$ Pa s, rock permeability $k = 10^{-15}$ m^2 and injection time t = 15 s. The parameter values, dimensionless toughness $\mathcal{K}$=0.51, viscosity $\mathcal{M} = 14.22$, and leak-off $\mathcal{C} = 0.0068$, ensure that fracture propagation stays in the storage-viscosity regime. Figure 4.7 displays (a) the net fluid injection pressure$\left(p_f + \sigma'_o\right)$, (b) the aperture at the fracture mouth, and (c) the predicted fracture length along the time. Excellent agreement is obtained between CZM and numerical results reported by (CARRIER; GRANET, 2012) for the storage-viscosity-dominated regime. The differences between the numerical and analytical results can be related to solid-fluid matrix hydromechanical coupling and the so-called back stress effect, as discussed in section 4.1.2.

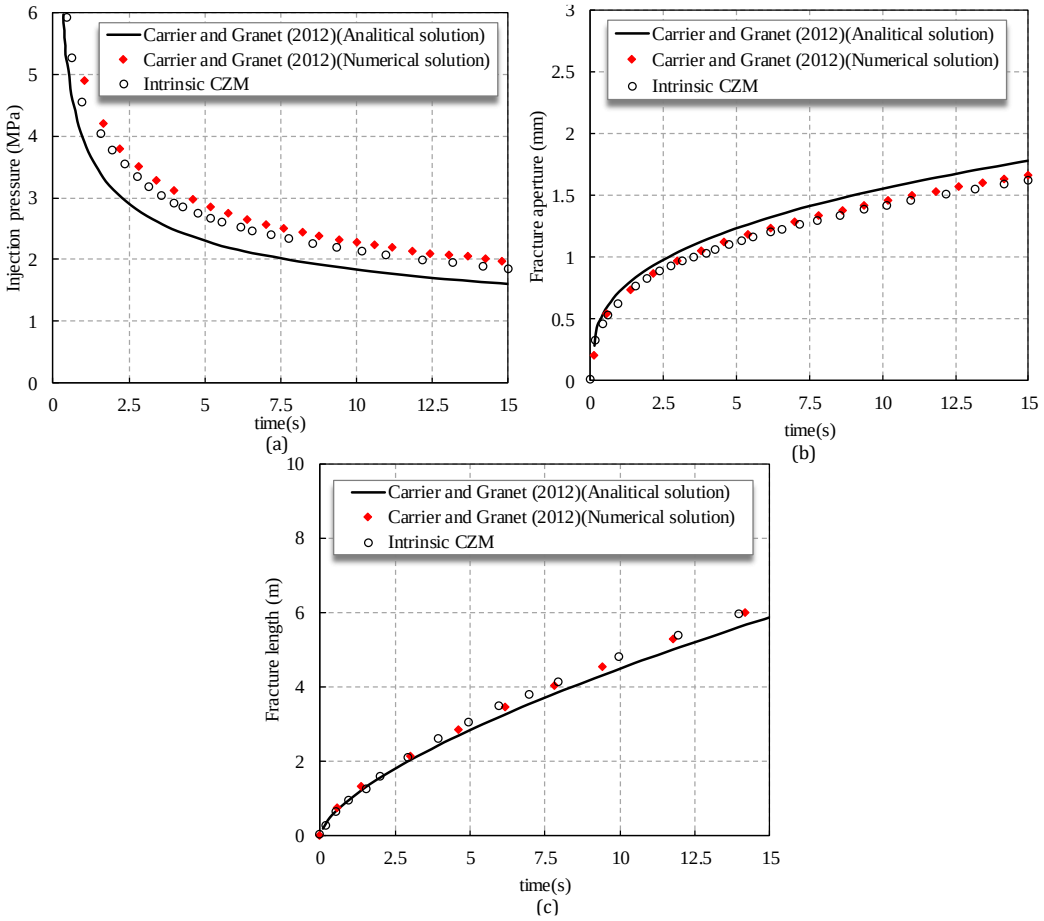

Figure 4.7. Comparison between the intrinsic CZM against analytical (Near-M) and numerical results reported by (CARRIER; GRANET, 2012): (a) injection net pressure, (b) fracture mouth aperture, and (c) fracture length.

For the storage-viscosity-dominated regime, the interaction between hydraulic fracture and natural fracture results in dilation and/or crossing (see Figure 4.8). Once again, the interaction between induced and natural fractures is demonstrated by the pore pressure distribution at different times (4.0, 6.0, and 15.0 s). In this regime, the NF undergoes mixed modes (compression and shearing) when the HF fracture approaches it (Figure 4.9). Therefore, for the intercepting angle of 30° and 60°, the HF induces shear stresses on the lower segment of the natural fracture. Consequently, the NF reaches the limit value $\tau_s/\tau_{slip} = 1$, inducing shear dilation, as shown in Figure 4.10a. On the other hand, for an angle of approach of 90°, the hydraulic fracture crosses the NF. In this case, dilation is restricted by the higher suction generated in front of the hydraulic fracture tip, which induces normal compressive stresses in the natural fracture (see Figure 4.10b). This effect is reduced for lower angles, generating special interaction cases (branching) as presented for the case of the intercepting angle of 60°. In addition,

Figure 4.10b shows that the pressure is higher at the crack mouth and lower at the tip of the hydraulic fracture.

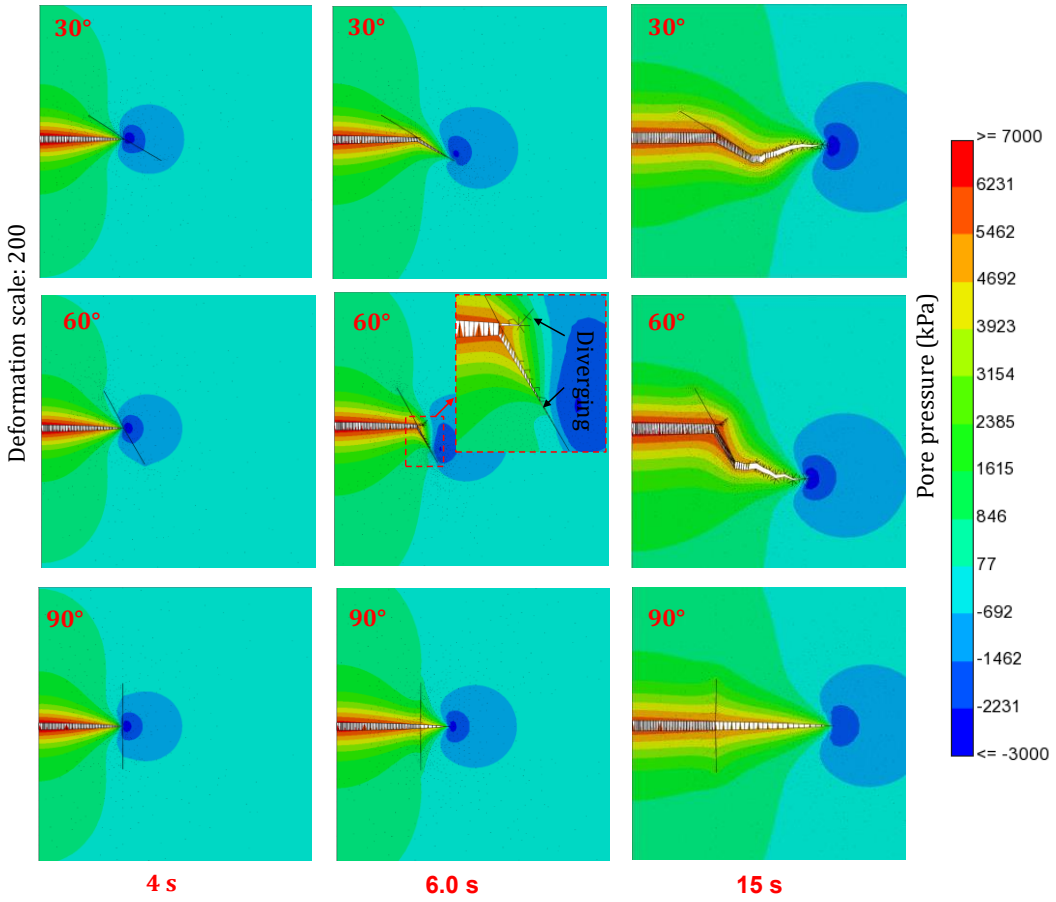

Figure 4.8. Fracture propagation process in the storage-viscosity-dominated regime for different angles of approach (30°, 60°, 90°).

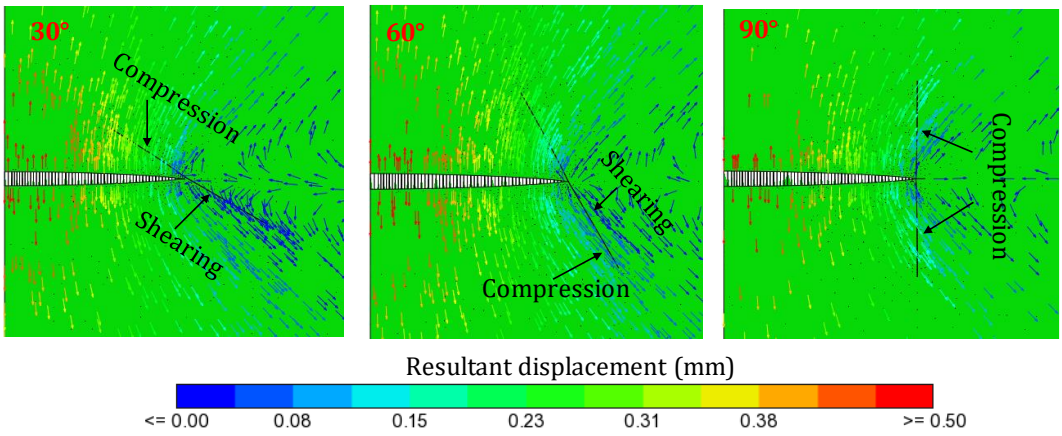

Figure 4.9. Displacement field for angles of approach (30°, 60°, 90°) when the HF intercepts the NF.

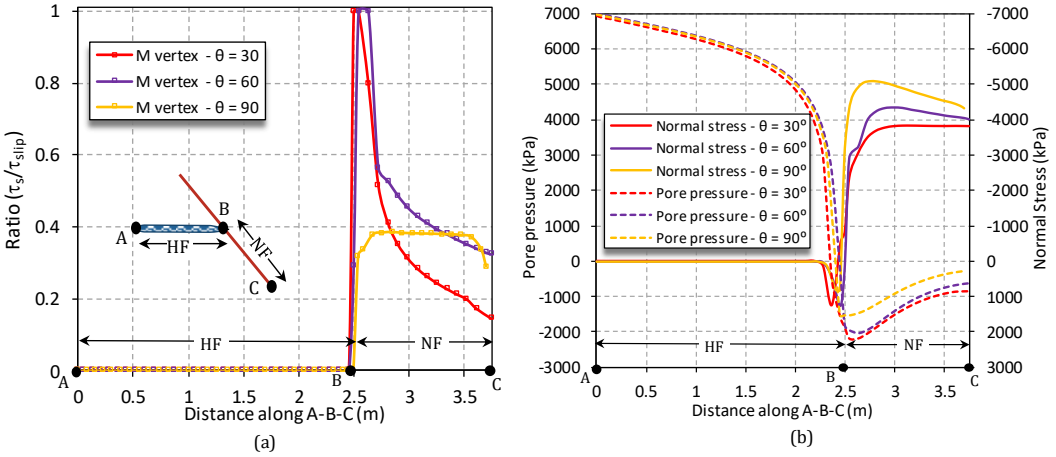

Figure 4.10. The ratio between shear stress τ_s and shear slip τ_{slip} on the fracture surface (a) , and pore pressure and normal stress along path A-B-C when the HF intercepts the NF (t = 4 s) (b)

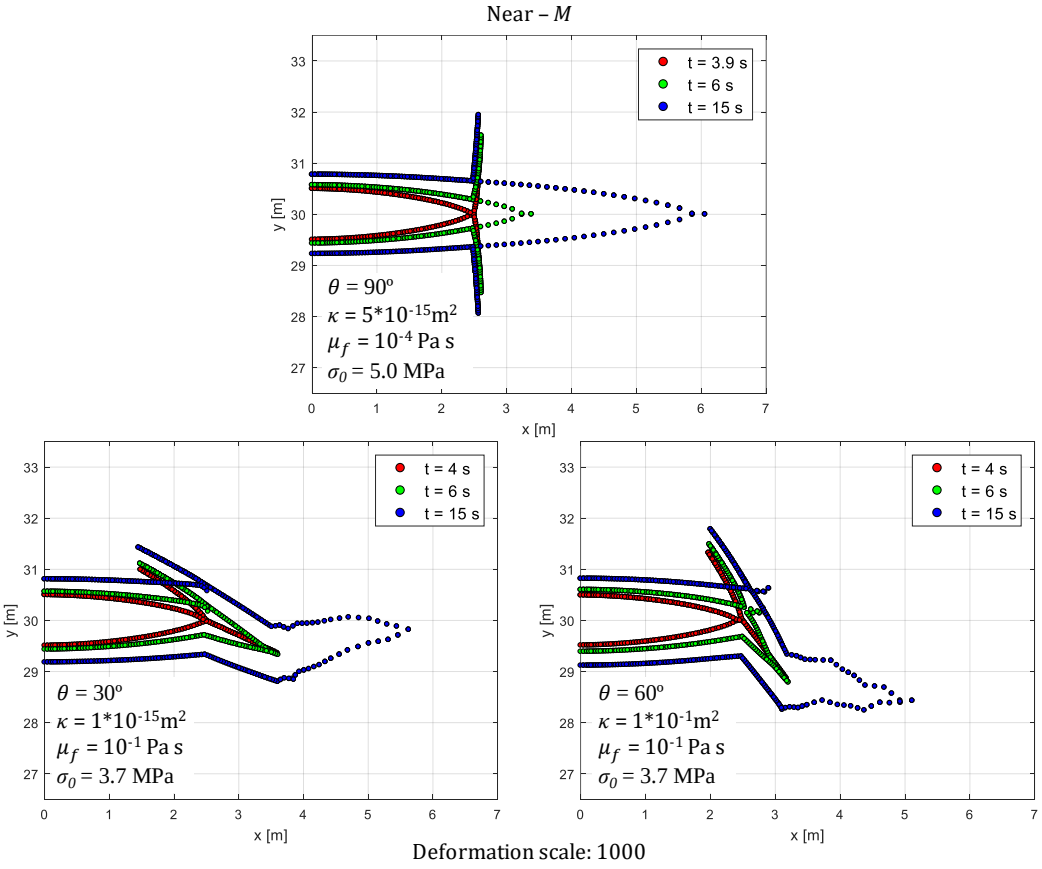

Figure 4.11. Fracture profile in storage-viscosity dominated regime for different angles of approach (30°, 60°, 90°).

Figure 4.11 shows the fracture profile at 4.0, 6.0, 15.0 s in a storage-viscosity-dominated regime for different angles of approach (30°, 60°, 90°). Figure 4.12 shows fluid injection pressure (a) and fracture aperture along the time (b). In this case, the effect of the natural fracture on pressure and aperture variations is lower. Notice that the pressure for the intercepting angle of 60° increases after the

HF propagates from the NF tip. This behavior can be attributed to stress shadowing effects. This event is directly reflected in the aperture of the HF, as shown in Figure 4.12b.

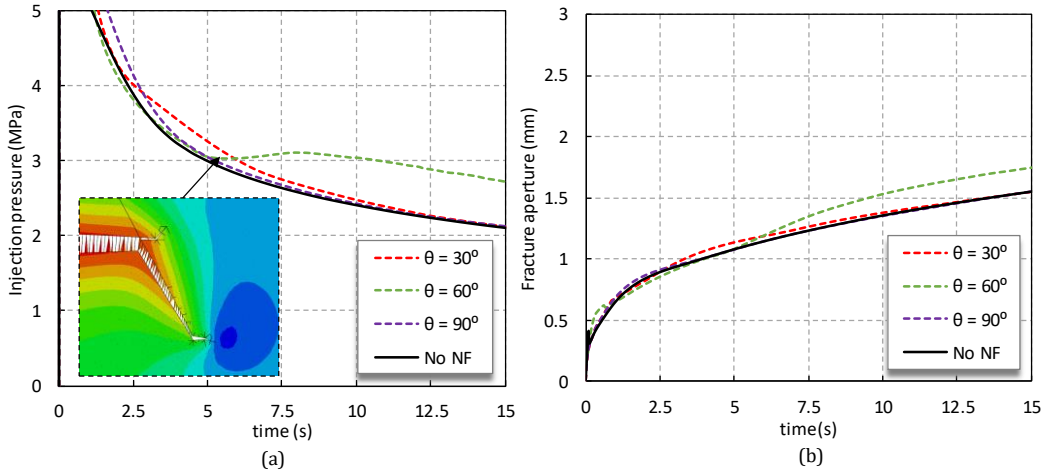

Figure 4.12. Injection net pressure (a) and fracture aperture (b) in the storage-viscosity-dominated regime.

4.1.4. Leak-off-toughness-dominated regime

In this scenario, the simulations are performed considering an initial compressive stress $\sigma'_o = -5$ MPa, fluid viscosity $\mu = 0.0001$ Pa.s, rock permeability $k = 5 * 10^{-15}$ m^2 and t = 100 s. With these parameters, the dimensionless toughness $\mathcal{K}$=2.89, viscosity $\mathcal{M} = 1.42 \times 10^{-2}$ and leak-off $\mathcal{C} = 2.83$, fracture propagation reaches the leak-toughness regime. Figure 4.13 displays (a) the aperture at the fracture mouth and (b) the predicted fracture length along the time. It is observed excellent agreement between both numerical approaches (i.e., (CARRIER; GRANET, 2012) and Intrinsic CZM). On the other hand, the numerical results show greater differences against the analytical (Near - K̃) solution. It is evident that the effect of bidimensional leak-off on solid-fluid matrix hydromechanical coupling is more significant.

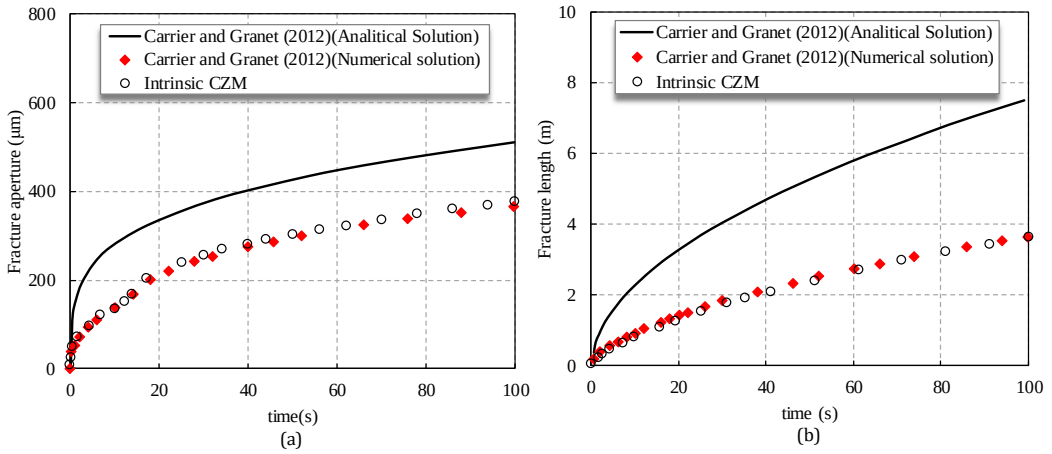

Figure 4.13. Comparison between the intrinsic CZM against the analytical (Near - K̃) and numerical results reported by (CARRIER; GRANET, 2012): (a) fracture mouth aperture and (b) fracture length.

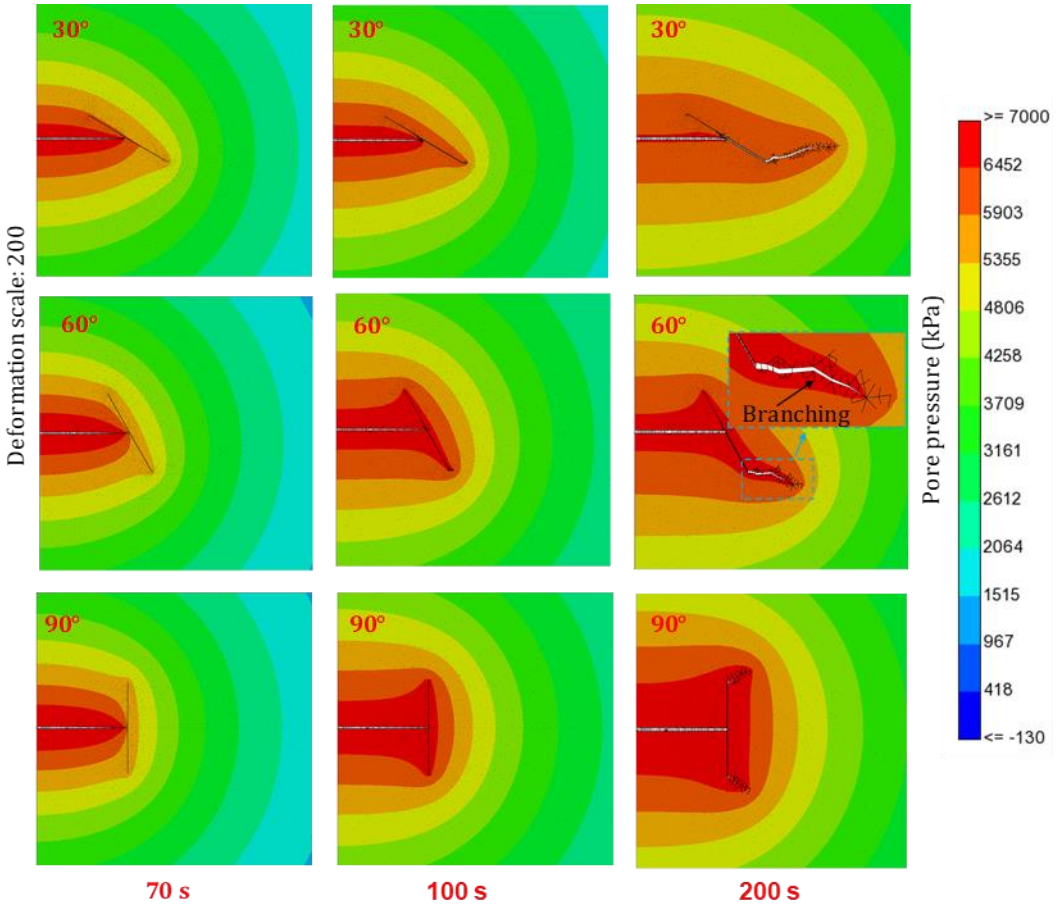

Figure 4.14. Fracture propagation processes in leak-off-toughness dominated regime for different angles of approach (30°, 60°, 90°).

Figure 4.14 shows the interaction between hydraulic and natural fractures for different interception angles (30°, 60°, 90°) in the leak-off-toughness-dominated regime. In all cases, the HF dilates the NFs. This behavior is similar to those obtained in the storage-toughness-dominated regime. The interaction between

induced and natural fractures is demonstrated again by the pore pressure distribution for different times (70, 100, and 200 s). It seems that (i) the hydraulic fracture intercepts the natural fracture at 70 s, (ii) the injected fluid reaches the tip of the natural fracture at 100 s, and finally (iii) the hydraulic fracture propagates again from the tip of the natural fracture into the rock formation. For the angle of approach of 60°, branching from the dominant hydraulic fracture occurs. However, the growth of these branches is inhibited by the fact that the HF forces them to propagate towards an unfavorable direction (stress shadowing).

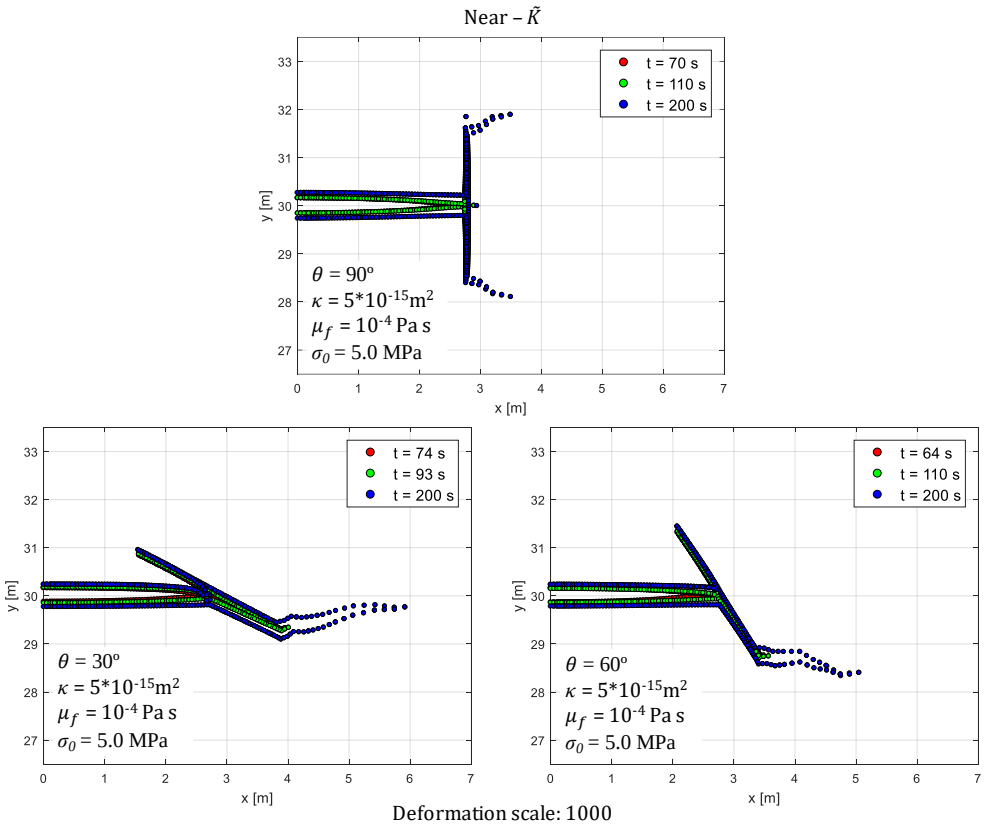

Figure 4.15. Fracture profile in leak-off-toughness dominated regime for different angles of approach (30°, 60°, 90°).

Figure 4.15 shows the fracture profile in the leak-off-toughness-dominated regime for different angles of approach (30°, 60°, 90°). Compared to the previous two cases, as expected, fracture width is smaller due to higher confinement and, consequently, higher fluid leak-off. Figure 4.16 shows fluid injection pressure (a) and fracture aperture along the time (b). High variation of pressure and fracture aperture along the time are present. These variations are directly related to the low viscosity of the injected fluid.

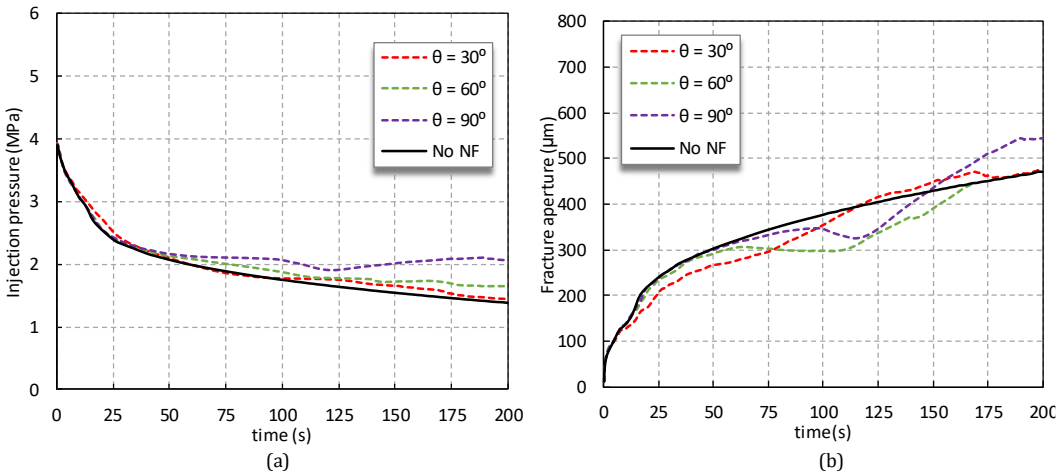

Figure 4.16. Injection net pressure (a) and fracture aperture (b).

4.1.5. Leak-off-viscosity-dominated regime

Finally, the simulation is performed considering an initial compressive stress σ'_o = -7.2 MPa, viscosity μ = 0.1 Pa s, rock permeability $k = 5 * 10^{-12}$ m^2 and injection time t = 200 s. With these parameters, dimensionless toughness $\mathcal{K}$=0.51, viscosity $\mathcal{M}$ = 14.22 and leak-off $\mathcal{C}$ = 1.45, fracture propagation reaches the leak-off-viscosity regime. Figure 4.17 displays (a) the net fluid injection pressure$\left(p_f + \sigma_o\right)$, (b) the aperture at the fracture mouth, and (c) the predicted fracture length along the time. Good agreement is present between CZM and numerical results reported by (CARRIER; GRANET, 2012) for the leak-off-viscosity-dominated regime. On the other hand, in comparison with the analytical (Near–M̃) solution, higher confinement and fluid leak-off appear to enhance the hydromechanical coupling effects, as discussed above. $\mathcal{K}$ = 2.89, viscosity $\mathcal{M}$

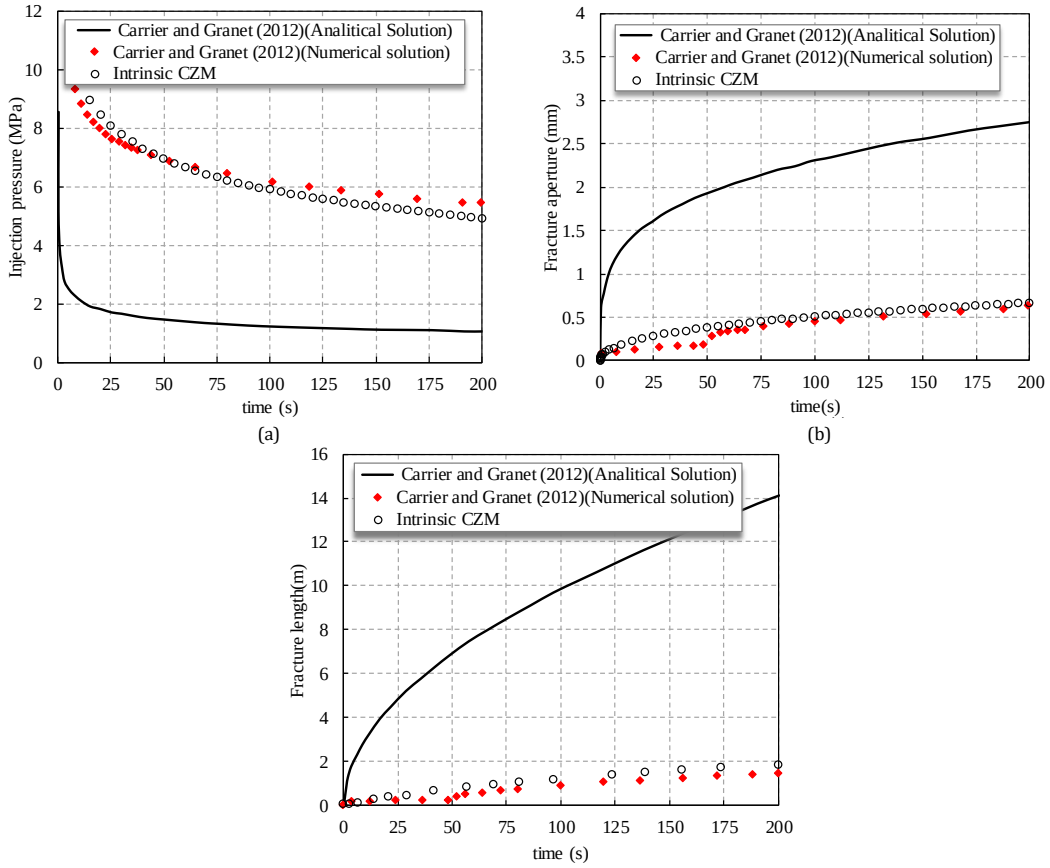

Figure 4.17. Comparison between the intrinsic CZM against the analytical (Near – M̃) and numerical results reported by (CARRIER; GRANET, 2012): (a) injection net pressure, (b) fracture mouth aperture, and (c) fracture length.

For the leak-off-viscosity-dominated regime, the interaction between the HF and the NF results in dilation and/or crossing (Figure 4.18). The pore pressure distribution at different times (300, 380, and 620 s) demonstrates this interaction. For the intercepting angle of 30° and 60°, the HF induces shear stresses on the lower segment of the NF. Moreover, compressional stresses arise at the NF when the HF approaches it. Consequently, shear displacements and stress concentration result in offset crossing of the hydraulic fracture. On the other hand, for an angle of approach of 90°, the HF crosses the NF. This behavior can be related to initial NF aperture and friction (ZHOU et al., 2008). Also, the normal compressive stresses on the natural fracture plane are higher than the fluid pressure of the HF tip.

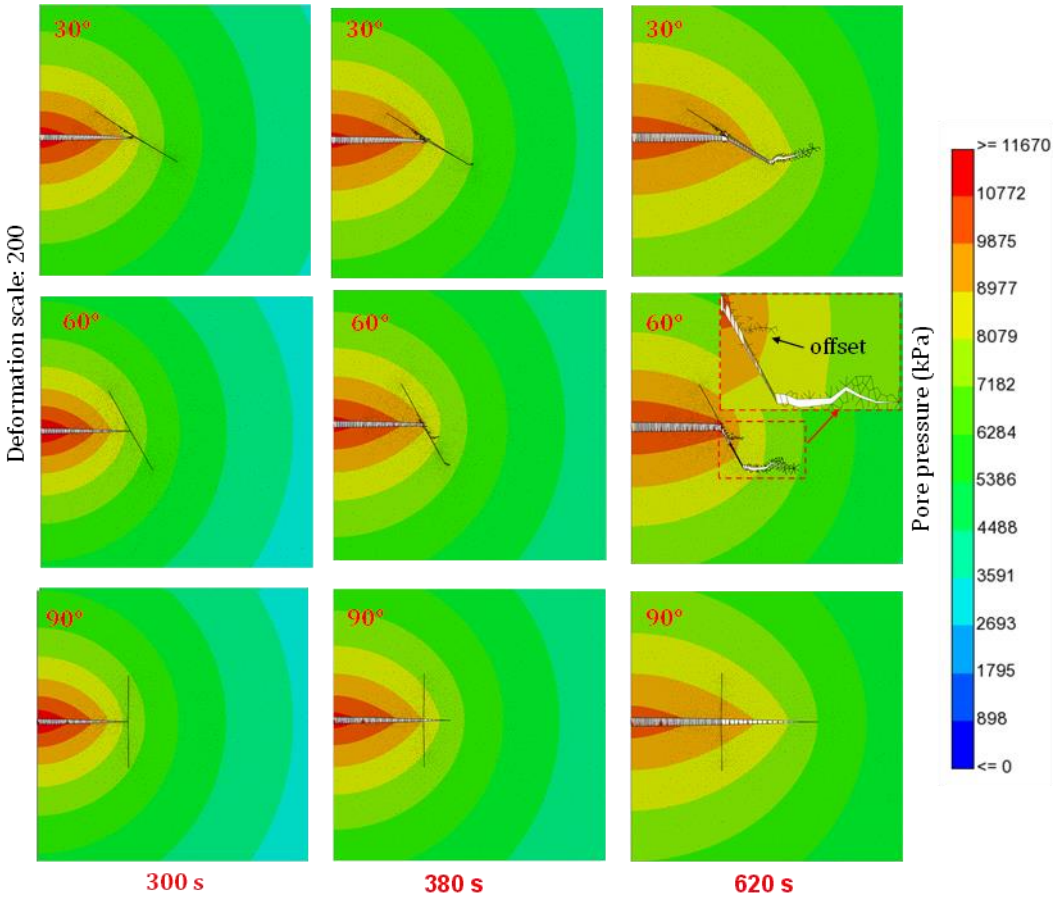

Figure 4.18. Fracture propagation processes in the leak-off-viscosity-dominated regime for different angles of approach (30°, 60°, 90°).

Figure 4.19 shows the fracture profile in the leak-off-viscosity-dominated regime for different angles of approach (30°, 60°, 90°). Figure 4.20 (a) shows fluid injection pressure and (b) fracture aperture along the time. Compared to the previous cases, it presents a low variation of net pressure and the fracture aperture along the time due to the high fluid viscosity and in-situ stress confinement.

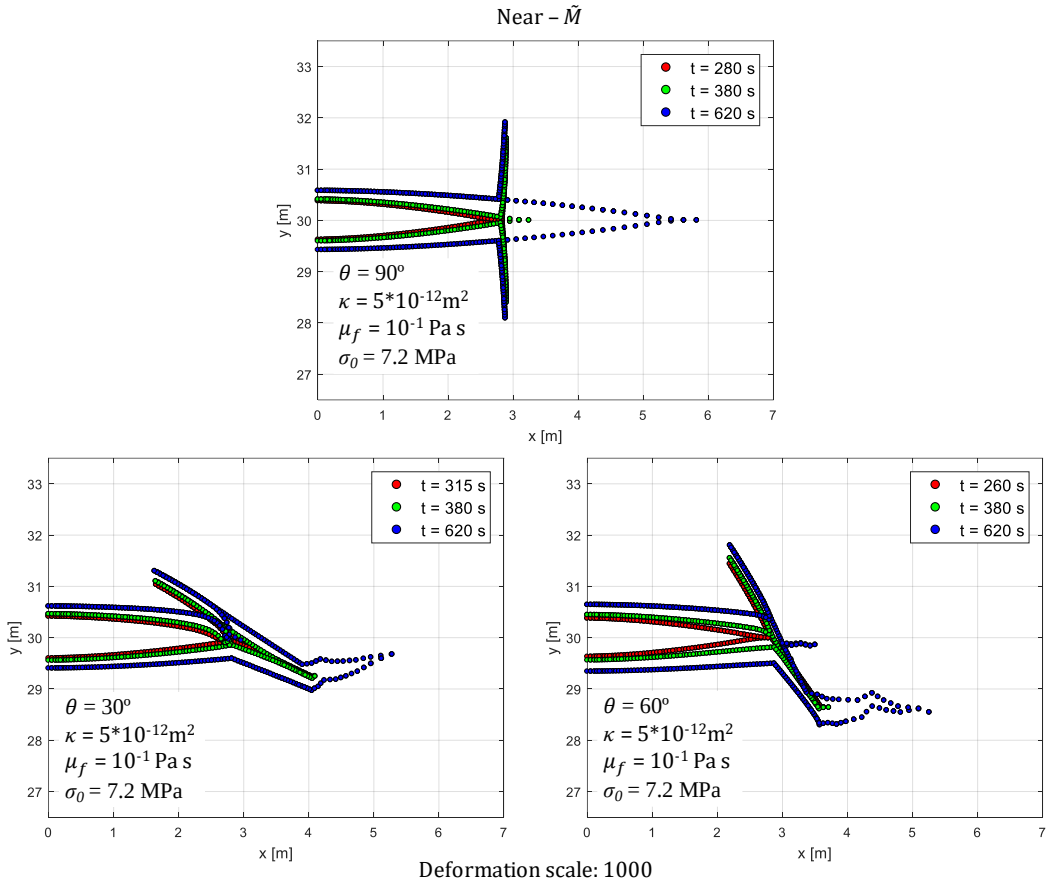

Figure 4.19. Fracture profile in the leak-off-viscosity-dominated regime for different angles of approach (30°, 60°, 90°).

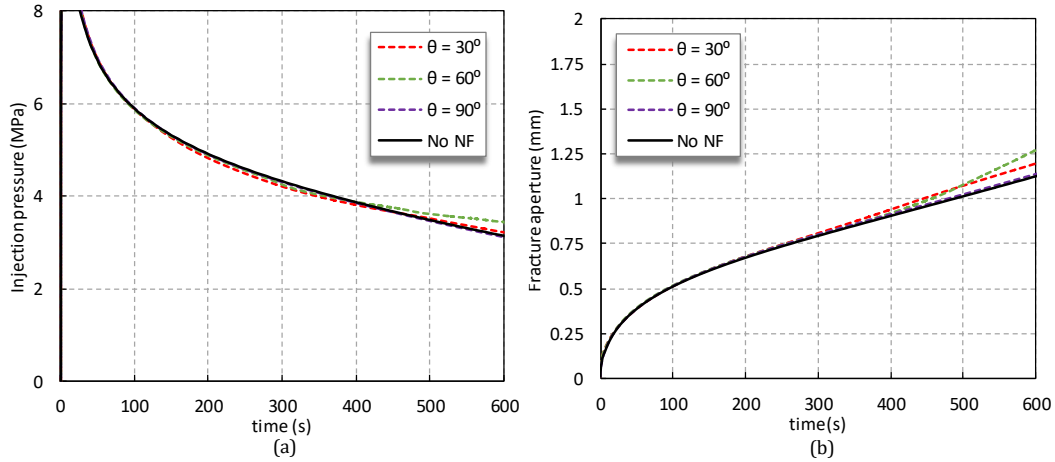

Figure 4.20. Injection net pressure (a) and fracture aperture (b) for different angles of approach (30°, 60°, 90°).

4.2.
Interaction between hydraulic and natural fractures

Fracture interaction is one of the most relevant issues to consider in the management of naturally fractured reservoirs. This problem includes the interaction between hydraulic fractures (HF) and natural fractures (NF) as well as the interaction among themselves. To study the effect of the NF orientation and horizontal stress contrast on hydraulic fracture propagation, (BLANTON, 1982, 1986) performed a group of hydraulic fracturing experiments in the laboratory. Hydrostone blocks of 30 cm x 30 cm were fabricated with a vertical pre-fracture oriented at different intercepting angles (30°, 45°, 60°, 90°) and subject to different triaxial compressive stresses. After that, fluid was injected to propagate the hydraulic fracture. Figure 4.21 shows the geometry, the in-situ stresses, and the natural fracture. Table 4.2 presents the experimental conditions and interaction types identified in the tests. The pre-fractured surface is frictional and non-cohesive, with a friction coefficient of 0.75. The tensile strength of the hydrostone is 3.1 MPa; Young's Modulus is 1e+07 kPa; Poisson's ratio is 0.2, and the fracture energy is 0.1 kN/m. The fracturing fluid is injected at a constant flow rate of 8.20e-07 m^3/s.

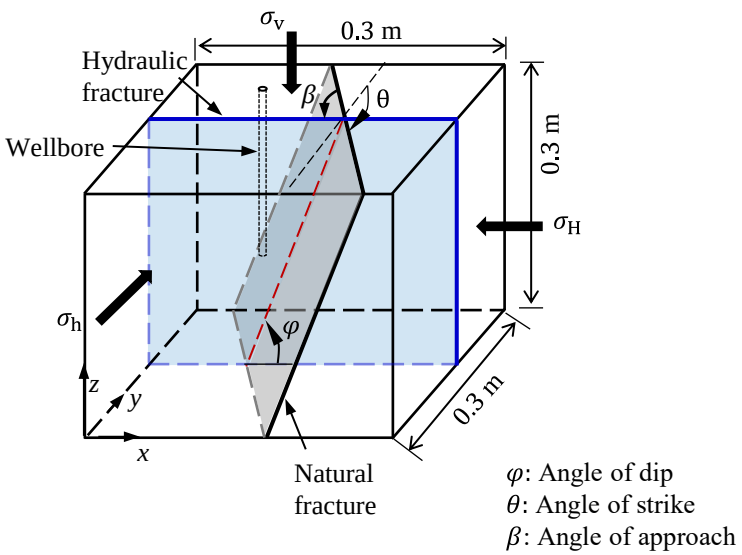

Figure 4.21. Schematic representation of the testing block geometry, in-situ stresses and, hydraulic and natural fractures (BLANTON, 1982).

The fluid viscosity used in these experiments is not specified in the reference. In this work, the fluid is assumed to be water. The behavior of the NF is governed by the Coulomb friction criterion with a zero tensile cut-off. It is assumed that the plastic response of NF is limited to shear only. That corresponds to a non-dilatant

(ψ = 0; plastically volume-preserving) material. Table 4.3 provides the hydraulic and mechanical properties for rock, natural fracture, hydraulic fracture, and fluid flow used in the numerical model. Hexahedron elements discretize the rock formation while triple-noded zero-thickness interface elements represent the hydraulic and natural fractures.

Table 4.2. Experimental condition and results for hydraulic fracture experiments on Hydrostone (BLANTON, 1982)

Test #	Intercepting angle	Horizontal stresses (MPa)		interaction type
		σ_{Hmax}	σ_{hmin}	
CT- 7	30 °	19	10	Opening
CT- 9	30 °	20	5	Arrest
CT-11	45 °	20	5	Arrest
CT-12	45 °	18	5	Arrest
CT-13	45 °	16	5	Arrest
CT-14	45 °	14	5	Arrest
CT-22	45 °	10	5	Opening
CT- 8	60 °	20	5	Crossing
CT- 21	60 °	14	5	Arrest
CT- 4	60 °	12	10	Opening
CT- 20	90 °	14	5	Crossing

Table 4.3. Hydraulic and mechanical properties

Categories	Properties	Unit	Value
Hydrostone block	Young Modulus	GPa	10.0
	Poisson coefficient	---	0.22
	Hydraulic conductivity	m/s	9.8e-9
Hydraulic fracture	Normal strength	MPa	3.1
	Shear strengths	MPa	3.1
	Normal stiffness	MPa/m	10.0e+6
	Shear stiffness	MPa/m	10.0e+6
Natural fracture	Normal stiffness	MPa/m	10.0e+5
	Shear stiffness	MPa/m	5.0e+5
	Fracture cohesion	MPa	0.01
	Friction angle	(°)	37.0
	Dilation angle	(°)	0.0
	Cut-off	MPa	0.0
Fracturing fluid	Fluid viscosity	cp	1.0
	Injection rate	m^3/s	8.2e-8

As observed in Table 4.2, the shale block with a pre-existing fracture at an angle of approach 60° (experimental test CT 4, 21, 8) presents three different interaction types (opening, crossing, and arresting, respectively). Then, the orientation of the natural fracture is defined at the strike angle $\theta = 150º$ and dip angle $\varphi = 90º$.

As Figure 4.22 shows for CT-4, the stress ratio $(\sigma_{hmin}/\sigma_{Hmax})$ is ≅ 0.83. In this case, the natural fracture dilates because the fluid pressure in the hydraulic

fracture is larger than the normal compressive stress on the natural fracture. As Figure 4.23 shows, for the CT-8, the stress ratio ($\sigma_{hmin}/\sigma_{Hmax}$) is $= 0.25$. The hydraulic fracture crosses the natural fracture because the dilatation is restricted by the maximal horizontal stress. For CT-21, the stress ratio ($\sigma_{hmin}/\sigma_{Hmax}$) is $\cong$ 0.36. In this case, hydraulic fracture fluid leaks into the natural fracture due to slippage, then the hydraulic fracture is arrested, as shown in Figure 4.24.

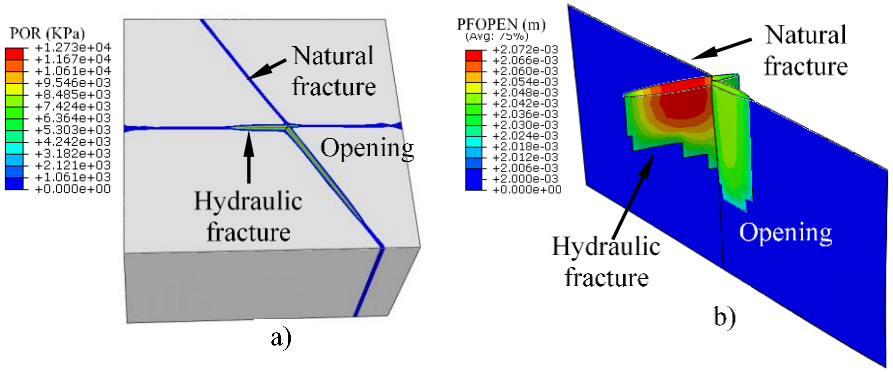

Figure 4.22. Fracture interaction for CT-4 test: a) opening of natural fracture and b) fracture geometry after opening.

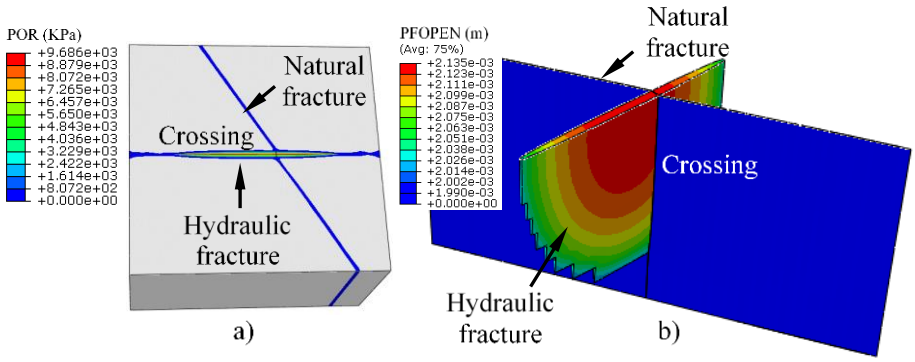

Figure 4.23. Fracture interaction for the CT-8 test: a) crossing of NF and b) hydraulic fracture geometry.

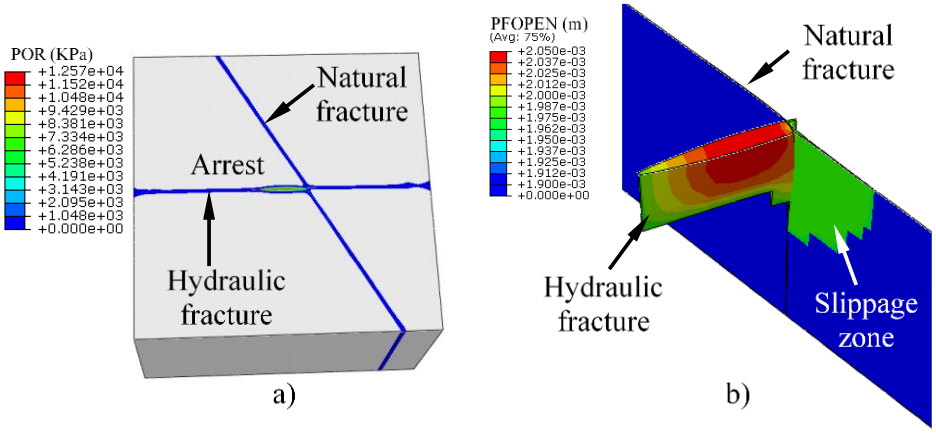

Figure 4.24. Hydraulic fracture- natural fracture interaction for the test (BLANTON, 1982) (CT-11) and intrinsic CZM fragmentation approach.

. Prediction of the experimental behavior of the shale blocks with a pre-existing fracture oriented at 30° (CT-7, CT-9), 45° (CT-11, CT-12, CT13, CT-14), 60° (CT 4, 8, 21) and at 90° (CT-20) is also achieved.

4.2.1.1. The effect of natural fracture orientation

In the previous results, we could identify a relation between the horizontal stress ratio ($\sigma_{hmin}/\sigma_{Hmax}$) and the type of interaction between hydraulic and natural fracture. Opening, arresting, and crossing occur following descendent stress ratio values. To confirm this hypothesis, several 2D analyses are run to identify a relation between approach angle (β), stress ratio ($\sigma_{hmin}/\sigma_{Hmax}$) and interaction type (opening, slipping, and crossing). In those analyses, we keep constant the vertical stress (σ_v = 20 MPa) and the minimum horizontal stress (σ_{hmin}= 5 MPa). The maximum horizontal stress (σ_{Hmax}) varies considering a normal fault regime ($\sigma_v \geq \sigma_{Hmax} \geq \sigma_{hmin}$). Pre-existing fractures oriented at 15° and 75° are included. The obtained numerical results (pre-fractures oriented between 0° to 90° degrees) are mirrored in the 2, 3, and 4 quadrants since the model is symmetric. Subsequently, a diagram of natural fracture interaction as a function of the approach angle (β) and the stress ratio ($\sigma_{hmin}/\sigma_{Hmax}$) is developed. Figure 4.25a shows the interaction diagram when the hydraulic fracture is aligned with the zero-axis. Analyzing the first quadrant (0°– 90°), we can see that the hydraulic fracture has more chances to cross the nature fracture with an approach angle between (60°–90°). Natural fractures slip with low values of the horizontal stress ratio and with approach angle between (15°–60°). The natural fracture is more susceptible to open with high values of horizontal stress ratio and low approach angle. This tendency decreases when the approach angle increases. The results presented by (BLANTON, 1982), reproduced in Table 4.2, are plotted into the diagram and have good agreement with the proposed tendency, as shown in Figure 4.25b.

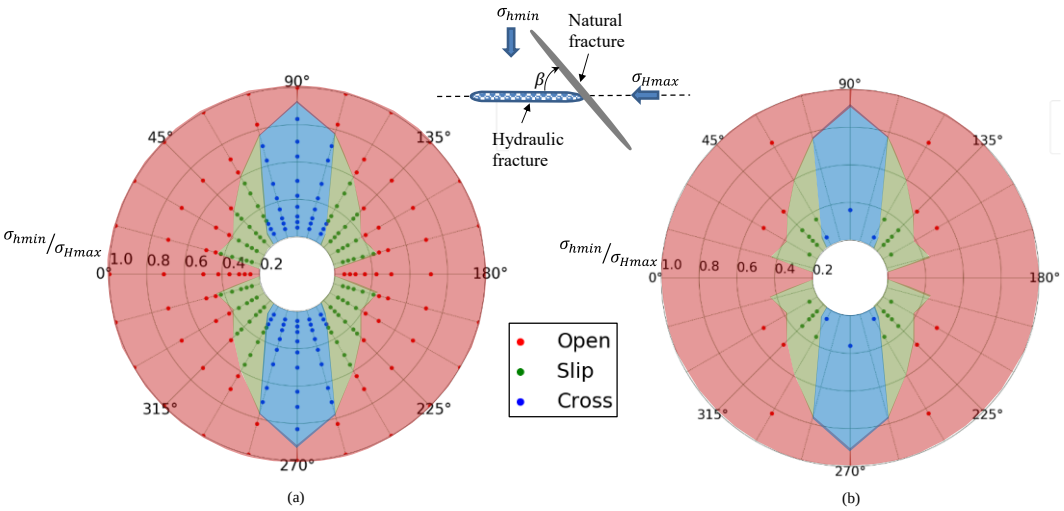

Figure 4.25. Diagram of HF/NF interaction as a function of approach angle (β) and stress ratio ($\sigma_{hmin}/\sigma_{Hmax}$): (a) numerical results; (b) experimental results (BLANTON, 1982).

The proposed diagram is now compared with two independent laboratory experiments presented by (ZHOU et al., 2008) and (GU et al., 2012). They are also performed with boreholes orthogonal to the horizontal stress direction. These experiments have been chosen by the similarity conditions (material properties, scale, and normal stress regime) with those reported by (BLANTON, 1982). The horizontal stresses and approach angles are presented in Table 4.4.

Table 4.4. Experimental condition and results for hydraulic fracture test on pre-fractured block

	Test #	Approaching angle	Horizontal stresses (MPa)		$\sigma_{hmin}/\sigma_{Hmax}$	Experimental interaction type
			σ_{Hmax}	σ_{hmin}		
(GU et al., 2012)	1	45	17.23	6.89	0.40	Turn into
	2	45	8.27	6.89	0.83	Turn into
	3	75	17.23	6.89	0.40	Crossing
	4	75	8.27	6.89	0.83	Turn into
	5	90	7.58	6.89	0.91	Turn into
	6	90	13.78	6.89	0.50	Crossing
(ZHOU et al., 2008)	2-3	30	10	5	0.50	Opening
	2-5	30	8	5	0.63	Opening
	2-7	30	13	3	0.23	Arrest
	2-8	60	8	5	0.63	Opening
	2-4	60	10	3	0.30	Crossing
	2-6	60	13	3	0.23	Crossing
	2-1	90	10	5	0.50	Crossing
	2-2	90	10	3	0.30	Crossing

From Table 4.4, the horizontal stress ratio ($\sigma_{hmin}/\sigma_{Hmax}$) is calculated in all tests and plotted into the diagram, as shown in Figure 4.26. The proposed interaction diagram correctly predicts the interaction type of the experimental data. Although these experiments have similar conditions, some parameters such as Young's modulus, injection rate, compressional stress state, and fracture

toughness are relatively different between them. Therefore, the interaction type is more influenced by the horizontal stress ratio ($\sigma_{hmin}/\sigma_{Hmax}$) and the NF and approach angles.

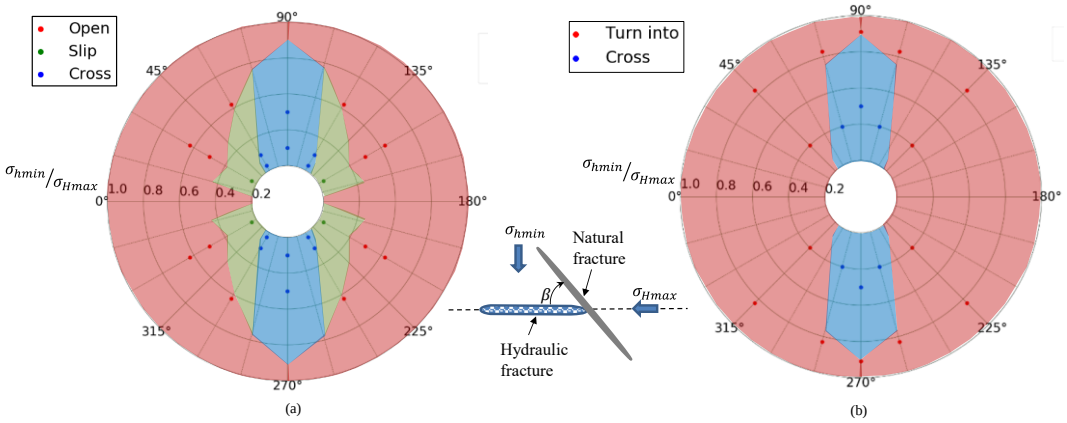

Figure 4.26. Diagram of HF/NF interaction as a function of approach angle (θ) and stress ratio ($\sigma_{hmin}/\sigma_{Hmax}$): experimental results (a) (ZHOU et al., 2008) and (b) (GU et al., 2012).

The presented interaction diagram is valid for pre-existing vertical fractures. However, in real field problems, the fracture orientation can vary in strike and dip angles and, consequently, alter the stress components on the fracture plane. These problems cannot be properly simulated in two dimensions. Therefore, the following section studies the influence of fracture orientation on the interaction of hydraulic and natural fractures.

4.2.1.2. The effect of natural fracture orientation

To study the effect of fracture orientation on the interaction between a hydraulic and a natural fracture, three Hydrostone blocks with a pre-existing natural fracture at different orientations are considered, as summarized in Table 4.5. For each model, the numerical simulations were performed under the same in-situ stresses of Blanton's tests CT-4, CT-8, and CT-21 (see Table 4.2). The analysis adopts the mechanical and hydraulic properties detailed in Table 4.3. Table 4.6 summarizes the initial normal compressive stresses σ_n on the natural fracture, estimated by equation (3.46).

Table 4.5. Natural fracture orientation.

Orientation	NF1	NF2	NF3
Strike	120º	150º	180º
Dip	60º	60º	60º

Table 4.6. Compressive stresses on the natural fracture at the beginning of the simulation.

Test #	Compressive stresses σ_n (MPa)		
	NF1	NF2	NF3
CT-4	12.87	13.62	14.0
CT-8	11.56	17.18	20.0
CT21	10.53	13.81	15.5

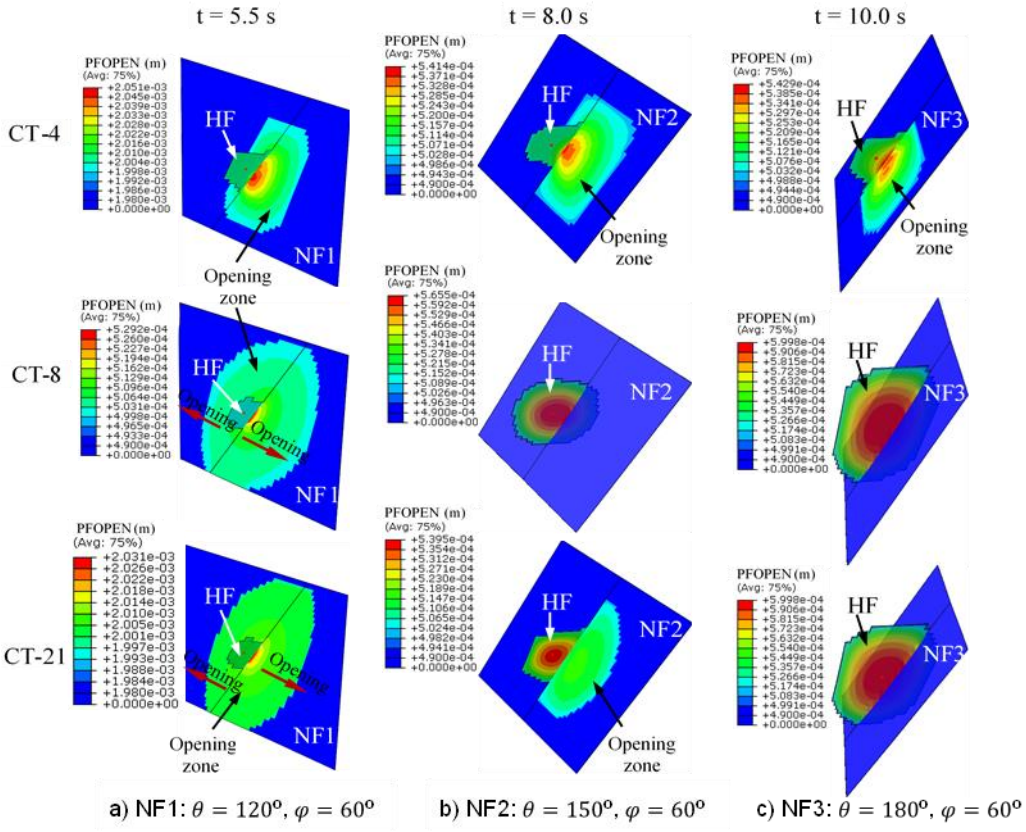

Figure 4.27. Interaction between hydraulic and natural fracture oriented at a) 120° strike, b) 150º strike, and c) 180º strike.

For the first model (NF1: dip 60º and strike 120º), the hydraulic fracture propagation opens the natural fracture NF1 under all values of in-situ stress (CT-4, CT-8 and CT-21), as shown in Figure 4.27a, first column. However, after t = 5.5 s, we can observe that the hydraulic fracture opens a small extension for CT-4 in comparison to the open extension obtained for CT-8 and CT-21. That difference in the opening extensions can be due to the differences in the initial normal stresses acting on NF1 in each case. The initial normal stress acting on NF1 (12.825 MPa) for CT-4 is higher in comparison to those obtained for CT-8 and CT-21, as summarized in the first column of Table 4.6. Therefore, for small relative angles of dip and strike between the natural and hydraulic fractures, the hydraulic fracture tends to dilate the natural fracture, increasing fluid leak-off and limiting the growth of the hydraulic fracture (Figure 4.27a).

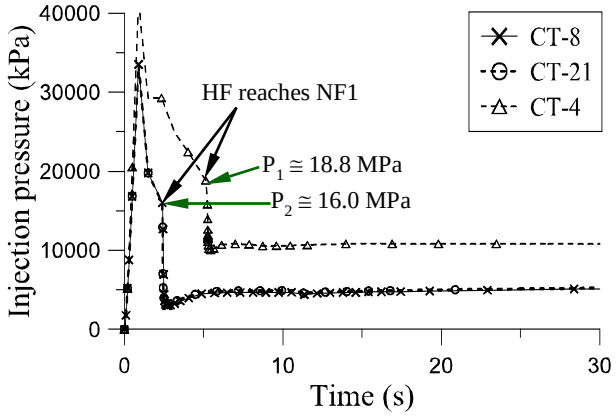

Figure 4.28. Injection pressure during the interaction between hydraulic and natural fracture NF1.

Figure 4.28 shows the borehole injection pressure when the hydraulic fracture interacts with NF1 for each in-situ stress (CT-4, CT-8, and CT-21). The injection pressure curves for CT-8 and CT-21 are identical since both tests are submitted to the same minimum horizontal stress (Sh =5 MPa), as detailed in Table 4.2. However, for CT-4 test, Figure 4.28 shows a higher injection pressure curve because the in-situ minimum horizontal stress of CT-4 is also higher (Sh= 10 MPa) in comparison to CT8 and CT-21 (Sh= 5 MPa), requiring higher fluid injection pressure to propagate the hydraulic fracture.

Figure 4.28 shows a sudden drop in the injection pressure when the hydraulic fracture opens the natural fracture, and the injection fluid flows into its channels. Under all in-situ conditions tested, the hydraulic fracture opens the natural fracture. This happens because the fluid pressure inside the hydraulic fracture (P1≅18.8 MPa for CT-4 and P2 ≅ 16 MPa for CT-8 and CT-21) is higher than the normal compressive stresses acting on the natural fracture NF1 ($\sigma_n \cong$ 12.8 MPa for CT-4, $\sigma_n \cong$ 11.5 MPa for CT-8, and $\sigma_n \cong$ 10.5 MPa for CT-21). In this scenario, NF1 opens in both directions (Figure 4.27a).

Figure 4.27b shows the interaction of the hydraulic fracture and natural fracture NF2 (dip 60º and strike 150º) after t = 8.0 s. For in-situ stresses CT-4 and CT-21, the hydraulic also opens the natural fracture NF2. While for CT-8, the hydraulic fracture propagates through the natural fracture NF2 because the normal compressive stress (17.2 MPa) on the fault plane is higher than the propagation pressure (12.3 MPa), as shown in Figure 4.29a. The hydraulic and natural fracture interaction results in crossing for a high difference in horizontal in-situ stresses and an intermediate value of relative angle (dip and strike) between hydraulic and natural fractures.

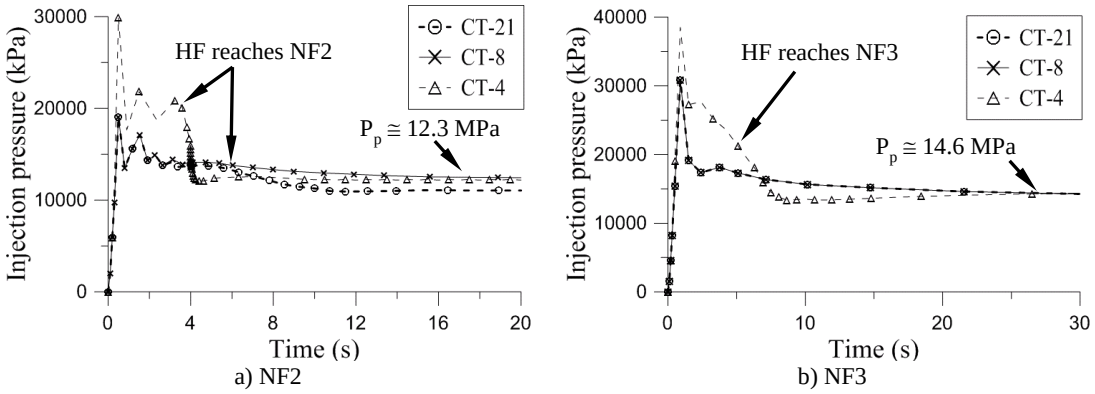

Figure 4.29. Injection pressure during hydraulic fracture interaction with a) natural fracture NF2 and b) natural fracture NF3.

For the last model (NF3: dip 60º and strike 180º), Figure 4.27c shows the interaction between the hydraulic and the natural fractures under the three in-situ stress values (CT-4, CT-8, and CT-21). For CT-8 and CT-21, the hydraulic fracture crosses natural fracture NF3 since the propagation pressure 14.6 MPa is lower than the confining normal stresses (15.5 MPa for CT-21 and 20 MPa for CT-8). Figure 4.29b shows the evolution of the injection pressure with time for these scenarios. However, NF3 opens under the in-situ stresses of CT-4 because the confining normal stress of 14.0 MPa is lower than the propagation pressure of 18.8MPa. Therefore, for a high difference of horizontal stresses and high relative angles of dip and strike between hydraulic and natural fractures, the hydraulic fracture tends to cross the natural fracture. According to the orientation of the natural fracture, reactivation may happen in both directions, as shown in Figure 4.27a. We can conclude that the fracture orientation (dip and strike) affects the results of fracture interaction (arrest, opening, and crossing), which cannot be represented correctly in a two-dimensional model.

4.2.1.3. The effect of friction angle

The friction angle is related to the shear strength of the natural fracture, affecting fracture interaction. In order to study the effect of the friction angle on fracture interaction, we adopt three values of friction angle $\phi_f = \{30, 37, 45\}$ for each natural fracture presented in the previous section (see Table 4.5). Figure 4.30 shows the interaction between the hydraulic fracture and natural fracture NF1 (dip 60º and strike 120º) for two values of friction angle ϕ_f=37º and ϕ_f=45º. We can observe the opening of natural fracture NF1 for all in-situ stresses (CT-4, CT-8, and CT-21). The opening zone obtained for ϕ_f= 37º after t = 6s is larger compared

to those obtained for ϕ_f= 45º because low friction angles flatten the Coulomb failure envelope reducing the shear strength. We also verified that NF1 fails under in-situ stress conditions for a friction angle of 30º, which considers the natural fracture open from the beginning of the analysis.

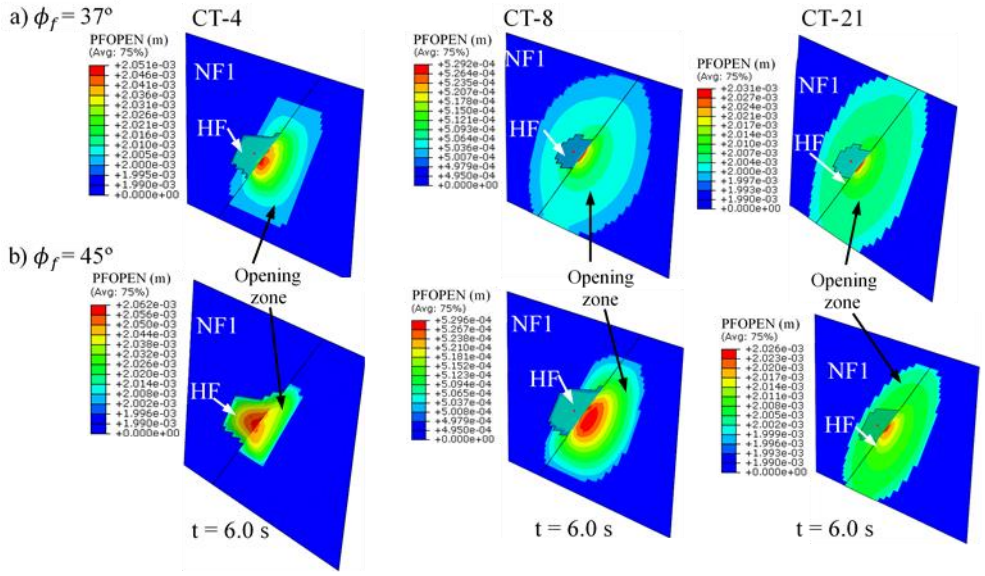

Figure 4.30. Interaction between hydraulic and natural fracture NF1 (dip 60º and strike 120º) with different values of angle of friction a) $\boldsymbol{\phi_f}$=37°, and b) $\boldsymbol{\phi_f}$=45°.

Figure 4.31 shows the effect of the friction angle in the interaction between the hydraulic fracture and NF2 (dip 60º and strike 150º) under different in-situ stresses. For a low difference of horizontal stresses (CT-4), the natural fracture reactivates, and the friction angle affects the opening area.

For a high difference of horizontal stresses (CT-8), we can observe that the hydraulic fracture propagates through the natural fracture NF2 for a lower friction angle, ϕ_f= 30º. An increment of friction angle does not affect the type of interaction (crossing) because a high friction angle increases the strength of NF2. Moreover, the injection pressure shows the same behavior as in Figure 4.32a. For an intermediate difference of horizontal stresses CT-21, NF2 with higher friction angle, ϕ_f= 45º, is crossed by the hydraulic fracture. However, reducing the friction angle, the hydraulic fracture can reactivate NF2, as shown in Figure 4.30. Figure 4.32b shows a drop in the injection pressure when the natural fracture NF2 reactivates for ϕ_f= 30º and ϕ_f= 37º. Fluid migration to the natural fracture leads to injection pressure drop, interrupting hydraulic fracture growth.

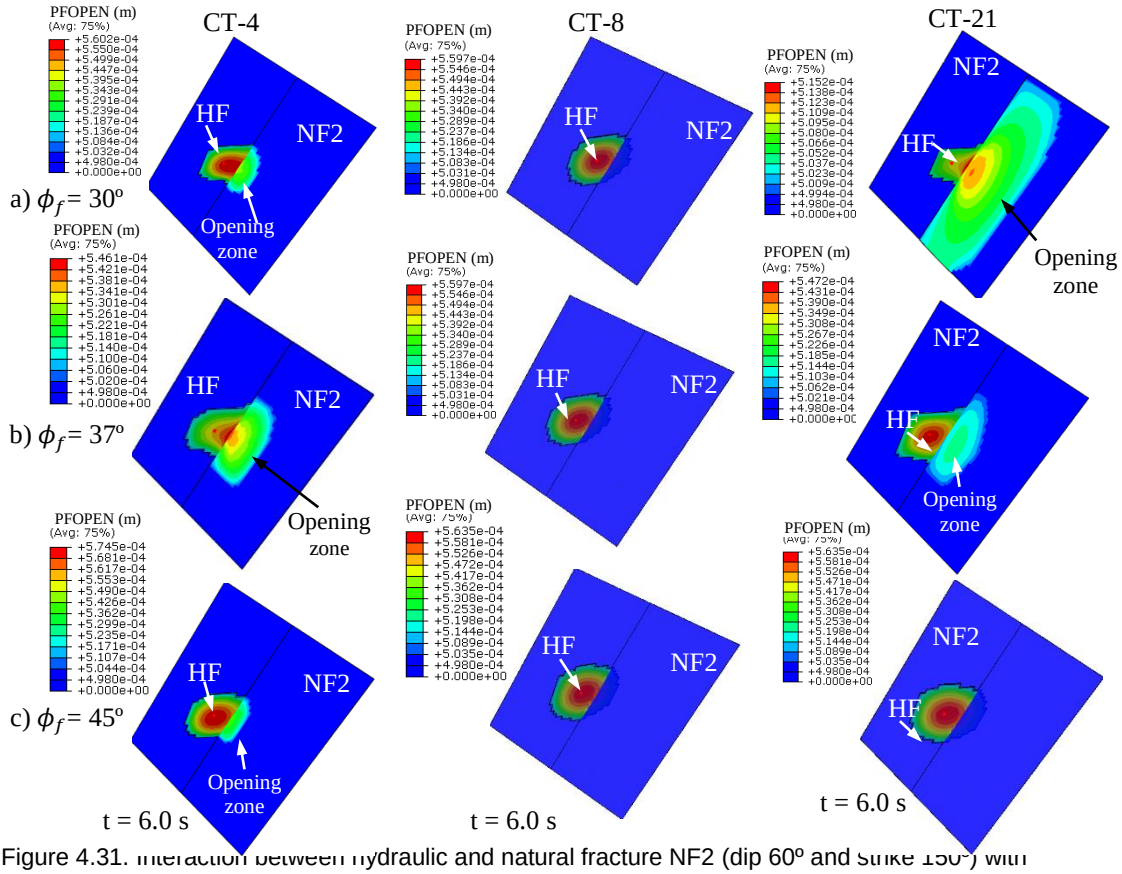

Figure 4.31. Interaction between hydraulic and natural fracture NF2 (dip 60º and strike 150º) with different angle of friction a) ϕ_f=30º, b) ϕ_f=37º and c) ϕ_f=45º.

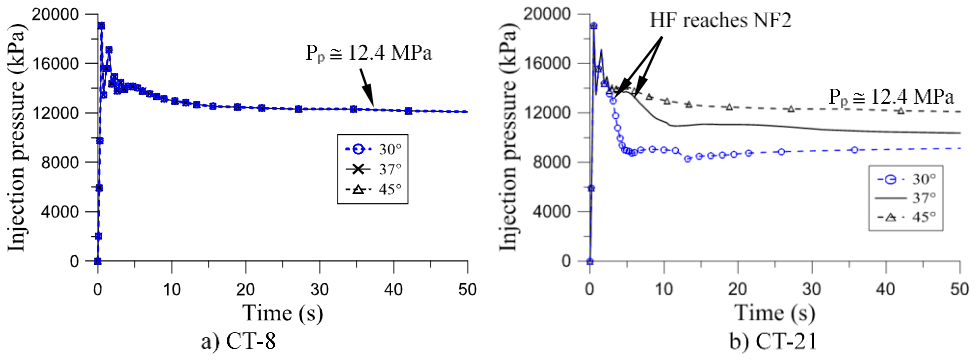

Figure 4.32. Effect of friction angle on the injection pressure during HF/NF interaction under in-situ stress of a) CT-8 and b) CT-21.

Figure 4.33 presents the interaction of the hydraulic fracture and NF3 (NF3: dip 60º and strike 180º) for different values of the friction angle (30º, 37º, and 45º) and under stresses corresponding to tests CT-4, CT-8, and CT-21. For a high (CT-8) and an intermediate (CT-21) difference of horizontal stresses, the hydraulic fracture propagates across natural fracture NF3 because the normal compressive stress on fracture plane NF3 is higher than the propagation pressure. However, for a low difference of horizontal stress (CT-4) and friction angle, the hydraulic fracture opens the natural fracture.

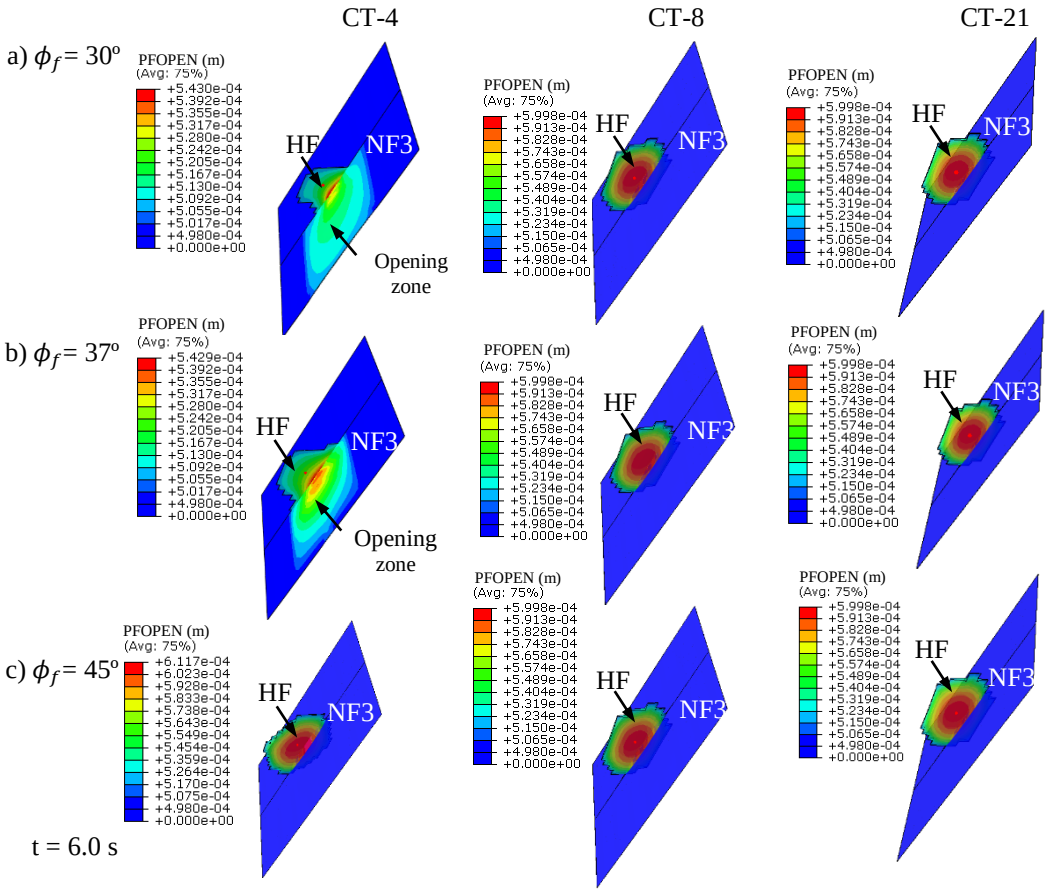

Figure 4.33. Interaction between hydraulic and natural fracture NF3 (dip 60º and strike 180º) with different angle of friction a) ϕ_f=30º, b) ϕ_f=37º and c) ϕ_f=45º.

The friction angle affects the shear strength of the natural fracture. Therefore, high values of friction angle increase the occurrences of crossing, while low values increase the occurrences of the opening of the natural fracture.

4.2.1.4. The effect of injection flow rate

In this section, we studied the effect of the injection rate on the interaction between hydraulic and natural fractures. The numerical simulation was carried out on a Hydrostone block with NF2 (strike angle of 150º and dip angle of 60º) under the in-situ stresses of CT4, CT-8, and CT-21. Two values of the injection rate q_w = 8.2e-08 m^3/s and q_w = 8.2e-07 m^3/s are adopted. Figure 4.34 shows the HF/NF interaction considering these injection rates. The rows indicate the in-situ stresses CT4, CT-8, and CT-21 while the columns indicate the injection rates: a) q_w = 8.2e-08 m^3/s and b) q_w = 8.2e-07 m^3/s.

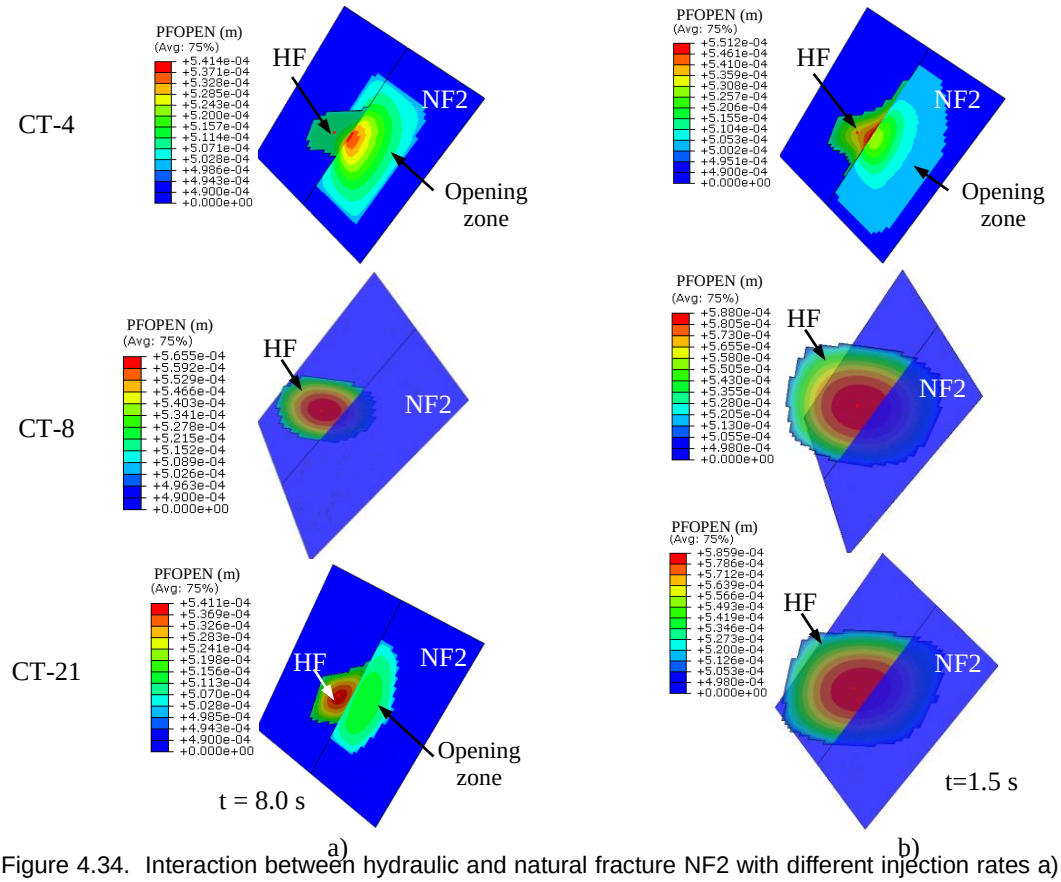

Figure 4.34. Interaction between hydraulic and natural fracture NF2 with different injection rates a) 8.2 e-8 and b) 8.2 e-7.

For CT4, first row, fracture interaction results in opening for both injection rates. For CT8, second row, the hydraulic fracture crosses the natural fracture in both cases. However, for CT21, a different fracture interaction result is observed. For a low injection rate, the hydraulic fracture merges with the natural fracture, while, for a high injection rate, the hydraulic fracture crosses the natural fracture. For a low difference of in-situ horizontal stresses (CT-4), the first row of Figure 4.34 shows that a high injection flow rate accelerates the opening of the natural fracture. For a high difference of in-situ horizontal stresses (CT-8), a high injection flow rate exacerbates the crossing of the natural fracture. However, for an intermediate difference of in-situ stresses (CT-21), fracture interaction results in crossing and opening for high and low injection rates, respectively. Finally, according to the numerical results, the injection flow rate intensifies the phenomena observed for a low injection rate.

4.2.1.5. The effect of distance from the borehole to natural fracture

We also studied the effect of the distance from the injection point to the natural fracture NF2 in the fracture interaction. The numerical simulation was performed

on a Hydrostone block with NF2 under in-situ stresses CT-04 and CT-21. The parametric study adopts four different lengths from the borehole to the natural fracture NF2: L1 = 14.3 mm, L2 = 28.6 mm, L3 = 42.9 mm and L4 = 57.1 mm. Figure 4.35 shows the numerical results of HF/NF interaction considering the effect of distance from the borehole to NF2. The rows indicate the in-situ stresses CT4 and CT-21, while the columns indicate the distances. For the in-situ stress values of CT-4, we can observe that the hydraulic fracture opens the NF2 having the distance from the injection point to NF2 (Figure 4.35a) no effect on the result. At the same time (t ≅ 8 s), a short distance from the borehole to NF2 leads to the stimulation of a larger region of NF2 than for a larger distance between the borehole and NF2.

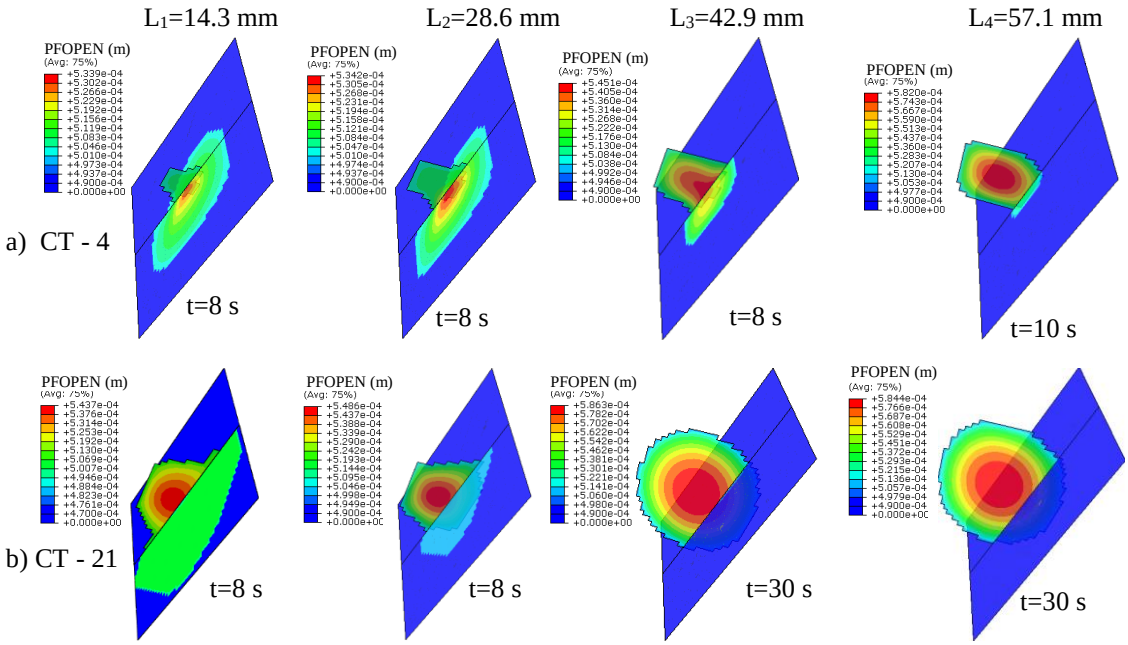

Figure 4.35. Numerical results of HF/NF interaction considering the effect of length from the borehole to NF2 (columns) under in-situ stress of a) CT-04 and b) CT-21.

Figure 4.36 presents the evolution of injection pressure along the time, assuming different distances from the injection to NF2. From Figure 4.36a, we can conclude that the fracture propagation pressure (Pp ≅ 22.0 MPa) is higher than the normal confining stress on NF2 (≅ 14.0 MPa). Therefore, high pore pressure inside the hydraulic fracture opens NF2 in all cases because for a low difference of horizontal stress (CT-4), the interaction between hydraulic and natural fracture results in opening, and it is not affected by the distance from the injection point to natural fracture.

For in-situ stress of CT-21, different HF/NF interaction outcomes are observed according to the distance from the injection point to NF2, see Figure 4.35b. As the distance from the borehole to NF2 decreases, the HF/NF interaction changes from crossing to opening, see Figure 4.36b, because the fracture propagation pressure (Pp ≅ 13.8 MPa) is close to the normal confining stress on NF2 (≅ 14.0 MPa). Consequently, if the borehole is close to NF2 (L1), the hydraulic fracture reaches NF2 at a short time (t1 ≅2.5s) with a pore pressure (≅ 16.43 MPa) above the normal confining stresses (≅ 14.0 MPa), that opens the natural fracture.

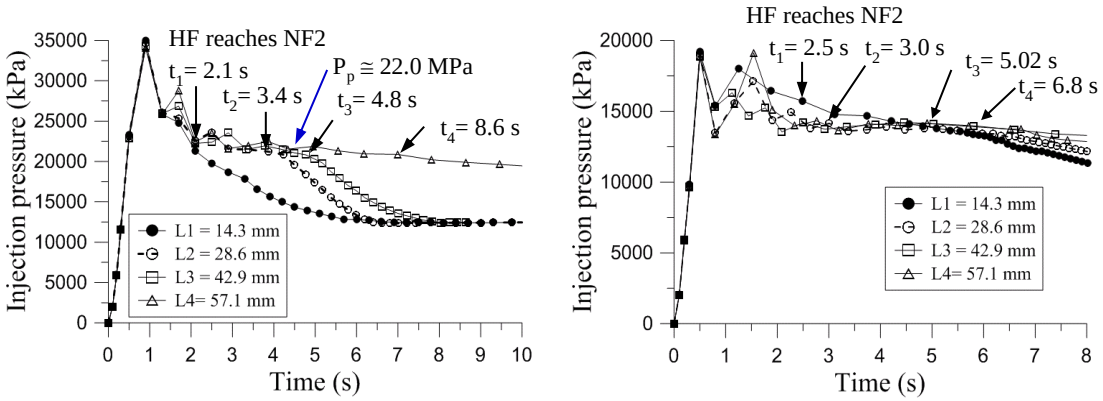

Figure 4.36. Injection pressure evolution along the time considering the distance from the borehole to NF2 under in-situ stress of a) CT-4 and b) CT-21.

Table 4.7 summarizes the injection pressure and time required for the hydraulic fractures to reach NF2 and the HF/NF interaction for each scenario distance - in-situ stresses.

Table 4.7. HF/NF interaction, injection pressure, and propagation time for the HF to reach NF2.

In-situ stress	Parameter	Distance from the borehole to NF2			
		L_1	L_2	L_3	L_4
CT-4	Interaction	Opening	Opening	Opening	Opening
	Time (s)	2.1	3.4	4.8	8.6
	Pressure (kPa)	21303	21481	20822	20877
CT-21	Interaction	Opening	Opening	Crossing	Crossing
	Time (s)	2.5	3.4	5.024	6.8
	Pressure (kPa)	16430	14140	13976	13746

Finally, we can conclude that the distance from the injection point to NF2 affects the HF/NF interaction when the fracture propagation pressure is close to the normal confining stress on the natural fracture plane.

4.3.
Hydraulic fracture propagation in a naturally fractured formation

In order to verify the robustness and applicability of the proposed computational methodology, a hydraulic fracturing scheme is simulated on the 3D DFN. The 10 x 10 x 1 m^3 domain is subjected to a compressive initial stress state of 15 MPa in a vertical direction, 8 MPa and 4 MPa, maximum and minimum horizontal stresses, respectively. Two scenarios are considered to study the orientation effect of the NF on the final hydraulic fracture network, as shown in Figure 4.37. Figure 4.37a shows that the NF1 is oriented with strike 310° and dip 53° in scenario 1. In scenario 2, the NF1 is oriented with strike 120° and dip 53° (see Figure 4.37b). The other fractures have the same orientations in both scenarios. Figure 4.38 shows the tetrahedral mesh with 39424 nodes and 26316 elements. The injection flow is increased linearly during 50 s until it reaches 0.0001 m^3/s. After that, the injection rate is kept constant.

Table 4.8 provides the properties of injection fluid, rock, and fractures.

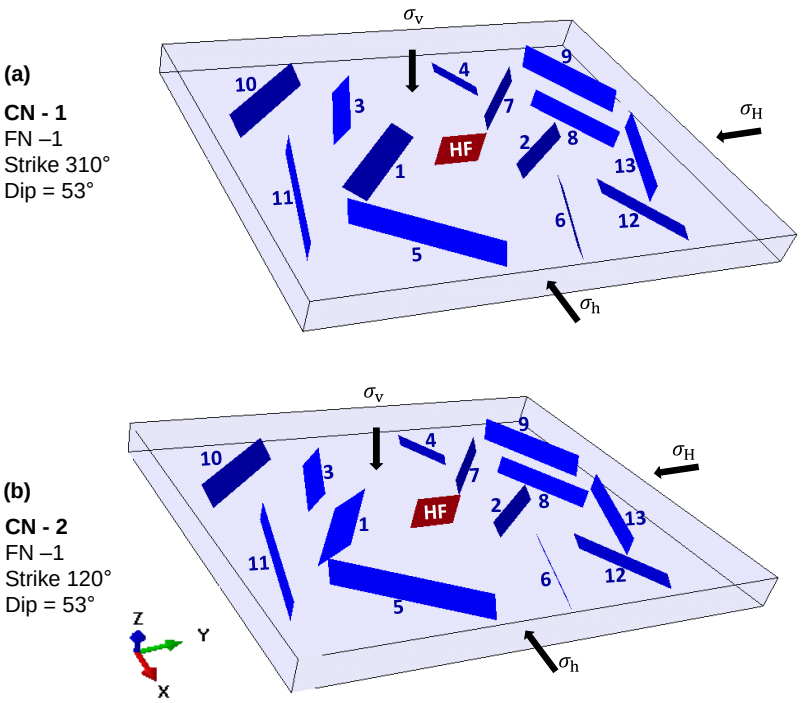

Figure 4.37. Discrete fracture network: (a) scenario 1, and (b) scenario 2.

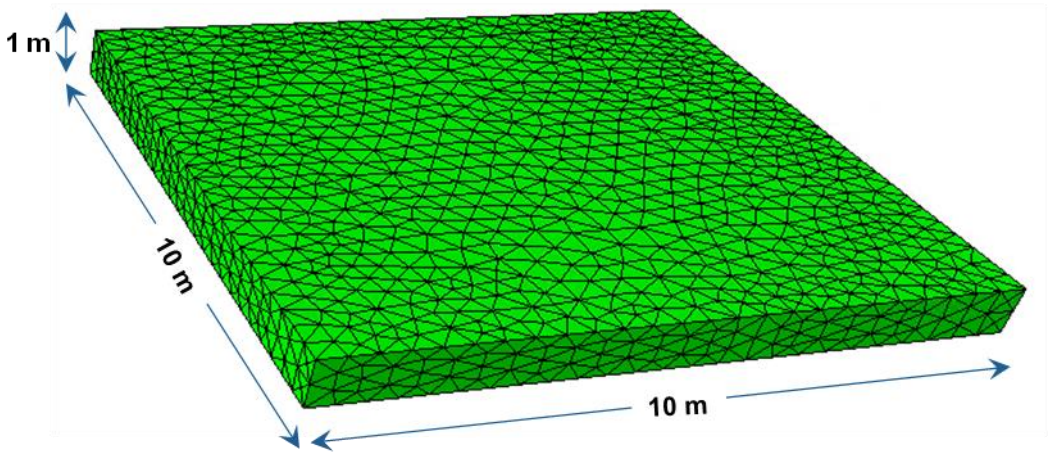

Figure 4.38. Tetrahedral mesh with 39424 nodes and 26316 elements.

Table 4.8. Hydraulic and mechanical properties

Categories	Properties	Unit	Value
Rock	Young Modulus	GPa	17.0
	Poisson coefficient	---	0.22
	Hydraulic conductivity	m/s	2e-9
Hydraulic fracture	Normal strength	MPa	3.0
	Shear strengths	MPa	12.0
	Normal stiffness	MPa/m	17.0e+6
	Shear stiffness	MPa/m	17.0e+6
Natural fracture	Normal stiffness	MPa/m	17.0e+4
	Shear stiffness	MPa/m	8.0e+4
	Fracture cohesion	MPa	0.0
	Friction angle	(°)	31.0
	Dilation angle	(°)	7.5
	Cut-off	MPa	0.0
Fracturing fluid	Fluid viscosity	cp	10.0
	Injection rate	m^3/s	1e-4

Figure 4.39 shows the initial effective normal stress on the fracture network. It is observed that NF1 is more compressive in CN2 than in CN1. Consequently, the slip tendency (τ_R/τ_{slip}) of NF1 in CN1 is higher than in CN2, as shown in Figure 4.40. This behavior can affect the hydraulic fracture propagation.

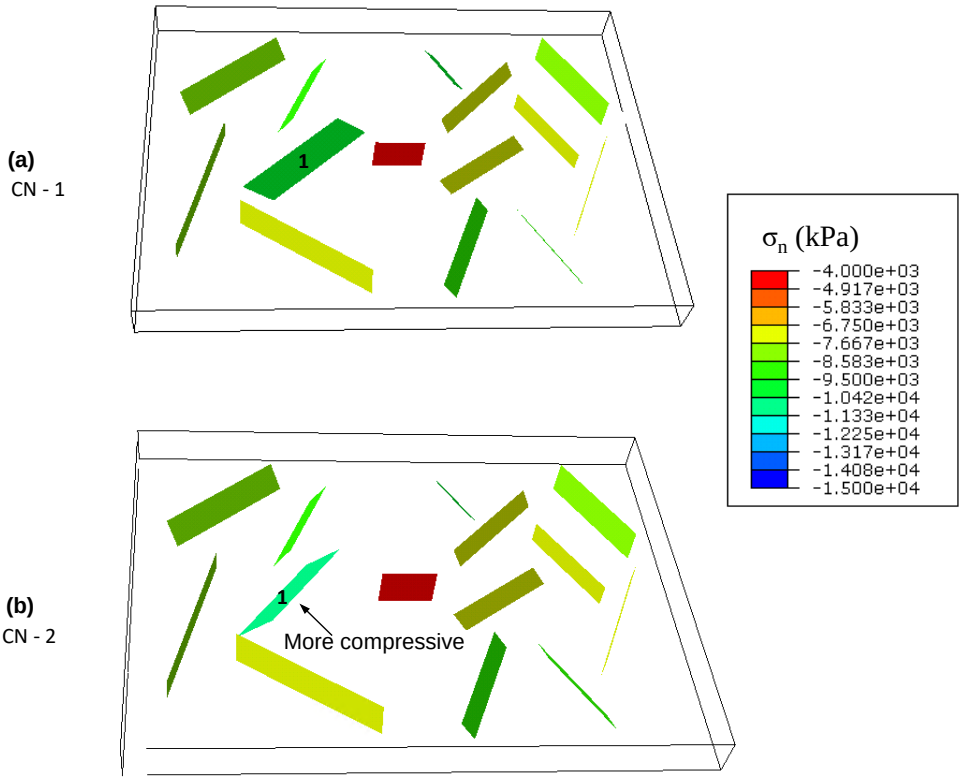

Figure 4.39. Initial normal stresses on the fracture network: (a) scenario-1, (b) scenario-2.

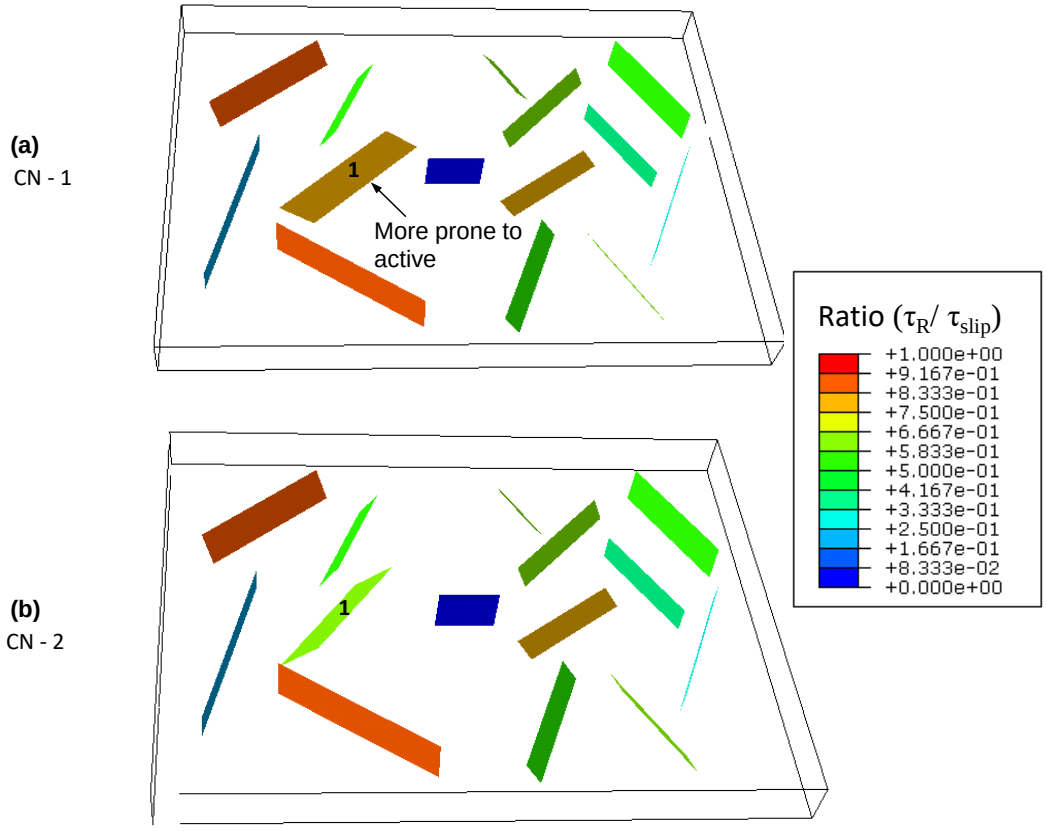

Figure 4.40. slip tendency (τ_R/τ_{slip}) on the fracture network: (a) scenario-1, (b) scenario-2.

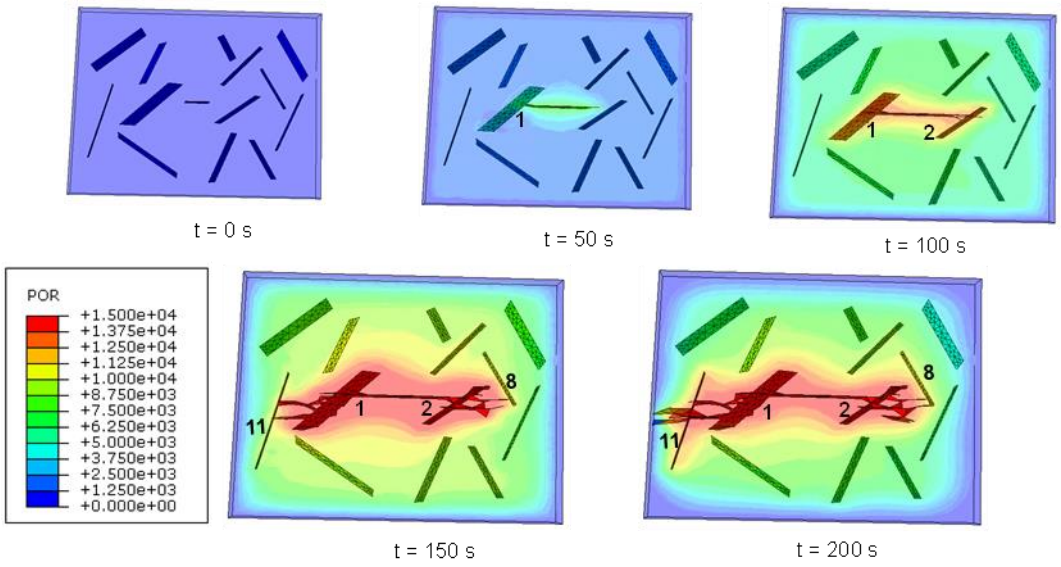

Figure 4.41. Pore pressure distribution and HF propagation for scenario-1 at different times.

Figure 4.41 shows the HF propagation for scenario-1 at different times. It is observed that the hydraulic fracture intercepts the NF1 at 50 s and NF2 at 100 s. After the dilation of those fractures, the HF crosses by offset and diverging until it intercepts the NFs 8 and 11 at 150 s. Subsequently, the HF crosses the NF 11, while the NF 8 arrests the HF propagation.

Figure 4.42 shows the HF propagation for scenario-2 at different times. In this case, the hydraulic fracture intercepts the NF1 and NF2 at 100 s. In contrast to scenario-1, the hydraulic fracture crosses the NF1 because the higher compressive normal stress restricts its dilatation. HF dilates NF2 and propagates from its tip, following the most favorable direction at 150 s. Finally, the HF is arrested by shear of the NF 11, while the HF crosses the NFs 8 and 13 at 200 s.

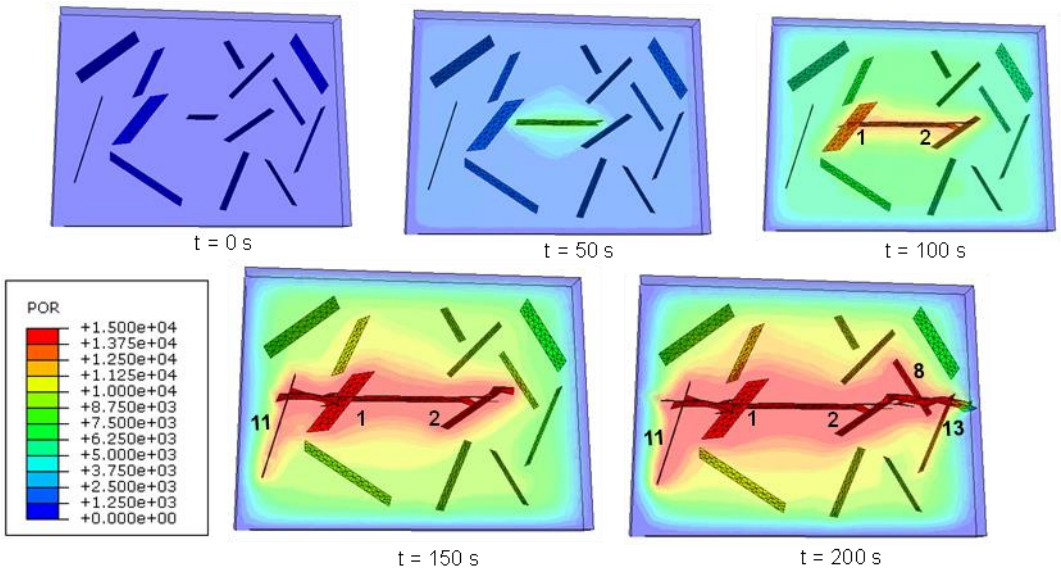

Figure 4.42. Pore pressure distribution and HF propagation for scenario-2 at different times.

Figure 4.40 shows that NF1 is more prone to reactivate during the hydraulic fracturing in scenario-1. This situation totally changed the behavior of the fluid-driven fracture propagation affecting the apertures and the final geometry of the fracture network, as shown in Figure 4.43. In that sense, the fracture propagation models prove to be an optimal tool to evaluate different scenarios aiming to study the dominant factors that affect the fluid-driven fracture propagation in naturally fractured formations. However, fracture propagation models cannot estimate the production performance of the stimulated reservoirs. Then, a methodology for reservoir simulation is addressed in the following chapter.

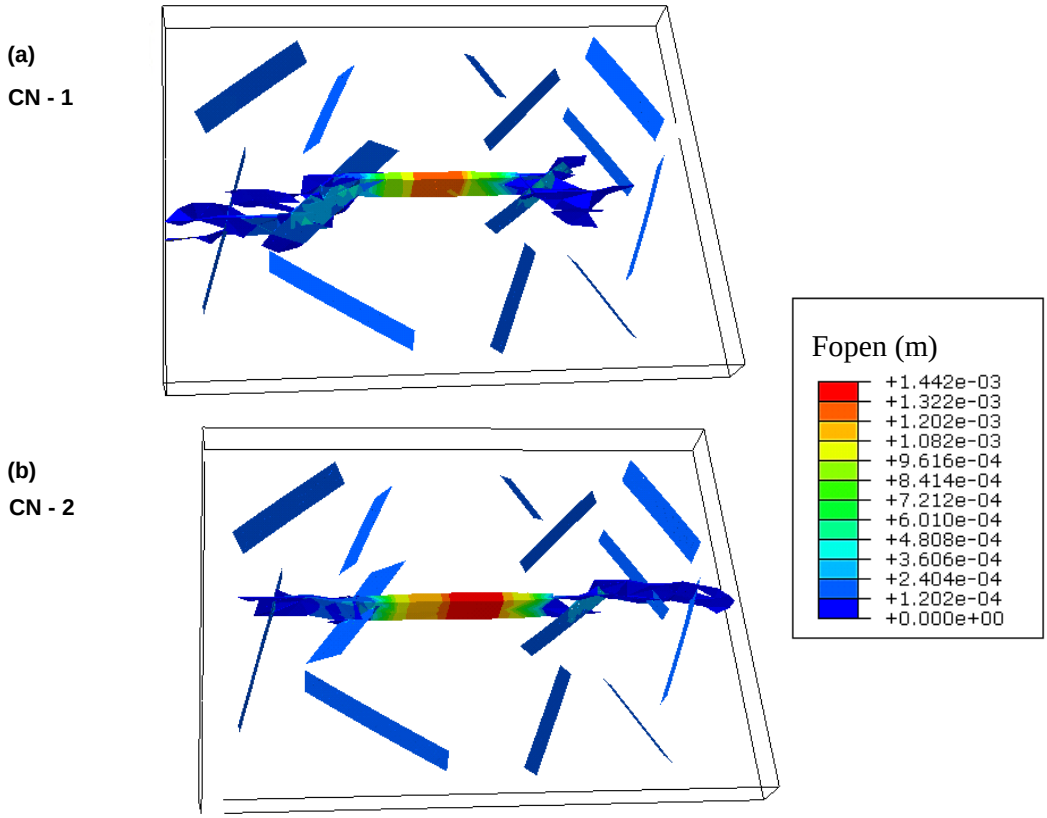

Figure 4.43. Fracture opening for the stimulated fracture network: (a) scenario 1, and (b) scenario 2.

4.4. Discussion and conclusions

In this study, a robust 2D/3D numerical methodology in the finite element method is developed to simulate hydraulic fracturing treatment in naturally fractured media. The developed approach is validated against analytical and numerical solutions considering fracture propagation through an intact porous medium in different propagation regimens. The results demonstrate the relevance of hydromechanical coupling within the porous media, which can alter the response

of the system and the interaction between hydraulic and natural fractures. This phenomenon is attributed to fluid leakage through the fracture faces, fluid pressure in the formation, and variation of effective stresses. Additional models include natural fractures with different orientations to evaluate their influence on the final configuration of the fracture network. The result obtained for storage-toughness and leak-off-toughness dominated regimes showed that the hydraulic fracture tends to turn into natural fractures. Subsequently, the hydraulic fracture propagates again into the formation in the most favorable direction. On the other hand, in storage-viscosity and leak-off-viscosity dominated regimes, the hydraulic fracture may result in different propagation types (opening, crossing, branching, and offset). Furthermore, for higher angles of approach, the dilation of the natural fracture is constrained by the higher suction generated in front of the hydraulic fracture tip. This study provides a better understanding of the interaction of hydraulic fractures and natural fractures in all asymptotic propagation regimes.

The developed scheme is also compared against three cases of fracturing experimental studies performed in the laboratory. Overall, it may be stated that the numerical procedure provides very good agreement with the laboratory tests. The first example studies the influence of the natural fracture on the trajectory of the hydraulic fracture propagation. Mesh dependency and computational time of the proposed methodology are also evaluated. The second example demonstrates the unrestricted fracture propagation under a normal stress regime. In this case, hydraulic fracture propagation is initiated from an unfavorable perforation angle. Then, the fracture initially propagates along the orientation of the perforations and gradually turns towards the maximum horizontal stress direction. The third example shows a pre-fractured block under different conditions to study the hydraulic and natural fracture interaction. Different possibilities of HF/NF interaction types (crossing, arrest, and opening) are predicted accurately when compared to the experimental data.

We observe that HF tends to cross NF for the low angle of approach and high horizontal stress contrast. In these conditions, NF is submitted to high compressive stresses that restrain its dilation. On the other hand, natural fractures are more prone to open for low horizontal stress contrast. In this case, a small variation of material and fluid properties may have a greater influence on the interaction. The proposed interaction diagrams can provide a general idea of the

hydraulic fracture behavior when it interacts with a pre-existing vertical fracture. However, those diagrams are sensitive to the in-situ conditions.

We noted that the NF with low friction angle tends to dilate by shear-slip, allowing fluid migration inside it and, consequently, arresting the HF growth. In contrast, NF with high friction angle hinders reactivation, and the hydraulic fracture is prone to cross it.

The injection rate also affects the interaction of hydraulic and natural fractures because it changes the pressure inside the hydraulic fracture. As a result, it increases the probability of propagating through the pre-existent natural fracture.

The distance from the injection point to the natural fracture affects the HF/NF interaction since the fracture propagation pressure is close to the normal confining stresses on the fracture plane. The HF/NF interaction changes from crossing to opening as the distance from the injection point to the natural fracture decreases.

Finally, we study the impacts of natural fractures with different values of approach and dip angles on hydraulic fracture propagation. These effects cannot be addressed under 2D assumptions. For a normal stress regime, high dip and low angle of approach, the hydraulic fracture increases the slip or opening of natural fractures. In this case, NF tends to be parallel to the HF. In contrast, for the low dip and high angle of approach, the hydraulic fracture tends to cross the natural fractures. In this case, the NF is restrained by vertical stress and/or the maximum horizontal stress. Therefore, the NF orientation affects the initial compressive normal stresses and the slip tendency. Consequently, the fracture network evolution. Some advantages and limitations of the proposed methodology are discussed briefly.

Simplicity in terms of mesh data structure and successful representation of a localized failure and complex crack patterns are the most important features of the developed intrinsic CZM. Furthermore, parallel implementation is straightforward once the topological mesh connectivity remains constant during the simulation process. With the proposed methodology, it is possible to simulate a re-initiated fracture from the crack tip, crossing with an offset, branching, and multiple cracks, not worrying about multiple crack interactions. The adopted cohesive crack approach avoids the singularity issues of the stress at the crack tip, which is present in linear elastic fracture mechanics.

The main drawback in the developed method is mesh dependence because the fracture can only propagate along continuum element faces. The numerical results reveal that coarse meshes can affect the correct fracture patterns. This effect is reduced for more refined meshes. However, higher refinement results in higher computational costs. Therefore, the initial mesh should be well balanced in terms of refinement, aiming to obtain a reliable solution and optimize the computational cost. In addition, we use unstructured meshes based on the Delaunay algorithm in order to reduce certain bias on crack propagation. Another well-known problem of the intrinsic CZM is that it introduces artificial compliance that alters the elastic response of the material prior to the onset of hydraulic fracture. This phenomenon of “artificial compliance” was reduced, increasing the initial stiffness of the cohesive elements in terms of a hardening factor.

5
An enhanced dual porosity and dual permeability approach for hydro-mechanical modeling of fluid flow in naturally fractured formations

This chapter comprises the papers of (RUEDA CORDERO et al., 2020a; RUEDA; MEJIA; ROEHL, 2019). Traditionally, naturally fractured reservoirs are simulated using dual-porosity and dual-permeability models. Conventional dual-porosity models adopt over-simplifications in terms of characterization of the fractured system. Generally, they focus on the hydraulic problem and do not consider the rock and fracture deformability. Besides, those models assume equally sized block matrix and orthogonal fracture sets with uniform properties. This chapter presents a new 3D hydro-mechanical formulation for an enhanced dual-porosity/dual-permeability model (EDPDP) to represent a fractured porous formation more realistically. The enhanced dual porosity and dual permeability (EDPDP) model allows incorporating multi-block domains formed by several multiscale fracture sets with arbitrary orientations, permeabilities, and sizes. We consider that the fracture scales are related to the connected sub-networks. We refer to dominant sub-network as primary fractures that can be formed by secondary and tertiary fractures. Figure 5.1 shows this model schematically. The fully coupled hydro-mechanical formulation includes fracture orientations and stress-induced aperture changes to update stiffness and permeability tensors. The EDPDP model is implemented in an in-house framework GeMA (Geo Modelling Analysis)(MENDES; GATTASS; ROEHL, 2016) using the finite element method (FEM) to study the effects of fractures at multiple scales on the hydro-mechanical behavior of the reservoir. The new 3D model allows the study of the impacts of natural fractures with different dip and strike angles on the hydro-mechanical behavior of a fractured formation. Mechanical, hydraulic, and fully coupled poromechanical examples are presented to demonstrate the proposed numerical methodology's applicability and robustness. Result comparison between the EDPDP and the discrete fracture model (DFM) shows excellent agreement and validates the EDPDP model. A parametric analysis demonstrates the influence of the fracture sets on reservoir behavior. Finally, we study the impacts of primary

and secondary fractures on the production performance and the final recovery of a naturally fractured reservoir.

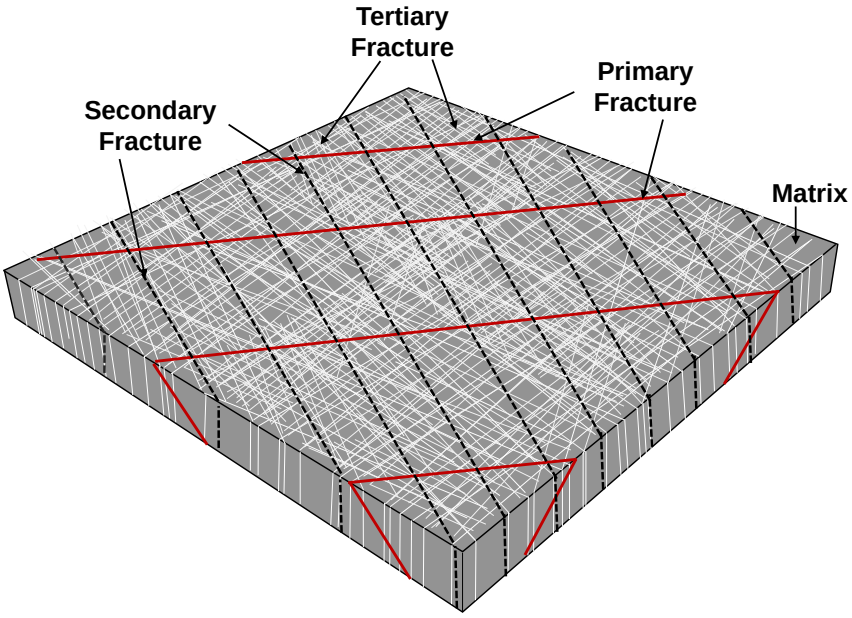

Figure 5.1. Schematic representation of fractured medium composed of several multiscale fracture sets with different orientations, spacing, and permeabilities.

5.1. Governing equations

The governing equations of the hydro-mechanical dual porosity and dual permeability formulations involve mechanical deformations induced by the fluid pressure, fluid flow through the fractures, and the fluid transfer between fractures and the surrounded porous media. Biot's theory (BIOT, 1941) is adopted to model the saturated porous media. The relationship between total stresses and effective stresses in dual-porosity media is given by:

$$\boldsymbol{\sigma}_m = \boldsymbol{\sigma'}_m - \boldsymbol{\alpha_m}\, p_m \tag{5.1}$$

$$\boldsymbol{\sigma}_{fr} = \boldsymbol{\sigma'}_{fr} - \boldsymbol{\alpha_{fr}}\, p_{fr} \tag{5.2}$$

The subscripts m and fr refer to matrix and fracture, respectively; p_m and p_{fr} represent the matrix and fracture fluid pressures, and $\boldsymbol{\alpha}_m$ and $\boldsymbol{\alpha}_{fr}$ are the pressure factor tensors (compatible with (BIOT, 1941)). Compressive stresses and strains are negatives. We use the concept of the equivalent continuum to develop the mechanics of the overall deformation $\boldsymbol{\varepsilon}_{mfr}$ of the naturally fractured formation:

$$\boldsymbol{\varepsilon}_{mfr} = \boldsymbol{\varepsilon}_m + \boldsymbol{\varepsilon}_{fr} \tag{5.3}$$

The deformation of the rock $\boldsymbol{\varepsilon}_m$ and the fractures $\boldsymbol{\varepsilon}_{fr}$ is calculated using the deformation mechanics individually, as follows:

$$\boldsymbol{\varepsilon}_m = \boldsymbol{C}_m : \boldsymbol{\sigma}'_m \tag{5.4}$$

$$\boldsymbol{\varepsilon}_{fr} = \boldsymbol{C}_{fr} : \boldsymbol{\sigma}'_{fr} \tag{5.5}$$

where $\boldsymbol{C}_m$ and $\boldsymbol{C}_{fr}$ are the compliance tensors of the rock matrix and the fracture system, respectively. The compliance tensor of isotropic rock matrix follows:

$$\boldsymbol{C}_m = \begin{bmatrix} \frac{1}{E} & -\frac{\nu}{E} & -\frac{\nu}{E} & 0 & 0 & 0 \\ -\frac{\nu}{E} & \frac{1}{E} & -\frac{\nu}{E} & 0 & 0 & 0 \\ -\frac{\nu}{E} & -\frac{\nu}{E} & \frac{1}{E} & 0 & 0 & 0 \\ 0 & 0 & 0 & \frac{2(1+\nu)}{E} & 0 & 0 \\ 0 & 0 & 0 & 0 & \frac{2(1+\nu)}{E} & 0 \\ 0 & 0 & 0 & 0 & 0 & \frac{2(1+\nu)}{E} \end{bmatrix} \tag{5.6}$$

where E is Young's modulus and ν is Poisson's coefficient. The compliance tensor of the fracture system in the global coordinates (*x*, *y*, *z*), is the sum of the compliance tensor of all fracture sets:

$$\boldsymbol{C}_{fr} = \sum_{i=1}^{nset} \left(\boldsymbol{T}^{\boldsymbol{T}}.\boldsymbol{C}_{fr}^{\boldsymbol{l}}.T\right)_i \tag{5.7}$$

where $\boldsymbol{C}_{fr}^{\boldsymbol{l}}$ is the compliance tensor of a single fracture set (Figure 5.2) in its local coordinate system (n, t_1, t_2):

$$\left(\boldsymbol{C}_{fr}^{\boldsymbol{l}}\right)_{\boldsymbol{i}} = \begin{bmatrix} 0 & 0 & 0 & 0 & 0 & 0 \\ 0 & 0 & 0 & 0 & 0 & 0 \\ 0 & 0 & 1/(k_n.s) & 0 & 0 & 0 \\ 0 & 0 & 0 & 0 & 0 & 0 \\ 0 & 0 & 0 & 0 & 1/(k_{t1}.s) & 0 \\ 0 & 0 & 0 & 0 & 0 & 1/(k_{t2}.s) \end{bmatrix} \tag{5.8}$$

where s is the fracture spacing, k_n, k_{t1} and k_{t2} are the normal and the shear fracture stiffness coefficients in n, t_1, and t_2 directions, respectively. $\boldsymbol{T}$ is the transformation tensor given by:

$$\boldsymbol{T} = \begin{bmatrix} \boldsymbol{T}_{11} & \boldsymbol{T}_{12} \\ \boldsymbol{T}_{21} & \boldsymbol{T}_{22} \end{bmatrix} \tag{5.9}$$

with

$$\boldsymbol{T}_{11} = \begin{bmatrix} l_1^2 & m_1^2 & n_1^2 \\ l_2^2 & m_2^2 & n_2^2 \\ l_3^2 & m_3^2 & n_3^2 \end{bmatrix} \tag{5.10}$$

$$\boldsymbol{T}_{12} = \begin{bmatrix} 2l_1m_1 & 2m_1n_1 & 2n_1l_1 \\ 2l_2m_2 & 2m_2n_2 & 2n_2l_2 \\ 2l_3m_3 & 2m_3n_3 & 2n_3l_3 \end{bmatrix} \tag{5.11}$$

$$\boldsymbol{T}_{21} = \begin{bmatrix} l_1l_2 & m_1m_2 & n_1n_2 \\ l_2l_3 & m_2m_3 & n_2n_3 \\ l_3l_1 & m_3m_1 & n_3n_1 \end{bmatrix} \tag{5.12}$$

$$\boldsymbol{T}_{22} = \begin{bmatrix} l_1m_2 + l_2m_1 & m_1n_2 + m_2n_1 & n_1l_2 + n_2l_1 \\ l_2m_3 + l_3m_2 & m_2n_3 + m_3n_2 & n_2l_3 + n_3l_2 \\ l_3m_1 + l_1m_3 & m_3n_1 + m_1n_3 & n_3l_1 + n_1l_3 \end{bmatrix} \tag{5.13}$$

where l_i, m_i and n_i are also used to define the rotation matrix $\boldsymbol{R}$ that transforms the local reference system of a fracture set to the global reference and is expressed by:

$$\boldsymbol{R} = \begin{bmatrix} l_1 & m_1 & n_1 \\ l_2 & m_2 & n_2 \\ l_3 & m_3 & n_3 \end{bmatrix} = \begin{bmatrix} \sin(\theta) & \cos(\theta) & 0 \\ \cos(\varphi)\cos(\theta) & -\cos(\varphi)\sin(\theta) & -\sin(\varphi) \\ -\sin(\varphi)\cos(\theta) & \sin(\varphi)\sin(\theta) & -\cos(\varphi) \end{bmatrix} \tag{5.14}$$

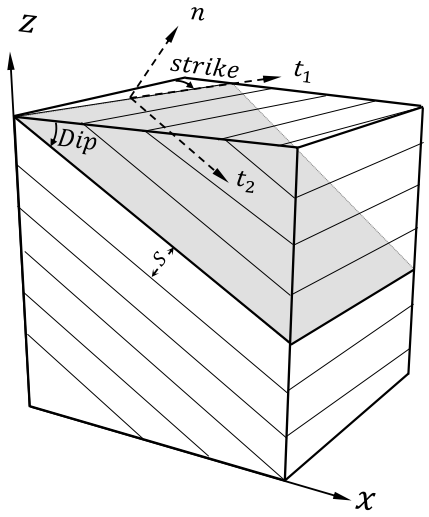

Figure 5.2. Schematic representation of an oriented fracture set and its local system.

The normal stiffness increases with the fracture closure. In this case, k_n follows the empirical model proposed by (BANDIS; LUMSDEN; BARTON, 1983), in which the fracture closure is stress-dependent, as presented in Eqs (3.20) and (3.21) in section 3.2.3.

Substituting the effective stresses of Eqs (5.1) and (5.2) into Eqs (5.4) and (5.5), the deformation of the rock matrix and fracture system results in:

$$\boldsymbol{\varepsilon}_m = \boldsymbol{C}_m : (\boldsymbol{\sigma}_m + \alpha_m \boldsymbol{p}_m) \tag{5.15}$$

$$\boldsymbol{\varepsilon}_{fr} = \boldsymbol{C}_{fr} : (\boldsymbol{\sigma}_{fr} + \alpha_{fr} \boldsymbol{p}_{fr}) \tag{5.16}$$

From Eq (5.3) and assuming stress equilibrium at the local level, $\boldsymbol{\sigma}_{mfr} = \boldsymbol{\sigma}_m = \boldsymbol{\sigma}_{fr}$, the total strain of the fractured rock system can be defined as:

$$\boldsymbol{\varepsilon}_{mfr} = (\boldsymbol{C}_m + \boldsymbol{C}_{fr}) : \boldsymbol{\sigma} + (\boldsymbol{C}_m : \boldsymbol{\alpha_m}\, p_m + \boldsymbol{C}_{fr} : \boldsymbol{\alpha_{fr}}\, p_{fr}) \tag{5.17}$$

From Eq (5.17), modified effective stress can be defined as:

$$\boldsymbol{\sigma'}_{mfr} = \boldsymbol{D}_{mfr} : \boldsymbol{\varepsilon}_{mfr} - \boldsymbol{\alpha}^*_{\boldsymbol{m}}\, p_m - \boldsymbol{\alpha}^*_{\boldsymbol{fr}}\, p_{fr} \tag{5.18}$$

where $\boldsymbol{\alpha}^*_{\boldsymbol{m}}$ and $\boldsymbol{\alpha}^*_{\boldsymbol{fr}}$ are the equivalent pressure tensors which take into account fracture and matrix relative deformability and are defined as:

$$\boldsymbol{\alpha}^*_{\boldsymbol{m}} = \boldsymbol{D}_{mfr} : \boldsymbol{C}_m : \boldsymbol{\alpha_m} \tag{5.19}$$

$$\boldsymbol{\alpha}^*_{\boldsymbol{fr}} = \boldsymbol{D}_{mfr} : \boldsymbol{C}_{fr} : \boldsymbol{\alpha_{fr}} \tag{5.20}$$

and $\boldsymbol{D}_{mfr}$ is the equivalent elastic tensor of the matrix-fracture system defined as:

$$\boldsymbol{D}_{mfr} = \left(\boldsymbol{C}_m + \boldsymbol{C}_{fr}\right)^{-1} \tag{5.21}$$

Finally, the equations that govern deformability and fluid continuity in the fractured rock formation take the form:

$$\nabla \cdot \left(\boldsymbol{D}_{mfr} : \boldsymbol{\varepsilon}_{mfr} - \boldsymbol{\alpha}_m^* p_m - \boldsymbol{\alpha}_{fr}^* p_{fr} \right) = \boldsymbol{f} \tag{5.22}$$

$$\nabla \cdot \left(\frac{\boldsymbol{k}_m}{\mu} \cdot \nabla p_m \right) + \boldsymbol{\alpha}_m^* : \frac{\partial \boldsymbol{\varepsilon}_{mfr}}{\partial t} + \beta_m \frac{\partial p_m}{\partial t} + \omega_{MD}\left(p_m - p_{fr}\right) = -q_m \tag{5.23}$$

$$\nabla \cdot \left(\frac{\boldsymbol{k}_{fr}}{\mu} \cdot \nabla p_{fr} \right) + \boldsymbol{\alpha}_{fr}^* : \frac{\partial \boldsymbol{\varepsilon}_{mfr}}{\partial t} + \beta_{fr} \frac{\partial p_{fr}}{\partial t} - \omega_{MD}\left(p_m - p_{fr}\right) = -q_{fr} \tag{5.24}$$

where $\boldsymbol{f}$ represents the external force vector, q_m and q_{fr} are the fluid flow applied in the block matrix and the fractures. β_m and β_{fr} are the relative compressibilities, μ is the dynamic fluid viscosity, t is the analysis time, $\boldsymbol{k}_m$ and $\boldsymbol{k}_{fr}$ are the rock and fracture permeability tensors, and ω_{MD} is the shape transfer factor that controls fluid transfer between the block matrix and the fracture systems.

5.1.1. Permeability of the fracture system

In this work, we assume small fracture apertures and fluid flow according to the simplified solution for flow between smooth parallel plates (ZIMMERMAN; YEO, 2000). The longitudinal permeability tensor $\boldsymbol{k}_{fr}^{\boldsymbol{l}}$ through a set of parallel fractures can be defined as a function of the fracture aperture a_n and spacing s such as:

$$\boldsymbol{k}_{fr}^{\boldsymbol{l}} = \begin{bmatrix} \frac{a_n^3}{12s} & 0 & 0 \\ 0 & \frac{a_n^3}{12s} & 0 \\ 0 & 0 & 0 \end{bmatrix} \tag{5.25}$$

The fracture aperture can be defined as:

$$a_n = a_0 + \Delta\delta_n \tag{5.26}$$

where a_0 is the initial fracture aperture and $\Delta\delta_n$ is the fracture closure variation.

The permeability tensor of the fracture system in a global coordinate (*x*, *y*, *z*) is defined as:

$$\boldsymbol{k}_{fr} = \sum_{i=1}^{nset} \left(\boldsymbol{R}^{\boldsymbol{T}}.\boldsymbol{k}_{fr}^{\boldsymbol{l}}.\boldsymbol{R}\right)_i \tag{5.27}$$

where $\boldsymbol{R}$ is the rotation matrix defined in Eq (5.14).

5.1.2. Enhanced shape factor

The shape factor reflects the geometry of the block matrix and controls the fluid transfer between a porous rock and surrounding fractures. In the last decades, several formulations have been developed (COATS, 1989; KAZEMI et al., 1976; LIM; AZIZ, 1995; WARREN; ROOT, 1963) to assess the shape factors accurately. However, those conventional shape factors consider block sizes of the same size surrounded by orthogonal fractures. We extend the concept presented by (KAZEMI et al., 1976; LEMONNIER; BOURBIAUX, 2010) to multi-block domains formed by different fracture sets with arbitrary orientations (Figure 5.1). Therefore, the shape factor ω for a rock block domain (Figure 5.3), assuming a pseudo (quasi) steady-state condition, can be expressed as:

$$\omega = \frac{1}{V} \sum_{i=1}^{nfaces} \left(\frac{A}{d_c} k_{mn}\right)_i \tag{5.28}$$

where V is the volume of the matrix block; A is the area of the open fracture surface; d_c is the distance from the centroid of the block matrix to fracture surface i; k_{mn} is the rock permeability normal to the open fracture plane, and $nfaces$ is the number of block faces in contact with open fractures. Considering the anisotropic permeability of the rock matrix k_{mx}, k_{my} , k_{mz} in the x, y and z- directions, the block-matrix permeability normal to the fracture surface i can be defined as:

$$(k_{mn})_i = \left(l^2\, k_{mx} + m^2\, k_{my} + n^2\, k_{mz}\right)_i \tag{5.29}$$

where $l = -\sin(\varphi)\cos(\theta)$, $m = \sin(\varphi)\sin(\theta)$, and $n = -\cos(\varphi)$.

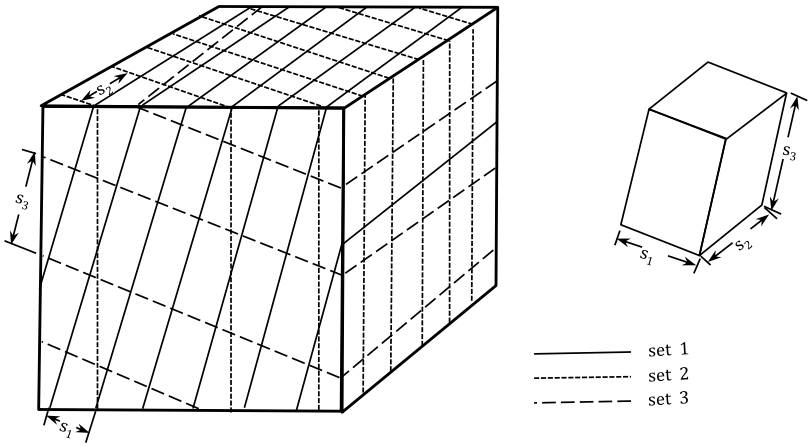

Figure 5.3. A rock block with three persistent fracture sets.

With fracture spacings s_1, s_2, s_3 (Figure 5.3) and considering anisotropic permeability, the shape factor for a rock block domain can be written as:

$$\omega = Sfc\left(\frac{k_{mn1}}{s_1^2} + \frac{k_{mn2}}{s_2^2} + \frac{k_{mn3}}{s_3^2}\right) \tag{5.30}$$

where Sfc is a shape factor constant of 4, 8 or π^2 as proposed by (KAZEMI et al., 1976), (COATS, 1989), and (LIM; AZIZ, 1995), respectively. Finally, the shape factor ω_{MD} that reflects the geometry of the multi-block domains formed by several fracture sets with different orientation (Figure 5.3) can be expressed as:

$$\omega_{MD} = \sum_{i=1}^{NMD} (\omega)_i \tag{5.31}$$

where NMD is the number of matrix block domains.

5.2. Finite element formulation

This section presents the formulation of the proposed approach to simulate fluid flow through highly fractured porous media. The governing equations are discretized using the residual weight method. Following the standard Galerkin Method, the discretization of the equilibrium equation (5.22) results in:

$$\boldsymbol{K u} - \boldsymbol{R}_m \boldsymbol{p}_m - \boldsymbol{R}_{fr} \boldsymbol{p}_{fr} = \hat{\boldsymbol{f}} \tag{5.32}$$

with

$$\boldsymbol{K} = \int_{\Omega} \boldsymbol{B}^T \boldsymbol{D}_{mfr} \boldsymbol{B} \partial\Omega \tag{5.33}$$

$$\boldsymbol{R}_m = \alpha_m \int_{\Omega} \boldsymbol{B}^T \boldsymbol{D}_{mfr} \boldsymbol{C}_m m \boldsymbol{N}_p \partial\Omega \tag{5.34}$$

$$\boldsymbol{R}_{fr} = \alpha_{fr} \int_{\Omega} \boldsymbol{B}^T \boldsymbol{D}_{mfr} \boldsymbol{C}_{fr} m \boldsymbol{N}_p \partial\Omega \tag{5.35}$$

$$\hat{\boldsymbol{f}} = \int_{\boldsymbol{S}} \boldsymbol{N} \boldsymbol{f} \, \partial S \tag{5.36}$$

where $\boldsymbol{K}$ is the stiffness matrix, $\boldsymbol{R}_m$ and $\boldsymbol{R}_{fr}$ are the coupling matrices, and $\hat{\boldsymbol{f}}$ is a vector of applied boundary conditions. Vectors $\boldsymbol{u}$, $\boldsymbol{p}_m$ and $\boldsymbol{p}_{fr}$ carry the nodal values of displacement and fluid pressures of the matrix and fracture system. Matrix $\boldsymbol{B}$ relates total strain and nodal displacements, $\boldsymbol{N}$ and $\boldsymbol{N}_p$ are the shape functions of displacement and pore pressure degrees of freedom, respectively; α_m and $\alpha_{fr} \approx 1$ are Biot's effective coefficients, and m is a unit vector with components in the normal direction.

The mass balance equation for rock matrix (5.23) and fractures (5.24), after discretization, can be written as:

$$\boldsymbol{R}_{\boldsymbol{m}}^T \frac{\partial \boldsymbol{u}}{\partial t} + (\boldsymbol{W} + \boldsymbol{K}_m)\boldsymbol{P}_m - \boldsymbol{W}\, \boldsymbol{P}_{fr} + \boldsymbol{S}_m \frac{\partial \boldsymbol{P}_m}{\partial t} = \hat{\boldsymbol{q}}_m \tag{5.37}$$

$$\boldsymbol{R}_{fr}^T \frac{\partial \boldsymbol{u}}{\partial t} - \boldsymbol{W}\, \boldsymbol{P}_m + \left(\boldsymbol{W} + \boldsymbol{K}_{fr}\right)\boldsymbol{P}_{fr} + \boldsymbol{S}_{fr} \frac{\partial \boldsymbol{P}_{fr}}{\partial t} = \hat{\boldsymbol{q}}_{fr} \tag{5.38}$$

with

$$\boldsymbol{K}_m = \frac{1}{\mu} \int_{\Omega} \nabla \boldsymbol{N}_p^T \, \boldsymbol{k}_m \nabla \boldsymbol{N}_p d\Omega \tag{5.39}$$

$$\boldsymbol{K}_{fr} = \frac{1}{\mu} \int_{\Omega} \nabla \boldsymbol{N}_p^T \, \boldsymbol{k}_{fr} \nabla \boldsymbol{N}_p d\Omega \tag{5.40}$$

$$\boldsymbol{S}_m = \beta_m \int_{\Omega} \boldsymbol{N}_p^T \boldsymbol{N}_p d\Omega \tag{5.41}$$

$$\boldsymbol{S}_{fr} = \beta_{fr} \int_{\Omega} \boldsymbol{N}_p^T \boldsymbol{N}_p d\Omega \tag{5.42}$$

$$\boldsymbol{W} = \omega_{MD} \int_{\Omega} \boldsymbol{N}_p^T \boldsymbol{N}_p d\Omega \tag{5.43}$$

$$\widehat{\boldsymbol{q}}_m = \int_{\Gamma} \boldsymbol{N}_p^T \boldsymbol{N}_p \boldsymbol{q}_m d\Gamma \tag{5.44}$$

$$\widehat{\boldsymbol{q}}_{fr} = \int_{\Gamma} \boldsymbol{N}_p^T \boldsymbol{N}_p \boldsymbol{q}_{fr} d\Gamma \tag{5.45}$$

where $\boldsymbol{K}_m$ and $\boldsymbol{K}_{fr}$ are the permeability matrices, $\boldsymbol{S}_m$ and $\boldsymbol{S}_{fr}$ are the storage matrix for the rock and fractures, respectively, $\boldsymbol{W}$ is the fluid transfer matrix, $\widehat{\boldsymbol{q}}_m$ and $\widehat{\boldsymbol{q}}_{fr}$ are the source vectors for the rock and fractures. The relative compressibilities for the block matrix, β_m, and fracture system, β_{fr}, are evaluated as (ZHANG; ROEGIERS, 2005):

$$\beta_m = \frac{n_m}{K_f} + \frac{\alpha_m - n_m}{K_s} \tag{5.46}$$

$$\beta_{fr} = \frac{n_{fr}}{K_f} + \frac{\alpha_{fr} - n_{fr}}{s\, k_n} \tag{5.47}$$

where K_f and K_s are the bulk moduli of the fluid and solid grains, respectively; α is Biot's coefficient (BIOT, 1941); for the fracture system $\alpha_{fr} \approx 1$; s is the fracture spacing and k_n is the normal stiffness of the fracture. Matrix porosity is given by n_m and fracture porosity n_{fr} is defined through the sum of a relation between aperture a_n and spacing s of the fracture set i:

$$n_{fr} = \sum_{i=1}^{Nset} \left(\frac{a_n}{s}\right)_i \tag{5.48}$$

where $Nset$ is the total number of fracture sets.

Finally, the matrix form of the fully coupled dual-porosity and dual-permeability model can be defined as:

$$\begin{bmatrix} \mathbf{0} & \mathbf{0} & \mathbf{0} \\ \boldsymbol{R}_m^T & \boldsymbol{S}_m & \mathbf{0} \\ \boldsymbol{R}_{fr}^T & \mathbf{0} & \boldsymbol{S}_{fr} \end{bmatrix} \frac{d}{dt} \begin{Bmatrix} \boldsymbol{u} \\ \boldsymbol{p}_m \\ \boldsymbol{p}_{fr} \end{Bmatrix} + \begin{bmatrix} \boldsymbol{K} & -\boldsymbol{R}_m & -\boldsymbol{R}_{fr} \\ \mathbf{0} & \boldsymbol{K}_m + \boldsymbol{W} & -\boldsymbol{W} \\ \mathbf{0} & -\boldsymbol{W} & \boldsymbol{K}_{fr} + \boldsymbol{W} \end{bmatrix} \begin{Bmatrix} \boldsymbol{u} \\ \boldsymbol{p}_m \\ \boldsymbol{p}_{fr} \end{Bmatrix} = \begin{Bmatrix} \hat{\boldsymbol{f}} \\ \hat{\boldsymbol{q}}_m \\ \hat{\boldsymbol{q}}_{fr} \end{Bmatrix} \tag{5.49}$$

5.2.1. Fully coupled solution scheme

A general form of system (5.49) is as follows:

$$\boldsymbol{C}_{(X)}\dot{\boldsymbol{x}} + \dot{\boldsymbol{K}}_{(X)}\boldsymbol{x} = \hat{\boldsymbol{f}}_{ext} \tag{5.50}$$

where

$$\boldsymbol{C} = \begin{bmatrix} \mathbf{0} & \mathbf{0} & \mathbf{0} \\ \boldsymbol{R}_m^T & \boldsymbol{S}_m & \mathbf{0} \\ \boldsymbol{R}_{fr}^T & \mathbf{0} & \boldsymbol{S}_{fr} \end{bmatrix} \tag{5.51}$$

$$\dot{\boldsymbol{K}} = \begin{bmatrix} \boldsymbol{K} & -\boldsymbol{R}_m & -\boldsymbol{R}_{fr} \\ \mathbf{0} & \boldsymbol{K}_m + \boldsymbol{W} & -\boldsymbol{W} \\ \mathbf{0} & -\boldsymbol{W} & \boldsymbol{K}_{fr} + \boldsymbol{W} \end{bmatrix} \tag{5.52}$$

$\hat{\boldsymbol{f}}_{ext}$ represents the right-hand side of equation (5.49). Equation (5.50) represents a nonlinear system of ordinary differential equations. The implicit θ-method was adopted for time integration of equation (5.50) due to its robustness and efficiency. This method uses the following approximations:

$$\boldsymbol{x}_{n+1} = \boldsymbol{x}_n + \Delta t\{(1-\theta')\boldsymbol{x}_n + \theta'\boldsymbol{x}_{n+1}\} \tag{5.53}$$

$$\dot{\boldsymbol{x}}_{n+\theta} = \frac{\{\boldsymbol{x}_{n+1} - \boldsymbol{x}_n\}}{\Delta t} \tag{5.54}$$

Including equations (5.53) and (5.54) in (5.50), the following equation is obtained:

$$\frac{\{\boldsymbol{x}_{n+1} - \boldsymbol{x}_n\}}{\Delta t} + \dot{\boldsymbol{K}}\{(1-\theta')\boldsymbol{x}_n + \theta'\boldsymbol{x}_{n+1}\} = \{(1-\theta')\hat{\boldsymbol{f}}_{ext,n} + \theta'\hat{\boldsymbol{f}}_{ext,n+1}\} \tag{5.55}$$

where Δt is the time step increment, and θ' is an integration parameter in the range $0 \le \theta' \le 1$; $\theta' = 0$ is the explicit time-stepping scheme and $\theta' = 1$ is the implicit Backward Euler scheme. The implicit scheme is unconditionally stable and has excellent damping characteristics. In this case, the incremental solution for the field variables is:

$$\left[\boldsymbol{C} + \Delta t\dot{\boldsymbol{K}}\right]\{\Delta \boldsymbol{x}_{n+1}\} = \Delta t\hat{\boldsymbol{f}}_{ext,n+1} - \Delta t\dot{\boldsymbol{K}}\boldsymbol{x}_n \tag{5.56}$$

In general, matrices $\boldsymbol{C}$ and $\dot{\boldsymbol{K}}$ can depend on the values of $\boldsymbol{x}_{n+1}$. In that case, the previous system is nonlinear, and an iterative method must be applied to obtain the solution. Here, the Newton-Raphson method is adopted due to its robustness and quadratic convergence rate. After an expansion of Eq (5.55), the residual vector ($\boldsymbol{r}$) of the system is defined as:

$$\boldsymbol{r}_{(\boldsymbol{x}_{n+1})} = \Delta t\widehat{\boldsymbol{F}}_{ext,n+1} - \Delta t\dot{\boldsymbol{K}}\boldsymbol{x}_n - \left[\boldsymbol{C} + \Delta t\dot{\boldsymbol{K}}\right]\{\boldsymbol{x}_{n+1} - \boldsymbol{x}_n\}\boldsymbol{x}_n \tag{5.57}$$

The Newton-Raphson method solves the governing equations by applying the unbalanced generalized forces, computing the corresponding field variables, and then iterating until the drift from the solution is small. Several techniques have been developed (CRISFIELD, 2000; SHENG; SLOAN, 2003, 2001; SHENG; SLOAN; ABBO, 2002) to improve the convergence of the method in the presence of strong nonlinearities.

5.3. Model verification and validation against DFM

The EDPDP model is implemented in an in-house framework GeMA (Geo Modelling Analysis)(MENDES; GATTASS; ROEHL, 2016) using conventional continuum finite elements. GeMA is a library intended to support the development of new multiphysics simulators and its integration with existing ones. One of its functionalities is the support for the efficient transfer of state variables among different meshes. The framework also implements some important concepts of extensibility through the combined use of plugins and abstract interfaces, configurable orchestration, and fast prototyping through the use of the Lua language. This versatility is very helpful to show specific results in any post processor package. We have implemented a user script function to represent variables of pore pressure, hydraulic conductivity, and aperture changes in the fractures, among others. These results are shown throughout this work.

The proposed approach is verified and validated against the discrete fracture model. In that case, fractures are represented explicitly using interface elements. Mechanical, hydraulic, and fully coupled poromechanical examples are simulated to demonstrate the capabilities of the methodology. The examples study the influence of fracture dip angle on the rock block stiffness and flow rate and

investigate the coupling effects. Also, we evaluate different mesh sizes to study mesh convergence of the proposed approach.

5.3.1. Effects of fractures on the elastic response of the rock block

Two uniaxial compressive models are simulated to study the influence of fractures on the deformability of fractured rock. In the first test, a cylinder with one fracture set is compressed by applying 10 MPa at the top surface. The base is constrained in the z-direction, while the lateral wall is constrained in the x and y directions. A second test considers two orthogonal fracture sets. Figure 5.4 shows the geometry and boundary conditions with set 1 in green and set 2 in red. Table 5.1 summarizes the material properties of the rock and the fracture sets.

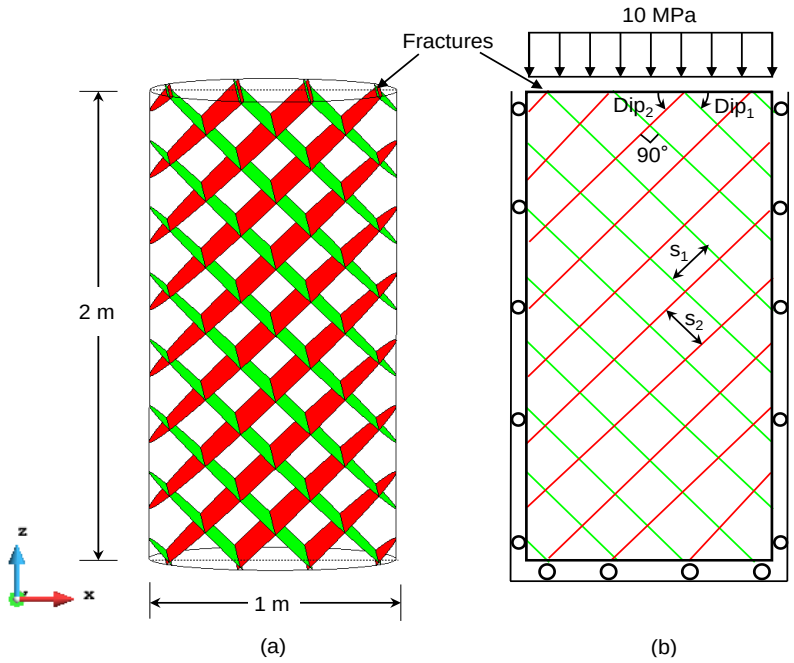

Figure 5.4. Uniaxial model: (a) 3D fractured rock cylinder with fracture set 1 (green) and fracture set 2 (red), (b) cross-section of the cylinder with boundary conditions.

Table 5.1. Mechanical properties of the intact rock and the fracture sets.

Parameters	Units	Rock	set 1	set 2
Young's modulus, E	kPa	1.0e+07		
Poisson's ratio, ν	--	0.2		
Normal stiffness, k_n	kPa/m		2.0e+07	3e+07
Tangential stiffness, $k_{t1} = k_{t2}$	kPa/m		2.0+e07	1.5e+07
Spacing, s	m		0.2	0.2

The numerical simulations are performed for dip angles of 0°, 30°, 45°, 60°, and 90° with constant strike angle of 0° and 180° for fracture sets 1 and 2,

respectively. For validation purposes, the numerical models were also carried out using the Discrete Fracture Model based on the zero-thickness interface element (SEGURA; CAROL, 2008b). Figure 5.5 and Figure 5.6 show the computed displacement in z-direction for tests 1 and 2, respectively, using discrete fracture and dual-porosity models. Figure 5.7 and Figure 5.8 show the vertical displacement at the top of the cylinder versus fracture inclination. The numerical results show good agreement between the discrete fracture and dual-porosity models.

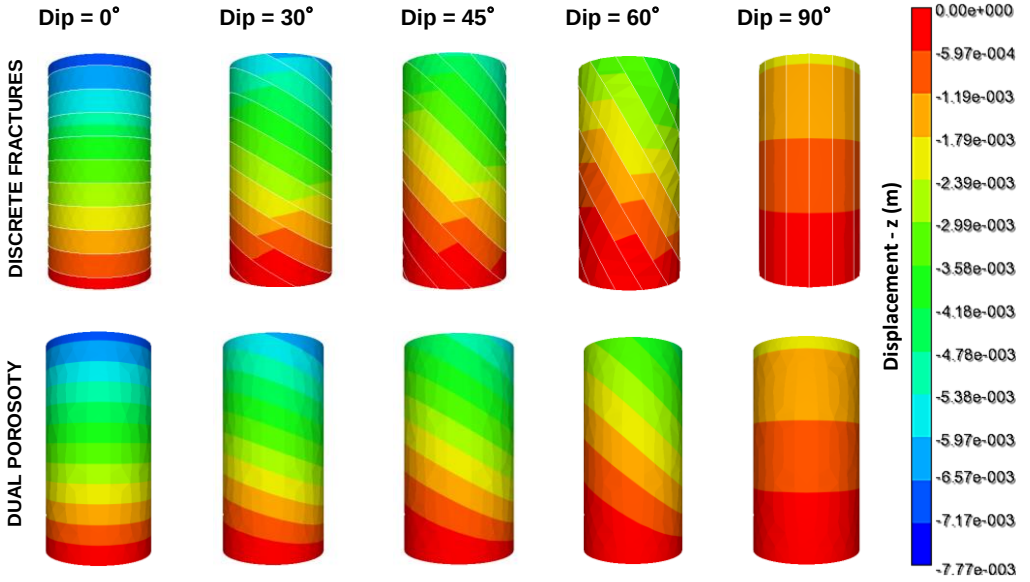

Figure 5.5. Uniaxial test 1 (one fracture set): Vertical displacement for different dip angles using discrete fractures (upper) and enhanced dual-porosity model (lower).

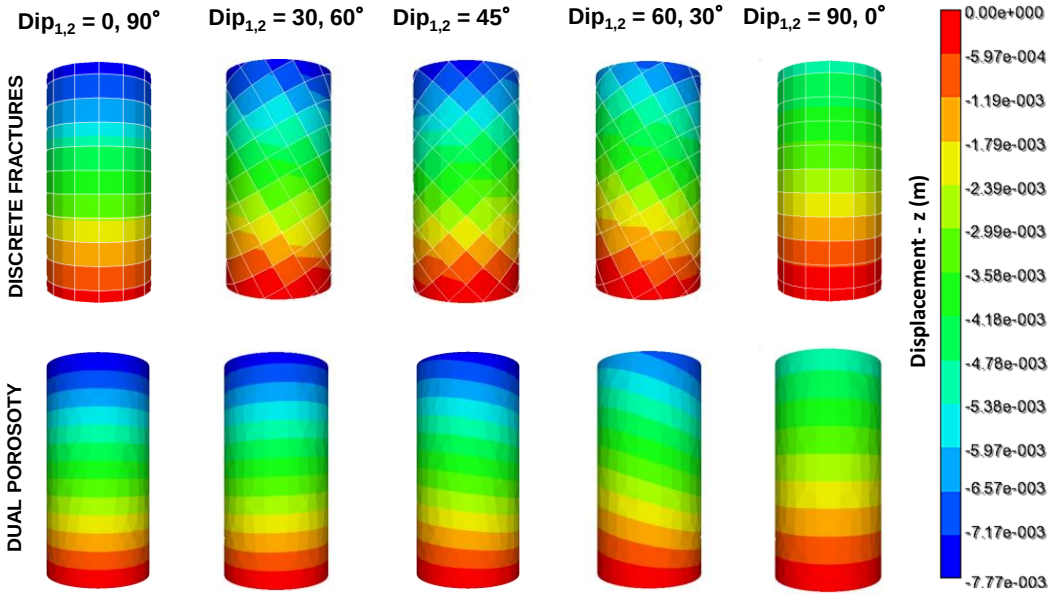

Figure 5.6. Uniaxial test 2 (two fracture sets): vertical displacement for different dip angles using discrete fractures (upper) and enhanced dual-porosity model (lower).

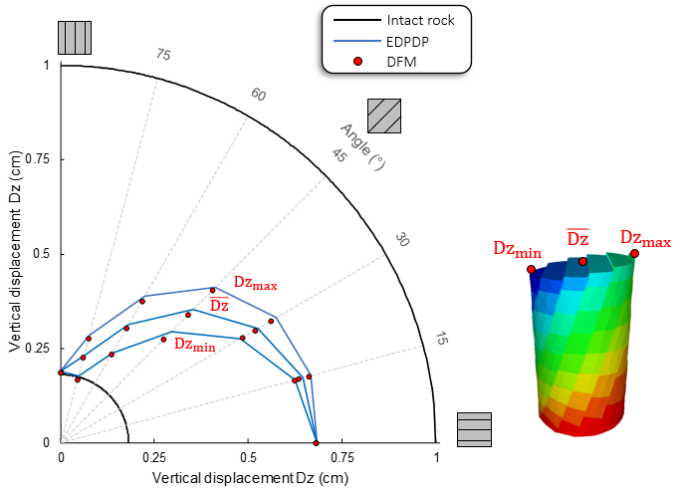

Figure 5.7. Uniaxial test 1 (one fracture set): vertical displacement at the top of the cylinder at points Dz_{min} , $\overline{Dz}$ and Dz_{max}.

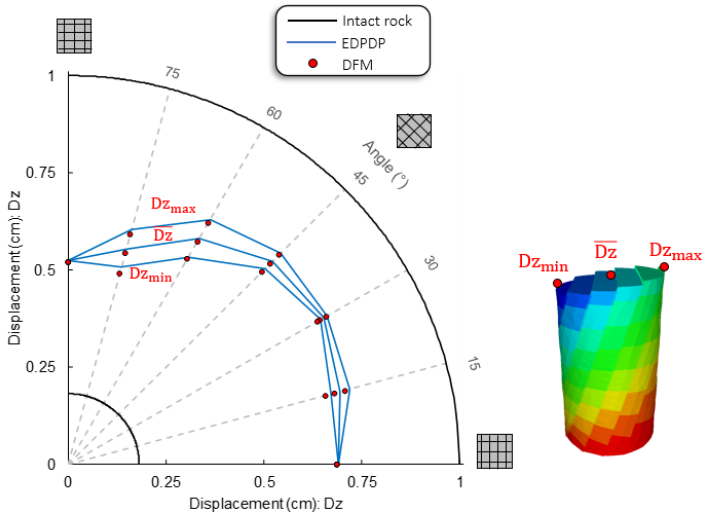

Figure 5.8. Uniaxial test 2 (two fracture sets): vertical displacement at the top of the cylinder at points Dz_{min} , $\overline{Dz}$ and Dz_{max}.

As depicted in Figure 5.5 and Figure 5.7, the cylinder containing one fracture set parallel to the load (dip angle of 90°) behaves as an intact rock. When the dip angle is reduced, the vertical displacement increases to the maximum vertical displacement value at a dip angle of 0° (perpendicular to loading). This behavior can be explained through unidimensional simplification, neglecting shear displacement and dilatation, giving the equivalent stiffness of the matrix and fracture system in the axial direction as:

$$\frac{1}{E_{mfr}} = \frac{1}{E} + \frac{1}{sk_n}\cos(\varphi) \tag{5.58}$$

where E_{mfr} is the equivalent stiffness of the rock and fracture system, E is Young's modulus of the rock, s is the fracture spacing, k_n is the normal stiffness of the

fracture, and φ is the dip angle of the fracture surface. In Figure 5.9, we can observe that a lower equivalent stiffness is obtained for a dip angle of 0°, increasing with fracture inclination up to the intact rock stiffness for a dip angle of 90°.

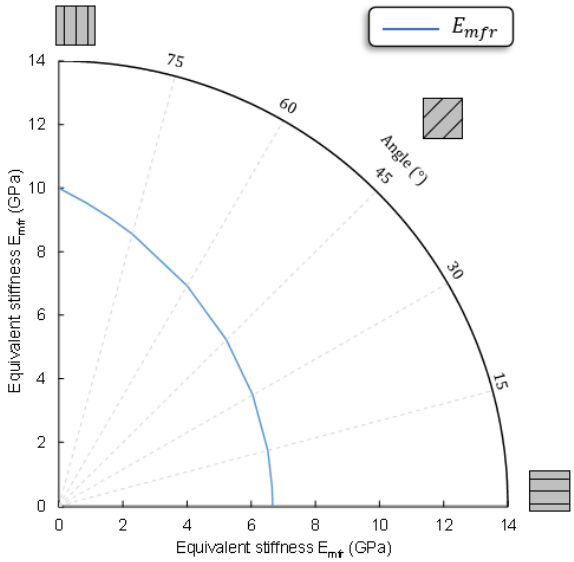

Figure 5.9. Equivalent stiffness (matrix and fracture system) for different dip angles of the fracture set.

In test 2, Figure 5.6 and Figure 5.8, the combined effect of two fracture sets increases the vertical deformability of the cylinder. Also, the deformability in the fractured rock system is not symmetric due to the lower stiffness of fracture set 1 in comparison to fracture set 2. Therefore, it is clear that fracture stiffness, spacing, inclination, and the interaction of fracture sets affect the fractured rock system's mechanical behavior.

5.3.2. Effects of fractures on the pore pressure distribution and fluid flow

In this case, we study the impact of fracture set orientation on the fluid flow. A saturated block is under an initial pore pressure (P_0) of 60 MPa. The transient flow results from the pressure differences between the right and left sides of the fractured rock. A pore pressure increment (ΔP_1) of 1 MPa is applied on the left side of the model while the right side keeps the initial pore pressure P_0. The top and bottom sides are assumed impermeable. Figure 5.10 shows the geometry and boundary conditions. Table 5.2 summarizes the material properties of the rock matrix and fracture sets.

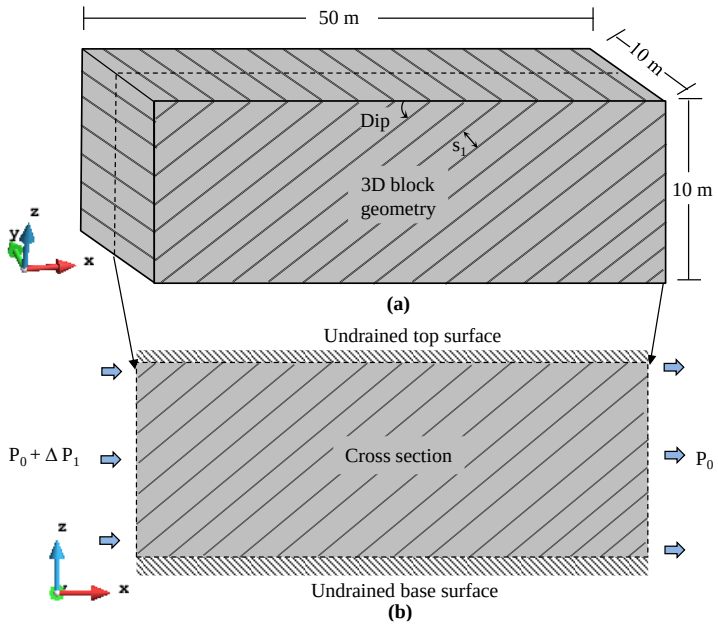

Figure 5.10. Hydraulic problem: (a) 3D fractured rock block geometry, (b) cross-section of the block with boundary conditions.

Table 5.2. Intact rock and fracture set properties for hydraulic model

Parameters	Units	Rock	Set 1
Rock permeability, k_m	mD	350	--
Dynamic fluid viscosity, μ	cp	1	1
Porosity, n_m	--	0.075	--
Initial pore pressure, P_0	MPa	60	60
Pore pressure increment, ΔP_1	MPa	1	1
Relative compressibility, β_{fr}	kPa^{-1}	3.41e-06	1.3e-10
Dip angle, φ	(°)	--	0/30/45/60/90
Fracture aperture, a_0	m	--	3.0e-04
Fracture spacing, s	m	--	1.0

Several scenarios are investigated considering a fracture set with a strike of 180° and dip of 0°, 15°, 30°, 45°, 60°, 75°, and 90°. The numerical simulations are performed over 1000 s. Figure 5.11 shows the computed pore pressure distribution in the cross-section using discrete fracture and enhanced dual-porosity models. It is clear how the fluid migration path is affected by fracture orientation. Figure 5.12 shows the fluid flow outing from the right side along time. Excellent agreement is present between the discrete fracture and enhanced dual-porosity models. Higher outflow happens when the fracture orientation tends to horizontal, where fracture orientation is parallel to fluid flow lines.

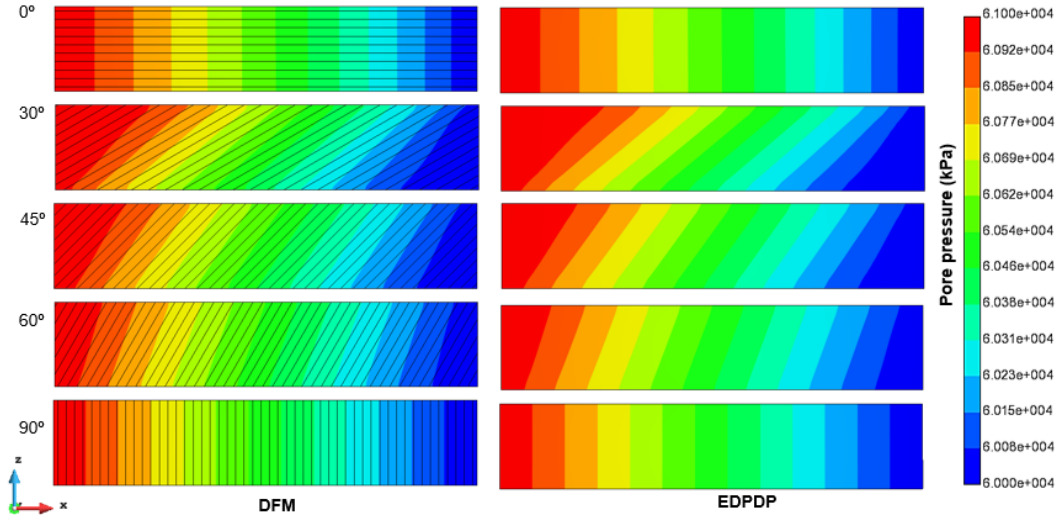

Figure 5.11. Pore pressure distribution in the cross-section of the fractured block for different dip angles.

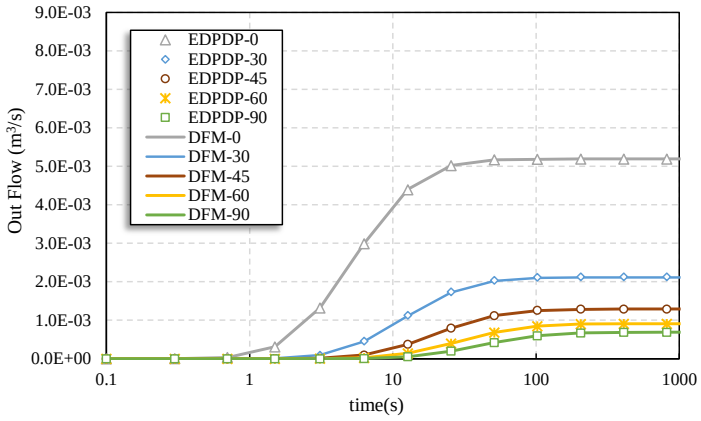

Figure 5.12. Fluid discharge on the right side along time for different fracture orientations.

This behavior can be explained by evaluating the equivalent permeability of the matrix and fracture systems in x-direction as:

$$k_{mfr} = k_m + k_{fr} = k_m + \frac{a_0^3}{12s}\cos(\varphi) \tag{5.59}$$

where k_{mfr} is the equivalent permeability of the rock-fracture system in the *x*-direction, k_m is the rock permeability, s is the fracture spacing, a_0 is the initial fracture aperture, and φ is the dip of the fracture surface. In Figure 5.13, we can observe that higher equivalent permeability is obtained for a dip of 0° and decreases with the dip angle until it reaches the permeability of the porous rock for $\varphi = 90°$.

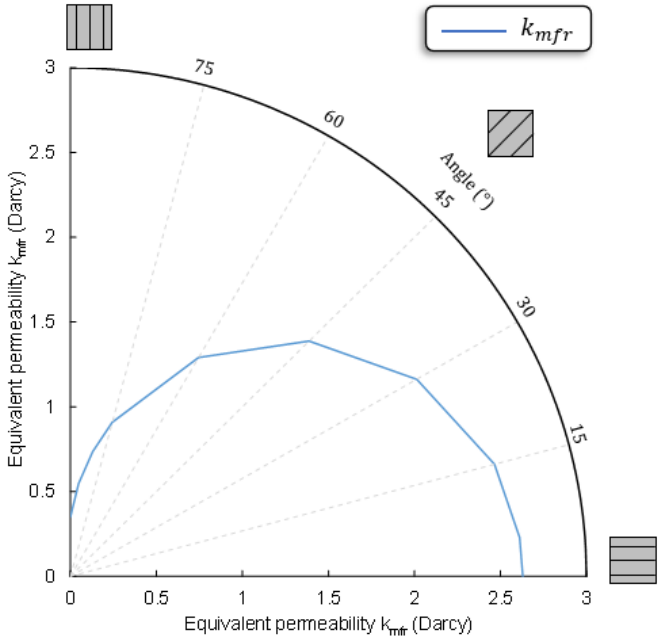

Figure 5.13. Equivalent permeability (matrix-fracture system) for different dip angles of the fracture set.

5.3.3. Coupled geomechanics and fluid flow in a fractured rock block

We also study the effects of coupled geomechanics and fluid flow in a fractured rock block. The model is based on the proposed hydraulic example presented in the previous section. In this case, the proposed approach considers stress-induced aperture changes to update stiffness and permeability tensors. The saturated block is under an initial pore pressure (P_0) of 55 MPa and initial effective stress state (σ'_0) of 30 MPa. The base is constrained vertically, while the lateral walls are constrained in the horizontal plane in both directions. The top and bottom sides are assumed to be impermeable.

The numerical test follows two steps. In the first step, a uniform pore pressure increment ($\Delta P_0 = 5$ MPa) is applied in the entire model, inducing fracture opening. In the second step, transient flow results from the pressure differences between the right and left sides of the fractured rock. On the left side, a pore pressure increment ($\Delta P_1 = 1$ MPa) is applied while the right side keeps the pore pressure ($P_0 + \Delta P_0 = 60$ MPa). Figure 5.14 shows a schematic representation of the block cross-section with the adopted boundary conditions in steps 1 and 2. Table 5.3 summarizes the material properties of the rock and fracture sets.

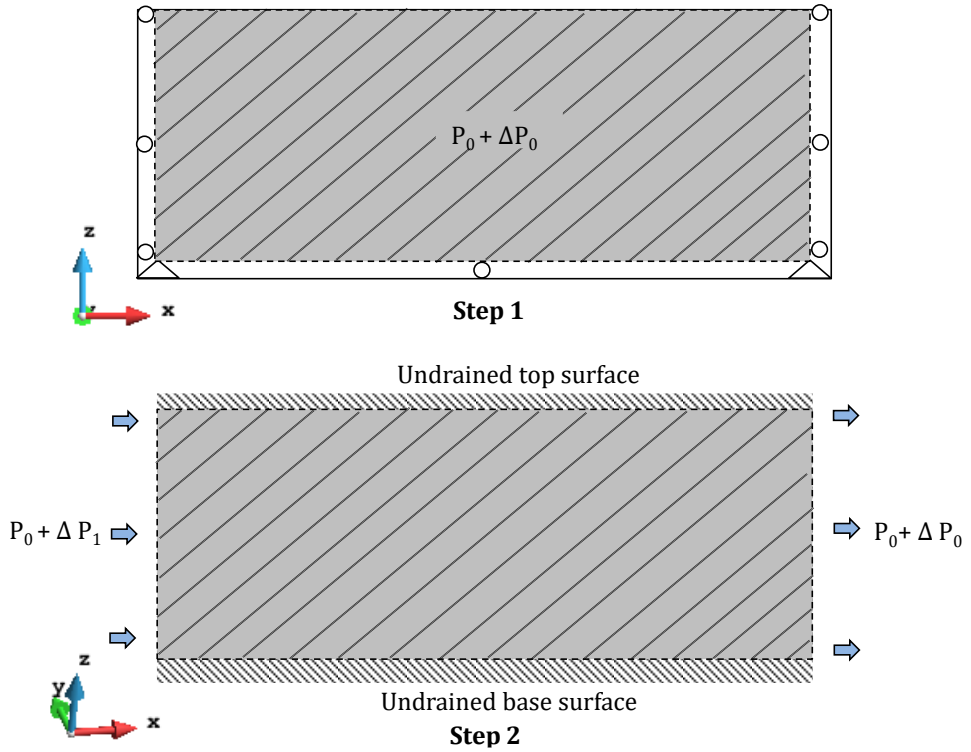

Figure 5.14. Cross-section of the block with boundary conditions in step 1 (upper) and step 2 (lower).

Table 5.3. Hydro-mechanical properties for the rock matrix and the fracture set.

Parameters	Units	Rock	Set 1
Young's modulus, E	kPa	1.69e7	--
Possion's ratio, υ	---	0.32	--
Permeability k_m	mD	350	--
Dynamic fluid viscosity, μ	cp	1	1
Porosity, n_m	---	0.075	--
Initial effective stress, σ'_0	MPa	30	30
Initial pore pressure, P_0	MPa	55	55
Pore pressure increment, $\Delta P_0/\Delta P_1$	MPa	5/6	5/6
Elastic normal stiffness of fracture, k_n	kPa/m	--	1.2e7
Elastic tangential stiffness of fracture, $k_{t1,2}$	kPa/m	--	5.5e6
Dip angle, φ	(°)	--	0/30/45/60/90
fracture aperture, a_0	m	--	3.0e-4
Small Fracture spacing, s	m	--	1.0

Several scenarios are investigated considering fracture sets with a strike of 180° and dip of 0°, 15°, 30°, 45°, 60°, 75°, and 90°. The numerical simulations are performed for 1000 s.

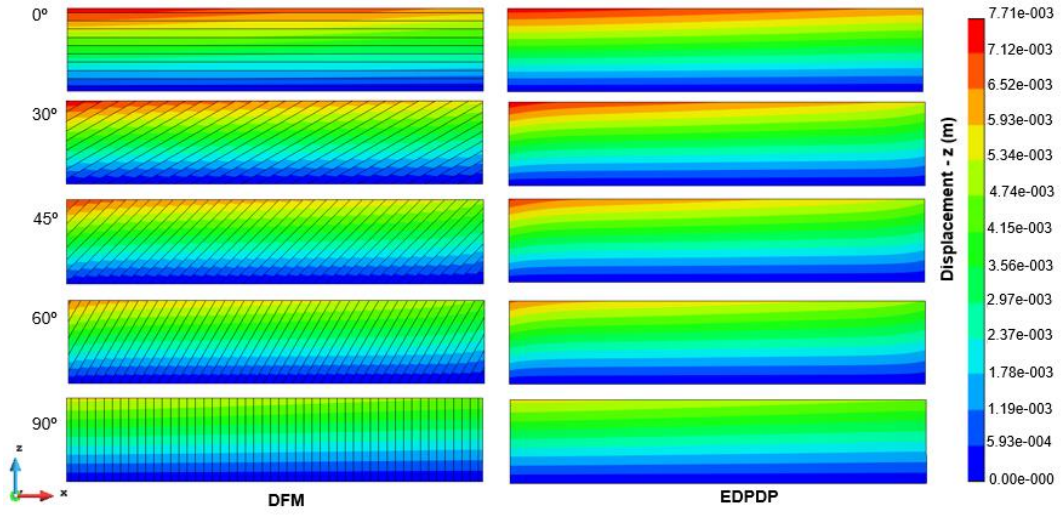

Figure 5.15.Vertical displacement in the cross-section of the block for different dip angles.

Figure 5.15 shows the computed vertical displacement using discrete fracture and enhanced dual-porosity models. In this case, the higher pore pressure on the left side results in a higher vertical displacement from left to right. Figure 5.16 shows the fluid discharge from the right side along time.

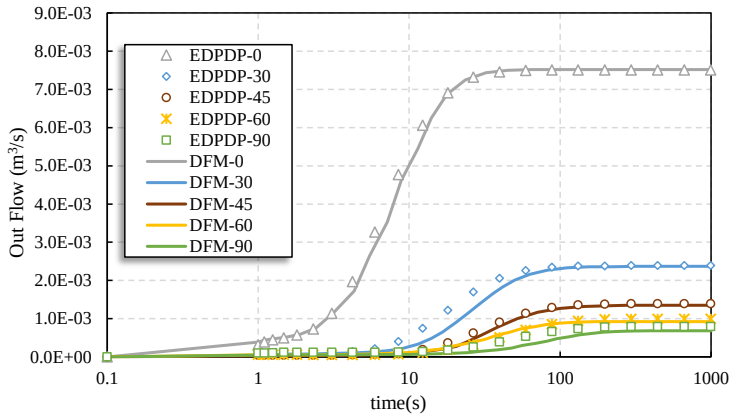

Figure 5.16. Fluid discharge on the right side along time.

Figure 5.17 shows the fracture opening induced by the coupled effect of fluid pressure and stress variation using the enhanced dual-porosity model. Larger fracture openings happen when fracture orientation is aligned with fluid flow lines. Consequently, Figure 5.16 shows that the outflow obtained in the hydro-mechanical model is higher than that in the hydraulic model (Figure 5.12). In contrast, smaller aperture changes and discharge are obtained when the fracture orientation is perpendicular to the fluid flow lines.

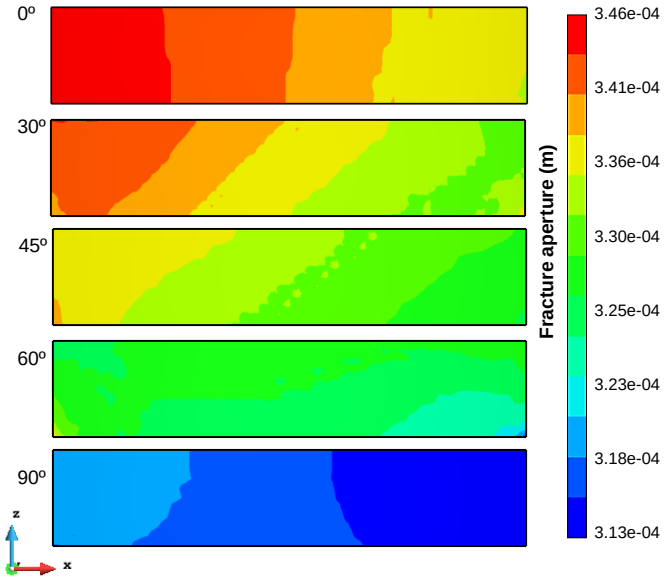

Figure 5.17. Fracture aperture in the cross-section of the block for different dip angles.

Considering a fracture set with a dip of 30°, we evaluate four different mesh sizes to study the mesh convergence of the proposed approach. We use a structured mesh formed by hexahedra elements with edges of 1, 2, 5, 10 m. The fracture spacing is 1 m in all cases. Figure 5.18 shows the computed vertical displacement, while Figure 5.19 presents the settlement along the top surface of the block using the enhanced dual-porosity model with different mesh sizes. The excellent agreement demonstrates that the numerical results using the proposed EDPDP approach do not depend on element size. Therefore, this new approach allows modeling highly fractured formations in field-scale reservoir simulations. In these cases, DFMs can be computationally expensive and practically unachievable.

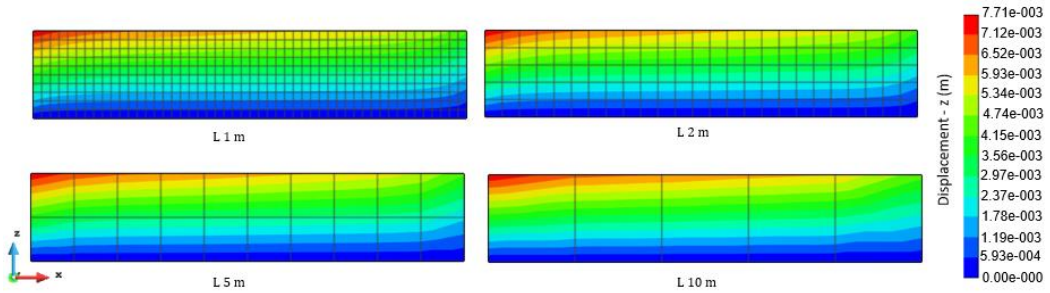

Figure 5.18. Vertical displacement in the cross-section of the block for different mesh sizes.

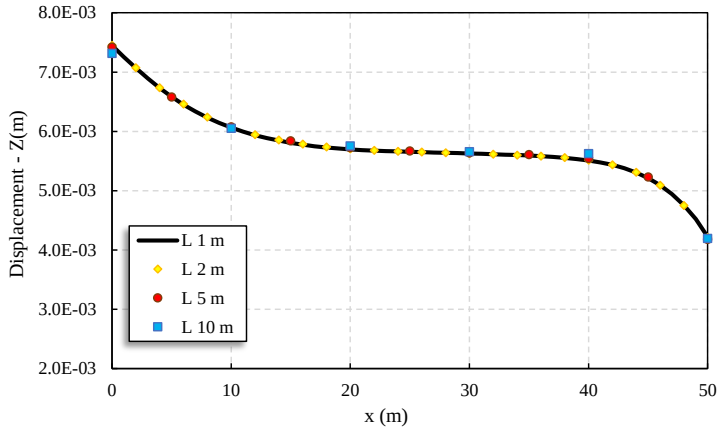

Figure 5.19. Vertical displacement along the top surface of the block for different mesh sizes.

We also show the impacts of dip and strike of the FN set on the hydro-mechanical behavior of a fractured formation. This example considers a fracture set with a spacing of 1 m, a strike of 315°, and a dip of 60°. Figure 5.20 shows the computed vertical displacement and pore pressure distribution using the DFM and EDPDP model. It is clear how the trajectory of fluid migration and mechanical deformation is affected by the fracture orientation.

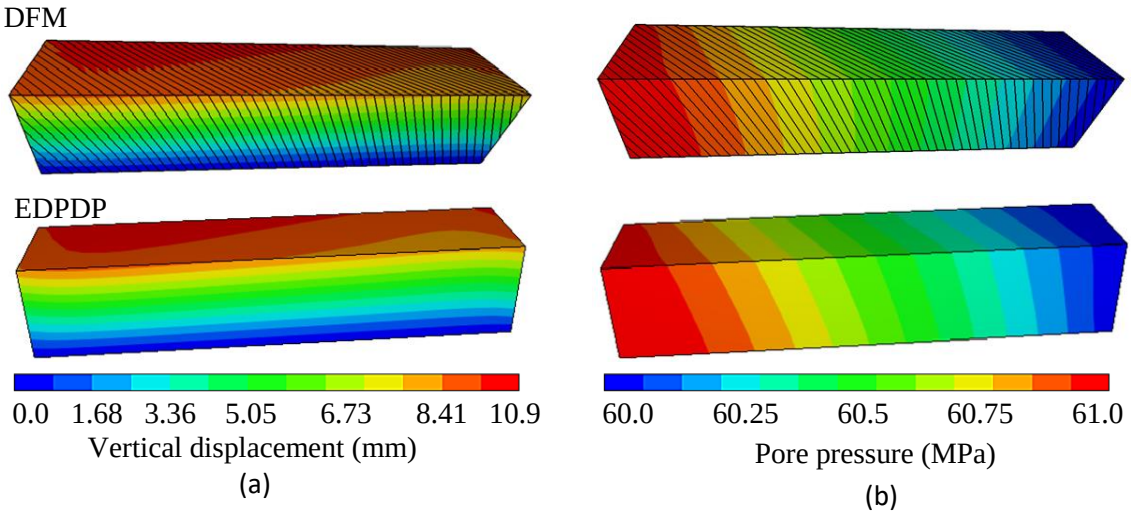

Figure 5.20. Comparison between DFM and EDPDP (a) vertical displacement and (b) pore pressure distribution.

Figure 5.21 shows the fluid discharge on the right side during the simulation time. The comparison between DFM and EDPDP shows excellent agreement that validates the proposed hydro-mechanical formulation of EDPDP model.

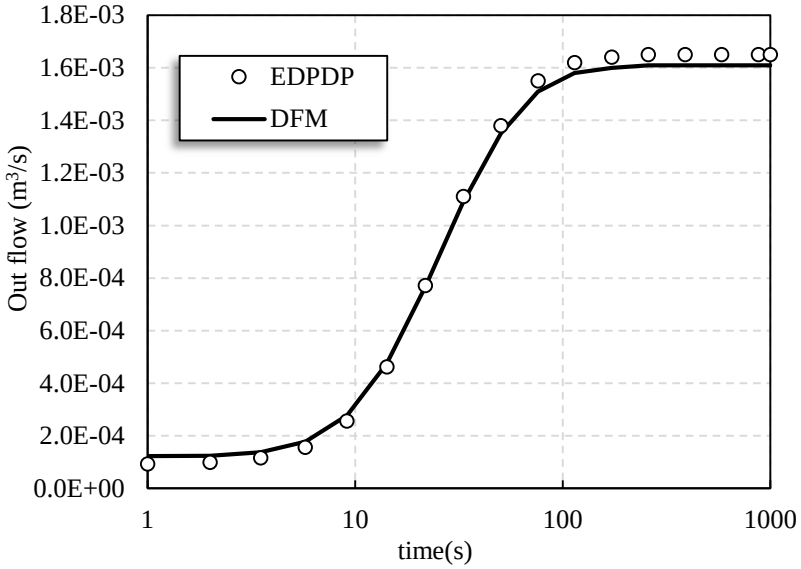

Figure 5.21. Discharge on the right side during the simulation time in the fractured block using EDPDP and DFM.

Finally, we study the hydromechanical effects of an anisotropic intact rock on the fractured block. In this case, we consider the Young modulus $E_x = E_y = E/2$, $E_z = E$, and the rock permeability $k_{mx} = k_{my} = 2\ k_m$, $k_{mz} = k_m$, where k_m and E are presented in Table 5.3. We also consider a fracture set with a spacing of 1 m, a strike of 315°, and a dip of 60°.

Figure 5.22 shows the fluid discharge on the right side during the simulation for isotropic and anisotropic intact rock blocks. As expected, initial higher discharge in the anisotropic block rock results from higher rock permeability in the horizontal direction. Figure 5.23 presents the settlement along the top surface of the block for isotropic and anisotropic rock materials. In this case, lower stiffness in the anisotropic rock results in a higher settlement of the fractured block, and consequently, in a smaller fracture opening. For that reason, the fluid discharge decreases over time, see Figure 5.22.

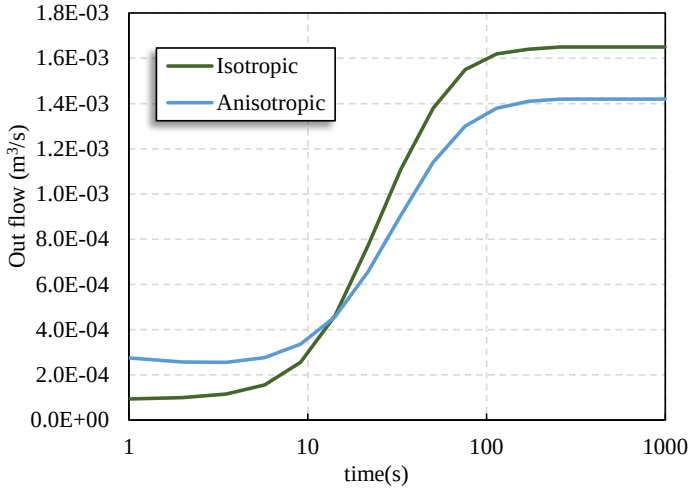

Figure 5.22. Discharge on the right side during the simulation time considering isotropic and anisotropic fractured blocks.

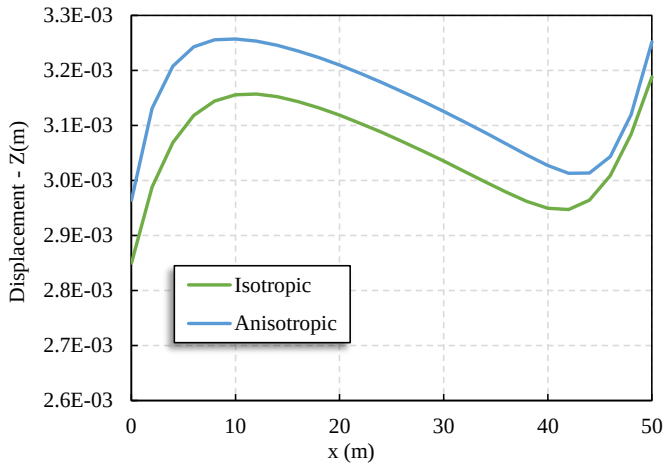

Figure 5.23. Vertical displacement along the top surface considering isotropic and anisotropic fractured blocks.

5.4. Fluid flow through a deformable reservoir with multiscale fracture sets

To show the proposed model's applicability and robustness, we simulate fluid flow through a deformable reservoir considering fracture sets of multiple scales and arbitrary orientations. Two cases are investigated to assess the impact of primary and secondary fractures on fluid flow. Figure 5.24 shows the geometry and boundary conditions of the reservoir formed by primary (sets 1 and 2) and secondary (sets 3 and 4) fractures. The first case considers only the primary fracture sets; the second case includes both primary and secondary fracture sets. The reservoir is under an initial pore pressure ($P_0 = 55$ MPa) and an initial effective stress state ($\sigma'_0 = 30$ MPa). The base is constrained in the vertical direction; right and left walls are constrained in the x-direction and upper and lower walls in the y-

direction. The surrounding rocks of the fractured reservoir are assumed impermeable. A producer well is in the center of the model with constant pressure ($P_w = 45$ MPa). The numerical simulation considers a period of 30,000 s. Table 5.4 summarizes the material properties of the rock matrix and fracture sets.

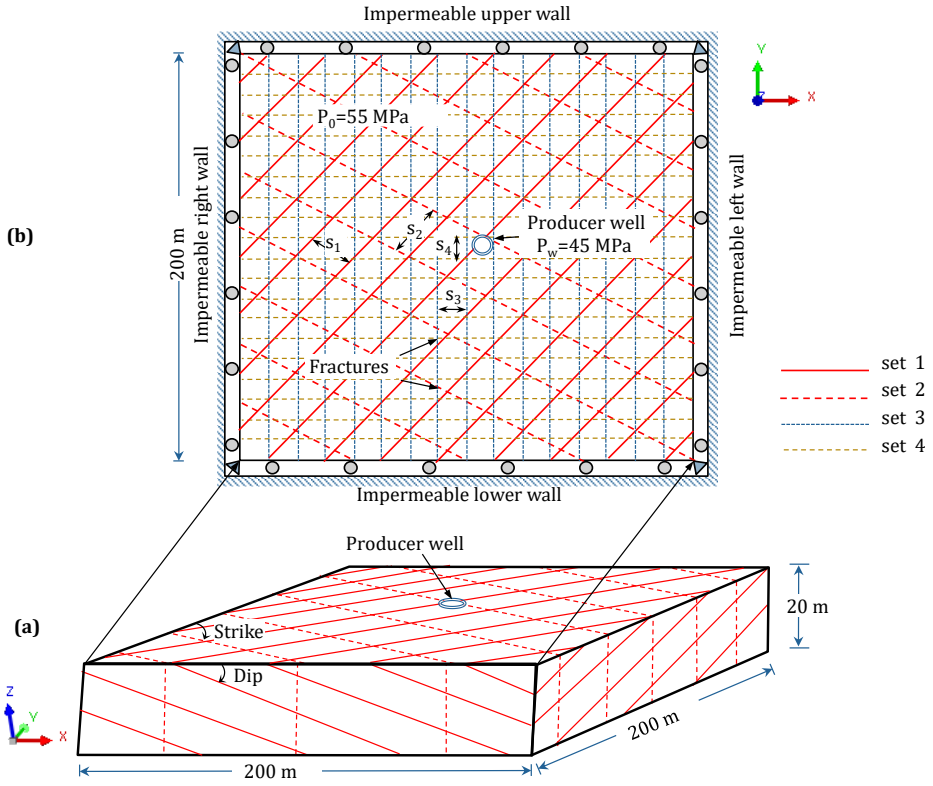

Figure 5.24. 3D reservoir model for coupled simulation: (a) Idealized reservoir with primary (sets 1 and set 2) fractures; (b) top view of reservoir model including secondary (set 3 and set 4) fractures and boundary conditions.

Table 5.4. Hydro-mechanical properties of the rock matrix and fracture sets.

Parameters	Units	Rock	Set i
Young's modulus, E	kPa	6e07	--
Possion's ratio, υ	---	0.28	--
Permeability k	mD	3	--
Porosity	--	0.25	--
Initial stress, σ'_0	MPa	30	30
Initial pore pressure, P_0	MPa	55	55
Bottom hole pressure at the producer, P_w	MPa	45	45
Elastic normal stiffness of fracture, k_n	kPa/m	--	3.0e07
Elastic tangential stiffness of fracture, $k_{t1,2}$	kPa/m	--	1.5e07
Fracture strike, θ_1 / θ_2 /θ_3 / θ_4 (°)	(°)	--	45/150/0/90
Fracture dip, φ_1 / φ_2 /φ_3 / φ_4 (°)	(°)	--	30/90/40/45
fracture aperture, $a_{01} = a_{02}$ /$a_{03} = a_{04}$	m	--	3e-04/1.5e-04
Fracture spacing, s_1 / s_2 /s_3 / s_4	m	--	12/15/4/4

Figure 5.25 shows the pore pressure distribution for cases 1 and 2 at 40,000 s. In case 1, the pore pressure through fracture set 2 becomes dominant. This effect is reduced in case 2 due to the presence of fracture sets 3 and 4, which enhance permeability leading to a higher initial production rate than in case 1, as shown in Figure 5.26. However, a higher production rate induces higher reservoir pore pressure gradients. Consequently, fracture aperture decreases more rapidly in case 2, as highlighted in Figure 5.27 and Figure 5.28, reducing the permeability of the system with a subsequent decrease in the production rate. Fracture orientation is another parameter that can influence the hydro-mechanical coupling mechanism. Figure 5.27 and Figure 5.28 show that fracture set 1 presents higher closure than fracture set 2. That happens because since fracture set 1 has a low dip, it is more sensitive to vertical displacements. For that reason, fracture set 2 is dominant regarding fluid flow, as shown in Figure 5.25.

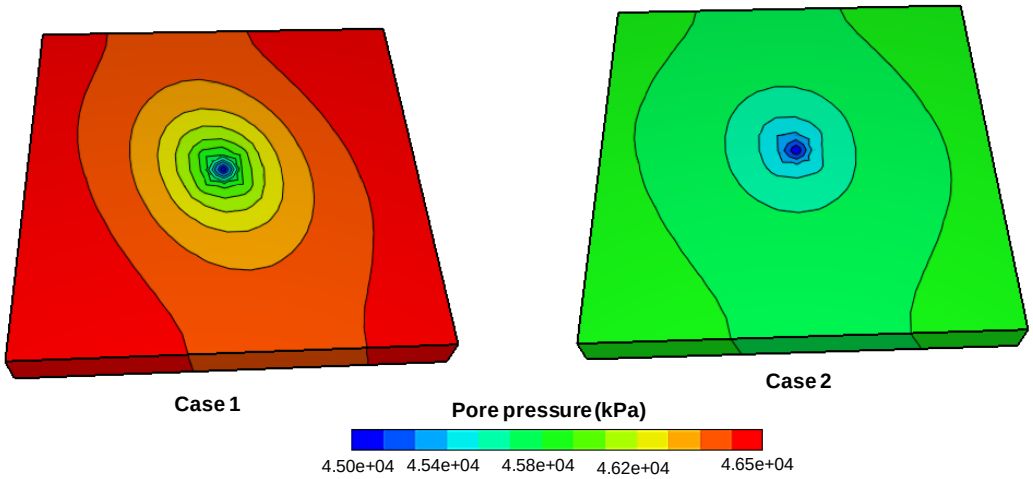

Figure 5.25. Pore pressure distribution in the fractured reservoir for cases 1 (left) and 2(right).

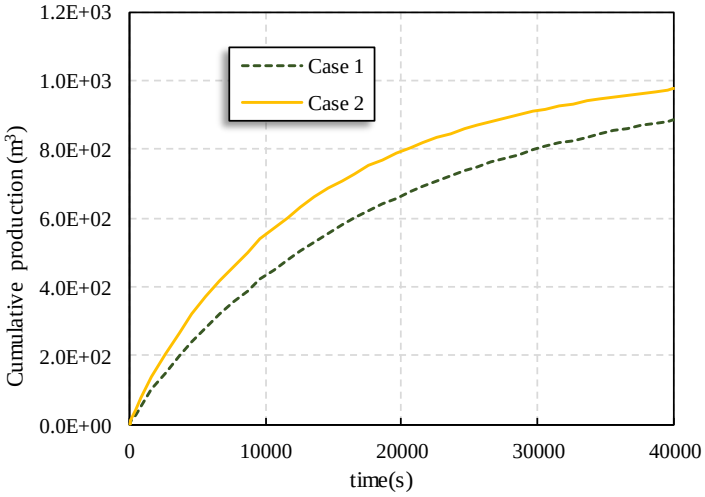

Figure 5.26. Cumulative production along the time.

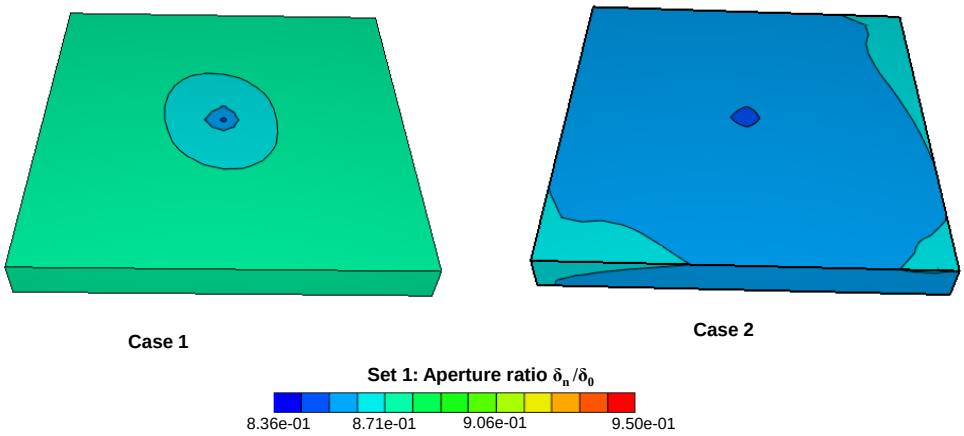

Figure 5.27. Fracture Set 1: Aperture ratio (δ_n / δ_0) for case 1 (left) and case 2(right).

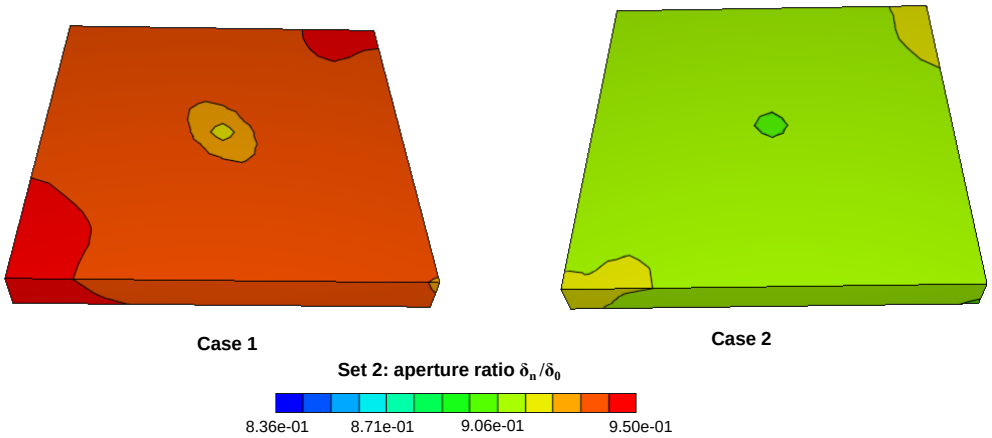

Figure 5.28. Fracture set 2: aperture ratio (δ_n / δ_0) for case 1 (left) and case 2(right).

Figure 5.29 shows the aperture variation in fracture sets 3 and 4 for case 2. It is observed that the closure of those fractures is higher than fracture sets 1 and 2. This behavior is related to the smaller spacing and higher fracture density reducing system stiffness.

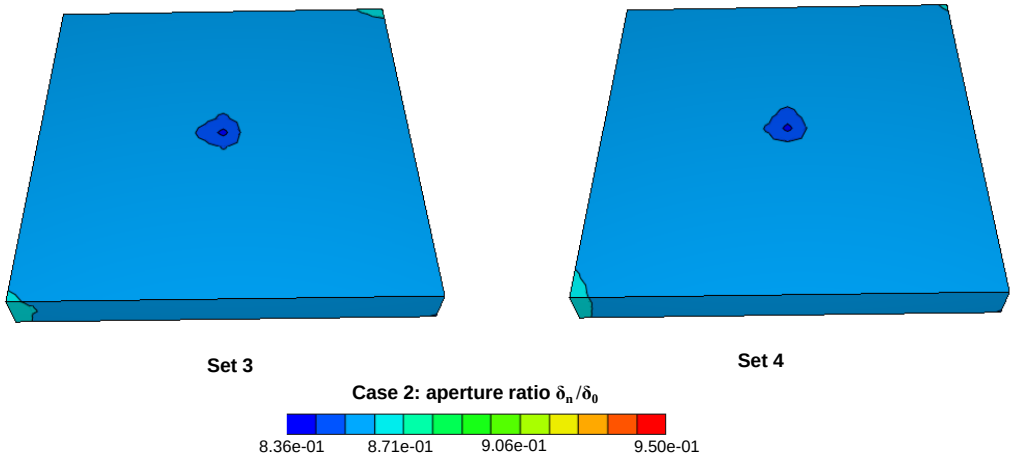

Figure 5.29. Case 2: aperture ratio (δ_n / δ_0) for the fracture set 3 (left) and set 4 (right).

The results show the importance of fracture spacing, aperture changes, and fracture orientation in the flow process in a deformable fractured formation. Smaller fracture spacing enhances the permeability and reduces the strength of the fractured rock mass. Aperture variation induced by pore pressure and stress changes affects the production performance and the final fluid recovery of a naturally fractured reservoir. This aperture variation can be more or less sensitive, depending on fracture orientation. Therefore, proper estimation of fluid drainage rate and pore pressure dissipation requires considering the hydro-mechanical coupling mechanism.

5.5. Concluding remarks

This study proposes a new hydro-mechanical formulation for an enhanced dual porosity and dual permeability model (EDPDP) using the finite element method (FEM) to represent a fractured porous formation more realistically. The formulation is implemented in the in-house multiphysics framework GeMA (Geo Modelling Analysis). The computational framework addresses fundamental challenges in the simulation of fluid flow in deformable fractured media: multi-rock block domains formed by several sets of fractures with multiple scales, arbitrary orientations, permeabilities, and sizes. The fully coupled hydro-mechanical model includes fracture orientations and stress-induced aperture changes to update stiffness and permeability tensors. Mechanical, hydraulic, and fully coupled poromechanical examples demonstrate the capabilities of the proposed numerical methodology. The numerical results are compared against those obtained using the discrete fracture method (DFM) to assess their accuracy. The comparisons validate the mechanical, hydraulic, and fully coupled hydro-mechanical formulations. The results show that fracture orientation has a significant impact on the stiffness of the fractured rock mass system and on the pore pressure migration path.

Finally, a synthetic case study of a naturally fractured reservoir is performed considering primary and secondary fracture sets. The case study showed that the presence of secondary fracture sets alters the pore pressure distribution in the formation. Those secondary fracture sets enhance permeability, inducing rapid pore pressure drops. Consequently, fractures close by effective compressive stresses reducing the permeability of the system with a subsequent decrease in

the production rate. In addition, fracture orientation plays a relevant role on the aperture changes of the fracture set, permeability in the flow lines, and the production rate of the fractured reservoir.

The results support applying the proposed enhanced dual porosity and dual permeability (EDPDP) model to simulate highly fractured formations with arbitrary fracture orientation, permeability, and size in field-scale reservoir simulations where the representation of fracture networks with DFMs can be computationally expensive and sometimes even practically unachievable. Also, the consideration of the hydro-mechanical coupling mechanism may play an important role in the proper estimation of the production performance and final recovery of a naturally fractured reservoir.

6
Integrated fracture propagation model and reservoir simulation for production performance evaluation

The hydraulic fracturing technique is indispensable in the development of unconventional reservoirs with ultra-low permeability. The efficiency of hydraulic stimulation is strongly affected by the presence of geological discontinuities such as faults, joints, and natural fractures (BARBIER, 2002; O'SULLIVAN; PRUESS; LIPPMANN, 2001). They can enhance the growth of complex induced-driven fracture networks, increasing the stimulated reservoir volume and production efficiency. In contrast, activated fractures or joints can arrest the HF growth and increase the fluid leak-off during the operations (RUEDA CORDERO; MEJIA SANCHEZ; ROEHL, 2019a). In that sense, fracture propagation models become indispensable for a better understanding of the interaction between hydraulic fractures and natural fractures under different conditions. However, those models cannot assess the production performance of the hydraulically stimulated reservoir. On the other hand, traditional reservoir simulations do not incorporate the complex fracture network created by hydraulic fracturing in naturally fractured formations. In some cases, it is assumed that only natural fractures intercepted by planar hydraulic fractures placed at predefined locations were stimulated (SUPPACHOKNIRUN; TUTUNCU, 2017). Such assumptions can result in inadequate models for a realistic representation of the reservoir conditions and inaccurate production forecasting. For that reason, this chapter presents a new methodology that combines a robust fracture propagation model and reservoir simulation to enhance accurate and realistic evaluation of production performance. With the proposed method, we simulate several hydraulic fracturing scenarios for the assessment of cumulative production of the stimulated reservoir. Moreover, we combined discrete fracture and enhanced dual porosity-dual permeability models to study the effects of fractures of multiple lengths on the production performance. Finally, some suggestions will be made from the numerical result interpretation.

6.1. Methodology

An integrated fracture propagation and fluid flow model has been developed for realistic evaluation of the production performance of naturally fractured and hydraulically stimulated reservoirs. As shown in Figure 6.1, the model consists of five stages. In the first stage, the fracture network with primary and secondary fractures is characterized. Subsequently, the hydraulic fracturing treatment is simulated, with the primary natural fractures represented explicitly. Then, we extract the stimulated fracture network from the results of the fracture propagation model and include in the hydromechanical reservoir model. Secondary natural fractures are introduced through the dual porosity/dual permeability model. Finally, a realistic evaluation of production performance is obtained.

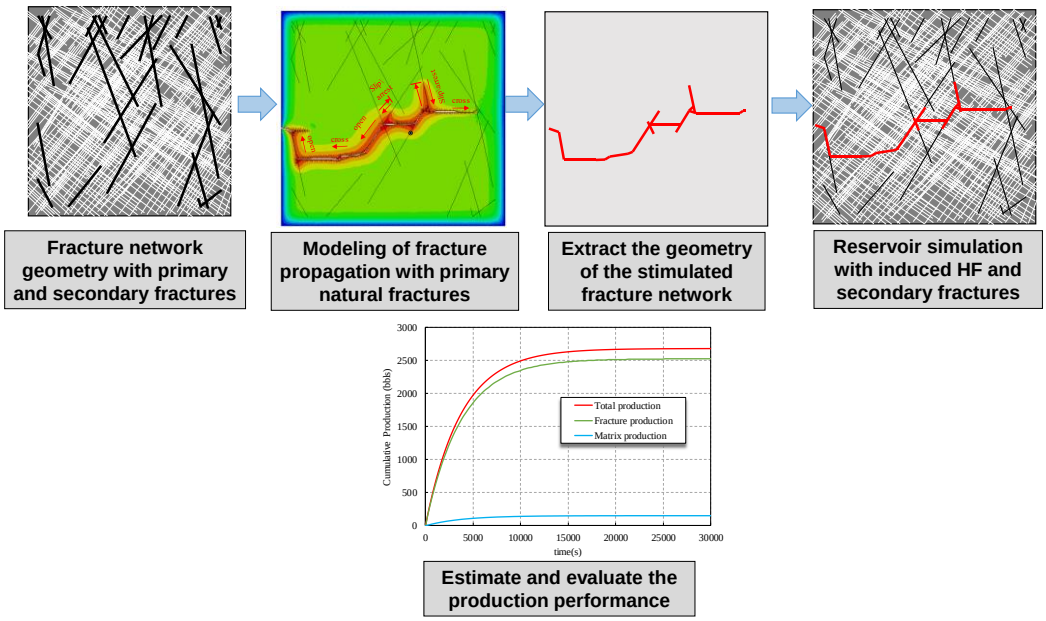

Figure 6.1. Numerical simulation framework for naturally fractured reservoir development

The workflow of the methodology follows the conventional procedure with the three main phases: model generation, solution, and result interpretation, as shown in Figure 6.3. An intrinsic mesh fragmentation technique is used in the pre-processing phase for the mesh generation of the unrestricted fracture propagation model and reservoir simulation. This technique is based on the insertion of interface elements at every face of the continuum elements. Then triple-noded interface is used for the fracture propagation model and single-noded interface elements for reservoir simulation, as shown in Figure 6.2. The same number of

interface elements are inserted in the hydraulic fracturing and the reservoir meshes. However, in the reservoir mesh (Figure 6.2c), the number of degrees of freedom is the same as in the conventional conforming mesh (Figure 6.2a).

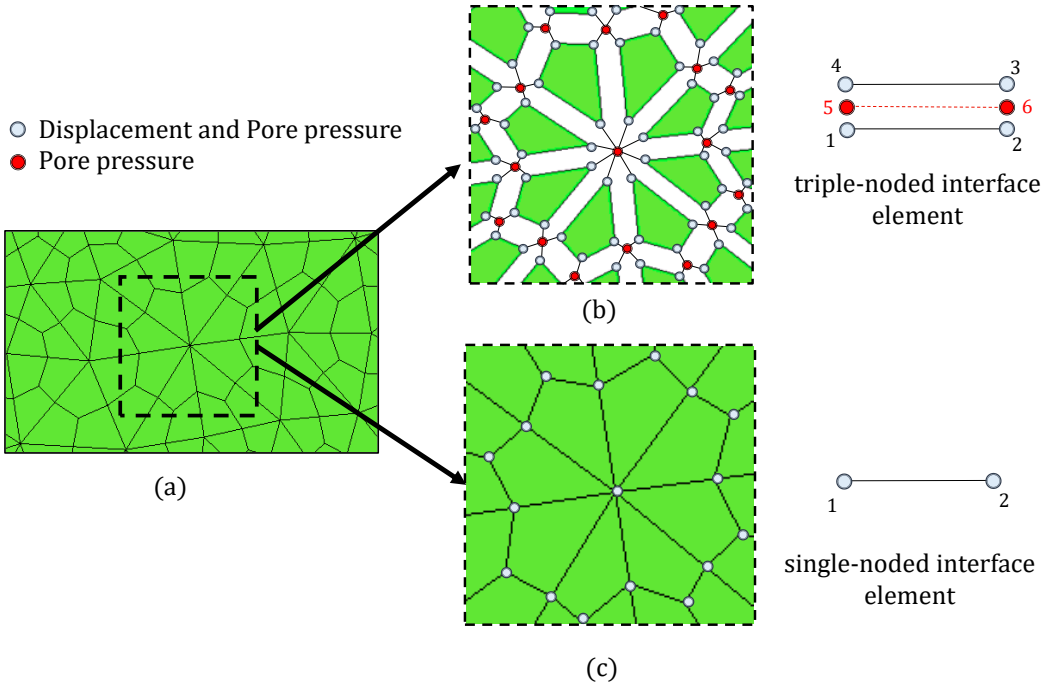

Figure 6.2. 2D zero thickness interface elements into continuum finite elements mesh (a) for hydraulic fracture propagation (b) and reservoir simulation (c).

The second phase simulates hydraulic fracturing in a naturally fractured medium to capture the hydraulically stimulated fracture network geometry. The obtained geometry is mapped through user script and included in the subsequent reservoir simulation. GeMA framework (Geo Modelling Analysis)(MENDES; GATTASS; ROEHL, 2016) was used to simulate the reservoir production. One of GeMA functionalities is the support to the efficient transfer of state variables among different meshes. The framework also implements some important extensibility concepts through the combined use of plugins and abstract interfaces, configurable orchestration, and fast prototyping through the use of Lua language. Then, a user script.lua updates the aperture of the hydraulic fracture network of the single-noded interface elements. During the production stage, the stimulated fracture aperture is kept open to simulate propped fractures. Closure effects after the hydraulic stimulation are neglected. Finally, we make some suggestions from the numerical result interpretation.

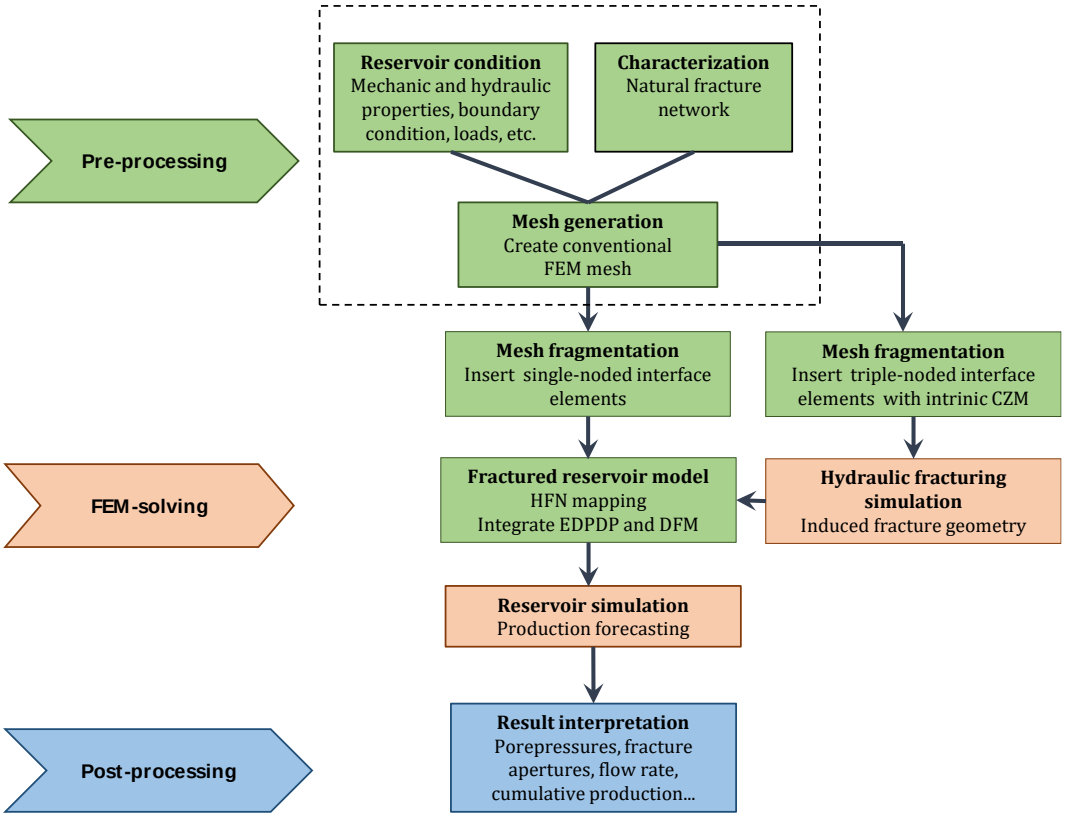

Figure 6.3. Workflow to simulate hydraulic fracturing treatment and the subsequent production of the stimulated fractured reservoir.

6.2. Study cases

This section studies the impacts of natural fractures on hydraulic fracturing and the associated production performance of the hydraulically stimulated reservoir. Parameters such as fracture network geometry, fluid viscosity, and injection rate are evaluated. Finally, we integrate the enhanced dual porosity and dual permeability with the discrete fracture model to study the effects of secondary fractures on the production efficiency of the naturally fractured reservoir.

6.2.1. Effect of fracture network geometry

We test three cases with different fracture network geometries. Figure 6.4 illustrates the reservoir finite element mesh: without NF (case 1), considering one fracture set with the strike of 30° (case 2), and considering two fracture sets with strikes of 30° and 120° (case 3). The reservoir of 60m x 60m x 12 m (length, width, and thickness) is under an initial pore pressure ($P_0 = 45$ MPa) and initial effective stress ($\sigma'_0 = 8$ MPa). The walls are constrained in x and y-directions. The injector/producer well is located at the center of the model. The injection flow is

increased linearly during 50 s until it reaches 0.006 m^3/s. After that, the injection rate is kept constant considering a fracturing fluid viscosity ($\mu_{ff} = 10$ cp) and a period of 100 s. In the production stage, it is assumed a producer well with a pressure ($P_w = 40$ MPa) after 86400s. In this case, a drawdown pressure of 1 MPa is instantaneously applied, followed by transient pore pressure drops of 0.046 kPa/s. In this stage, it is assumed oil viscosity ($\mu_{oil} = 1$ cp) in all cases. Table 6.1 summarizes the parameters used in the numerical simulations of hydraulic fracturing and reservoir production.

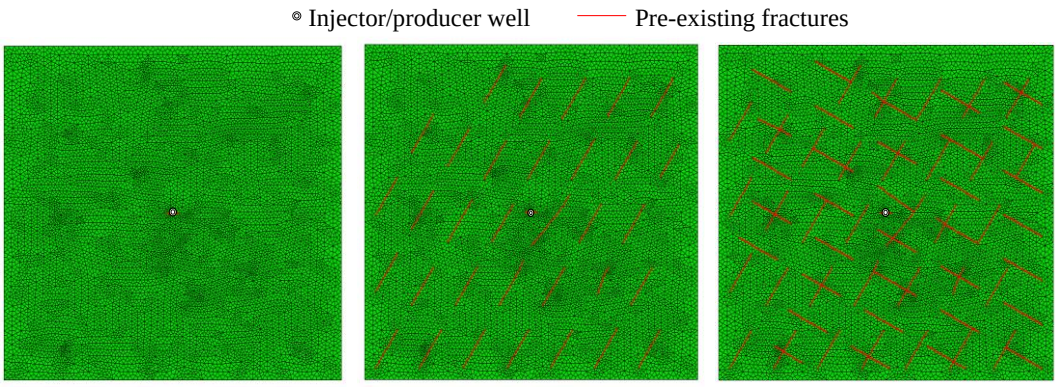

Figure 6.4. Reservoir model (a) without NF and (b) with one NF set, and (c) two NF sets.

Table 6.1. Hydro-mechanical properties of the rock matrix and fracture sets.

Parameters	Units	Rock	NFs
Young's modulus, E	kPa	1.7e+07	--
Possion's ratio, υ	---	0.22	--
Permeability k	mD	0.2	--
Porosity, n_m	--	0.25	--
Initial effective stress, σ'_0	MPa	8	8
Initial pore pressure, P_0	MPa	45	45
Bottom hole pressure at the producer, P_w	MPa	40	40
HF stiffness, $k_n = k_s = k_t$	kPa/m	--	1.7e10
NF stiffness, $k_n = k_s = k_t$	kPa/m	--	1.2e08
NF strike, θ_1 / θ_2 (°)	(°)	--	30/120
Initial NF aperture, a_0	m	--	1e-04

Figure 6.5 shows the hydraulic fracturing results of the deformable reservoir without NF (Case 1), considering one (Case 2) and two fracture sets (Case 3). Figure 6.5a shows the maximum principal stress distribution for each scenario. Figure 6.5b shows the aperture of the stimulated fracture network. It is evident that the presence of natural fractures affects the pore pressure distribution in the production stage (see Figure 6.5c).

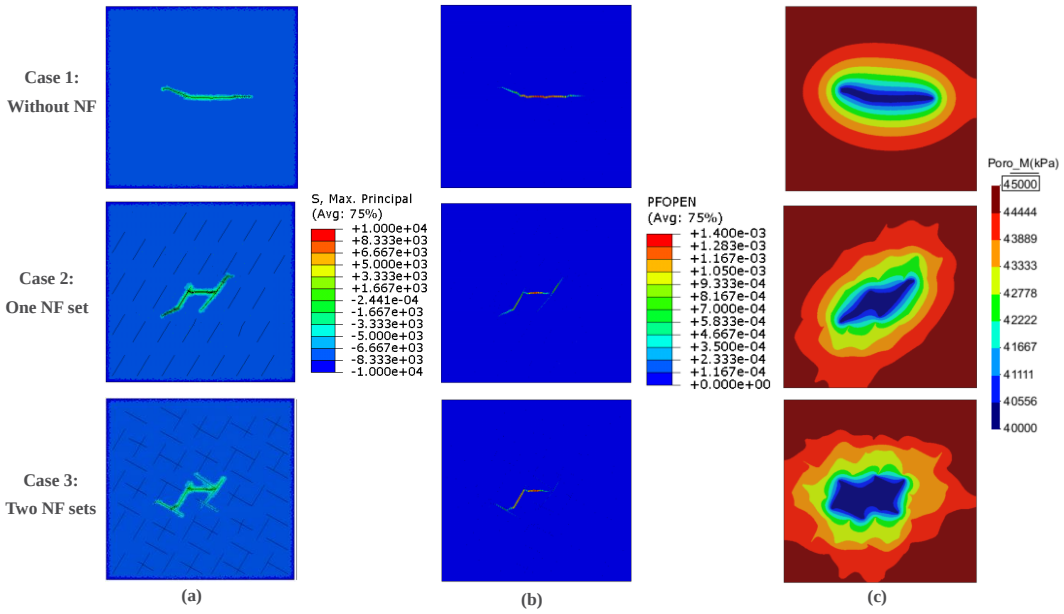

Figure 6.5. Case studies of three different natural fracture network geometries: (a) maximum principal stress, (b) aperture of the stimulated fracture network, and (c) pore pressure distribution in the production stage.

Figure 6.6 shows fracture aperture frequency according to minimum and maximum ranges (a) without NF, (b) with one NF set, and (c) with two NF sets. The result shows the importance of considering the presence of NFs in the assessment of the fracture network behavior and reservoir performance. Effects of stress shadowing, fluid leak-off and fractured formation permeability reduce the aperture of the stimulated fracture. Additionally, the assessment of fracture opening is necessary by proppant design.

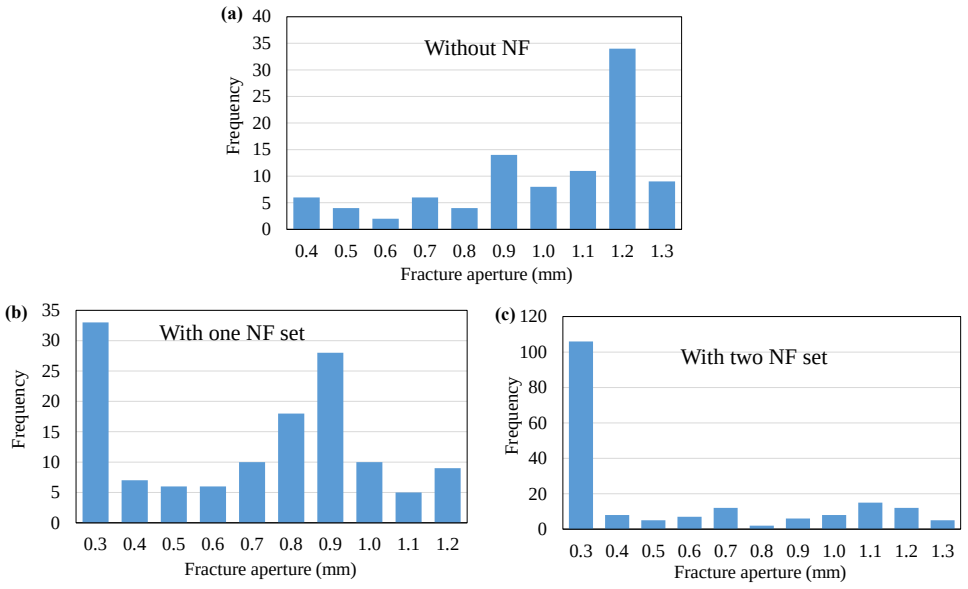

Figure 6.6. Fracture aperture frequency (a) without NFs, (b) with one NF set, and (c) with two NF sets.

Figure 6.7 presents a quantitative evaluation of some properties of the stimulated fracture network. We can appreciate in Figure 6.7a that the total HF length is higher in case 3 than those obtained in case 1 and case 2 (with two NF sets > with one NF set > without NF). Then, fractures form preferential paths of HF propagation, enlarging contact surfaces (Figure 6.7b) and enhancing well reservoir connectivity. On the other hand, the stimulation of natural fractures reduces hydraulic fracture volume, which is directly dependent on hydraulic fracture aperture, as shown in Figure 6.7c and Figure 6.7d. Finally, Figure 6.8 presents the produced fluid rate and cumulative oil production. As a consequence of the contact area fracture/reservoir (Figure 6.7b), production performance in case 3 is 31% higher than in case 2 and 48% higher than in case 1 without NF sets (Figure 6.8).

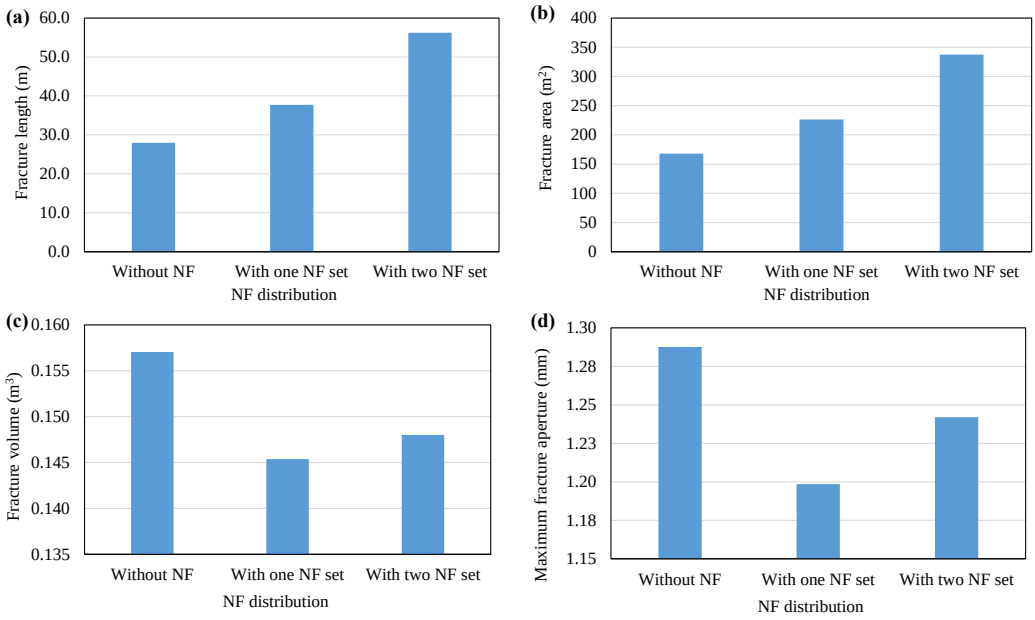

Figure 6.7. Evaluation of stimulated fracture properties: (a) fracture length, (b) fracture area, (c) fracture volume and (d) maximum fracture aperture.

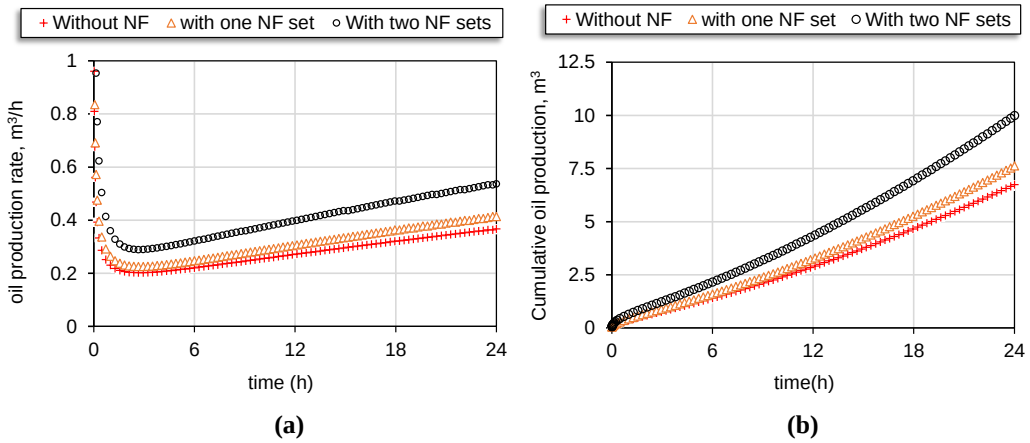

Figure 6.8. Production performance: (a) oil production rate, and (b) cumulative oil production.

We can conclude from the results that the common practice of considering that the fracturing process occurs in intact and homogeneous domains may result unrealistic. Neglecting the characteristics of the natural fracture network can result in large differences in numerical results from those observed in the field.

6.2.2. Effect of fluid viscosity

Fluid viscosity plays an important role to control fracture width, fracture growth, fluid leak-off and proppant transport. There is a broad range of fracturing fluids with a wide range of viscosities (1 cp - 1000 cp) and additives with their advantages and disadvantages for the hydraulic fracturing (MONTGOMERY, 2013). Hence, the final choice of the fluid system depends on the characteristics of the reservoir. This section investigates the effect of the fracturing fluid viscosity (μ_{ff}) on the NF stimulation and the associated production performance. We assess the hydraulic fracturing treatment in Case 3 (Figure 6.4c) considering fluid viscosities μ_{ff} = 1 cp, 10 cp, and 100 cp. The production stage considers an oil viscosity $\mu_{oil} = 1\ cp$ in all cases. Figure 6.9 depicts the case studies of hydraulic stimulation and production stages of Case 3a with μ_{ff} =1 cp, Case 3b with μ_{ff} =10 cp, and Case 3c with μ_{ff} =100 cp. The first observation is that for low fracturing fluid viscosity, it is easier to penetrate into the natural fracture and stimulate it, as shown in Figure 6.9a. In contrast, high fracturing fluid viscosity generates a wider hydraulic fracture, whereas low fracturing viscosity fluid a tight hydraulic fracture, as shown in Figure 6.9b. Although it is easier to penetrate into the HF for low fracturing fluid viscosity, the fluid pressure was not enough to open the natural fractures in Case 3a, as shown in Figure 6.9c. This happens because, given a rock permeability value, a lower fluid viscosity increases the hydraulic conductivity in

the rock formation. Consequently, excessive fluid leak-off prevents fracture propagation due to insufficient fluid volume accumulation in the fracture. In addition, the stress shadow effects between HF and NF reduce the fracture aperture. Then, the relation of rock permeability, fracturing fluid viscosity, hydraulic conductivity, and stress changes affect the stimulated fracture network (Figure 6.9a), fracture aperture (Figure 6.9b), pore pressure distribution (Figure 6.9c), and consequently, production performance, as depicted in Figure 6.11.

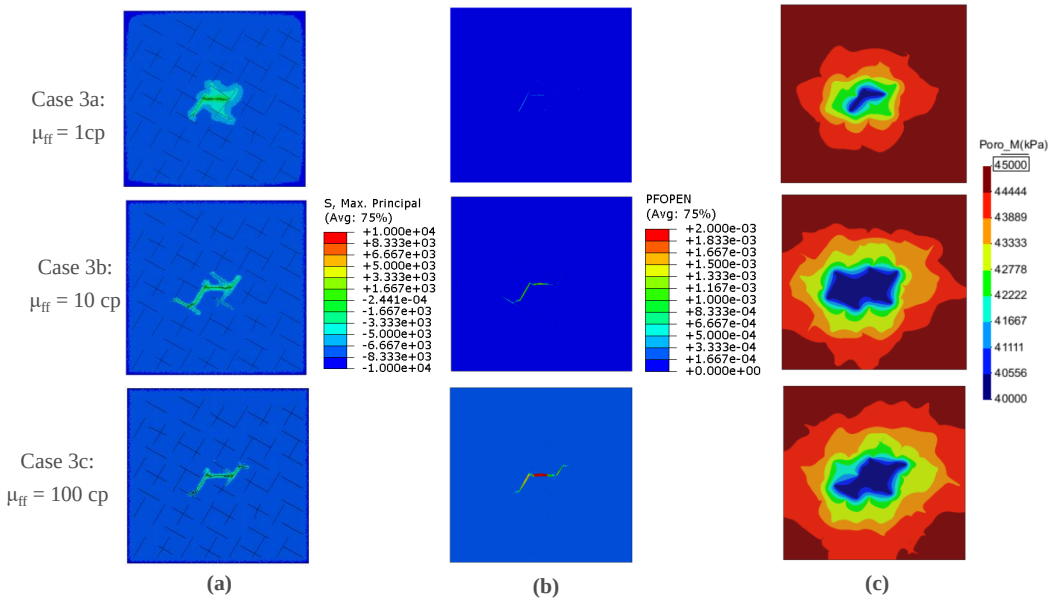

Figure 6.9. Case studies with different injection fluid viscosities: (a) maximum principal stress, (b) aperture of the stimulated fracture network, and (c) pore pressure distribution in the production stage.

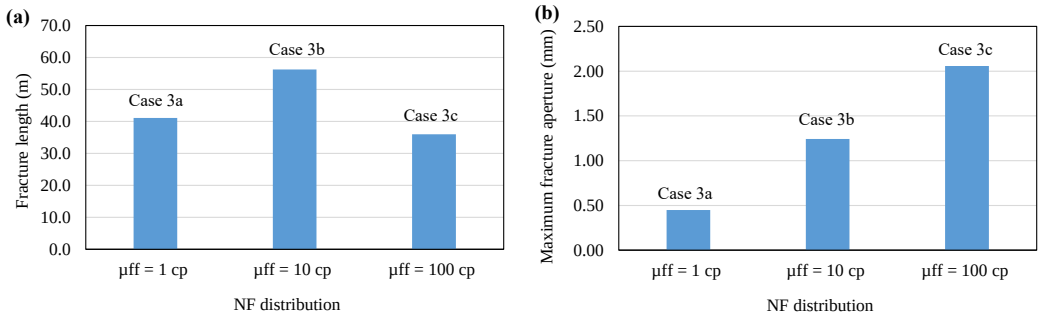

Figure 6.10. Evaluation of stimulated fracture properties for different fluid viscosities: (a) fracture length, and (b) maximum fracture aperture.

In case 3c, the higher fracturing fluid viscosity induces a larger fracture aperture, but shorter total HF length than in case 3b (Figure 6.10b, Figure 6.10a). This effect results in a higher fluid production rate and cumulative oil production in case 3b than in case 3c, as shown in Figure 6.11. In that case, stimulated fracture length plays a more important role than the aperture along the fracture. In contrast, case 3a, with a lower fluid viscosity, results in a lower fluid production rate and

cumulative oil production than in case 3c, since the stimulated fracture apertures are too small. This study highlights that a suitable fluid viscosity is necessary for a good balance between fracture aperture and fracture length to obtain optimal production performance of the stimulated fractured formation.

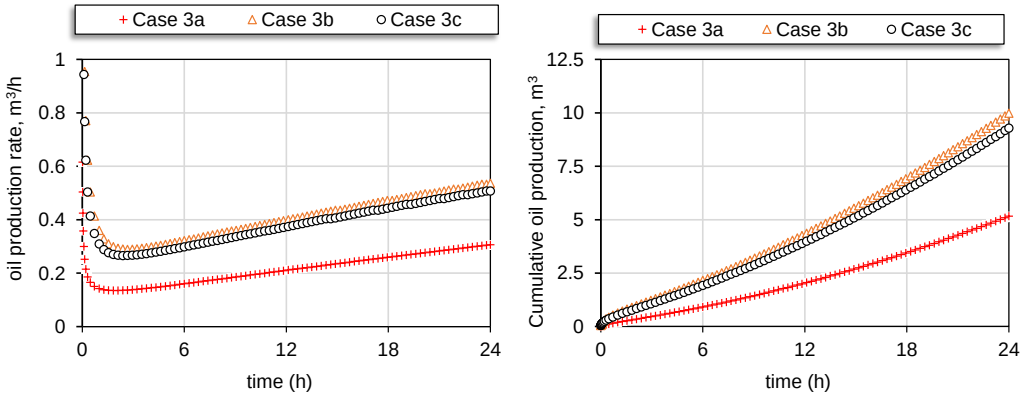

Figure 6.11. Production performance for different fracturing fluid viscosities, (a) oil production rate, and (b) cumulative oil production.

6.2.3. Effect of injection rate

The cases presented in section 6.2.2 will be considered again to demonstrate the effect of the injection rate on the production. The base case of injection rate Q_0 = 6e-3 m³/s is also considered and compared with an additional case of $Q = 2Q_0$.

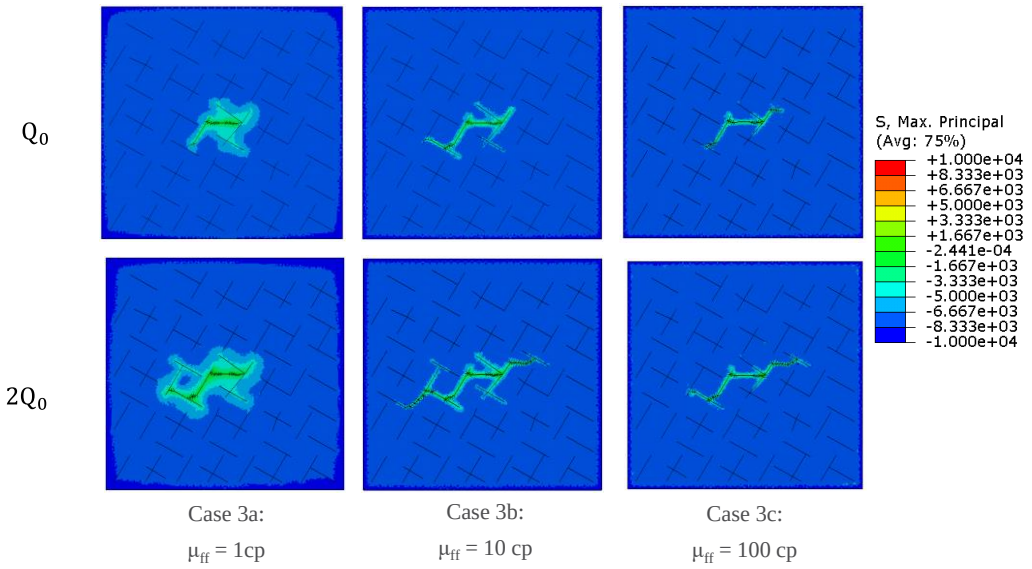

Figure 6.12. Influence of injection rate on the hydraulic fracture network for (Case 3a) with μ_{ff} =1 cp, (Case 3b) with μ_{ff} =10 cp, and (Case 3c) with μ_{ff} =100 cp.

Figure 6.12 shows that the stimulated fracture network becomes more complex when the injection rate is increased. This behavior is related to the higher

total fluid volume that increases the fluid pressure and tensile failure. Moreover, higher fluid pressure results in higher fracture opening, as shown in Figure 6.13.

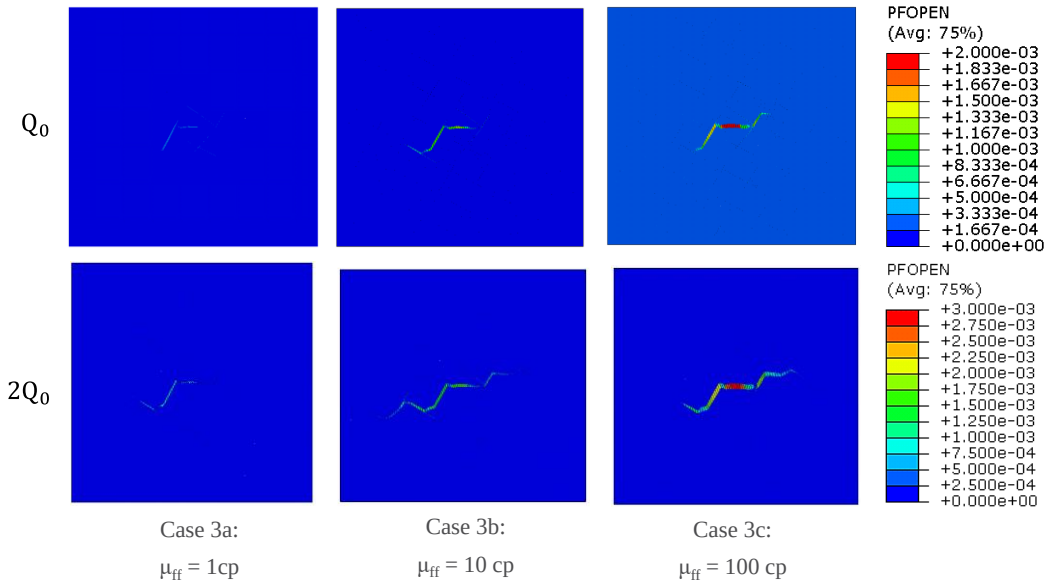

Figure 6.13. Influence of injection rate on the fracture aperture for (Case 3a) with μ_{ff} =1 cp, (Case 3b) with μ_{ff} =10 cp, and (Case 3c) with μ_{ff} =100 cp.

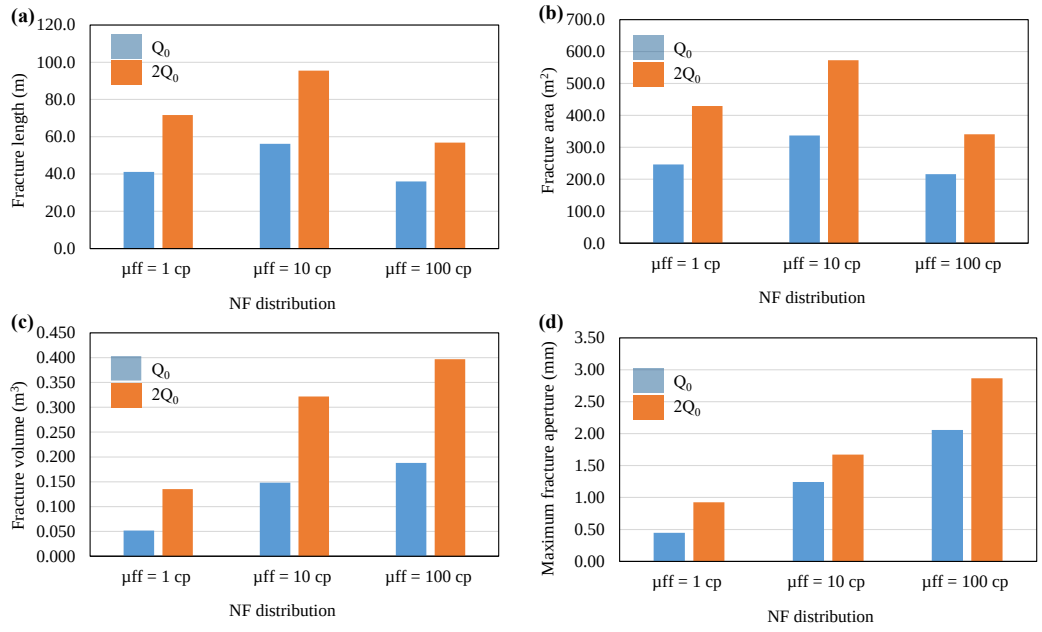

Figure 6.14. Evaluation of stimulated fracture properties for different fluid viscosities and injection rates: (a) fracture length, (b) fracture area, (c) fracture volume, and (d) maximum fracture aperture.

The influence of higher injection rate ($Q = 2Q_0$) with different fracturing fluid viscosities is more evident in the quantitative evaluation of some properties of the stimulated fracture network (Figure 6.14) and the associated production performance (Figure 6.15). In this case, the cumulative oil production of case 3b is 18% higher than of Case 3c and 46% higher than of Case 3a. Therefore, for the

considered rock permeability, the fracturing fluid viscosity of 10 cp results in the most efficient production of the hydraulically stimulated reservoir.

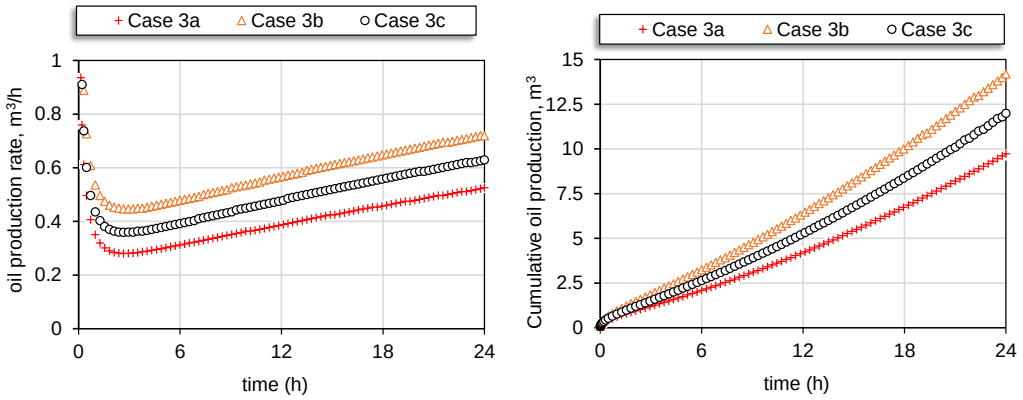

(a) **(b)**

Figure 6.15. Influence of higher injection production rate Q = $2Q_0$ on the production performance with different fracturing fluid viscosities, (a) oil production rate, and (b) cumulative oil production.

6.2.4. Effect of pre-existing secondary fractures

Naturally fractured reservoirs are formed by fractures of multiple scales (primary and secondary fractures, as shown in Figure 6.16). Conventional hydraulic fracturing simulations neglect secondary fractures because they do not play a relevant role in fracture propagation due to their small apertures, sizes, and presence in large numbers. Modeling of secondary fractures using explicit methods can be computationally unfeasible. However, secondary fractures can alter reservoir behavior during production operations (GONG; ROSSEN, 2018). In this context, we integrate discrete fracture and enhanced dual porosity-dual permeability models to simulate fluid flow in naturally fractured reservoirs with discontinuities of multiple lengths. Interface elements discretize the stimulated fracture network, while EDPDP bridges between the main fractures and the matrix fracture network. Figure 6.17 shows the schematic representation of the integration between DPDP and DFM models.

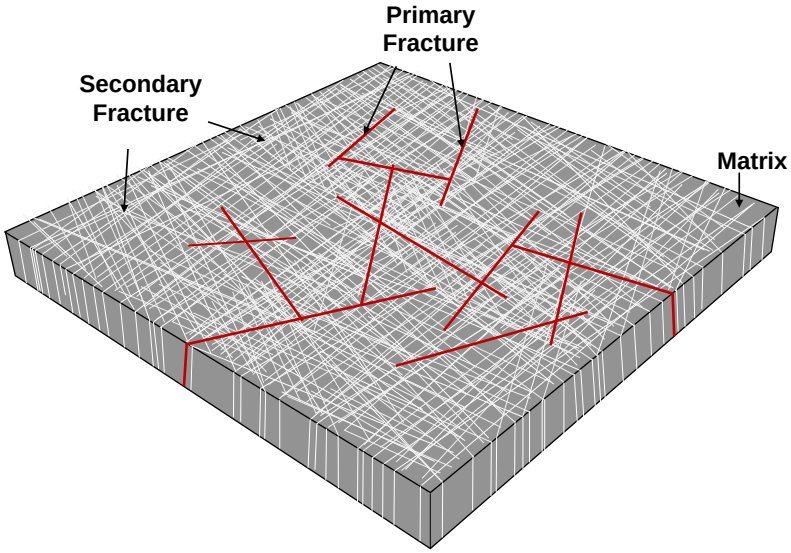

Figure 6.16. Schematic representation of fractured rock media, DFM discretizes primary fractures while EDPDP bridges between the main fractures and the rock matrix /secondary fracture network.

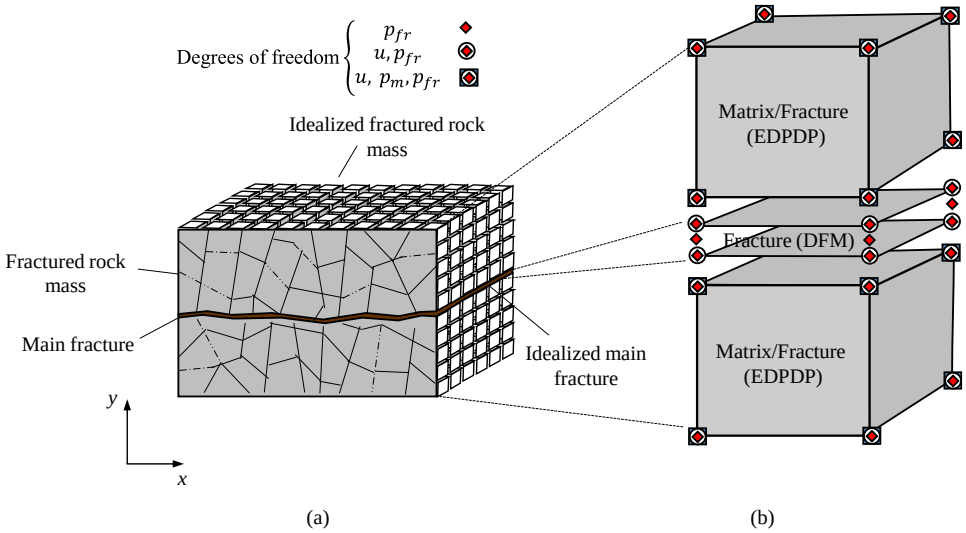

Figure 6.17. Schematic representation of the integration between EDPDP and DFM models: (a) strong discontinuity in a fractured medium; (b) integrated EDPDP and DFM finite elements.

The reservoir of size 60m x 60m x 6 m is under an initial pore pressure ($P_0 = 45$ MPa) and initial effective stresses of 15 MPa in the vertical direction, 12 MPa, and 8 MPa, maximum and minimum horizontal stresses, respectively. Figure 6.18 illustrates the model of the fractured reservoir and the finite element mesh using wedge elements. In this case, mesh fragmentation is more challenging due to the correct insertion of triangle and quadrilateral interface elements at the wedge element faces. The top and bottom surfaces of the model have zero vertical displacement constraints, and all lateral surfaces have zero displacement constraints normal to the surface. The injector/producer well is located at the center of the model. In the hydraulic fracturing simulation, it is considered a constant

injection rate ($Q_0 = 0.003\ \mathrm{m}^3/\mathrm{s}$) with fracturing fluid viscosity of 10 cp for a period of 100s. This stage considers only primary fractures. In the production stage, it is assumed a producer well with a pressure ($P_w = 40\ \mathrm{MPa}$) after 86400s. The production stage considers the produced oil with a viscosity of 1 cp in all cases. Table 6.2 summarizes the parameters used in the numerical simulations of hydraulic fracturing.

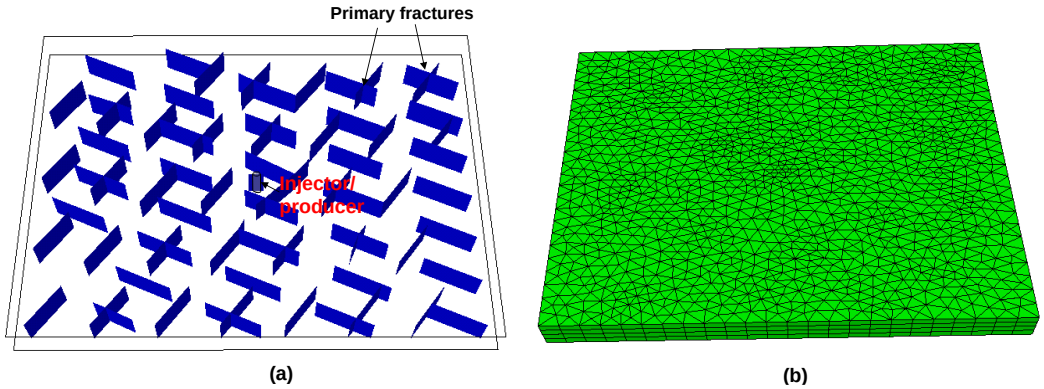

Figure 6.18. Fractured reservoir model (a) finite element mesh (b).

Table 6.2. Hydro-mechanical properties of the rock matrix and primary fracture sets.

Parameters	Units	Rock	Primary NF
Young's modulus, E	MPa	1.0e+04	--
Possion's ratio, υ	---	0.22	--
Permeability k	mD	0.2	--
Porosity, n_m	--	0.25	--
Initial pore pressure, P_0	MPa	45	45
Bottom hole pressure at the producer, P_w	MPa	40	40
HF stiffness, $k_n = k_s = k_t$	MPa/m	--	1.7e+07
NF stiffness, $k_n = k_s = k_t$	MPa/m	--	1.2e+05
NF strike, θ_1 / θ_2	(°)	--	30/120
Initial NF aperture, a_0	m	--	1e-04

Figure 6.19a shows the opening of the stimulated fracture network and the end of the hydraulic fracturing simulation. Figure 6.19b illustrates the pore pressure variation during the production stage. We can observe the impact of the stimulated fracture network on the pore pressure variation and fluid migration throughout the production stage.

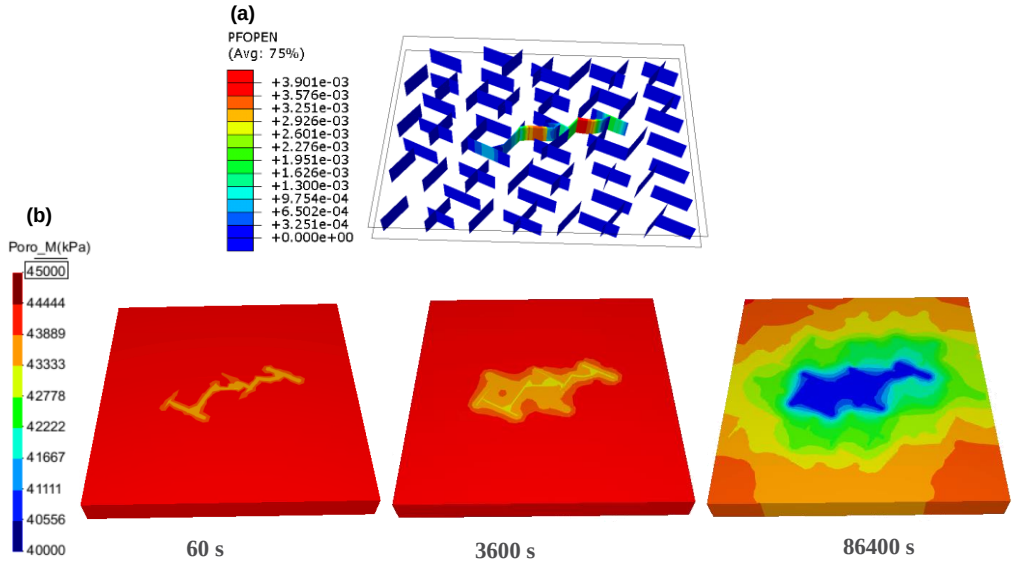

Figure 6.19. Opening of the stimulated fracture network (a) pore pressure distribution during the production stage (b).

Now, we study the effect of secondary fracture network geometry with different characteristics: considering one (case 1), two (case 2), and three (case 3) secondary natural fracture (Sec-NF) sets. Table 6.3 summarizes the properties of the secondary fracture sets. In those cases, Sec-NF set 1 and Sec-NF set 2 are vertical and perpendicular to each other. Moreover, the aperture and fracture spacing of Sec-NF set 2 are twice those of Sec-NF set 1. On the other hand, Sec-NF set 3 is horizontal and has a higher fracture density than Sec-NF set 1 and Sec-NF set 2.

Table 6.3. Hydro-mechanical properties of the secondary natural fracture (Sec-NF) sets

Parameter	Units	Sec-NF set 1	Sec-NF set 2	Sec-NF set 3
HF stiffness, $k_n = k_s = k_t$	MPa/m	1.2e+05	1.2e+05	1.2e+05
NF strike, θ	(°)	60	150	10
NF dip, φ	(°)	80	80	0
Initial NF aperture, a_0	m	1e-05	2e-05	1e-05
Spacing, s	m	0.5	1	0.25

Figure 6.20 and Figure 6.21 show the comparison of pore pressure distribution and production performance for the models. We observe that the presence of one secondary fracture set (case 1) has a slight effect on increasing the permeability of the fractured rock system, pore pressure dissipation, and oil production rate. In this case, the cumulative oil production in case 1 is 15% higher than without secondary fracture sets. The cumulative oil production in case 2 is 46% higher than in case 1. Hence, the secondary NF set 2 has a higher contribution than Sec-NF set 1. In this case, we can note that the initial fracture aperture has a stronger impact than the fracture spacing. For case 3, the horizontal Sec-NF set 3 increases the cumulative oil production by 16% compared to case 2.

With the presence of three secondary fracture sets, the cumulative oil production is 96% more than without secondary fractures. Therefore, the consideration of the secondary fractures has a high impact on the estimation of fluid drainage and pore pressure dissipation.

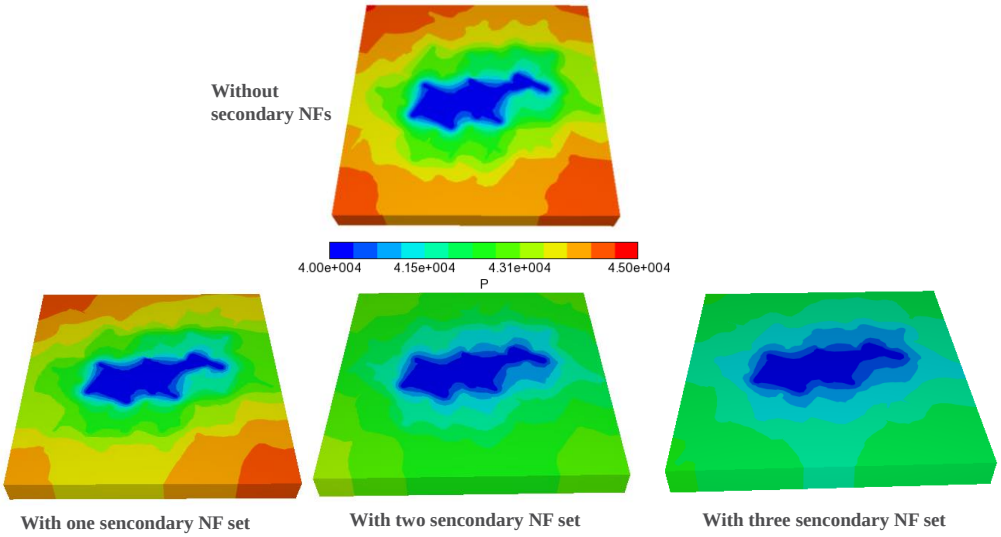

Figure 6.20. Comparison of pore pressure distribution at the end of the production stage for different scenarios of primary and secondary fracture sets

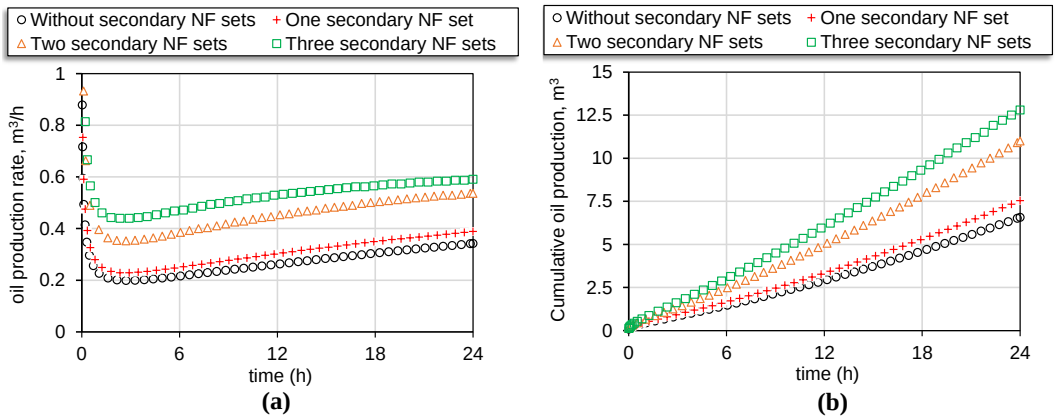

Figure 6.21. Influence of secondary fractures on the production performance: (a) oil production rate, and (b) cumulative oil production.

6.3. Concluding remarks

This study presents a new methodology that integrates unrestricted fracture propagation models and reservoir simulations to study the main factors affecting the hydraulic fracturing treatment and the associated production performance of the stimulated reservoirs. Parameters such as fracture network geometry, fluid viscosity, and injection rate are evaluated. Finally, we integrate the enhanced dual porosity and dual permeability with the discrete fracture model to study the effects

of secondary fractures on the production of the stimulated naturally fractured reservoir.

A quantitative evaluation of some stimulated fracture properties shows the impact of the natural fracture characteristics on the stimulated fracture network geometry and the production performance of the reservoir. In this case, natural fractures form preferential paths of HF propagation, enlarging contact area, enhancing well reservoir connectivity and increasing reservoir productivity. We also observed that fracturing fluid viscosity plays an important role in the hydraulic stimulation treatment and the associated production performance of the reservoir. Fluid viscosity controls fracture opening, fracture pressure, fracture growth, fracture conductivity and fluid leak-off. Low fracturing fluid viscosity increases the dilation of natural fractures and enhances fracture/rock conductivity. Consequently, given a rock permeability, excessive fluid leak-off prevents fracture propagation due to insufficient fluid volume accumulation inside the fracture. In contrast, excessive fracturing fluid viscosity generates a wider and shorter hydraulic fracture, whereas low fracturing viscosity fluid produces a tight and larger hydraulic fracture. The numerical results also show that the stimulated fracture network becomes more complex when the injection rate increases, enhancing fracture length, fracture opening and the contact area between fractures and reservoir. This behavior is related to the higher total fluid volume inside hydraulic fractures which increases fluid pressure.

The simulation of reservoirs, including fractures of multiples scales with different orientations, spacing and apertures, shows that secondary fractures enhance the permeability of the fractured rock system and oil production rate. The numerical results indicate that the initial fracture aperture has a stronger impact on production than the fracture spacing, as expected. Therefore, the consideration of the secondary fractures has a high impact on the estimation of fluid drainage and pore pressure dissipation.

Finally, the proposed methodologies contribute to the progress in the understanding of the complex phenomena presented into the hydraulic fracturing in naturally fractured reservoir. The developed tools are useful in the evaluation of production performance of naturally fractured reservoirs, stimulation design, and finally, available in the commercial software.

7
Conclusions

This research work aims at studying the dominant factors that affect hydraulic fracturing and the production performance of naturally fractured and hydraulically stimulated reservoirs. The main contributions of this research work include the development of a robust 2D/3D numerical methodology using finite elements to simulate unrestricted fluid-driven fracture propagation in naturally fractured media. A mesh fragmentation scheme is implemented to simulate fracture propagation with arbitrary paths. The successful simulation of multiple conditions of fracture interaction (re-initiated fracture from the crack tip, crossing with an offset, branching, and propagation of multiple cracks) demonstrates the robustness of the proposed methodology. In general, the interaction between hydraulic fracture (HF) and natural fracture (NF) is more influenced by horizontal stress contrast, internal friction angle of the NF, and NF orientation. Fluid injection rate, fluid viscosity, rock permeability, and the distance from the borehole to the NF can also alter the HF - NF interaction.

The second main contribution is the development of a new hydro-mechanical formulation for an enhanced dual porosity and dual permeability (EDPDP) model to represent a fractured porous formation more accurately. The proposed model generalizes the assessment of the equivalent compliance tensor of the fractured rock, stiffness and permeability tensors of the fracture system, and shape factor for a fractured porous media with multiple fracture sets. This new approach opens opportunities to model regions of high fracture density in a heavily fractured reservoir where the representation with DFMs can be computationally expensive and sometimes even practically unachievable. The results of the EDPDP considering well-connected fracture networks are in good agreement with those obtained with DFM. In this study, we can conclude that fracture orientation, aperture, spacing, and fracture density are critical parameters that affect the hydro-mechanical behavior and the production performance of the naturally fractured reservoir.

Finally, the research work proposes a new methodology that integrates a robust hydraulic fracturing model and reservoir simulation to enhance accurate and realistic evaluation of production performance. The proposed methodology incorporates the complex fracture network created by hydraulic fracturing into the reservoir simulation. Moreover, we combined the discrete fracture and enhanced dual porosity-dual permeability models to study the effects of fractures of multiple scales on the production stage. In this case, EDPDP discretizes well-connected fractured media with secondary fractures, while the DFM through interface elements represents the complex fracture network created by hydraulic fracturing.

In general, this research study provides better insight for understanding the complex process of hydraulic fracturing and its impact on the fluid flow in naturally fractured formations.

With the current state of the fracture propagation model, it is possible to simulate multi-staged fracturing into multilayered fractured rock formations. That is an important issue to control unfavorable fracture propagation, reducing the environment-associated risks and increasing oil recovery in unconventional reservoirs. Other studies, including chemical and temperature changes, could be developed.

The EDPDP model can be extended to multiphase fluid flow problems, production of geothermal reservoirs, fractured formations with multiple porosities and permeabilities, and reactive transport with fluid-solid interactions. Finally, integrating those methodologies can open the opportunity for different robust numerical simulations considering a more realistic production forecast.

Nomenclature

$\boldsymbol{\sigma}$	Stress tensor
$\boldsymbol{\sigma'}$	Effective stress tensor
$\boldsymbol{g}$	Gravity vector
$\boldsymbol{p}$	Pore pressure in the porous medium
ρ	Density of the materials
α	Biot coefficient
K	Volumetric deformation moduli of the porous medium
$\boldsymbol{D_e}$	Elasticity matrix
$\boldsymbol{\varepsilon}$	Total strain vector
$\Delta\varepsilon_n^p$	Normal plastic strain increment
$\Delta\varepsilon_s^P$	Tangential plastic strains increment
λ	Plastic multiplier
$P(\boldsymbol{\sigma})$	Plastic potential function
$\dot{\boldsymbol{u}}$	Deformation velocity vector
$\boldsymbol{q}$	Darcy's velocity vector of the pore fluid
M	Biot's modulus
K_w	Bulk modulus of the fluid
K_u	Undrained bulk modulus
n_m	Porosity of the porous medium
$\boldsymbol{q}$	Specific fluid flow
$\boldsymbol{k_m}$	Permeability of the porous medium
A	Cross-section area
μ	Fluid viscosity
$\boldsymbol{m}$	Vector form of the Kronecker delta
τ_s	Shear stress at the first direction on the fracture surface
τ_t	Shear stress at the second direction on the fracture surface
σ'_n	Normal effective stress on the fracture surface
$\delta_{s,t}$	Shear separations on the fracture surface
δ_n	Normal separation on the fracture surface

δ_{max}	Maximum closure
a_0	Initial fracture aperture
k_{n0}	Initial normal stiffness
k_n	Normal stiffness of the fracture
$k_{t,s}$	Shear stiffness in two orthogonal in plane directions of the fracture
σ'^0_n	Effective tensile strength
$\tau^0_{s,t}$	Shear strengths
$\bar{\sigma'}_n$	normal effective stress predicted by the elastic traction separation law for the current relative displacements
$\bar{\tau}_{s,t}$	Shear stresses predicted by the elastic traction separation law for the current relative displacements
D	Damage variable
δ_m^{max}	maximum value of the effective displacement attained during the loading history
$\delta_m^{\mathbf{0}}$	Effective displacements at damage initiation
δ_m^f	Effective displacements at complete failure
δ_m	Effective displacement
ϑ	Non-dimensional material parameter
G^c	Fracture energy
G_n^c	Mode-I critical fracture energy
G_s^c	Mode-II critical fracture energy
T^0_{eff}	Effective traction at damage initiation
τ_R	Resultant shear stress acting on the fracture surface
τ_{slip}	Critical shear stress
c	Material cohesion
ϕ	Friction angle
ψ	Dilatancy angle
σ'_{cut}	Tension cutoff
q_s	Tangential flow inside the fracture
$v_{t,b}$	Fluid flow velocities leaking through the top and bottom fracture surfaces
p_f	Internal fluid pressure along the fracture

$p_{t,b}$	Pore pressures in the adjacent porous material on the top and bottom fracture surfaces
$c_{t,b}$	Pressure-dependent leak-off coefficients
c_v	Fluid diffusivity coefficient
C_l	Carter's leak-off coefficient
E	Young's Modulus
G	Shear modulus
ν	Poisson's coefficient
s	Fracture spacing
φ	Dip angle
θ	Strike angle

Bibliographic references

ADACHI, J. I.; DETOURNAY, E. Self-similar solution of a plane-strain fracture driven by a power-law fluid. **International Journal for Numerical and Analytical Methods in Geomechanics**, *[S. l.]*, v. 26, n. 6, p. 579–604, 2002. DOI: 10.1002/nag.213.

ADACHI, J. I.; DETOURNAY, E. Plane strain propagation of a hydraulic fracture in a permeable rock. **Engineering Fracture Mechanics**, *[S. l.]*, v. 75, n. 16, p. 4666–4694, 2008. DOI: 10.1016/j.engfracmech.2008.04.006.

ASHWORTH, Mark; DOSTER, Florian. Foundations and Their Practical Implications for the Constitutive Coefficients of Poromechanical Dual-Continuum Models. **Transport in Porous Media**, *[S. l.]*, v. 130, n. 3, p. 699–730, 2019. DOI: 10.1007/s11242-019-01335-6. Disponível em: https://doi.org/10.1007/s11242-019-01335-6.

BAGHERI, Mohammad A.; SETTARI, Antonin. Modeling of Geomechanics in Naturally Fractured Reservoirs. **SPE Reservoir Evaluation & Engineering**, *[S. l.]*, v. 11, n. 01, p. 108–118, 2008. DOI: 10.2118/93083-PA. Disponível em: https://doi.org/10.2118/93083-PA.

BALDONI, Francesco; MILLARD, Alain. A finite element formulation for the coupled hydro-mechanical behaviour of porous rock joints. *In*: POROMECHANICS: A TRIBUTE TO MAURICE A BIOT. PROCEEDINGS OF THE 1ST BIOT CONFERENCE 1998, **Anais** [...]. : Taylor & Francis: Louvain-la-Neuve, Belgium, 1998. p. 339–344.

BANDIS, S. C.; LUMSDEN, A. C.; BARTON, N. R. Fundamentals of rock joint deformation. **International Journal of Rock Mechanics and Mining Sciences & Geomechanics Abstracts**, *[S. l.]*, v. 20, n. 6, p. 249–268, 1983. DOI: https://doi.org/10.1016/0148-9062(83)90595-8. Disponível em: http://www.sciencedirect.com/science/article/pii/0148906283905958.

BARBIER, Enrico. Geothermal energy technology and current status: An overview. **Renewable and Sustainable Energy Reviews**, *[S. l.]*, v. 6, n. 1–2, p. 3–65, 2002. DOI: 10.1016/S1364-0321(02)00002-3.

BARBOZA, LUIS. **APPLICATION OF COHESIVE FRACTURE MODELS TO THE ANALYSIS OF STEELFIBER REINFORCED CONCRETE STRUCTURES**. 2015. PUC-Rio, *[S. l.]*, 2015. DOI: https://doi.org/10.17771/PUCRio.acad.25779.

BARENBLATT, G. I.; ZHELTOV, I. P.; KOCHINA, I. N. Basic concepts in the theory of seepage of homogeneous liquids in fissured rocks [strata]. **Journal of Applied Mathematics and Mechanics**, *[S. l.]*, v. 24, p. 1286–1303, 1960. DOI: https://doi.org/10.1016/0021-8928(60)90107-6.

BENDEZU, MARKO. **NUMERICAL SIMULATION OF BLASTING-INDUCED ROCK FRACTURES CONSIDERING THE COHESIVE ZONE MODEL**. 2017. PUC-Rio, *[S. l.]*, 2017. DOI: https://doi.org/10.17771/PUCRio.acad.30457.

BENEDETTO, Matías Fernando; CAGGIANO, Antonio; ETSE, Guillermo. Virtual elements and zero thickness interface-based approach for fracture analysis of heterogeneous materials. **Computer Methods in Applied Mechanics and Engineering**, *[S. l.]*, v. 338, p. 41–67, 2018. DOI: https://doi.org/10.1016/j.cma.2018.04.001. Disponível em: http://www.sciencedirect.com/science/article/pii/S0045782518301713.

BENZEGGAGH, M. L.; KENANE, M. Measurement of mixed-mode delamination fracture toughness of unidirectional glass/epoxy composites with mixed-mode bending apparatus. **Composites Science and Technology**, *[S. l.]*, v. 56, n. 4, p. 439–449, 1996. DOI: https://doi.org/10.1016/0266-3538(96)00005-X. Disponível em:

http://www.sciencedirect.com/science/article/pii/026635389600005X.

BIGI, S.; BATTAGLIA, M.; ALEMANNI, A.; LOMBARDI, S.; CAMPANA, A.; BORISOVA, E.; LOIZZO, M. CO2 flow through a fractured rock volume: Insights from field data, 3D fractures representation and fluid flow modeling. **International Journal of Greenhouse Gas Control**, *[S. l.]*, v. 18, p. 183–199, 2013. DOI: 10.1016/j.ijggc.2013.07.011. Disponível em: http://dx.doi.org/10.1016/j.ijggc.2013.07.011.

BIOT, Maurice A. General Theory of Three- Dimensional Consolidation. **Journal of Applied Physics**, *[S. l.]*, v. 12, n. 2, p. 155–164, 1941. DOI: 10.1063/1.1712886.

BLANTON, T. L. An Experimental Study of Interaction Between Hydraulically Induced and Pre-Existing Fractures. **SPE Unconventional Gas Recovery Symposium**, *[S. l.]*, 1982. DOI: 10.2118/10847-MS. Disponível em: http://www.onepetro.org/doi/10.2118/10847-MS.

BLANTON, T. L. Propagation of Hydraulically and Dynamically Induced Fractures in Naturally Fractured Reservoirs. **SPE Unconventional Gas Technology Symposium**, *[S. l.]*, 1986. DOI: 10.2118/15261-MS. Disponível em: https://www.onepetro.org/conference-paper/SPE-15261-MS.

BLASKOVICH, F. T.; CAIN, G. M.; SONIER, Fernand; WALDREN, David; WEBB, S. J. A Multicomponent Isothermal System for Efficient Reservoir Simulation. **Middle East Oil Technical Conference and Exhibition**, *[S. l.]*, 1983. DOI: 10.2118/11480-MS. Disponível em: http://www.onepetro.org/doi/10.2118/11480-MS.

BOARD, Mark; RORKE, Tony; WILLIAMS, Gary; GAY, Nick. Fluid injection for rockburst control in deep mining. *In*: U.S. SYMPOSIUM ON ROCK MECHANICS 1992, **Anais** [...]. [s.l: s.n.] p. 111–120. DOI: 10.1016/0148-9062(93)90694-9.

BRATTON, Tom; GILLESPIE, Paul; LI, Bingjian; MARCINEW, Richard; RAY, Satyaki; NELSON, Ron; SCHODERBEK, David; SONNELAND, Lars. The Nature of Naturally Fractured Reservoirs. **Oilfield Review, do not reffer to**, *[S. l.]*, n. June, p. 4–23, 2006. DOI: 10.1007/s00392-007-0560-6.

BRUSH, David J.; THOMSON, Neil R. Fluid flow in synthetic rough-walled fractures: Navier-Stokes, Stokes, and local cubic law simulations. **Water Resources Research**, *[S. l.]*, v. 39, n. 4, 2003. DOI: 10.1029/2002WR001346. Disponível em: https://doi.org/10.1029/2002WR001346.

BUNGER, Andrew P.; DETOURNAY, Emmanuel; GARAGASH, Dmitry I. Toughness-dominated hydraulic fracture with leak-off. **International Journal of Fracture**, *[S. l.]*, v. 134, n. 2, p. 175–190, 2005. DOI: 10.1007/s10704-005-0154-0.

CAMACHO, G. T.; ORTIZ, M. Computational modelling of impact damage in brittle materials. **International Journal of Solids and Structures**, *[S. l.]*, v. 33, n. 20, p. 2899–2938, 1996. DOI: https://doi.org/10.1016/0020-7683(95)00255-3. Disponível em: http://www.sciencedirect.com/science/article/pii/0020768395002553.

CAMANHO, P. P.; DÁVILA, C. G. Mixed-Mode Decohesion Finite Elements for the Simulation of Delamination in Composite Materials. **Nasa/Tm-2002-211737**, *[S. l.]*, n. June 2002, p. 1–37, 2002. DOI: 10.1177/002199803034505. Disponível em: http://www.researchgate.net/publication/24327361_Mixed-Mode_Decohesion_Finite_Elements_for_the_Simulation_of_Delamination_in_Composite_Materials/file/e0b49527d4918f3b65.pdf.

CAO, Renyi; FANG, Sidong; JIA, Pin; CHENG, Linsong; RAO, Xiang. An efficient embedded discrete-fracture model for 2D anisotropic reservoir simulation. **Journal of Petroleum Science and Engineering**, *[S. l.]*, v. 174, p. 115–130, 2019. DOI: 10.1016/j.petrol.2018.11.004.

CARRIER, Benoit; GRANET, Sylvie. Numerical modeling of hydraulic fracture problem in permeable medium using cohesive zone model. **Engineering Fracture Mechanics**, *[S. l.]*, v. 79, p. 312–328, 2012. DOI: 10.1016/j.engfracmech.2011.11.012.

CASTANEDA, JAIME. **NUMERICAL SIMULATION OF HYDRAULIC**

FRACTURING BY THE EXTENDED FINITE ELEMENT METHOD. 2017. PUC-Rio, *[S. l.]*, 2017. DOI: https://doi.org/10.17771/PUCRio.acad.31482.

CHEN, Her-Yuan; TEUFEL, Lawrence W. **Coupling Fluid-Flow and Geomechanics in Dual-Porosity Modeling of Naturally Fractured Reservoirs - Model Description and ComparisonSPE International Petroleum Conference and Exhibition in Mexico**Villahermosa, MexicoSociety of Petroleum Engineers, , 2000. DOI: 10.2118/59043-MS. Disponível em: https://doi.org/10.2118/59043-MS.

CHEN, Hongquan; ONISHI, Tsubasa; OLALOTITI-LAWAL, Feyi; DATTA-GUPTA, Akhil. Streamline tracing and applications in embedded discrete fracture models. **Journal of Petroleum Science and Engineering**, *[S. l.]*, v. 188, p. 106865, 2020. DOI: 10.1016/j.petrol.2019.106865.

CHEN, Huimei; ZHAO, Zhiye; SUN, Jianping. Coupled hydro-mechanical model for fractured rock masses using the discontinuous deformation analysis. **Tunnelling and Underground Space Technology**, *[S. l.]*, v. 38, p. 506–516, 2013. DOI: https://doi.org/10.1016/j.tust.2013.08.006. Disponível em: http://www.sciencedirect.com/science/article/pii/S0886779813001260.

CHEN, Zuorong. Finite element modelling of viscosity-dominated hydraulic fractures. **Journal of Petroleum Science and Engineering**, *[S. l.]*, v. 88–89, p. 136–144, 2012. DOI: 10.1016/j.petrol.2011.12.021. Disponível em: http://dx.doi.org/10.1016/j.petrol.2011.12.021.

CHEN, Zuorong; BUNGER, A. P.; ZHANG, Xi; JEFFREY, Robert G. Cohesive zone finite element-based modeling of hydraulic fractures. **Acta Mechanica Solida Sinica**, *[S. l.]*, v. 22, n. 5, p. 443–452, 2009. DOI: 10.1016/S0894-9166(09)60295-0. Disponível em: http://dx.doi.org/10.1016/S0894-9166(09)60295-0.

CHENG, Wan; JIN, Yan; CHEN, Mian. Reactivation mechanism of natural fractures by hydraulic fracturing in naturally fractured shale reservoirs. **Journal of Natural Gas Science and Engineering**, *[S. l.]*, v. 23, p. 431–439, 2015. DOI: 10.1016/j.jngse.2015.11.018. Disponível em: http://dx.doi.org/10.1016/j.jngse.2015.01.031.

CHUPRAKOV, D.; MELCHAEVA, O.; PRIOUL, R. Injection-sensitive mechanics of hydraulic fracture interaction with discontinuities. **Rock Mechanics and Rock Engineering**, *[S. l.]*, v. 47, n. 5, p. 1625–1640, 2014. DOI: 10.1007/s00603-014-0596-7.

CLEMO, Thomas Meldon. **Dual permeability modeling of fractured media**, 1994. Disponível em: https://open.library.ubc.ca/collections/831/items/1.0052916.

COATS, K. H. **Implicit Compositional Simulation of Single-Porosity and Dual-Porosity ReservoirsSPE Symposium on Reservoir Simulation**Houston, TexasSociety of Petroleum Engineers, , 1989. DOI: 10.2118/18427-MS.

COUSSY, Olivier. **Poromechanics.** [s.l.] : John Wiley & Sons, Ltd, 2004. DOI: 10.1002/0470092718.

CRISFIELD, M. A. **Non-linear Finite Element Analysis of Solids and Structures**. 1. ed. [s.l: s.n.].

CROUCH, S. L. Solution of plane elasticity problems by the displacement discontinuity method. I. Infinite body solution. **International Journal for Numerical Methods in Engineering**, *[S. l.]*, v. 10, n. 2, p. 301–343, 1976. DOI: 10.1002/nme.1620100206. Disponível em: https://doi.org/10.1002/nme.1620100206.

CRUZ, FRANCISCO. **AN XFEM ELEMENT TO MODEL INTERSECTIONS BETWEEN HYDRAULIC AND NATURAL FRACTURES IN POROUS ROCKS**. 2018. PUC-Rio, *[S. l.]*, 2018. DOI: https://doi.org/10.17771/PUCRio.acad.35888.

CRUZ, Francisco; ROEHL, Deane; VARGAS, Eurípedes do Amaral. An XFEM element to model intersections between hydraulic and natural fractures in porous rocks. **International Journal of Rock Mechanics and Mining Sciences**, *[S. l.]*, v. 112, n. March, p. 385–397, 2018. DOI: 10.1016/j.ijrmms.2018.10.001.

DAHI TALEGHANI, Arash; GONZALEZ-CHAVEZ, Miguel; YU, Hao; ASALA, Hope. Numerical simulation of hydraulic fracture propagation in naturally fractured formations using the cohesive zone model. **Journal of Petroleum Science and Engineering**, *[S. l.]*, v. 165, n. February, p. 42–57, 2018. DOI: 10.1016/j.petrol.2018.01.063. Disponível em: https://doi.org/10.1016/j.petrol.2018.01.063.

DAHI TALEGHANI, Arash; GONZALEZ, Miguel; SHOJAEI, Amir. Overview of numerical models for interactions between hydraulic fractures and natural fractures: Challenges and limitations. **Computers and Geotechnics**, *[S. l.]*, v. 71, p. 361–368, 2016. DOI: 10.1016/j.compgeo.2015.09.009.

DAI, Qingli; NG, Kenny. 2D cohesive zone modeling of crack development in cementitious digital samples with microstructure characterization. **Construction and Building Materials**, *[S. l.]*, v. 54, p. 584–595, 2014. DOI: 10.1016/j.conbuildmat.2013.12.095.

DAVIES, Richard J.; ALMOND, Sam; WARD, Robert S.; JACKSON, Robert B.; ADAMS, Charlotte; WORRALL, Fred; HERRINGSHAW, Liam G.; GLUYAS, Jon G.; WHITEHEAD, Mark A. Oil and gas wells and their integrity: Implications for shale and unconventional resource exploitation. **Marine and Petroleum Geology**, *[S. l.]*, v. 56, p. 239–254, 2014. DOI: 10.1016/j.marpetgeo.2014.03.001.

DE LAGUNA, Wallace. Disposal of radioactive wastes by hydraulic fracturing. Part I. General concept and first field experiments. **Nuclear Engineering and Design**, *[S. l.]*, v. 3, n. 2, p. 338–352, 1966. DOI: 10.1016/0029-5493(66)90120-8.

DERSHOWITZ, Bill; LAPOINTE, Paul; EIBEN, Thorsten; WEI, Lingli. Integration of Discrete Feature Network Methods With Conventional Simulator Approaches. **SPE Reservoir Evaluation & Engineering**, *[S. l.]*, v. 3, n. 02, p. 165–170, 2000. DOI: 10.2118/62498-PA. Disponível em: https://doi.org/10.2118/62498-PA.

DESROCHES, J. Stress testing with the micro-hydraulic fracturing technique: Focus on fracture reopening. *In*: IN PROCEEDINGS OF THE 35TH US SYMPOSIUM ON ROCK MECHANICS 1995, Balkema, Rotterdam. **Anais** [...]. Balkema, Rotterdam: American Rock Mechanics Association, 1995. p. 217–223. DOI: 10.1016/b978-0-408-50030-2.50030-4. Disponível em: https://www.onepetro.org/conference-paper/ARMA-95-0217.

DETOURNAY, E. Propagation Regimes of Fluid-Driven Fractures in Impermeable Rocks. **International Journal of Geomechanics**, *[S. l.]*, v. 4, n. 1, p. 35–45, 2004. DOI: 10.1061/(ASCE)1532-3641(2004)4:1(35). Disponível em: http://ascelibrary.org/doi/10.1061/%28ASCE%291532-3641%282004%294%3A1%2835%29.

DETOURNAY, Emmanuel. Mechanics of Hydraulic Fractures. **Annual Review of Fluid Mechanics**, *[S. l.]*, v. 48, n. 1, p. 311–339, 2016. DOI: 10.1146/annurev-fluid-010814-014736.

DONG, Zhenzhen; LI, Weirong; LEI, Gang; WANG, Huijie; WANG, Cai. Embedded Discrete Fracture Modeling as a Method to Upscale Permeability for Fractured Reservoirs. **Energies**, *[S. l.]*, v. 12, n. 5, p. 812bb, 2017. DOI: 10.3390/en10101471. Disponível em: https://doi.org/10.3390/en10101471.

DONTSOV, E. V. An approximate solution for a penny-shaped hydraulic fracture that accounts for fracture toughness, fluid viscosity, and leak-off. **International Journal of Fracture**, *[S. l.]*, v. 205, n. 2, p. 221–237, 2016. DOI: 10.1098/rsos.160737.

DONTSOV, E. V. An approximate solution for a plane strain hydraulic fracture that accounts for fracture toughness, fluid viscosity, and leak-off. **International Journal of Fracture**, *[S. l.]*, v. 205, n. 2, p. 221–237, 2017. DOI: 10.1007/s10704-017-0192-4.

FADAKAR ALGHALANDIS, Younes. ADFNE: Open source software for discrete fracture network engineering, two and three dimensional applications. **Computers and Geosciences**, *[S. l.]*, v. 102, p. 1–11, 2017. DOI: 10.1016/j.cageo.2017.02.002.

FATAHI, Hassan; HOSSAIN, Md Mofazzal; SARMADIVALEH, Mohammad.

Numerical and experimental investigation of the interaction of natural and propagated hydraulic fracture. **Journal of Natural Gas Science and Engineering**, *[S. l.]*, v. 37, p. 409–424, 2017. DOI: 10.1016/j.jngse.2016.11.054. Disponível em: http://dx.doi.org/10.1016/j.jngse.2016.11.054.

FLEMISCH, Bernd; BERRE, Inga; BOON, Wietse; FUMAGALLI, Alessio; SCHWENCK, Nicolas; SCOTTI, Anna; STEFANSSON, Ivar; TATOMIR, Alexandru. Benchmarks for single-phase flow in fractured porous media. **Advances in Water Resources**, *[S. l.]*, v. 111, p. 239–258, 2018. DOI: 10.1016/j.advwatres.2017.10.036.

FOSSEN, Haakon; SCHULTZ, Richard A.; SHIPTON, Zoe K.; MAIR, Karen. **Deformation bands in sandstone: A reviewJournal of the Geological Society**Geological Society of London, , 2007. DOI: 10.1144/0016-76492006-036.

FUMAGALLI, Alessio; KEILEGAVLEN, Eirik; SCIALÒ, Stefano. Conforming, non-conforming and non-matching discretization couplings in discrete fracture network simulations. **Journal of Computational Physics**, *[S. l.]*, v. 376, p. 694–712, 2019. DOI: 10.1016/j.jcp.2018.09.048.

GARAGASH, Dmitry I. Cohesive-Zone Effects in Hydraulic Fracture Propagation Cohesive-Zone E ff ects in Hydraulic Fracture Propagation. *[S. l.]*, n. August, 2019. DOI: 10.13140/RG.2.2.30061.54241.

GARAGASH, Dmitry I.; DETOURNAY, Emmanuel; ADACHI, Jose I. **Multiscale tip asymptotics in hydraulic fracture with leak-off**. [s.l: s.n.]. v. 669 DOI: 10.1017/S002211201000501X.

GEUBELLE, Philippe H.; BAYLOR, Jeffrey S. Impact-induced delamination of composites: A 2D simulation. **Composites Part B: Engineering**, *[S. l.]*, v. 29, n. 5, p. 589–602, 1998. DOI: 10.1016/S1359-8368(98)00013-4.

GEUZAINE, Christophe; REMACLE, Jean-François. Gmsh: A 3-D finite element mesh generator with built-in pre- and post-processing facilities. **International Journal for Numerical Methods in Engineering**, *[S. l.]*, v. 79, n. 11, p. 1309–1331, 2009. DOI: 10.1002/nme.2579. Disponível em: https://doi.org/10.1002/nme.2579.

GHASSEMI, A.; ZHOU, X. A three-dimensional thermo-poroelastic model for fracture response to injection/extraction in enhanced geothermal systems. **Geothermics**, *[S. l.]*, v. 40, n. 1, p. 39–49, 2011. DOI: 10.1016/j.geothermics.2010.12.001. Disponível em: http://dx.doi.org/10.1016/j.geothermics.2010.12.001.

GONG, Bin. Effective Models of Fractured Systems. *[S. l.]*, n. September, p. 1–151, 2007. Disponível em: https://pangea.stanford.edu/ERE/pdf/pereports/PhD/Gong07.pdf?

GONG, J.; ROSSEN, W. R. Characteristic fracture spacing in primary and secondary recovery for naturally fractured reservoirs. **Fuel**, *[S. l.]*, v. 223, n. February, p. 470–485, 2018. DOI: 10.1016/j.fuel.2018.02.046. Disponível em: https://doi.org/10.1016/j.fuel.2018.02.046.

GONZALEZ, M.; TALEGHANI, A. Dahi; OLSEN, J. E. SPE-173384-MS A Cohesive Model for Modeling Hydraulic Fractures in Naturally Fractured Formations. *[S. l.]*, v. d, p. 3–5, 2015. DOI: 10.2118/173384-MS. Disponível em: https://www.onepetro.org/download/conference-paper/SPE-173384-MS?id=conference-paper%2FSPE-173384-MS.

GRANET, S.; FABRIE, P.; LEMONNIER, P.; QUINTARD, M. A Single-Phase Flow Simulation of Fractured Reservoir Using a Discrete Representation of Fractures. *In*: 2014, **Anais** [...]. : EAGE Publications, 2014. p. cp-102-00025. DOI: 10.3997/2214-4609.201406633.

GRASSL, P.; FAHY, C.; GALLIPOLI, D.; WHEELER, S. J. On a 2D hydro-mechanical lattice approach for modelling hydraulic fracture. **Journal of the Mechanics and Physics of Solids**, *[S. l.]*, v. 75, p. 104–118, 2015. DOI: 10.1016/j.jmps.2014.11.011.

GREEN, A. E.; SNEDDON, I. N. The distribution of stress in the neighbourhood of a flat elliptical crack in an elastic solid. **Mathematical Proceedings of the Cambridge**

Philosophical Society, *[S. l.]*, v. 46, n. 1, p. 159–163, 1950. DOI: 10.1017/S0305004100025585.

GU, Hongren; WENG, X.; LUND, Jeffrey B.; MACK, Mark G.; GANGULY, Utpal; SUAREZ-RIVERA, Roberto. Hydraulic Fracture Crossing Natural Fracture at Nonorthogonal Angles: A Criterion and Its Validation. **SPE Production & Operations**, *[S. l.]*, v. 27, n. 01, p. 20–26, 2012. DOI: 10.2118/139984-PA. Disponível em: http://www.onepetro.org/doi/10.2118/139984-PA.

GUIDUCCI, Chiara; PELLEGRINO, Antonio; RADU, Jean-Pol; COLLIN, Frédéric; CHARLIER, Robert. Numerical modeling of hydro-mechanical fracture behavior. **Numerical models in Geomechanics**, *[S. l.]*, p. 293–299, 2002. DOI: 10.1111/j.1752-8062.2012.00338.x. Disponível em: http://hdl.handle.net/2268/490.

GUO, Jianchun; LIU, Yuxuan. A comprehensive model for simulating fracturing fluid leakoff in natural fractures. **Journal of Natural Gas Science and Engineering**, *[S. l.]*, v. 21, p. 9770–985, 2014. DOI: 10.1016/j.jngse.2014.10.020. Disponível em: http://dx.doi.org/10.1016/j.jngse.2014.10.020.

GUO, Jianchun; ZHAO, Xing; ZHU, Haiyan; ZHANG, Xudong; PAN, Rui. Numerical simulation of interaction of hydraulic fracture and natural fracture based on the cohesive zone finite element method. **Journal of Natural Gas Science and Engineering**, *[S. l.]*, v. 25, p. 180–188, 2015. DOI: 10.1016/j.jngse.2015.05.008. Disponível em: http://dx.doi.org/10.1016/j.jngse.2015.05.008.

GUTIERREZ, Marte; YOUN, Dong Joon. Effects of fracture distribution and length scale on the equivalent continuum elastic compliance of fractured rock masses. **Journal of Rock Mechanics and Geotechnical Engineering**, *[S. l.]*, v. 7, n. 6, p. 626–637, 2015. DOI: 10.1016/j.jrmge.2015.07.006. Disponível em: http://dx.doi.org/10.1016/j.jrmge.2015.07.006.

GUTIÉRREZ, RENATO. **INVESTIGATION OF HYDRAULIC FRACTURING THROUGH ANALYTICAL AND NUMERICAL MODELS**. 2016. PUC-Rio, *[S. l.]*, 2016. DOI: https://doi.org/10.17771/PUCRio.acad.28072.

HADDAD, Mahdi; DU, Jing; VIDAL-GILBERT, Sandrine. Integration of Dynamic Microseismic Data With a True 3D Modeling of Hydraulic-Fracture Propagation in the Vaca Muerta Shale. **SPE Journal**, *[S. l.]*, v. 22, n. 06, p. 1714–1738, 2017. DOI: 10.2118/179164-PA. Disponível em: http://www.onepetro.org/doi/10.2118/179164-PA.

HEINEMANN, Zoltán E.; MITTERMEIR, Georg M. Derivation of the Kazemi-Gilman-Elsharkawy Generalized Dual Porosity Shape Factor. **Transport in Porous Media**, *[S. l.]*, v. 91, n. 1, p. 123–132, 2012. DOI: 10.1007/s11242-011-9836-4.

HERMANSEN, H.; LANDA, G. H.; SYLTE, J. E.; THOMAS, L. K. Experiences after 10 years of waterflooding the Ekofisk Field, Norway. **Journal of Petroleum Science and Engineering**, *[S. l.]*, v. 26, n. 1, p. 11–18, 2000. DOI: https://doi.org/10.1016/S0920-4105(00)00016-4. Disponível em: http://www.sciencedirect.com/science/article/pii/S0920410500000164.

HILL, A. C.; THOMAS, G. W. A New Approach for Simulating Complex Fractured Reservoirs. **Middle East Oil Technical Conference and Exhibition**, *[S. l.]*, p. 429–436, 1985. DOI: 10.2118/13537-MS. Disponível em: http://www.onepetro.org/doi/10.2118/13537-MS.

HOLDITCH, Stephen A. Tight Gas Sands. **Journal of Petroleum Technology**, *[S. l.]*, v. 58, n. 06, p. 86–93, 2006. DOI: 10.2118/103356-JPT. Disponível em: http://www.onepetro.org/doi/10.2118/103356-JPT.

HOWARD, George C.; FAST, C. R. Optimum fluid characteristics for fracture extension. **Drilling and Production Practice 1957**, *[S. l.]*, p. 261–270, 1957.

JEFFREY, R. G.; MILLS, K. W. Hydraulic fracturing applied to inducing longwall coal mine goaf falls. *In*: 4TH NORTH AMERICAN ROCK MECHANICS SYMPOSIUM 2000, **Anais** [...]. : American Rock Mechanics Association, 2000. p. 423–430. Disponível em:

https://www.onepetro.org/conference-paper/ARMA-2000-0423.

JEFFREY, R. G.; ZHANG, X.; BUNGER, A. P. Hydraulic fracturing of naturally fractured reservoirs. **Thirty-Fifth Workshop on Geothermal Reservoir Engineering, Stanford University, Stanford, California**, *[S. l.]*, p. 1–3, 2010.

JEFFREY, Robert G.; ZHANG, Xi; THIERCELIN, Marc J. Hydraulic Fracture Offsetting in Naturally Fractures Reservoirs: Quantifying a Long-Recognized Process. **SPE Hydraulic Fracturing Technology Conference**, *[S. l.]*, 2009. DOI: 10.2118/119351-MS. Disponível em: http://www.onepetro.org/doi/10.2118/119351-MS.

JIN, W.; ARSON, C.; BUSETTI, S. **Simulation of Mode II Unconstrained Fracture Path Formation Coupled with Continuum Anisotropic Damage Propagation in Shale50th U.S. Rock Mechanics/Geomechanics Symposium**Houston, TexasAmerican Rock Mechanics Association, , 2016. Disponível em: https://doi.org/.

JIN, Wencheng; XU, Hao; ARSON, Chloé; BUSETTI, Seth. Computational model coupling mode II discrete fracture propagation with continuum damage zone evolution. **International Journal for Numerical and Analytical Methods in Geomechanics**, *[S. l.]*, v. 41, n. 2, p. 223–250, 2017. DOI: 10.1002/nag.2553. Disponível em: https://doi.org/10.1002/nag.2553.

KARIMI-FARD, Mohammad; DURLOFSKY, Louis J.; AZIZ, Khalid. An Efficient Discrete Fracture Model Applicable for General Purpose Reservoir Simulators. **SPE Journal**, *[S. l.]*, v. 9, n. 2, p. 227–236, 2004. DOI: https://doi.org/10.2118/88812-PA. Disponível em: https://doi.org/10.2118/88812-PA.

KAZEMI, H.; MERRILL, L. S.; PORTERFIELD, K. L.; ZEMAN, P. R. Numerical Simulation of Water-Oil Flow in Naturally Fractured Reservoirs. **Society of Petroleum Engineers Journal**, *[S. l.]*, v. 16, n. 06, p. 317–326, 1976. DOI: 10.2118/5719-PA. Disponível em: http://www.onepetro.org/doi/10.2118/5719-PA.

KESHAVARZI, Reza; JAHANBAKHSHI, Reza. Investigation of Hydraulic and Natural Fracture Interaction: Numerical Modeling or Artificial Intelligence? **Effective and Sustainable Hydraulic Fracturing**, *[S. l.]*, p. 1039–1058, 2013. DOI: 10.5772/56382. Disponível em: http://cdn.intechopen.com/pdfs/44673/InTech-Investigation_of_hydraulic_and_natural_fracture_interaction_numerical_modeling_or_artificial_intelligence_.pdf.

KHOEI, A. R.; HIRMAND, M.; VAHAB, M.; BAZARGAN, M. An enriched FEM technique for modeling hydraulically driven cohesive fracture propagation in impermeable media with frictional natural faults: Numerical and experimental investigations. **International Journal for Numerical Methods in Engineering**, *[S. l.]*, v. 104, n. 6, p. 439–468, 2015. DOI: 10.1002/nme.4944. Disponível em: http://doi.wiley.com/10.1002/nme.4944.

KHOEI, A. R.; VAHAB, M.; HIRMAND, M. Modeling the interaction between fluid-driven fracture and natural fault using an enriched-FEM technique. **International Journal of Fracture**, *[S. l.]*, v. 197, n. 1, p. 1–24, 2016. DOI: 10.1007/s10704-015-0051-0.

KHRISTIANOVIC, S.; ZHELTOV, Y. **Formation of Vertical Fractures by Means of Highly Viscous Liquid4th World Petroleum Congress**Rome, ItalyWorld Petroleum Congress, , 1955. Disponível em: https://doi.org/.

KIM, Jong Gyun; DEO, Milind D. Finite element, discrete-fracture model for multiphase flow in porous media. **AIChE Journal**, *[S. l.]*, v. 46, n. 6, p. 1120–1130, 2000. DOI: 10.1002/aic.690460604.

KIM, Won Seok; HAN, Sangsoo; AHN, Jinmo; UM, Wooyong. Investigation of 3 H, 99 Tc, and 90 Sr transport in fractured rock and the effects of fracture-filling/coating material at LILW disposal facility. **Environmental Geochemistry and Health**, *[S. l.]*, v. 41, n. 1, p. 411–425, 2019. DOI: 10.1007/s10653-018-0123-y. Disponível em: https://doi.org/10.1007/s10653-018-0123-y.

KOVALYSHEN, Yevhen. **Fluid-Driven Fracture in Poroelastic Medium**. 2010.

University of Minnesota, *[S. l.]*, 2010. Disponível em: https://conservancy.umn.edu/bitstream/handle/11299/59581/1/Kovalyshen_umn_0130E_10962.pdf.

KUCHUK, Fikri; BIRYUKOV, Denis. Pressure-Transient Behavior of Continuously and Discretely Fractured Reservoirs. **SPE Reservoir Evaluation & Engineering**, *[S. l.]*, v. 17, n. 01, p. 82–97, 2014. DOI: 10.2118/158096-PA. Disponível em: https://doi.org/10.2118/158096-PA.

LEE, Jeongwoo; CHOI, Sung-Uk; CHO, Woncheol. A comparative study of dual-porosity model and discrete fracture network model. **KSCE Journal of Civil Engineering**, *[S. l.]*, v. 3, n. 2, p. 171–180, 1999. DOI: 10.1007/BF02829057. Disponível em: https://doi.org/10.1007/BF02829057.

LEE, S. H.; LOUGH, M. F.; JENSEN, C. L. Hierarchical modeling of flow in naturally fractured formations with multiple length scales. **Water Resources Research**, *[S. l.]*, v. 37, n. 3, p. 443–455, 2001. DOI: 10.1029/2000WR900340.

LEMONNIER, P.; BOURBIAUX, B. Simulation of Naturally Fractured Reservoirs. State of the Art. **Oil & Gas Science and Technology – Revue de l'Institut Français du Pétrole**, *[S. l.]*, v. 65, n. 2, p. 263–286, 2010. DOI: 10.2516/ogst/2009067. Disponível em: http://ogst.ifpenergiesnouvelles.fr/10.2516/ogst/2009067.

LI, Liyong; LEE, Seong Hee. Efficient Field-Scale Simulation for Black Oil in a Naturally Fractured Reservoir via Discrete Fracture Networks and Homogenized Media. *In*: INTERNATIONAL OIL & GAS CONFERENCE AND EXHIBITION IN CHINA 2006, **Anais** [...]. : Society of Petroleum Engineers, 2006. DOI: 10.2118/103901-MS.

LI, Quanshu; XING, Huilin; LIU, Jianjun; LIU, Xiangchon. A review on hydraulic fracturing of unconventional reservoir. **Petroleum**, *[S. l.]*, v. 1, n. 1, p. 8–15, 2015. DOI: 10.1016/j.petlm.2015.03.008. Disponível em: http://linkinghub.elsevier.com/retrieve/pii/S2405656115000140.

LI, Y.; DENG, J. G.; LIU, W.; FENG, Y. Modeling hydraulic fracture propagation using cohesive zone model equipped with frictional contact capability. **Computers and Geotechnics**, *[S. l.]*, v. 91, p. 58–70, 2017. DOI: 10.1016/j.compgeo.2017.07.001.

LIM, K. T.; AZIZ, K. Matrix-fracture transfer shape factors for dual-porosity simulators. **Journal of Petroleum Science and Engineering**, *[S. l.]*, v. 13, n. 3, p. 169–178, 1995. DOI: https://doi.org/10.1016/0920-4105(95)00010-F. Disponível em: http://www.sciencedirect.com/science/article/pii/092041059500010F.

LIU, Zhenghe; REN, Xiaokai; LIN, Xiao; LIAN, Haojie; YANG, Lusheng; YANG, Jianfeng. Effects of Confining Stresses , Pre - crack Inclination Angles and Injection Rates : Observations from Large - Scale True Triaxial and Hydraulic Fracturing Tests in Laboratory. **Rock Mechanics and Rock Engineering**, *[S. l.]*, v. 53, n. 4, p. 1991–2000, 2020. DOI: 10.1007/s00603-019-01995-2. Disponível em: https://doi.org/10.1007/s00603-019-01995-2.

MAIER, Christine; SCHMID, Karen S.; AHMED, Mohamed; GEIGER, Sebastian. Multi-Rate Mass-Transfer Dual-Porosity Modelling Using the Exact Analytical Solution for Spontaneous Imbibition. *In*: EAGE ANNUAL CONFERENCE & EXHIBITION INCORPORATING SPE EUROPEC 2013, London, UK. **Anais** [...]. London, UK: Society of Petroleum Engineers, 2013. p. 13. DOI: 10.2118/164926-MS. Disponível em: https://doi.org/10.2118/164926-MS.

MALONEY, Kelly O.; YOXTHEIMER, David A. Production and disposal of waste materials from gas and oil extraction from the marcellus shale Play in Pennsylvania. **Environmental Practice**, *[S. l.]*, v. 14, n. 4, p. 278–287, 2012. DOI: 10.1017/S146604661200035X.

MANZOLI, Osvaldo L.; CLETO, Pedro R.; SÁNCHEZ, Marcelo; GUIMARÃES, Leonardo J. N.; MAEDO, Michael A. On the use of high aspect ratio finite elements to model hydraulic fracturing in deformable porous media. **Computer Methods in Applied Mechanics and Engineering**, *[S. l.]*, v. 350, p. 57–80, 2019. DOI:

10.1016/j.cma.2019.03.006. Disponível em: https://doi.org/10.1016/j.cma.2019.03.006.

MARCH, Rafael; DOSTER, Florian; GEIGER, Sebastian. Assessment of CO2 Storage Potential in Naturally Fractured Reservoirs With Dual-Porosity Models. **Water Resources Research**, *[S. l.]*, v. 54, n. 3, p. 1650–1668, 2018. DOI: 10.1002/2017WR022159.

MCCLURE, M.; HORNE, R. Characterizing Hydraulic Fracturing With a Tendency-for-Shear-Stimulation Test. **SPE Reservoir Evaluation & Engineering**, *[S. l.]*, v. 17, n. 2, p. 233–243, 2014. DOI: 10.2118/166332-PA.

MEJIA, Cristian; ROEHL, Deane; RUEDA, Julio; QUEVEDO, Roberto. A new approach for modeling three-dimensional fractured reservoirs with embedded complex fracture networks. **Computers and Geotechnics**, *[S. l.]*, v. 130, 2021. DOI: 10.1016/j.compgeo.2020.103928.

MEJIA SANCHEZ, Eleazar Cristian; RUEDA CORDERO, Julio Alberto; ROEHL, Deane. Numerical simulation of three-dimensional fracture interaction. **Computers and Geotechnics**, *[S. l.]*, v. 122, n. March, p. 103528, 2020. DOI: 10.1016/j.compgeo.2020.103528. Disponível em: https://doi.org/10.1016/j.compgeo.2020.103528.

MENDES, Carlos A. T.; GATTASS, Marcelo; ROEHL, Deane. The gema framework - An innovative framework for the development of multiphysics and multiscale simulations. **ECCOMAS Congress 2016 - Proceedings of the 7th European Congress on Computational Methods in Applied Sciences and Engineering**, *[S. l.]*, v. 4, n. June, p. 7886–7894, 2016. DOI: 10.7712/100016.2383.6771.

MOINFAR, Ali; NARR, Wayne; HUI, Mun-Hong; MALLISON, Bradley T.; LEE, Seong Hee. **Comparison of Discrete-Fracture and Dual-Permeability Models for Multiphase Flow in Naturally Fractured ReservoirsSPE Reservoir Simulation Symposium**The Woodlands, Texas, USASociety of Petroleum Engineers, , 2011. DOI: 10.2118/142295-MS. Disponível em: https://doi.org/10.2118/142295-MS.

MONTEAGUDO, Jorge E. Palomin.; FIROOZABADI, Abbas. Control-volume model for simulation of water injection in fractured media: Incorporating matrix heterogeneity and reservoir wettability effects. **SPE Journal**, *[S. l.]*, v. 12, n. 3, p. 355–366, 2007. DOI: 10.2118/98108-PA.

MONTGOMERY, Carl. Fracturing Fluids. *In*: JEFFREY, Rob; MCLENNAN, John; BUNGER, Andrew (org.). **Effective and Sustainable Hydraulic Fracturing**. Oklahoma , USA: intechopen, 2013. v. 32p. 137–144. DOI: http://dx.doi.org/10.5772/56192.

NASIRISAVADKOUHI, Arash. A Comparison Study of KGD , PKN and a A Comparison Study of KGD , PKN and a Modified P3D Model . *[S. l.]*, n. November, p. 8, 2015. DOI: 10.13140/RG.2.1.3860.7201.

NG, K. L. A.; SMALL, J. C. Behavior of joints and interfaces subjected to water pressure. **Computers and Geotechnics**, *[S. l.]*, v. 20, n. 1, p. 71–93, 1997. DOI: https://doi.org/10.1016/S0266-352X(96)00015-8.

NIKAM, Aditya; AWOLEKE, Obadare O.; AHMADI, Mohabbat; FAIRBANKS, Alaska. Modeling the Interaction Between Natural and Hydraulic Fractures Using. **Society of Petroleum Engineers**, *[S. l.]*, n. 1987, 2016. DOI: 10.2118/180364-MS. Disponível em: https://doi.org/10.2118/180364-MS.

NIKOLIĆ, Mijo; KARAVELIĆ, Emir; IBRAHIMBEGOVIC, Adnan; MIŠČEVIĆ, Predrag. **Lattice Element Models and Their Peculiarities**. [s.l.] : Springer Netherlands, 2018. v. 25 DOI: 10.1007/s11831-017-9210-y.

NOORISHAD, Jahan; MEHRAN, Mohsen. An upstream finite element method for solution of transient transport equation in fractured porous media. **Water Resources Research**, *[S. l.]*, v. 18, n. 3, p. 588–596, 1982. DOI: 10.1029/WR018i003p00588.

NORBECK, Jack H.; MCCLURE, Mark W.; LO, Jonathan W.; HORNE, Roland N. An embedded fracture modeling framework for simulation of hydraulic fracturing and shear

stimulation. **Computational Geosciences**, *[S. l.]*, v. 20, n. 1, 2016. DOI: 10.1007/s10596-015-9543-2.

NORDGREN, R. P. Propagation of a Vertical Hydraulic Fracture. **Society of Petroleum Engineers Journal**, *[S. l.]*, v. 12, n. 04, p. 306–314, 1972. DOI: 10.2118/3009-PA. Disponível em: https://doi.org/10.2118/3009-PA.

O'SULLIVAN, Michael J.; PRUESS, Karsten; LIPPMANN, Marcelo J. State of the art geothermal reservoir simulation. **Geothermics**, *[S. l.]*, v. 30, n. 4, p. 395–429, 2001. DOI: 10.1016/S0375-6505(01)00005-0.

ORTIZ, M.; PANDOLFI, A. Finite-Deformation Irreversible Cohesive Elements for Three-Dimensional Crack-Propagation Analysis. **INTERNATIONAL JOURNAL FOR NUMERICAL METHODS IN ENGINEERING Int. J. Numer. Meth. Engng**, *[S. l.]*, v. 1282, n. September 1997, p. 1267–1282, 1999. DOI: 10.1002/(SICI)1097-0207(19990330)44:9<1267::AID-NME486>3.0.CO;2-7.

PEREIRA, Fernanda L. G.; ROEHL, Deane; PAULO LAQUINI, João; OLIVEIRA, Maria Fernanda F.; COSTA, Alvaro M. Fault reactivation case study for probabilistic assessment of carbon dioxide sequestration. **International Journal of Rock Mechanics and Mining Sciences**, *[S. l.]*, v. 71, p. 310–319, 2014. DOI: 10.1016/j.ijrmms.2014.08.003. Disponível em: http://dx.doi.org/10.1016/j.ijrmms.2014.08.003.

PEREIRA, RENAN. **ASPECTS OF MODELING FRACTURE PROPAGATION WITH THE EXTENDED FINITE ELEMENT METHOD (XFEM)**. 2018. PUC-Rio, *[S. l.]*, 2018. DOI: https://doi.org/10.17771/PUCRio.acad.37613.

PERKINS, T. K.; KERN, L. R. Widths of Hydraulic Fractures. **Journal of Petroleum Technology**, *[S. l.]*, v. 13, n. 09, p. 937–949, 1961. DOI: 10.2118/89-PA. Disponível em: https://doi.org/10.2118/89-PA.

POTLURI, N.; ZHU, D.; HILL, A. D. Effect of Natural Fractures on Hydraulic Fracture Propagation. **Society of Petroleum Engineers**, *[S. l.]*, v. 94568, 2005. DOI: 10.2118/94568-ms.

RADOVITZKY, R.; SEAGRAVES, A.; TUPEK, M.; NOELS, L. A scalable 3D fracture and fragmentation algorithm based on a hybrid, discontinuous Galerkin, cohesive element method. **Computer Methods in Applied Mechanics and Engineering**, *[S. l.]*, v. 200, n. 1–4, p. 326–344, 2011. DOI: 10.1016/j.cma.2010.08.014.

RAHMAN, M. M.; RAHMAN, S. S. Studies of Hydraulic Fracture-Propagation Behavior in Presence of Natural Fractures: Fully Coupled Fractured-Reservoir Modeling in Poroelastic Environments. **International Journal of Geomechanics**, *[S. l.]*, v. 13, n. 6, p. 809–826, 2013. DOI: 10.1061/(ASCE)GM.1943-5622.0000274. Disponível em: http://ascelibrary.org/doi/10.1061/%28ASCE%29GM.1943-5622.0000274.

RAMIREZ, MARIO. **2D AND 3D MODELING TO EVALUATE REACTIVATION OF GEOLOGICAL FAULTS IN OIL RESERVOIRS**. 2016. PUC-Rio, *[S. l.]*, 2016. DOI: https://doi.org/10.17771/PUCRio.acad.32495.

RAO, Xiang; CHENG, Linsong; CAO, Renyi; JIA, Pin; LIU, Hao; DU, Xulin. A modified projection-based embedded discrete fracture model (pEDFM) for practical and accurate numerical simulation of fractured reservoir. **Journal of Petroleum Science and Engineering**, *[S. l.]*, v. 187, p. 106852, 2020. DOI: 10.1016/j.petrol.2019.106852.

REMIJ, E. W.; REMMERS, J. J. C.; HUYGHE, J. M.; SMEULDERS, D. M. J. The enhanced local pressure model for the accurate analysis of fluid pressure driven fracture in porous materials. **Computer Methods in Applied Mechanics and Engineering**, *[S. l.]*, v. 286, p. 293–312, 2015. DOI: 10.1016/j.cma.2014.12.025. Disponível em: http://dx.doi.org/10.1016/j.cma.2014.12.025.

RENSHAW, C. E.; POLLARD, D. D. Are large differential stresses required for straight fracture propagation paths? **Journal of Structural Geology**, *[S. l.]*, v. 16, n. 6, p. 817–822, 1994. DOI: https://doi.org/10.1016/0191-8141(94)90147-3. Disponível em: http://www.sciencedirect.com/science/article/pii/0191814194901473.

RICE, James R.; CLEARY, Michael P. Some basic stress diffusion solutions for fluid-saturated elastic porous media with compressible constituents. **Reviews of Geophysics**, *[S. l.]*, v. 14, n. 2, 1976. DOI: https://doi.org/10.1029/RG014i002p00227.

RUEDA CORDERO, Julio Alberto.; MEJIA SANCHEZ, Eleazar Cristian.; ROEHL, Deane.; PEREIRA, Leonardo Cabral. Hydro-mechanical modeling of hydraulic fracture propagation and its interactions with frictional natural fractures. **Computers and Geotechnics**, *[S. l.]*, v. 111, p. 290–300, 2019. DOI: 10.1016/j.compgeo.2019.03.020. Disponível em: https://linkinghub.elsevier.com/retrieve/pii/S0266352X19300953.

RUEDA CORDERO, Julio Alberto; MEJIA, Cristian; NOREÑA, Nilthson; ROEHL, Deane. A three-dimensional enhanced dual porosity and dual permeability approach for hydro-mechanical modeling of naturally fractured rocks. **International Journal for Numerical Methods in Engineering**, *[S. l.]*, p. 1–37, 2020. a. DOI: 10.1002/nme.6594. Disponível em: https://doi.org/10.1002/nme.6594.

RUEDA CORDERO, Julio Alberto; MEJIA, Cristian; QUEVEDO, Roberto; ROEHL, Deane. Impacts of natural fractures on hydraulic fracturing treatment in all asymptotic propagation regimes. **Computer Methods in Applied Mechanics and Engineering**, *[S. l.]*, v. 371, p. 113296, 2020. b. DOI: 10.1016/j.cma.2020.113296. Disponível em: https://linkinghub.elsevier.com/retrieve/pii/S0045782520304813.

RUEDA CORDERO, Julio Alberto; MEJIA, Cristian; ROEHL, Deane. Numerical simulation of hydraulic and natural fracture interaction and propagation. **Cilamce 2017**, *[S. l.]*, 2017.

RUEDA CORDERO, Julio Alberto; MEJIA SANCHEZ, Eleazar Cristian; ROEHL, Deane. Hydraulic fracture propagation and its interaction with open and sealed natural fractures. *In*: 53ND U.S. ROCK MECHANICS/GEOMECHANICS SYMPOSIUM 2019a, **Anais** [...]. [s.l: s.n.]

RUEDA CORDERO, Julio Alberto; MEJIA SANCHEZ, Eleazar Cristian; ROEHL, Deane. Hydromechanical modeling of unrestricted crack propagation in fractured formations using intrinsic cohesive zone model. **Engineering Fracture Mechanics**, *[S. l.]*, v. 221, p. 106655, 2019. b. DOI: 10.1016/J.ENGFRACMECH.2019.106655.

RUEDA, J. **REACTIVATION OF GEOLOGICAL FAULTS WITH DISCRETE AND DISTRIBUTED NUMERICAL MODELS**. 2013. MSc. Thesis, Pontifical Catholic University of Rio de Janeiro, *[S. l.]*, 2013. DOI: https://doi.org/10.17771/PUCRio.acad.25164.

RUEDA, J. C.; NOREÑA, N. V; OLIVEIRA, M. F. F.; ROEHL, D. **Numerical Models for Detection of Fault Reactivation in Oil and Gas Fields48th U.S. Rock Mechanics/Geomechanics Symposium**Minneapolis, MinnesotaAmerican Rock Mechanics Association, , 2014. Disponível em: https://doi.org/.

RUEDA, Julio A.; MEJIA, Eleazar C.; ROEHL, Deane. Integrated discrete fracture and dual porosity - Dual permeability models for fluid flow in deformable fractured media. **Journal of Petroleum Science and Engineering**, *[S. l.]*, v. 175, n. December 2018, p. 644–653, 2019. DOI: 10.1016/j.petrol.2018.12.053. Disponível em: https://doi.org/10.1016/j.petrol.2018.12.053.

RUTLEDGE, J. T.; MAYERHOFER, M. J.; PHILLIPS, W. S. Faulting Induced by Forced Fluid Injection and Fluid Flow Forced by Faulting: An Interpretation of Hydraulic-Fracture Microseismicity, Carthage Cotton Valley Gas Field, Texas. **Bulletin of the Seismological Society of America**, *[S. l.]*, v. 94, n. 5, p. 1817–1830, 2004. DOI: 10.1785/012003257. Disponível em: https://dx.doi.org/10.1785/012003257.

RUTQVIST, Jonny; RINALDI, Antonio P.; CAPPA, Frédéric; MORIDIS, George J. Modeling of fault reactivation and induced seismicity during hydraulic fracturing of shale-gas reservoirs. **Journal of Petroleum Science and Engineering**, *[S. l.]*, v. 107, p. 31–44, 2013. DOI: https://doi.org/10.1016/j.petrol.2013.04.023. Disponível em: http://www.sciencedirect.com/science/article/pii/S0920410513001241.

SARKAR, Sudipta; TOKSOZ, M. Nafi; BURNS, Daniel R. **Fluid flow modeling in fractures**. [s.l.] : Massachusetts Institute of Technology. Earth Resources Laboratory,

2004. Disponível em: http://hdl.handle.net/1721.1/68616.

SAVITSKI, A. A.; DETOURNAY, E. Propagation of a penny-shaped fluid-driven fracture in an impermeable rock: Asymptotic solutions. **International Journal of Solids and Structures**, *[S. l.]*, v. 39, n. 26, p. 6311–6337, 2002. DOI: 10.1016/S0020-7683(02)00492-4.

SEGURA, J. M.; CAROL, I. Coupled HM analysis using zero-thickness interface elements with double nodes—Part II: Verification and application. **International Journal for Numerical and Analytical Methods in Geomechanics**, *[S. l.]*, v. 32, n. 18, p. 2103–2123, 2008. a. DOI: 10.1002/nag.730. Disponível em: https://doi.org/10.1002/nag.730.

SEGURA, J. M.; CAROL, I. Coupled HM analysis using zero-thickness interface elements with double nodes. Part I: Theoretical model. **International Journal for Numerical and Analytical Methods in Geomechanics**, *[S. l.]*, v. 32, n. 18, p. 2083–2101, 2008. b. DOI: 10.1002/nag.735. Disponível em: https://doi.org/10.1002/nag.735.

SEGURA, J. M.; CAROL, Ignacio. On zero-thickness interface elements for diffusion problems. **International Journal for Numerical and Analytical Methods in Geomechanics**, *[S. l.]*, v. 28, n. 9, p. 947–962, 2004. DOI: 10.1002/nag.358.

SETTARI, A.; PRICE H.S. Simulation of Hydraulic Fracturing In Low-Penneability Reservoirs. **Soc. Petroleum Eng. J.**, *[S. l.]*, v. 24, n. 2, p. 141–152, 1984. DOI: 10.2118/8939-PA. Disponível em: https://www.onepetro.org/download/journal-paper/SPE-8939-PA?id=journal-paper%2FSPE-8939-PA.

SHAHID, A. S. A.; FOKKER, P. A.; ROCCA, V. A review of numerical simulation strategies for hydraulic fracturing, natural fracture reactivation and induced microseismicity prediction. **Open Petroleum Engineering Journal**, *[S. l.]*, v. 9, p. 72–91, 2016. DOI: 10.2174/1874834101609010072.

SHEN, Xinpu; SHEN, Guoyang. Poro-elasto-plastic Calculation on Fault Reactivation Caused by Hydraulic Fracturing in a Field Offshore West Africa. *[S. l.]*, p. 8–13, 2014.

SHENG, D.; SLOAN, S. W. Time stepping schemes for coupled displacement and pore pressur e e analysis. **Computational Mechanics**, *[S. l.]*, v. 31, p. 122–134, 2003. DOI: 10.1007/s00466-002-0399-7. Disponível em: https://www.newcastle.edu.au/__data/assets/pdf_file/0011/22610/60_Time-stepping-schemes-for-coupled-displacement-and-pore-pressure-analysis.pdf. Acesso em: 23 nov. 2018.

SHENG, Daichao; SLOAN, Scott W. **Load stepping schemes for critical state modelsINTERNATIONAL JOURNAL FOR NUMERICAL METHODS IN ENGINEERING Int. J. Numer. Meth. Engng**. [s.l: s.n.]. DOI: 10.1002/1097-0207(20010110)50:1<67::AID-NME22>3.0.CO;2-N. Disponível em: https://www.newcastle.edu.au/__data/assets/pdf_file/0005/22577/46_Load-stepping-schemes-for-critical-state-models.pdf. Acesso em: 23 nov. 2018.

SHENG, Daichao; SLOAN, Scott W.; ABBO, Andrew J. An Automatic Newton–Raphson Scheme. **International Journal of Geomechanics**, *[S. l.]*, v. 2, n. 4, p. 471–502, 2002. DOI: 10.1080/15323640208500187. Disponível em: https://www.tandfonline.com/doi/abs/10.1080/15323640208500187.

SHIN, Hosung; SANTAMARINA, J. Carlos. An implicit joint-continuum model for the hydro-mechanical analysis of fractured rock masses. **International Journal of Rock Mechanics and Mining Sciences**, *[S. l.]*, v. 119, n. March, p. 140–148, 2019. DOI: 10.1016/j.ijrmms.2019.04.006. Disponível em: https://doi.org/10.1016/j.ijrmms.2019.04.006.

SIBSON, Richard H. **Fluid Flow Accompanying Faulting: Field Evidence and ModelsEarthquake Prediction**: Maurice Ewing Series., 1981. DOI: doi:10.1029/ME004p0593. Disponível em: https://doi.org/10.1029/ME004p0593.

SILVA, Patrick. **AN IMPLEMENTATION OF THE EXTENDED FINITE ELEMENT**

METHOD FOR ANALYSIS OF TWO-DIMENSIONAL FRACTURE PROPAGATION. 2015. PUC-Rio, *[S. l.]*, 2015. DOI: https://doi.org/10.17771/PUCRio.acad.25699.

SILVEIRA, Claudia Siqueira Da; ALVIM, Antonio Carlos Marques; RIVERO OLIVA, Jose De Jesus. Radionuclide transport in fractured rock: Numerical assessment for high level waste repository. **Science and Technology of Nuclear Installations**, *[S. l.]*, v. 2013, 2013. DOI: 10.1155/2013/827961.

SMITH, Michael. **ABAQUS/Standard User's Manual, Version 16**Providence, RISimulia, , 2016. Disponível em: http://130.149.89.49:2080/v2016/index.html.

SNEDDON, I. N. The Distribution of Stress in the Neighbourhood of a Crack in an Elastic Solid. **Proceedings of the Royal Society A: Mathematical, Physical and Engineering Sciences**, *[S. l.]*, v. 187, n. 1009, p. 229–260, 1946. DOI: 10.1098/rspa.1946.0077. Disponível em: http://rspa.royalsocietypublishing.org/cgi/doi/10.1098/rspa.1946.0077.

SUPPACHOKNIRUN, Theerapat; TUTUNCU, Azra N. Hydraulic Fracturing and Production Optimization in Eagle Ford Shale Using Coupled Geomechanics and Fluid Flow Model. **Rock Mechanics and Rock Engineering**, *[S. l.]*, v. 50, n. 12, p. 3361–3378, 2017. DOI: 10.1007/s00603-017-1357-1.

TALEGHANI, Arash Dahi. Fracture Re-Initiation As a Possible Branching Mechanism During Hydraulic Fracturing. **44th U.S. Rock Mechanics Symposium and 5th U.S.-Canada Rock Mechanics Symposium**, *[S. l.]*, 2010. Disponível em: http://www.onepetro.org/mslib/app/Preview.do?paperNumber=ARMA-10-278&societyCode=ARMA.

ŢENE, Matei; BOSMA, Sebastian B. M.; AL KOBAISI, Mohammed Saad; HAJIBEYGI, Hadi. Projection-based Embedded Discrete Fracture Model (pEDFM). **Advances in Water Resources**, *[S. l.]*, v. 105, p. 205–216, 2017. DOI: 10.1016/j.advwatres.2017.05.009.

TERZAGHI, Karl. **Subject IndexTheoretical Soil Mechanics**: Wiley Online Books., 1943. DOI: doi:10.1002/9780470172766.indsub. Disponível em: https://doi.org/10.1002/9780470172766.indsub.

THOMAS, Robin N.; PALUSZNY, Adriana; ZIMMERMAN, Robert W. Permeability of Three-Dimensional Numerically Grown Geomechanical Discrete Fracture Networks With Evolving Geometry and Mechanical Apertures. **Journal of Geophysical Research: Solid Earth**, *[S. l.]*, v. 125, n. 4, 2020. DOI: 10.1029/2019jb018899.

TURON, Albert; DÁVILA, Carlos G.; CAMANHO, Pedro Ponces; COSTA, Josep. An Engineering Solution for using Coarse Meshes in the Simulation of Delamination With Cohesive Zone Models. **Nasa/Tm-2005-213547**, *[S. l.]*, n. March, p. 1–26, 2005. DOI: 10.1007/978-3-540-79056-3_2.

VAN AS, A.; JEFFREY, R. G. Caving induced by hydraulic fracturing at Northparkes Mines. *In*: 4TH NORTH AMERICAN ROCK MECHANICS SYMPOSIUM 2000, **Anais** [...]. : American Rock Mechanics Association, 2000. p. 353–360. Disponível em: https://www.onepetro.org/conference-paper/ARMA-2000-0353.

VANDAMME, Luc M.; ROEGIERS, Jean Claude. Poroelasticity in hydraulic fracturing simulators. **JPT, Journal of Petroleum Technology**, *[S. l.]*, v. 42, n. 9, p. 1199–1203, 1990. DOI: 10.2118/16911-PA.

VERMEER, P.A., DE BORST, R. Non-Associated Plasticity for Soils, Concrete and Rock. **Heron**, *[S. l.]*, v. 29, p. 1–64, 1984. Disponível em: http://resolver.tudelft.nl/uuid:4ee188ab-8ce0-4df3-adf5-9010ebfaabf0.

WANG, Hanyi. Journal of Natural Gas Science and Engineering Hydraulic fracture propagation in naturally fractured reservoirs : Complex fracture or fracture networks. **Journal of Natural Gas Science and Engineering**, *[S. l.]*, v. 68, n. August 2018, p. 102911, 2019. DOI: 10.1016/j.jngse.2019.102911. Disponível em: https://doi.org/10.1016/j.jngse.2019.102911.

WANG, X. F.; YANG, Z. J.; YATES, J. R.; JIVKOV, A. P.; ZHANG, Ch. Monte Carlo simulations of mesoscale fracture modelling of concrete with random aggregates and pores. **Construction and Building Materials**, *[S. l.]*, v. 75, p. 35–45, 2015. DOI: https://doi.org/10.1016/j.conbuildmat.2014.09.069. Disponível em: http://www.sciencedirect.com/science/article/pii/S095006181401085X.

WANG, Xiao Long; SHI, Fang; LIU, Chuang; LU, De Tang; LIU, He; WU, Heng An. Extended finite element simulation of fracture network propagation in formation containing frictional and cemented natural fractures. **Journal of Natural Gas Science and Engineering**, *[S. l.]*, v. 50, n. March 2017, p. 309–324, 2018. DOI: 10.1016/j.jngse.2017.12.013. Disponível em: https://doi.org/10.1016/j.jngse.2017.12.013.

WARPINSKI, N. R.; TEUFEL, L. W. Influence of Geologic Discontinuities on Hydraulic Fracture Propagation. **Journal of Petroleum Technology**, *[S. l.]*, p. 689–696, 1987. DOI: https://doi.org/10.2118/13224-PA. Disponível em: http://www.sciencedirect.com/science/article/pii/B978081551554850015X.

WARREN, J. E. E.; ROOT, P. J. Jj. The Behavior of Naturally Fractured Reservoirs. **Society of Petroleum Engineers Journal**, *[S. l.]*, v. 3, n. 03, p. 245–255, 1963. DOI: 10.2118/426-PA. Disponível em: http://www.onepetro.org/doi/10.2118/426-PA.

WENG, Xiaowei. Modeling of complex hydraulic fractures in naturally fractured formation. **Journal of Unconventional Oil and Gas Resources**, *[S. l.]*, v. 9, p. 114–135, 2015. DOI: 10.1016/j.juogr.2014.07.001. Disponível em: http://dx.doi.org/10.1016/j.juogr.2014.07.001.

WENG, Xiaowei; KRESSE, Olga; COHEN, Charles-Edouard; WU, Ruiting; GU, Hongren. Modeling of Hydraulic-Fracture-Network Propagation in a Naturally Fractured Formation. **SPE Production & Operations**, *[S. l.]*, v. 26, n. 04, p. 368–380, 2011. DOI: 10.2118/140253-PA. Disponível em: http://www.onepetro.org/doi/10.2118/140253-PA.

WENG, Xiaowei; VARAHANARESH, Sesetty; KRESSE, Olga. Investigation of Shear-Induced Permeability in Unconventional Reservoirs. **American Rock Mechanics Association**, *[S. l.]*, p. 1–15, 2015. DOI: 10.1016/j.molcata.2014.01.013.

WONG, J. K. W.; SOGA, K.; XU, X.; DELENNE, J. Y. **Three Dimensional Simulation of Hydraulic Fracturing on Fault using Lattice Element Method13th ISRM International Congress of Rock Mechanics**Montreal, CanadaInternational Society for Rock Mechanics and Rock Engineering, , 2015. Disponível em: https://doi.org/.

WONG, John Kam-wing. **multi-scale hydraulic fracturing stimulation in heterogeneous material using Dual Lattice Model**. 2017. University of Cambridge, *[S. l.]*, 2017. DOI: https://doi.org/10.17863/CAM.17439. Disponível em: https://doi.org/10.17863/CAM.17439.

WU, L.; TJAHJANTO, D.; BECKER, G.; MAKRADI, A.; JÉRUSALEM, A.; NOELS, L. A micro–meso-model of intra-laminar fracture in fiber-reinforced composites based on a discontinuous Galerkin/cohesive zone method. **Engineering Fracture Mechanics**, *[S. l.]*, v. 104, p. 162–183, 2013. DOI: https://doi.org/10.1016/j.engfracmech.2013.03.018. Disponível em: http://www.sciencedirect.com/science/article/pii/S0013794413001252.

XIE, Jun; HUANG, Haoyong; MA, Huiyun; ZENG, Bo; TANG, Jizhou; YU, Wei; WU, Kan. Journal of Natural Gas Science and Engineering Numerical investigation of effect of natural fractures on hydraulic-fracture propagation in unconventional reservoirs. **Journal of Natural Gas Science and Engineering**, *[S. l.]*, v. 54, n. September 2017, p. 143–153, 2018. DOI: 10.1016/j.jngse.2018.04.006. Disponível em: https://doi.org/10.1016/j.jngse.2018.04.006.

XIE, Linmao; MIN, Ki Bok; SHEN, Baotang. Simulation of hydraulic fracturing and its interactions with a pre-existing fracture using displacement discontinuity method. **Journal of Natural Gas Science and Engineering**, *[S. l.]*, v. 36, p. 1284–1294, 2016. DOI: 10.1016/j.jngse.2016.03.050. Disponível em: http://dx.doi.org/10.1016/j.jngse.2016.03.050.

XU, Chaoshui; DOWD, Peter Alan; TIAN, Zhao Feng. A simplified coupled hydro-

thermal model for enhanced geothermal systems. **Applied Energy**, *[S. l.]*, v. 140, p. 135–145, 2015. DOI: 10.1016/j.apenergy.2014.11.050. Disponível em: http://dx.doi.org/10.1016/j.apenergy.2014.11.050.

XU, Shiqian; FENG, Qihong; WANG, Sen; JAVADPOUR, Farzam; LI, Yuyao. Optimization of multistage fractured horizontal well in tight oil based on embedded discrete fracture model. **Computers and Chemical Engineering**, *[S. l.]*, v. 117, p. 291–308, 2018. DOI: 10.1016/j.compchemeng.2018.06.015.

XU, Yifei; FERNANDES, Bruno Ramon Batista; MARCONDES, Francisco; SEPEHRNOORI, Kamy. Embedded discrete fracture modeling for compositional reservoir simulation using corner-point grids. **Journal of Petroleum Science and Engineering**, *[S. l.]*, v. 177, p. 41–52, 2019. DOI: 10.1016/j.petrol.2019.02.024.

YAN, Xia; HUANG, Zhaoqin; YAO, Jun; LI, Yang; FAN, Dongyan. An efficient embedded discrete fracture model based on mimetic finite difference method. **Journal of Petroleum Science and Engineering**, *[S. l.]*, v. 145, p. 11–21, 2016. DOI: 10.1016/j.petrol.2016.03.013.

YAN, Xia; HUANG, Zhaoqin; YAO, Jun; ZHANG, Zhao; LIU, Piyang; LI, Yang; FAN, Dongyan. Numerical simulation of hydro-mechanical coupling in fractured vuggy porous media using the equivalent continuum model and embedded discrete fracture model. **Advances in Water Resources**, *[S. l.]*, v. 126, p. 137–154, 2019. DOI: 10.1016/j.advwatres.2019.02.013.

YANG, Jianwen. Reactive silica transport in fractured porous media: Analytical solution for a single fracture. **Computers and Geosciences**, *[S. l.]*, v. 38, n. 1, p. 80–86, 2012. DOI: 10.1016/j.cageo.2011.05.008.

YAO, Jun; HUANG, Zhao-Qin. **Fractured Vuggy Carbonate Reservoir Simulation**. Berlin, Heidelberg: Springer Berlin Heidelberg, 2017. DOI: 10.1007/978-3-662-55032-8.

ZAVATTIERI, Pablo D.; ESPINOSA, Horacio D. Grain Level Analysis of Crack Initiation and. *[S. l.]*, v. 4, p. 4291–4311, 2001. DOI: 10.1016/S1359-6454(01)00292-0. Disponível em: ect.com/science/article/pii/S1359645401002920.

ZHANG, J.; ROEGIERS, J. C. Double porosity finite element method for borehole modeling. **Rock Mechanics and Rock Engineering**, *[S. l.]*, v. 38, n. 3, p. 217–242, 2005. DOI: 10.1007/s00603-005-0052-9.

ZHANG, Zhengyu (Jenny); PAULINO, Glaucio H.; CELES, Waldemar. Extrinsic cohesive modelling of dynamic fracture and microbranching instability in brittle materials. **International Journal for Numerical Methods in Engineering**, *[S. l.]*, v. 72, n. 8, p. 893–923, 2007. DOI: 10.1002/nme.2030. Disponível em: https://doi.org/10.1002/nme.2030.

ZHOU, Fangqi; SHI, Anfeng; WANG, Xiaohong. An efficient finite difference model for multiphase flow in fractured reservoirs. **Petroleum Exploration and Development**, *[S. l.]*, v. 41, n. 2, p. 262–266, 2014. DOI: 10.1016/S1876-3804(14)60031-8.

ZHOU, Jian; CHEN, Mian; JIN, Yan; ZHANG, Guang-qing. Analysis of fracture propagation behavior and fracture geometry using a tri-axial fracturing system in naturally fractured reservoirs. **International Journal of Rock Mechanics and Mining Sciences**, *[S. l.]*, v. 45, n. 7, p. 1143–1152, 2008. DOI: https://doi.org/10.1016/j.ijrmms.2008.01.001. Disponível em: http://www.sciencedirect.com/science/article/pii/S1365160908000105.

ZHOU, Jian; XUE, Chengjin. Experimental Investigation of Fracture Interaction between Natural Fractures and Hydraulic Fracture in Naturally Fractured Reservoirs. **Proceedings of SPE EUROPEC/EAGE Annual Conference and Exhibition**, *[S. l.]*, n. May 2011, p. 1–12, 2011. DOI: 10.2118/142890-MS. Disponível em: http://www.onepetro.org/mslib/servlet/onepetropreview?id=SPE-142890-MS&soc=SPE.

ZHOU, Jian; ZHANG, Luqing; PAN, Zhejun; HAN, Zhenhua. Numerical studies of interactions between hydraulic and natural fractures by Smooth Joint Model. **Journal of Natural Gas Science and Engineering**, *[S. l.]*, v. 46, p. 592–602, 2017. DOI:

10.1016/j.jngse.2017.07.030. Disponível em: https://doi.org/10.1016/j.jngse.2017.07.030.

ZIDANE, Ali; FIROOZABADI, Abbas. **Efficient Simulation of Two-Phase Compositional Flow in Fractured Reservoirs Using 3D Unstructured Gridding in Complex GeometriesSPE Annual Technical Conference and Exhibition**Dallas, Texas, USASociety of Petroleum Engineers, , 2018. DOI: 10.2118/191405-MS. Disponível em: https://doi.org/10.2118/191405-MS.

ZIELONKA, Matias G.; SEARLES, Kevin H.; NING, Jing; BUECHLER, Scott R. Development and Validation of Fully-Coupled Hydraulic Fracturing Simulation Capabilities. **SIMULIA Community Conference, SCC2014**, *[S. l.]*, p. 1–31, 2014.

ZIMMERMAN, Robert W.; YEO, In-Wook. **Fluid Flow in Rock Fractures: From the Navier-Stokes Equations to the Cubic LawDynamics of Fluids in Fractured Rock**: Geophysical Monograph Series., 2000. DOI: doi:10.1029/GM122p0213. Disponível em: https://agupubs.onlinelibrary.wiley.com/doi/10.1029/GM122p0213.

ZYVOLOSKI, George A.; ROBINSON, Bruce A.; VISWANATHAN, Hari S. Generalized dual porosity: A numerical method for representing spatially variable sub-grid scale processes. **Advances in Water Resources**, *[S. l.]*, v. 31, n. 3, p. 535–544, 2008. DOI: 10.1016/j.advwatres.2007.11.006.